

**Determining Cellular and Molecular Mechanisms of
Multivalent Soluble Antigen Arrays that Contribute to
Therapeutic Efficacy Against a Murine Model of Multiple
Sclerosis**

By

Brittany L. Hartwell

Submitted to the graduate degree program in Bioengineering and the Graduate Faculty of the
University of Kansas in partial fulfillment of the requirements for the degree of Doctor of
Philosophy.

Chairperson Dr. Cory Berkland

Dr. Stevin Gehrke

Dr. Teruna Siahaan

Dr. Arghya Paul

Dr. Elizabeth Friis

Date Defended: December 5, 2016

The Dissertation Committee for Brittany Hartwell
certifies that this is the approved version of the following dissertation:

**Determining Cellular and Molecular Mechanisms of
Multivalent Soluble Antigen Arrays that Contribute to
Therapeutic Efficacy Against a Murine Model of Multiple
Sclerosis**

Chairperson Dr. Cory Berkland

Date approved: December 5, 2016

Abstract

A pressing need exists for antigen-specific immunotherapies (ASIT) that induce selective tolerance in autoimmune disease while avoiding deleterious global immunosuppression. Multivalent soluble antigen arrays (SAgA_{PLP:LABL}), consisting of a hyaluronic acid (HA) linear polymer backbone co-grafted with multiple copies of autoantigen (PLP) and cell adhesion inhibitor (LABL) peptides, are designed to induce tolerance to a specific multiple sclerosis (MS) autoantigen. Previous *in vivo* studies established that SAgA_{PLP:LABL} was therapeutic in experimental autoimmune encephalomyelitis (EAE), a murine model of MS. This dissertation sought to elucidate SAgA therapeutic cellular mechanisms while identifying therapeutic molecular properties. In Chapter 2, the role of two-signal co-delivery was explored by evaluating EAE *in vivo* results in conjunction with *in silico* molecular dynamics simulations and nanomaterial properties for various covalent and physical combinations of HA, PLP, and LABL. We found that co-delivery of both primary autoantigen and secondary inhibitory signal was necessary for therapeutic efficacy against EAE. In Chapters 3 and 4, the SAgA_{PLP:LABL} cellular mechanism was investigated in a model B cell system by evaluating binding, specificity, and signaling modulation *in vitro*. Here, we developed click-conjugated cSAgA_{PLP:LABL} which, unlike SAgA_{PLP:LABL}, employed a non-hydrolyzable linker chemistry to conjugate PLP and LABL to HA. cSAgA_{PLP:LABL} exhibited significantly enhanced *in vivo* efficacy compared to hydrolyzable SAgA_{PLP:LABL}. We found that cSAgA_{PLP:LABL} acted through high avidity, antigen-specific B cell binding, targeting the B cell receptor (BCR) to dampen BCR-mediated signaling. Our conclusions point to induction of antigen-specific B cell anergy as the cSAgA_{PLP:LABL} therapeutic mechanism and present a promising option for ASIT.

Acknowledgements

I would first like to express my sincere appreciation to my advisor, Cory Berkland: I am so grateful for having had the opportunity to work with you. You helped me find my passion for research. Thank you for having faith in me from the beginning, back when I didn't know what I was doing (or really what I wanted to do). Thank you for offering me the flexibility and freedom to figure that out. With your guidance and direction, support and patience, I discovered a fascination for immunology and learned how to approach problems in this field from a unique engineering perspective. Most of all, thank you for your mentorship and friendship. It has been a privilege to work with someone who I look up to both professionally and personally.

I am also grateful for the past and present members of my dissertation committee: Stevin Gehrke, Teruna Siahaan, Arghya Paul, Elizabeth Friis, Michael Detamore, and Jennifer Laurence. Thank you for offering your time, guidance, feedback, and expertise throughout my PhD.

To my fellow Berkland Lab Group members, who have been my teammates over the past five years: thank you for your camaraderie, friendship, and support! Much of this work would not have been possible without you, in particular Lorena Antunez, Laura Northrup, Chad Pickens, Sharadvi Thati, Martin Leon, Matthew Christopher, Danny Griffin, Jian Qian, Bradley Sullivan, Joshua Sestak, Nashwa El-Gendy, and my undergraduate researchers Aaron Garza, Michelle Sarnowski, and Annie Lynn.

I would like to thank my collaborators in the Microscopy and Analytical Imaging Lab (MAI), the Kansas Vaccine Institute (KVI), and the Molecular Dynamics and Modeling Lab, especially Heather Shinogle of MAI and Francisco Martinez-Becerra of KVI for their advice and

assistance. These collaborations enabled me to work on creative interdisciplinary projects, an aspect of my doctoral research that I really enjoyed and valued.

I am grateful for the Bioengineering Graduate Program, which allowed me the freedom to explore different research areas and the flexibility to shape my curriculum to my interests. To Denise Bridwell, the BioE program assistant who makes the world go 'round: thank you for being awesome and ever supportive.

I am indebted to Madison 'Al' and Lila Self for their generosity and vision. Thanks to them, the Self Graduate Fellowship funded four years of my graduate career and the accompanying Development Program provided me with unparalleled opportunities for training in leadership, policy, and communication. I am grateful for the wonderful and inspiring members of my 2011-2015 cohort, who have become good friends: Sarah Borland, Angela Pierce, Nikki Galvis, Matthew Josephson, Lei Shi, and Karl Kammerer. Additionally, I would like to thank current and former Self Graduate Fellowship staff for their dedication to the program and for giving me the opportunity to be a part of it: Cathy Dwigans, Patty Dannenberg, Stefani Buchwitz, Sharon Graham, Howard Mossberg, and Michael Roberts.

Lastly, I am deeply thankful for my family and friends, and for their unwavering love, support, and patience. To my mother- and father-in-law, Jean and John Hartwell, thank you for your continued encouragement and confidence. To my brother, Alex Rover, your creativity, passion, and fearlessness inspire me. To my parents, thank you for providing me with opportunities that have enabled me to be where I am today.

To my dad, Craig Rover, thank you for being my coach, running partner, and friend. Through the thousands of miles we have run together, you have taught me about hard work,

perseverance, heart, and how to push myself out of my comfort zone. Over the past few years I have found these lessons to be invaluable in the lab as well as on the roads and trails.

To my mom, Diane Rover, thank you for being an amazing role model; for cultivating in me from a young age a knack for creativity and an interest in math, science, and problem solving; and for encouraging me to go into engineering. You have always been at the ready with motivation and counsel. Thank you for teaching me to keep my chin up, think positive, and believe in myself.

To my husband, Doug Hartwell, thank you for your love, support, encouragement, sacrifice, and patience. You have put up with endless discussions of ‘FITCs’, ‘HPLCs’, and ‘SAGAs’, countless late nights at lab, and repeated dinner duty. Thank you for being my teammate and my rock throughout this experience; I could not have done it without you.

Above all, I thank God, and aspire to give of the gifts I’ve been given.

Brittany L. Hartwell

December 5, 2016

Table of Contents

Chapter I: Introduction	1
1. Multivalent Nanomaterials: Learning from Vaccines and Progressing to Antigen-Specific Immunotherapies	2
1.1 Mechanisms of the Immune Response	2
1.2 Introduction to Vaccines	4
2. Multivalent Nanomaterials	6
2.1 Valency	7
2.2 Size	9
2.3 Shape	10
2.4 Flexibility	10
3. Multivalent Ligand Display on Linear Polymers	12
4. Multivalent Display of Two Different Ligands on Linear Polymers	18
5. Proposed Mechanisms for Immune Response to Multivalent Nanomaterials	22
6. Conclusions and Future Directions	27
References	38
Chapter II: Molecular Dynamics of Multivalent Soluble Antigen Arrays Support Two-Signal Co-delivery Mechanism in the Treatment of Experimental Autoimmune Encephalomyelitis	47
1. Introduction	48
2. Materials and Methods	50
2.1 Materials	50
2.2 Preparation and Characterization of Soluble Antigen Arrays	50
2.3 Particle Characterization by Dynamic Light Scattering	51
2.4 Clinical EAE Study in Mice	52
2.5 Molecular Dynamics Simulations of Soluble Antigen Arrays	53
2.6 Statistical Analysis	54
3. Results	55
3.1 Synthesis and Characterization of Soluble Antigen Arrays	55
3.2 Dynamic Light Scattering Demonstrates Aggregation and Formation of Nanoparticles	56
3.3 Clinical EAE Studies Indicate Therapeutic Efficacy	57
3.4 Molecular Dynamics Simulations of Soluble Antigen Arrays	59
4. Discussion	61
5. Conclusions	64
References	82
Chapter III: Antigen-Specific Binding of Multivalent Soluble Antigen Arrays Induces Receptor Clustering and Impedes B Cell Receptor Mediated Signaling	88
1. Introduction	89
2. Materials and Methods	91
2.1 Materials	91
2.2 Peptide Synthesis	92

2.3	SAgA and FITC-Labeled SAgA Synthesis	92
2.4	SAgA and FITC-Labeled SAgA Characterization	93
2.5	Cell Culture and Activation	94
2.6	Flow Cytometry Binding Studies	94
2.7	Fluorescence Microscopy Using a Microfluidics Platform	96
2.8	Calcium Flux Signaling Flow Cytometry Assay	97
2.9	Resazurin Cell Metabolism Assay	98
2.10	Statistical Analysis	98
3.	Results	98
3.1	SAgA and FITC-Labeled SAgA Characterization	98
3.2	Cell Activation	99
3.3	Flow Cytometry Binding Studies: Association and Competitive Dissociation	99
3.4	Fluorescence Microscopy Using a Microfluidics Platform	102
3.5	Calcium Flux Signaling Flow Cytometry Assay	103
3.6	IgM Blocking	104
4.	Discussion	104
5.	Conclusions	109
	References	123

Chapter IV: Multivalent Antigen Arrays Exhibit High Avidity Binding and Modulation of B Cell Receptor-Mediated Signaling to Drive Efficacy Against Experimental Autoimmune Encephalomyelitis	130
1. Introduction	131
2. Materials and Methods	133
2.1 Materials	133
2.2 SAgA Synthesis and FITC Labeling	134
2.3 SAgA and FITC-SAgA Analytical Characterization	135
2.4 Click-conjugated ‘cSAgA’ Synthesis and PennGreen Labeling	135
2.5 Cell Culture	137
2.6 Flow Cytometry Binding Assay	137
2.7 Calcium Flux Signaling Assay	138
2.8 Fluorescence Microscopy	139
2.9 Clinical EAE Study in Mice	139
2.10 Statistical Analysis	140
3. Results and Discussion	141
3.1 cSAgA Structural Design	141
3.2 cSAgA Analytical Characterization	141
3.3 SAgA Analytical Characterization	143
3.4 Flow Cytometry Binding Assay	143
3.5 Calcium Flux Signaling Flow Cytometry Assay	144
3.6 Fluorescence Microscopy	146
3.7 Clinical EAE Studies	147
4. Conclusions	149
References	166

Chapter V: Conclusions and Future Work	170
1. Conclusions	171
2. Future Work.....	174
References	184

Chapter I: Introduction

1. Multivalent Nanomaterials: Learning from Vaccines and Progressing to Antigen-Specific Immunotherapies

The use of nanomaterials such as polymers and colloids in medicine has grown dramatically over the past two decades ¹. While the applications vary greatly, many have explored the ability of these materials to generate an immune response. Nanomaterials can be engineered to have specific characteristics such as size, charge, and shape, properties that influence biodistribution and immune response. Furthermore, current techniques allow researchers to modify nanomaterial display, such as the number, density, and ratio of ligands or antigens on the nanomaterial itself. Although appreciated retrospectively, prophylactic vaccines used to invoke a protective immune response have primarily been colloidal microparticles, which have paved the road towards the development of therapeutic nanomaterials ². To help explain immune response to nanomaterials, research has continued to explore linkages between nanomaterial characteristics, route of administration, transport, final deposition site, and the resultant immune response ^{2,3}. In particular, researchers must continue to probe the ability of nanomaterials presenting small molecules, peptides, or other ligands to elicit specific and sustained immune responses not only in the context of vaccines, but also for other immunomodulatory therapies. Finally, new insights for designing multivalent nanomaterial immunotherapies for autoimmune diseases should emerge when considering the backdrop of vaccine design.

1.1 Mechanisms of the Immune Response

Unlike many other organ systems of the body, the immune system has a unique and vital conscious component in its ability to distinguish ‘self’ (endogenous) and ‘non-self’ (exogenous) antigens. Critical studies reviewed elsewhere have laid the groundwork for identifying

mechanisms and communication networks between specialized cell types and resultant immunological responses. In general, a healthy immune system has the ability to act in an antigen-specific manner and can opt to make several decisions after recognition of antigen: recognize antigen as 1) “self” and elicit a non-response to that antigen, 2) “non-self” and elicit a non-response (generally termed anergy), or 3) “non-self” evoking an immune response against that antigen, potentially leading to immunological memory to that antigen. Specific discrimination between “self” and “non-self” antigens is an essential feature of the immune system. Breakdown in this recognition is thought to be a key player in autoimmune diseases.

One simple model that has helped researchers describe this discrimination phenomenon is the 2-signal model of lymphocyte activation, suggesting the context of antigen presentation helps determine the downstream immune response. In general, interaction of naive B or T cells with antigen is not sufficient to initiate an immune response. It has been proposed that lack of stimulation is a mechanism whereby autoreactive B and T cells, which have evaded negative selection processes, are prevented from reacting with self-antigens in the periphery, thereby preventing them from causing autoimmune disease. The model proposes that antigen delivered with a secondary activation “context” signal (i.e. costimulation) can evoke a robust immune response toward the offending antigen and can lead to long-term immunological memory. Many of these costimulatory molecules are thought to be mediated by cell-cell interactions of surface receptors (e.g. CD28:CD80, CD40:CD40L)⁴⁻⁶. Soluble mediators such as innate immune receptor ligands (e.g. lipopolysaccharide, Poly I:C) have also been shown to enhance antigen-specific immune response and continue to be actively researched as adjuvants in vaccine formulations^{7,8}. Conversely, recent evidence shows secondary signals can also regulate the immune response, suggesting immunological memory can be reprogrammed to elicit an anergic

response leading to antigen-specific immune tolerance⁹⁻¹¹. While new mechanisms of immune system activation are being discovered at a rapid pace, many identified mechanisms of immune response can be applied to this 2-signal approach to antigen recognition, especially for vaccine formulation strategies classically defined as antigen (signal 1) and adjuvant (signal 2).

1.2 Introduction to Vaccines

Vaccines have historically used colloidal suspensions in the 10 µm range to stimulate adaptive immunity and to provide prophylactic protection from infectious diseases^{12,13}. The immune system can be primed to prevent and eliminate disease by exposure to a weakened form of the causative pathogen¹⁴⁻¹⁶. As vaccines have evolved, they have moved toward incorporating safer, more purified pathogen components. Subunit or recombinant vaccines, which deliver only necessary protective antigens, help to eliminate exposure to portions of the pathogen that may cause unnecessary reactivity or harmful side effects. Unfortunately, simple delivery of specific antigen epitopes without immunogenic components (i.e. innate immune system agonists) is often not sufficient to produce long-lasting protective immunity. Therefore, subunit vaccines have been designed to deliver antigen with immunogenic particles, or adjuvants¹⁷.

While there is no unified mechanism of action for the array of vaccines currently on the market, the success of colloidal or emulsion-based adjuvants is hypothesized to lie in their ability to 1) enhance and/or stabilize the physical presentation of antigen by acting as an antigen carrier and/or depot, and 2) provide direct stimulatory signals critical for immune cell recruitment and activation. Characteristics of the interaction between adjuvant and antigen such as surface adsorption, changes in protein folding, and antigen epitope stability impact the release of stable antigen as well as the potency and long-term efficacy of a vaccine¹⁸.

Of the adjuvants approved for human use, the majority have been postulated to form a depot at the injection site ¹⁹. Depots are thought to provide high local concentration of antigen and extend its release over time, allowing for adequate recruitment of immune cells required for establishing long-term immunological memory. Adjuvants also enhance antigen recognition and uptake by making antigen more particulate in nature. Antigens adsorbed to the surface of polydisperse nanometer- to micron-sized aluminum adjuvant particles in suspension, or delivered with oil droplets within an emulsion, fall within a size range comparable to that of a virus or bacteria, and thus more readily undergo phagocytosis by APCs ^{14,20}. Consequently, portions of, if not entire, viruses and bacteria have been used to create nanoparticles to potentiate immune responses. Intrinsically immunogenic particles such as virus-like particles (VLPs), virosomes, and AS04 provide costimulatory signals for specific innate immune-stimulating receptors ^{18,20}. For instance, the highly repetitive viral proteins delivered on VLPs can effectively stimulate the pattern recognition receptors (PRRs) of the innate immune system. The adjuvant AS04 combines aluminum phosphate and monophosphoryl lipid A (MPL), a less reactive and less toxic derivative of LPS, to activate TLR4 on the cell surface and thereby initiate the TLR4 signaling pathway ^{21,22}. The use of molecular adjuvants provides the opportunity to more specifically direct immune responses and, in the case of MPL, can help augment the antibody response as much as 100-fold ²³.

Though adjuvants have played a vital role in creating effective vaccines out of safer and more purified antigens, there remains room for improvement. As mentioned above, antigens associated with adjuvants may suffer from unknown or inadequate structure, stability, orientation, or organization. Aluminum adjuvants were commonly thought to form depots; however, there is evidence to suggest otherwise depending on how the antigen associates with

the aluminum particle. Antigens within aluminum-adjuvanted vaccines may bind the particle by ligand exchange, especially when the antigen contains phosphate groups, or may be adsorbed to the surface of the aluminum via electrostatic or hydrophobic interactions. Upon contact with interstitial fluid, aluminum begins to degrade and antigen adsorbed to the particle is particularly prone to elute from the aluminum, such that both may diffuse from the injection site. Regardless, aluminum helps maintain the antigen at a high concentration at the injection site while building robust immunity to the antigen, possibly by inducing necrosis and inflammation to attract APCs^{7,13,24,25}. Similarly, antigen mixed with MF59 does not incorporate into the oil droplets to any appreciable extent, but is supposedly better recognized within the microenvironment created by the emulsion antigen^{13,26}. As our understanding of immune system complexity has improved, the importance of antigen presentation (and even secondary signal presentation) in the appropriate time and space has become apparent. Nanomaterials such as colloids and polymers offer a highly capable delivery system to covalently anchor and more efficiently deliver antigens or ligands directing the immune response in an orientation and pattern that serves to induce desired responses.

2. Multivalent Nanomaterials

Multivalent nanomaterials are rooted in historic vaccine approaches and present new opportunities for restoring immune tolerance. Nanomaterials can be synthesized from diverse raw materials with unique physical and chemical properties well suited for immune modulation and multivalent antigen presentation. Several materials and architectures have been explored as nanomaterial scaffolds for ligand presentation, such as virions, VLPs, linear polymers, polymeric nanoparticles, liposomes, dendrimers, globular proteins, carbon nanotubes, gold nanoparticles

(GNPs), and others (Figure 1). VLPs, for instance, have traditionally been used in nanoparticle vaccines, but have recently found use as scaffolds in the development of new nanomaterials due to their structural stability and manipulability²⁷⁻²⁹.

As previously mentioned, some nanomaterials are used in vaccines to bolster immunity using intrinsically immunogenic constituents (i.e. VLPs, TLRs); other materials, such as polymers and liposomes, can remain more immunologically silent. Selecting immunologically inert scaffolds and linker materials reduces the risk of unintended reactivity toward degradation products and may favor specific immune response against the antigen. Conversely, selecting intrinsically immunogenic backbone materials provides a molecular adjuvant to enhance immunogenicity toward the given antigen. While a multitude of nanomaterials can be created to effect an immune response, this review will briefly overview properties of nanomaterials that affect immune response and then explore multivalent linear polymeric nanomaterials, especially in the context of antigen-specific immune tolerization.

2.1 Valency

Multivalency is indicative of multiple copies of the same ligand on a polymer or colloid. Multivalent nanomaterials specified in this review are distinct from multivalent vaccines that deliver several different antigens or epitopes (i.e. to provide cross-protection). Also, we refer to ligands derived specifically from immunogenic epitopes as *antigenic ligands*. In other cases, we refer more generally to *ligands* as primary (antigenic) or secondary signals. Although the jargon deviates slightly from vaccinology, the terms provide useful reference points as we proceed to antigen-specific immunotherapies. Many multivalent nanomaterials also contain a linker attaching the ligand to the selected material. Multivalent ligands interact with cell surface receptors to effect a biological response through various mechanisms: 1) decreasing ligand

binding off-rate by the chelate effect, 2) subsite binding in a secondary region of the receptor, 3) steric stabilization and blocking of competing binding agents, 4) statistical rebinding of ligands due to their proximity and high local concentration, and 5) receptor clustering to activate signaling pathways³⁰. Whitesides *et al* have discussed the importance of multivalency as a design strategy to target viruses, toxins, proteins, antibodies, and cell surfaces, as many of these biological targets have multiple repetitive binding sites³¹.

Ultimately, choice of scaffold affects the size, shape, valency, ligand spacing, conformation, rigidity, and hydrophilicity of the multivalent array, all of which can have significant biological effects³² (Figure 2). For example, the physical characteristics of the chosen backbone material and linker affect a molecule's interactions with biological surfaces, as well as size of the molecule and its geometric relationship to other surface ligands³³⁻³⁷. Linker size and hydrophobicity play a role in appropriate ligand spacing, illustrated in multiple studies such as with GNPs^{38,39}. Ligand valency (Figure 2a) and spacing (Figure 2b) are important determinants for the strength and nature of a nanomaterial-immune cell interaction, and therefore affect biological recognition and immune response. Increasing valency can increase the apparent binding for a given multivalent ligand through avidity³¹, and also influence cell surface receptor clustering to initiate or amplify signal transduction^{30,34,40-43}.

Increased ligand binding creates another consideration for multivalent nanomaterials, which is the potential for increased clearance *in vivo* by macrophages, in particular for liposomes with high ligand densities⁴⁴⁻⁴⁸. APC uptake can be further amplified through addition of secondary targeting ligands⁴⁹. This is an important consideration depending on the application. For many therapeutics, phagocytosis by macrophages is undesired, but for some vaccines improved particle uptake may augment an immunogenic response¹⁶. Interplay of ligand valency,

density, linker length and flexibility, and incorporation of secondary ligands is important for biological effector function, as these properties drive receptor engagement, interaction, signaling, and phagocytic uptake.

2.2 Size

In addition to the backbone, linker, and ligand properties, size influences transport and recognition of the nanomaterial. Size of the nanomaterial is known to alter the drug distribution and pharmacokinetic profiles, in part by affecting diffusion and cellular uptake⁵⁰. Nanomaterials most likely will have one of four fates after peripheral administration: 1) smaller materials (<10 nm) tend to drain to capillaries and into systemic circulation, 2) negatively charged nanomaterials between ~10-70 nm favor lymphatic drainage, 3) larger nanomaterials (>70 nm) have a higher probability of remaining at the injection site, and 4) these larger nanomaterials, especially when cationic, may be phagocytosed and potentially actively transported to lymph nodes⁵¹⁻⁵⁴.

Studies show particle size is an important determinant for vaccine immunogenicity^{39,55}. Often, large foreign particles are inherently immunogenic^{56,57}. Traditional adjuvant vaccines such as aluminum salts typically create an antigen:adjuvant depot at the injection site. As alluded to above, recruitment of immune cells to the injection site, particularly pAPCs, is considered a primary mechanism for activating a protective immune response. As such, large (>70 nm) nanomaterials may be ideal antigen carriers for traditional prophylactic protective vaccines. In contrast, vaccines that do not necessarily require immune cell recruitment and active transport could be delivered directly to the lymphatic tissue by selecting 10-70 nm nanomaterials. Very small (<10 nm) nanomaterials may be plagued by high clearance rates⁵⁸.

2.3 Shape

Several researchers have found that shape of a nanomaterial might also play a role in transport. Like size, shape affects particle behaviors such as diffusion and deposition or adhesion to vessel walls^{50,59}. Furthermore, shape can determine surface area and the shear forces experienced by particles in systemic circulation, affecting particle biodistribution. For example, linear, polymeric nanomaterials and elongated, elliptical particles are observed to have longer half-lives^{60,61} and an increased propensity to deposit in the liver compared to spherical particles and disk-shaped particles, which tend to deposit in the lungs and heart of mice^{62,63}. The difference in distribution and systemic persistence between the shapes could perhaps be due to alignment with flow and reduced adhesion to vessel walls^{61,64,65}.

Other researchers have found that nanoparticle size and shape can influence not only biodistribution, but also cellular response^{63,65,66}. Linear and more elongated nanomaterials are not easily phagocytized by macrophages or endocytosed by endothelial cells^{67,68}. The decreased clearance rate could contribute to the longer half-life of linear or elongated nanomaterials compared to more spherical nanomaterials^{50,63,69-71}. If a nanoparticle is taken up by a cell, size and shape can determine the cellular compartment to which the particle is trafficked⁶³. Local particle curvature also impacts the effective presentation of ligands to the targeted cell surface, depending on the contour of the cell membrane⁵⁰.

2.4 Flexibility

Nanomaterial scaffolds possess inherent rigidity or flexibility depending on their physical properties and shape (Figure 2c). Research suggests flexibility can also play a significant role in both *in vivo* transport and effective ligand presentation to cell surface receptors. Soluble, linear polymers can be flexible and can take on various molecular conformations. Therefore, the

orientation and spacing of ligands can be adapted to match the contour and receptor spacing of a given cell surface, which can be dynamic. In contrast, spherical or globular particles such as dendrimers, GNPs, liposomes, and proteins are inherently more rigid and have a more structured orientation and spacing of ligands^{72,73}. It follows that rigidity may play a role in cell receptor clustering, on both the number and proximity of receptors clustered together. In a ConA model receptor system, for example, clusters produced by linear polymers contained fewer receptors, but in proximity to each other, compared to clusters produced by globular protein conjugates of equal valency that contained more receptors spaced farther apart³⁰.

Kobayashi *et al* explored the effects of rigidity in two different architectures of linear saccharide polymers for binding of surface lectins: poly(phenyl isocyanides) (PPI) which are rigid and helical, and phenyl acrylamides (PAP) which are flexible and extended. PAP showed significantly higher binding in both receptor systems, suggesting rigidity can inhibit binding to recognition elements on cell surfaces⁷⁴. In the context of colloids, flexibility has been reported to render a particle less likely to be phagocytosed by macrophages^{50,75}.

Rigidity also affects the transport behavior of a particle *in vivo*, in particular the ability of a particle to flow through tortuous pathways and penetrate pores. Flexible particles can pass through pores that a spherical particle of equal size cannot^{50,76,77}. This plays a role in filtration through the liver and spleen and also permeability through extracellular space into tissues, thereby affecting clearance and delivery to target environments^{50,72,73}.

Taken together, physical characteristics of nanomaterials are important considerations for the design of immunomodulatory nanomaterials. The vast majority of clinical understanding is linked to a retrospective appreciation of nanomaterial properties of vaccines. A few research

endeavors have illuminated how nanomaterials may induce tolerance, including seminal work by Dintzis *et al.*

3. Multivalent Ligand Display on Linear Polymers

Given the historic properties of vaccines overlaid with our current understanding of nanomaterials, it is important to reconsider seminal research by Howard Dintzis and the latest developments in multivalent antigen delivery. The importance of multivalent antigen display for the ability of linear polymers to direct immune response was explored by Dintzis and others beginning in the late 1970s^{78,79}. Initially, Dintzis studied dinitrophenyl (DNP) antigenic ligands systematically grafted to linear acrylamide polymers of discrete molecular weight to assess their ability to evoke an immune response using a typical repeating polymeric template of a T cell independent antigen⁸⁰⁻⁸⁶. In these early studies, Dintzis found that immune response in mice treated with the engineered multivalent polymers appeared to be driven by the antigenic ligand characteristics along the polymer backbone.

Ligand valency and spacing, along with polymer size, were important nanomaterial parameters required to elicit specific immunological responses (Table 1). Specifically, Dintzis found that polymers less than 100 kDa were not immunogenic. However, size did not solely dictate an immune response, as large polymers without a sufficient number of conjugated antigenic ligands per molecule (low valency) failed to be immunogenic. Based on these observations, Dintzis hypothesized that a polymer of at least 100 kDa was required to evoke a strong immunogenic response. At this molecular weight, a polymer could theoretically accommodate at least 20 ligands approximately 100 Å apart, features Dintzis observed to provide a maximal immune response. They hypothesized a molecular mechanism whereby ligands

presented at this valency and spacing would create a threshold sufficient to bind and cluster a “minimum sized unit” of receptors on B cells and thus form an “immunon,” or a continuous cluster of ligands capable of initiating an immunogenic response⁷⁸ (Figure 3).

Expanding upon his initial findings, Dintzis further explored the role of multivalent ligand display utilizing several different polymer backbones to evaluate immune response. In some of Dintzis’ earliest work, while he identified large polymers (>100 kDa) with sufficient valency as being immunogenic, Dintzis showed the cellular signaling caused by large immunogenic multivalent arrays could also be inhibited by administration of similar multivalent arrays of smaller size⁸². Further investigation into these compounds revealed the smaller polymers of sufficient valency were not just inhibitory molecules, but rather induced long-term deficiencies to the immune response against the antigenic ligand. Specifically, he found that treatment of antigen-immunized mice with small polymers displaying multivalent antigenic ligand could repress the antibody response to the antigen. Furthermore, in a series of adoptive transfer experiments, Dintzis found the absence of immune response in animals treated with small multivalent molecules was B cell-dependent. Of importance, the antibody response to other antigens present at the time of immunization was not inhibited. This suggests 1) the small multivalent polymers could provide tolerance by specifically targeting a subset of antigen-specific B cells, and 2) these multivalent polymers were not generally immunotoxic, thus avoiding global immunosuppression^{84,87}.

More recently, Kiessling and others have sought to explain the ability of multivalent systems to elicit specific immune responses *in vitro*. They illustrated how structural features of a multivalent antigen array can cluster receptors, an essential determinant of B cell response. B cell receptor (BCR) clustering is important for signaling and B cell activation, directing the antigen-

specific immune response towards immunity (clonal expansion and antibody production) or tolerance (clonal expansion, quiescence and/or cell death). Antigen avidity, dose, and valency can all affect response. Like Dintzis, Kiessling used linear polymer backbones of different lengths conjugated with DNP as a 'hapten' (i.e. small molecule antigen). Similar to Dintzis' findings, Kiessling also found that increased valency led to increased antibody production in mice immunized with polymers of defined ligand density but variable valency (ligands per polymer) by varying the length of the final polymer. Multiple other studies have shown high valency is required to induce antibody production *in vivo* ^{78,88,89}.

Valency-dependence of signaling activity occurs *in vitro*, as evidenced by observations of B cell activation. In B cells treated with a defined molar concentration of DNP antigenic ligand, Kiessling found polymers of high valency (and size) had a greater capacity to induce calcium flux in DNP-sensitive B cells, suggesting polymers of increased valency and length have a higher capacity to activate B cells due to their ability to better cluster receptors. Interestingly, using this B cell system, Kiessling also observed a threshold at which increasing the dose of defined antigenic ligand-conjugated polymer no longer had a positive effect on signaling. This phenomenon was observed *in vivo* by both Snippe and Dintzis when looking at immune response as a function of antigenic ligand concentration ^{80,82,87,88,90-92}. These studies suggest for a given polymer conjugated to antigenic ligand, signaling activity increases with ligand concentration as more receptors are clustered; however, at very high ligand concentrations where ligand is in great excess, ligands overwhelm the available binding sites and the resultant binding events favor formation of fewer receptors bound to each polymer complex. Discontinuous or incomplete binding of a single multivalent backbone may not facilitate the critical BCR clustering, which could account for the diminished immune response observed at very high ligand doses ^{34,43}.

Kiessling further explored the importance of ligand density on the ability of a multivalent ligand to cluster receptors. Using concanavalin A (ConA) as a model receptor in an isolated system, Kiessling focused on three important aspects of receptor clustering: number of receptors in a cluster, rate of clustering, and receptor proximity. Upon comparing various multivalent architectures such as low molecular weight (MW) dimers and trimers, dendrimers, globular proteins, ROMP linear polymers of defined length, and high MW polydisperse linear polymers, Kiessling found that ROMP linear polymers favored receptor clustering over the other architectures. In particular, ROMP linear polymers formed tighter clusters of proximal receptors, especially compared to dendrimers and globular proteins³⁰.

In general, there appeared to be a strong dependence of clustering on ligand density and valency across different scaffold architectures^{30,41}. In mannose-conjugated linear polymers, the number of receptors in the cluster, rate of cluster formation, and receptor proximity increased as ligand density per polymer increased. It appeared low density arrays favored efficient receptor binding on a per ligand basis, while high density arrays favored greater total receptor binding per polymer array⁴¹. Contrasting trends were observed in other receptor systems. In a DNP-conjugated polymer system targeting the BCR, antigenic ligand density had negligible effect on signaling activity compared to total antigen valency and polymer length^{34,43}. Similarly, Minguet *et al* observed that bi- and trivalent soluble haptened peptides triggered activation through BCR clustering *in vitro* but there was no effect of ligand spacing⁴². As such, observations of tetrameric ConA clustering may not be an accurate reflection of clustering capabilities for all signal transduction pathways with other receptors (i.e. MHC, BCR, TCR, others).

The dependence of receptor clustering on the structure of the target receptor has been illustrated in other studies³². In a study using ConA as a model receptor, Kiessling observed the

ability of multivalent linear polymers with mannose ligand valencies ranging from approximately 20-140 to cluster ConA and subsequently aggregate T cells *in vitro*. Moderate valency (>20) was sufficient to complex and precipitate tetravalent ConA receptors, but high valency (>60) was required to complex and precipitate a bivalent form of ConA⁹³. The number of receptors clustered per polymer increased with increasing ligand valency. As before, Kiessling observed a threshold for the positive relationship between ligand concentration and clustering in both ConA systems, but a bell-shaped curve was only observed with increasing ligand concentration in the bivalent ConA system. This suggests the valency of both ligands and receptors are important for determining overall binding events. Thus, as clustering potential of multivalent ligands depends on both the nanomaterial and the targeted receptor system, nanomaterial design should perhaps be tailored according to the respective number, orientation, and spacing of epitopes in the target receptor⁹⁴.

Overall, studies by Kiessling support the idea that high multivalent presentation of a single ligand type induces receptor clustering and localization, enables high levels of calcium signaling, and leads to upregulation of genes necessary for antibody production and an immunogenic response. In contrast, low valency produces low levels of calcium signaling that fail to trigger gene expression for antibody production, and are proposed to induce quiescence/apoptosis conducive to a tolerogenic response. This agrees with others who also observed a trend of tolerance induction using low molecular weight, low valency arrays, with the exception of Dintzis who also observed tolerance induction using low molecular weight, high valency arrays^{34,79,84,95-97}.

Like Dintzis and Kiessling, Desaymard *et al* investigated multivalent DNP-conjugated linear polymers but used levan, dextran, pneumococcal polysaccharide, and D-glutamic acid/D-

lysine (D-GL) copolymer as backbones. They observed similar density trends across all architectures, and found that antigen-specific tolerance could be induced in B cells with high valency polymers as evidenced by inhibition of antibody production⁹⁸. Tolerance induction to specific classes of immunoglobulins depended on antigenic ligand density. Their results partly contradicted Dintzis' observations that nanomaterials under 100 kDa are not immunogenic: they found 20,000 kDa levan and 200 kDa dextran conjugates were immunogenic, while 70 kDa dextran conjugates were weakly immunogenic against the polymer but strongly immunogenic against the antigen. Other observations with the D-GL copolymer align with Dintzis' theory that nanomaterials with a valency >20 and density >10 antigens/50 kDa are immunogenic if MW>100 kDa, but tolerogenic if MW<100 kDa. The D-GL copolymer, containing a high antigen density of 37 antigen/50 kDa and a MW below the 100 kDa threshold, was observed to be strongly tolerogenic. The high density D-GL conjugates were tolerogenic regardless of dose *in vitro*, but lower density conjugates were immunogenic at low antigen dose and inhibitory at high antigen dose. A bell-shaped dose-response curve was observed with the immunogenic levan and dextran conjugates^{99,100}. These contradictory results highlight the complex interplay of nanomaterial physical properties and structural components in multivalent systems.

Dintzis' work provided strong and convincing evidence that polymeric antigen arrays can provide selective immune stimulation. Furthermore, this work is some of the first to suggest immunological memory can be reversed depending upon the context of subsequent antigen delivery. A simplistic explanation for Dintzis' observations is that small multivalent arrays may inhibit the proposed (approximate) 20-BCR cluster threshold required for B cell activation, leading to an anergic response by the targeted cell(s). Recently, other multivalent systems such as autoantigen-conjugated poly(lactic-co-glycolic acid) (PLGA) and polystyrene (PS)

nanoparticles have been observed to mediate tolerance in autoimmune disease ^{101,102}.

Experiments conducted with various polymeric nanomaterials suggest these constructs work in large part due to their ability to occupy or divert immune cells (i.e. decoy mechanism) rather than induce anergy or any kind of lasting tolerance ¹⁰³. For example, some studies suggest multivalent polymers may function in part through their ability to coat the cell and sterically inhibit competitive binding, thereby inhibiting cell-cell interactions by creating a hydrophilic, swollen gel layer that coats the cell surface ¹⁰⁴. Whether these molecules specifically delete or simply inhibit antigen-sensitive clones has yet to be determined. In other studies by Dintzis utilizing polymers of similar size and valency, he observed polymers in splenic tissue were associated with a pattern that suggested interaction with dendritic cells ⁸³. However, more studies are required to elucidate whether dendritic cells can be specifically targeted by multivalent polymeric arrays and whether true tolerance can be induced by multivalent display of other ligand types.

4. Multivalent Display of Two Different Ligands on Linear Polymers

Hetero-ligand presentation, which is the display of two or more signals, on linear polymers has also been investigated for directing immune response (Figure 4a). A summary of various multivalent linear polymer systems with either one or two signals may be viewed in Table 2. In addition to the primary antigen, inclusion of an ancillary signal may contribute to the overall specific or nonspecific binding of multivalent nanomaterials, as well as influence response. Secondary signals can drive both molecular conformation and the final effect of the antigen by directing or enhancing its response ³². For example, Whitesides *et al* incorporated a secondary ligand into sialic acid-bearing polyacrylamide arrays to inhibit influenza viral

adhesion to erythrocytes. Inhibition by multivalent arrays greatly exceeded that of the monomer equivalent, and was further improved by the addition of secondary functional groups.

Hydrophobic and aromatic secondary ligands were especially effective, perhaps due to the binding of hydrophobic sites on the cell surface to sterically block virus attachment¹⁰⁴. In other cases, secondary ligands have been added to enhance¹⁰⁵, suppress^{106,107}, or shift the cellular response¹⁰⁸.

Using her original DNP-displaying polymer, Kiessling *et al* developed a series of homo- and hetero-ligand multivalent (250 unit) polymers conjugated with DNP and a ligand for CD22 (CD22L). DNP antigenic homo-polymer containing ~83 DNP, CD22L co-receptor homo-polymer containing ~58 CD22L, and DNP/CD22L copolymer containing ~90 DNP and 60 CD22L were studied. Treatment of B cells expressing DNP-specific BCRs with a multivalent hetero-polymer displaying both DNP antigenic ligand and CD22L exhibited reduced cell signaling and suppressed B cell activation, due to the molecule's ability to interact simultaneously with both the BCR and CD22. Several other groups have made similar findings^{107,109,110} suggesting co-presentation of antigen and CD22L on either polymers or liposomes can reduce B cell-dependent immune responses. Interestingly, the reduced B cell-dependent immune response in mice treated with liposomes co-presenting antigen and inhibitory CD22L was associated with an increase in B cell apoptosis. B cell responses to other antigens were not affected, suggesting these molecules were not overtly immunotoxic to all B cells. Inclusion of an appropriate secondary ligand was critical for reducing an antigen-specific immune response. Furthermore, addition of targeting and inhibitory ligands on immunomodulatory nanomaterials may be a potential avenue to specifically delete antigen-sensitive B cell clones, which has significant implications in autoimmune disease and immune hypersensitivity¹¹¹.

More recently, Sestak *et al* employed a similar strategy, co-delivering antigenic ligand and immune inhibitor by developing a multivalent hetero-ligand polymer to reverse disease in experimental autoimmune encephalomyelitis (EAE), the murine model of multiple sclerosis^{108,112}. Sestak utilized small hyaluronic acid polymers (16 kDa, HA) complexed with a disease-specific autoantigen (proteolipid protein peptide epitope, PLP₁₃₉₋₁₅₁) and a peptide ligand (LABL) that binds intracellular cell-adhesion molecule-1 (ICAM-1). ICAM-1 contributes to immune cell adhesion¹¹³⁻¹¹⁵ and costimulation of the immune response¹¹⁶⁻¹¹⁸. Co-delivery of antigenic peptide and LABL peptide in a multivalent array was significantly more effective in reducing disease compared to a mixture of the free components (HA, PLP, LABL) or homopolymers containing either PLP or LABL. Interestingly, delivery of a mixture of the two homopolymers (PLP homo-polymer and LABL homo-polymer) was sufficient to repress disease in EAE mice. Adaptation of this technology utilizing multivalent hetero-ligands of antigen (PLP) and peptides that bind immune cell surface receptors (CD80 and CD86) has also been effective at reducing disease in EAE mice¹¹⁹.

GNP vaccine research suggests inclusion of a secondary ligand can be used to activate additional cell subsets that would not typically be targeted by antigen, such as Th2^{49,105,120} or T_{reg}¹²¹. For example, T-helper peptide (molecular adjuvant) can be delivered alongside B cell carbohydrate antigen to trigger a robust T-helper response and prolong immunological memory¹⁰⁵. In these studies, a specific ratio of antigen, molecular adjuvant, and spacer ligand (45:5:50) was necessary to induce a strong Th2-aided antigen-specific response. Thus, when multiple ligand types are presented, their ratio may be important for eliciting a specific and robust response. This ratio appears to vary for different immunogenic nanomaterials and may be dependent upon the intrinsic affinity of the ligand, but observations by Kiessling, Duong, and

Sestak suggest an approximate ratio of 1:1 antigenic ligand to co-receptor ligand is able to elicit a tolerogenic response^{106-108,112}.

Studies with nanomaterials other than linear polymers suggest co-delivery of two signals on the same backbone is critical for inducing an immune response^{49,105,121}. Hassane *et al* found that incorporation of B cell epitope and Th epitope ligands onto the same liposome was necessary to promote BCR clustering, B cell activation, and immune protection⁴⁹. Hence, it is necessary to consider co-delivery of antigen and molecular adjuvant in the same spatial and temporal context. Similarly, co-presentation of antigen and CD22 ligands on liposomes was required to inhibit B cell signaling¹²². In linear polymers, there are mixed indications as to whether co-delivery of multiple signals on the same backbone enhances the resultant immune response. Kiessling *et al* observed that co-presentation of a CD22 ligand alongside antigen on the same linear polymer backbone was necessary to suppress antigen-specific B cell activation, whereas delivery of a mixture of antigen- and CD22L-homo-polymers was not sufficient to reduce B cell activation¹⁰⁶. In contrast, Sestak *et al* observed similar therapeutic efficacy in EAE from treating mice with a copolymer presenting both antigen and cell adhesion inhibitory peptides (PLP and LABL) versus a mixture of homo-polymers presenting either antigen (PLP) or inhibitor peptide (LABL)¹¹². Sestak's work may suggest that co-presentation of multiple ligand types on separate, flexible, linear polymers may be sufficient when blocking cell adhesion molecules to inhibit immune response.

One hypothesis for efficacy upon delivering a mixture of homo-polymers is the potential for interactions between the side chains and backbones of neighboring molecules which could allow for accidental "bystander" entanglement of homo-polymers, effectively co-delivering the two signals (Figure 4b). Indeed, work by Dintzis suggested very large flexible polymers with

appropriate valency, but large (inappropriate) spacing between ligands, could be immunogenic due to conformational rearrangement of the polymer (Figure 3cd). Such flexibility could theoretically decrease the “effective” spacing between ligands in a folded polymer to the proposed ideal ~ 100 Å spacing required to elicit a full immune response⁷⁸. This is not the case for rigid scaffolds and particles, which cannot intimately interact with neighboring molecules due to the rigidity of the material and set organization and orientation of ligands, that is unless very long flexible linkers are employed (Figure 4).

In Kiessling’s case the hetero-polymer suppressed BCR activation due to its ability to interact with proximal receptors (BCR and CD22) on the same B cell surface in a purified B cell system. Thus, co-presentation of ligands on a single polymer with controlled ligand spacing may be required for targeting the cell surface to accommodate receptors in proximity. In contrast, Sestak’s observations were based in an animal model (EAE) requiring B cells, T cells and other immune cells such as dendritic cells to establish disease. As alluded to above, some of Dintzis’ work suggested multivalent polymers could directly interact with dendritic cells. Taken together, this may indicate that at least for some antigenic ligands, delivery of two independent homo-polymers can effectively deliver two signals in the same time and space. The mechanisms whereby homo-ligand polymer pairs and hetero-ligand polymers tailor immune response require further investigation.

5. Proposed Mechanisms for Immune Response to Multivalent Nanomaterials

Similar to the colloidal adjuvants used in traditional vaccines, the physical carrier and delivery system of multivalent nanomaterials is an important aspect of the design of safe and efficacious antigen-specific immunomodulators. Nanomaterial science brings a large, diverse

library of carrier molecules to the fields of vaccines and immunotherapy. The physical and chemical characteristics of each independent nanomaterial component must be carefully chosen. Not only do size, shape, rigidity, and chemistry determine the transport fate of a compound, which consequently determines immune exposure, but these properties can direct and amplify immune response. Importantly, the structure of the nanomaterial and conjugation to available functional groups will determine ligand valency and density, both having a direct impact on immunological outcome.

Although the exact molecular mechanisms for how ligand valency and density affect immune response have yet to be resolved, much of the work by Dintzis, Kiessling, and other researchers are in agreement that these principles heavily weight the resultant immune response. While Dintzis and Kiessling showed large flexible polymers meeting some minimum valency and density criteria may be prime candidates to evoke a protective prophylactic immune response, Dintzis found small polymers (<100 kDa) may actually induce a long-term antigen-specific immune deficit, or tolerance, towards a given antigen. The studies reviewed here highlight the complex interplay of physical properties in multivalent nanomaterials, and also reflect the complexity of antigenic immune response. For instance, while it is known that co-receptor engagement may direct the polarity of a response towards immunogenicity or tolerance^{123,124}, it is less well understood when antigen receptor engagement alone will induce either immunogenicity or tolerance. It may be driven by the degree of receptor engagement, clustering, and cross-linking, such that highly cross-linked receptors produce an immunogenic response while poorly cross-linked receptors produce tolerance^{78,84,125}. Dintzis' 'immunon hypothesis' and Kiessling's studies with receptor clustering support this idea. Other studies suggest antigen response may be driven by dose.

Desaymard observed an interesting dose-dependent response by high density copolymer conjugates, which elicited an immunogenic response at low antigen dose and a tolerogenic response at high antigen dose¹⁰⁰. However, there is more agreement among Dintzis, Kiessling, and Desaymard regarding a “bell-shaped” dose response curve to immunogenic multivalent polymers in which both high and low doses fail to promote an immune response. Since long-term, low antigen exposure is utilized for allergic hyposensitization treatment, it would be interesting to test whether low, sub-optimally stimulating doses of multivalent polymers could actually induce tolerance over time^{126,127}. Conversely, as high antigen doses can induce clonal deletion or anergy in lymphocytes^{128,129}, would extremely high doses of multivalent polymers induce a robust tolerogenic effect as well? Future studies can explore these possibilities in both multivalent polymers and other nanomaterial systems. Additionally, further investigation is needed to establish a set of rules about physical parameters of multivalent soluble, linear polymers that elicit either an immunogenic or tolerogenic response, as Dintzis proposed, especially when treating larger mammals and humans. Seminal work by Dintzis may be illuminated by the advanced tools available today for characterizing nanomaterials.

As discussed, Dintzis and Kiessling have heavily investigated the **molecular mechanisms** enacted by multivalent soluble, linear polymers in order to direct an immune response (Figure 3). Dintzis established the ‘immunon hypothesis’ and proposed multivalent nanomaterial parameters (length, valency, and spacing) that lead to an immunogenic versus tolerogenic response. In support of a molecular mechanism, Kiessling has shown that multivalent ligands influence cell surface receptor clustering, signal transduction, and immune activation *in vitro*. Kiessling and others have also shown that secondary ligands, in addition to antigen, may contribute to overall binding, costimulation or inhibition of signaling, and augmentation of

immune response. The idea that multivalent nanomaterials enact an immune response through a molecular mechanism has been well established.

However, there have been some discrepancies between studies, in particular studies by Kiessling and Dintzis relating to a threshold polymer length and antigenic ligand valency required to elicit immunogenicity. These discrepancies, and some of our current lack of understanding surrounding the immunomodulatory abilities of nanomaterials, may be attributed to a deficiency in transport and pharmacokinetic observations with these systems. For example, many of Kiessling's studies were performed with B cells *in vitro*, bypassing any transport step, whereas Dintzis observed responses to nanomaterials delivered *in vivo* (often after intraperitoneal administration), which were affected by transport and exposure to additional immune cell subsets such as phagocytes and T cells. In another case, Desaymard observed contrasting results with high-density copolymers that were exclusively tolerogenic regardless of dose *in vitro* but not *in vivo*^{99,100}. Therefore, a **transport mechanism** must also play a key role in the way a multivalent nanomaterial enacts an immune response (Figure 5).

Local transport and pharmacokinetic considerations are critically linked to the molecular interactions that lead to immune response, especially in the nanomaterial arena where there is a large, diverse library of carrier molecules. For instance, adjuvants used in vaccines are typically colloids comprised of relatively rigid particles, which encourage depot formation at the injection site and recruitment of APCs. In contrast, soluble, linear polymers are flexible and may be more prone to diffuse throughout the tissue and even into systemic or lymphatic circulation, potentiating a fundamentally different immune response than colloidal depot systems (Figure 5). Specifically, smaller, soluble, linear polymers may bypass peripheral immune activation by quiet drainage to secondary lymphoid organs and therefore favor tolerance induction. Thus, delivery

and subsequent transport of a therapeutic nanomaterial should be considered during design and study.

Transport of antigen to the lymphatic system is thought to be a vital component of the immune response and may offer insight into the different immunological effects of nanomaterials. Lymph nodes provide discrete immunological environments with specific cell populations sequestered in a very highly structured architecture that can facilitate immune response^{130,131}. A nanomaterial designed to initiate an immune response may be delivered to the lymphatics through a much different route compared to one intended to induce tolerance, as mentioned above. Classic routes of administration such as subcutaneous, intramuscular, and intravenous injection depend on different methods of antigen transport. Subcutaneous delivery may utilize both passive and active transport to the lymphatic system, as the antigen can either diffuse from the site of injection or be carried by peripheral macrophages to the lymph node¹³². Intramuscular delivery may be more likely to form a depot at the site of injection, such that recognition in the periphery and active transport by immune cells is the likely mechanism of transport to the lymphatics. Intravenous delivery is typically used to systemically deliver the injectable, in which case the antigen can be taken up by circulating immune cells in the blood and directed to the liver or spleen¹³³. Since clearance of the antigen from blood circulation can occur at an accelerated rate, a complete immunological response may not take place¹³⁴.

In addition to these classic routes, direct intranodal injection of antigen was recently explored for hyposensitization therapy. While traditional methods to promote hyposensitization toward specific allergens required multiple subcutaneous injections of allergen at low concentration over the course of years, recent clinical trials demonstrated injection of the allergen directly into the lymph nodes resulted in more rapid hyposensitization toward the

allergen, requiring fewer injections^{131-132,135-137}. Similarly, intranodal injection of colloidal or particulate systems that are traditionally immunogenic may actually induce tolerance, perhaps by bypassing peripheral recognition mechanisms and activation. Striking differences in immune response when changing the injection site underscore the importance of the transport and pharmacokinetics of nanomaterial vaccines and immunotherapies.

6. Conclusions and Future Directions

The diversity and continued development of nanomaterials have provided many opportunities for improving immunomodulatory therapies. Vaccinologists have long known that non-immunogenic epitopes make for poor prophylactic vaccine candidates and therefore have added adjuvants to boost their efficacy. Several examples outlined within this review illustrate how multivalent nanomaterials may provide a stepping-stone in the evolution of vaccines. For instance, the selection of an intrinsically immunogenic nanomaterial scaffold may itself act as a molecular adjuvant while also improving binding avidity and antigen-specificity through multivalent presentation of antigen. Additionally, co-presentation of a secondary ligand as a molecular adjuvant on the nanomaterial scaffold can direct or boost the immune response towards a given antigen. For these reasons, multivalent nanomaterials may be suitable for future prophylactic vaccine design and formulation.

Multivalent nanomaterials have also evolved for applications where immune tolerance is desired, such as autoimmune diseases or allergies. As research dating back to Howard Dintzis suggests, modulating polymer length, antigenic ligand valency, and antigenic ligand density may enable a nanomaterial to induce tolerance instead of immunogenicity. Using principles of molecular adjuvants, new research has emerged suggesting co-delivery of a secondary signal can

also promote a tolerogenic response to a given antigen, although the proposed mechanisms of tolerance induction vary widely. Ligand display and other physical properties of multivalent nanomaterials play a role not only in a molecular mechanism for immune response, such as the classic ‘immunon hypothesis’, but also in a transport mechanism for biodistribution. We propose both mechanisms are important considerations for nanomaterial design, and necessary for advancements in antigen-specific immunotherapies for autoimmune diseases. Creation of antigen-specific tolerogenic therapies in humans would be groundbreaking, reducing or eliminating the risk of global immunosuppression.

Table 1. Dintzis' Rules

MW (kDa)	Valency (# Haptens/Molecule)	Immunogenicity	Tolerogenicity
>100 kDa	>20	Increases with valency	-
	<20	-	-
<100 kDa	>20	-	High
	<20	-	Increases with valency

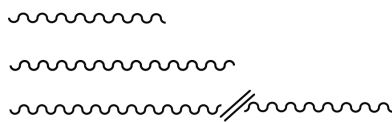
Table 2. Summary of Multivalent Linear Polymer Systems.

Polymer	Signal 1	Signal 2	Valency	Size	Immune Response	Ref.	
Polyacrylamide	Dinitrophenol		38	360 kDa	Immunogenic	74	
	Dinitrophenol		53	145 kDa	Immunogenic	74	
	Dinitrophenol		59	460 kDa	Immunogenic	74	
	Dinitrophenol		97	460 kDa	Immunogenic	74	
	Dinitrophenol		126	430 kDa	Immunogenic	74	
	Dinitrophenol		17	330 kDa	Immunogenic	72	
	Dinitrophenol		48	140 kDa	Immunogenic	72	
	Dinitrophenol		66	180 kDa	Immunogenic	72	
	Dinitrophenol		20	380 kDa	Immunogenic	81	
	Dinitrophenol		38	360 kDa	Immunogenic	81	
	Dinitrophenol		53	145 kDa	Immunogenic	81	
	Dinitrophenol		59	460 kDa	Immunogenic	81	
	Dinitrophenol		97	460 kDa	Immunogenic	81	
	Dinitrophenol		126	430 kDa	Immunogenic	81	
	Dinitrophenol	Siglec-G ligand		200	1,000 kDa	Tolerogenic	101
	Dinitrophenol	CD22		400	1,000 kDa	Tolerogenic	101
	Dinitrophenol			19	60 kDa	Other	74
	Dinitrophenol			20	380 kDa	Other	74
	Dinitrophenol			19	60 kDa	Other	82
	Dinitrophenol			43	130 kDa	Other	82
	Dinitrophenol			8	130 kDa	Other	72
	Dinitrophenol			14	50 kDa	Other	72
	Dinitrophenol			25	80 kDa	Other	72
	Dinitrophenol			2	350 kDa	Other	81
	Dinitrophenol			3	350 kDa	Other	81
	Dinitrophenol			4	350 kDa	Other	81
	Dinitrophenol			6	350 kDa	Other	81
	Dinitrophenol			7	350 kDa	Other	81
	Dinitrophenol			10	350 kDa	Other	81
	Dinitrophenol			11	40 kDa	Other	81
	Dinitrophenol			19	60 kDa	Other	81
	Fluorescein			95	300 kDa	Immunogenic	90
	Fluorescein			230	400 kDa	Immunogenic	90
Fluorescein			150	630 kDa	Immunogenic	76	
Fluorescein			12	53 kDa	Other	76	
Fluorescein			340	600 kDa	Other	75	
Fluorescein			21	40 kDa	Other	75	
Fluorescein			47	80 kDa	Other	90	
Dextran	Fluorescein		65	400 kDa	Immunogenic	90	
	Fluorescein		60	170 kDa	Immunogenic	90	

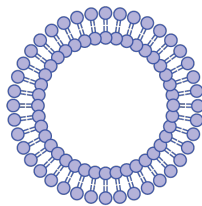
	Fluorescein		960	2,300 kDa	Immunogenic	76
	Fluorescein		3600	10,000 kDa	Immunogenic	76
	Fluorescein		7	30 kDa	Immunogenic	77
	Fluorescein		35	100 kDa	Immunogenic	77
	Fluorescein		150	500 kDa	Immunogenic	77
	Fluorescein		30	70 kDa	Tolerogenic	89
	Fluorescein		8	21 kDa	Tolerogenic	76
	Fluorescein		7	30 kDa	Tolerogenic	78
	Fluorescein		14	40 kDa	Other	90
	Fluorescein		8	21 kDa	Other	76
	Nitrohydroxy-phenylacetyl		15	30 kDa	Tolerogenic	78
	LPL		14	27 kDa	Tolerogenic	80
Ring-opening metathesis polymerization	Dinitrophenol		8 - 10%	100-mer	Immunogenic	28
	Dinitrophenol		8 - 10%	250-mer	Immunogenic	28
	Dinitrophenol		8 - 10%	500-mer	Immunogenic	28
	Dinitrophenol	CD22 ligand	33 - 36%	250-mer	Tolerogenic	100
	Mannose		100%	143-mer	Other	35
	Mannose		71%	145-mer	Other	35
	Mannose		45%	115-m34	Other	35
	Mannose		31%	86-mer	Other	35
	Mannose		18%	102-mer	Other	35
	Mannose		10%	116-mer	Other	35
	Mannose		2%	129-mer	Other	35
	Mannose		21		Other	87
	Mannose		38		Other	87
	Mannose		65		Other	87
	Mannose		142		Other	87
	Mannose		5 - 100	3 - 34 kDa	Other	24
		Monovalent galactose		10		Other
	Monovalent galactose		25		Other	83
	Monovalent galactose		50		Other	83
Ficoll	Fluorescein		240	750 kDa	Immunogenic	90
	Fluorescein		90	750 kDa	Immunogenic	90
	Fluorescein		50	200 kDa	Immunogenic	76
	Fluorescein		260	770 kDa	Immunogenic	76
	Fluorescein		12	53 kDa	Other	76
	Fluorescein		20	96 kDa	Other	76
	Fluorescein		14	40 kDa	Other	90
	Fluorescein		6	35 kDa	Other	90
	Fluorescein		600	2,000 kDa	Other	75
	Fluorescein		14	40 kDa	Other	75
	Fluorescein		225	700 kDa	Other	75
	Fluorescein		87	700 kDa	Other	75

Carboxymethyl cellulose	Fluorescein		160	520 kDa	Immunogenic	90
	Fluorescein		26	110 kDa	Immunogenic	90
	Fluorescein		6	27 kDa	Other	90
	Dinitrophenol		8-32	100 kDa	Tolerogenic	91
Polyethylene- maleic anhydride	Mannose		700	100 kDa	Other	24
Polyvinyl alcohol	Fluorescein		110	400 kDa	Immunogenic	90
	Fluorescein		55	200 kDa	Immunogenic	90
	Fluorescein		14	40 kDa	Other	90
Hyaluronic acid	LABL		31	16.9 kDa	Tolerogenic	102
	PLP ₁₃₉₋₁₅₁		38	16.9 kDa	Tolerogenic	102
	PLP ₁₃₉₋₁₅₁	LABL	37	16.9 kDa	Tolerogenic	102

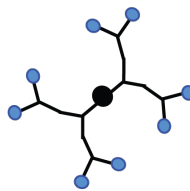
a) Linear polymers



b) Liposome



c) Dendrimer



d) Spherical nanoparticles

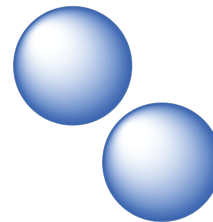


Figure 1. Nanomaterial architectures: a) linear polymers of different lengths, b) liposome, c) 2nd generation dendrimer, d) spherical nanoparticles such as gold nanoparticles (GNPs) or polymeric nanoparticles.

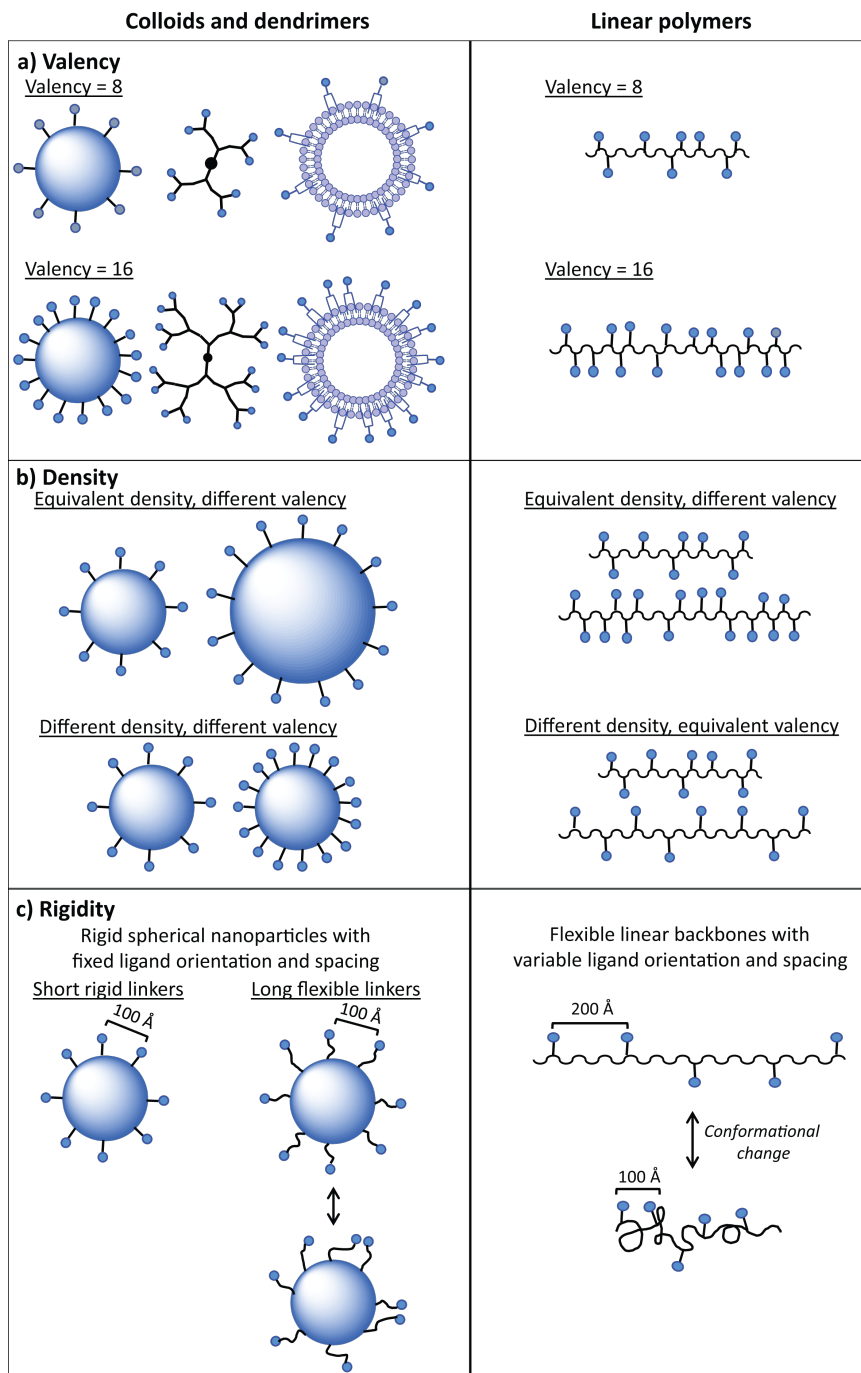


Figure 2. Important multivalent nanomaterial properties: a) ligand valency of 8 and 16 for different nanomaterials; b) ligand density; c) variations in rigidity between linear polymers and spherical particles. The spacing of ligands on a linear polymers is variable due to multiple conformations of the polymer chain, while the ligands on a rigid sphere are relatively fixed in spacing and orientation, even when utilizing flexible linkers.

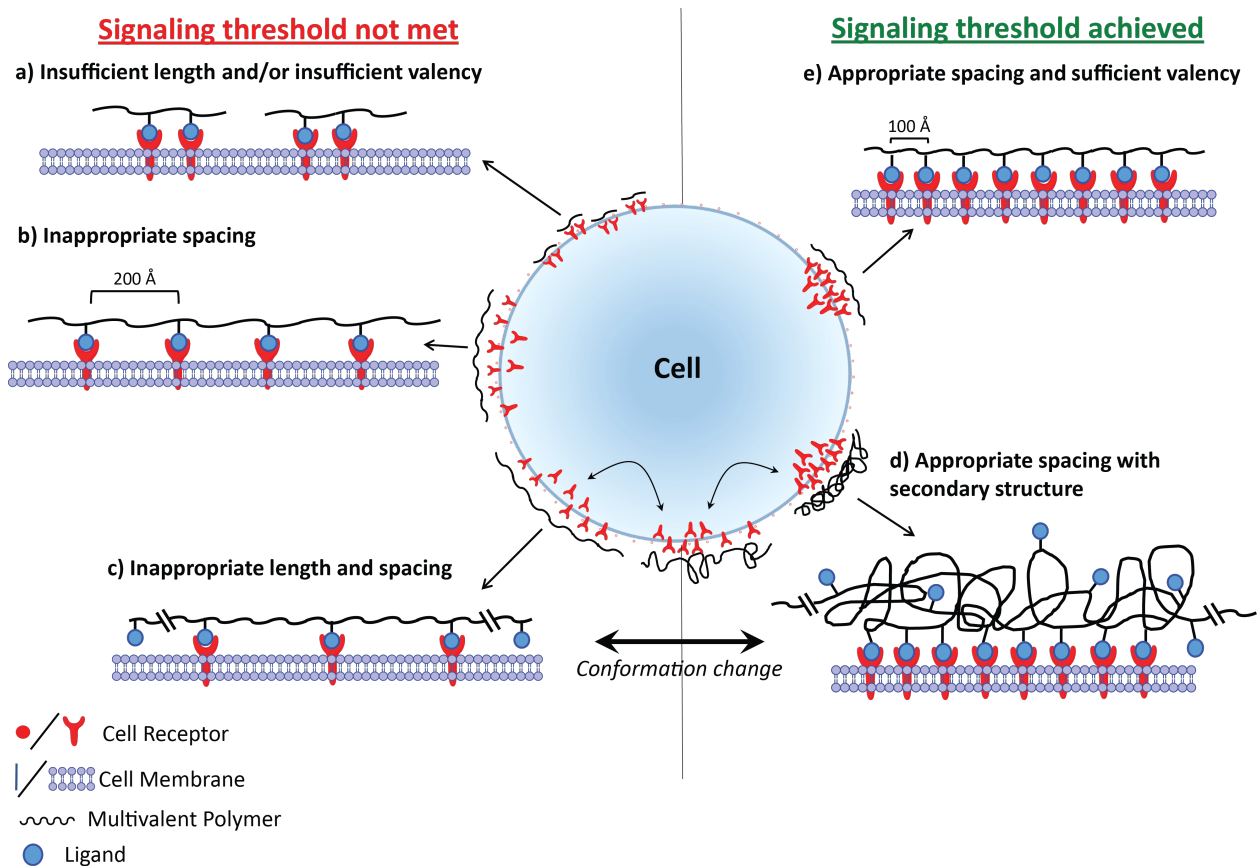
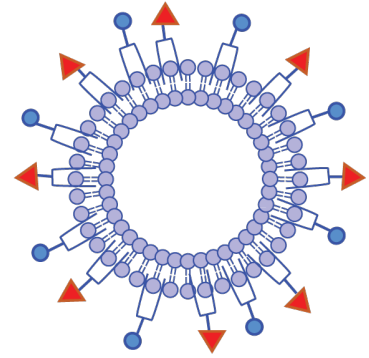
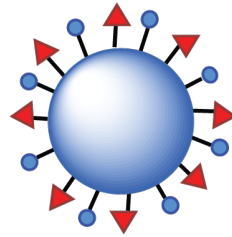
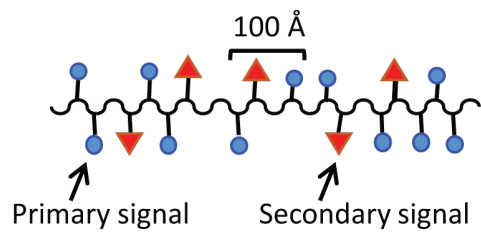
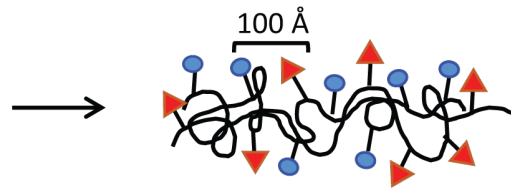
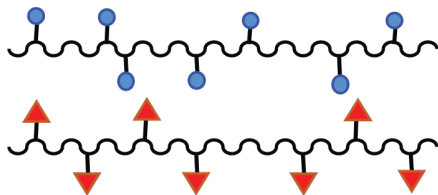


Figure 3. Molecular mechanism for multivalent linear polymers: Polymers must be of sufficient length, ligand valency, and ligand density to adequately cluster cell surface receptors for signal transduction. Potential signaling outcomes of multivalent linear polymers with a) insufficient length and/or insufficient valency, b) inappropriate spacing, c) inappropriate length and spacing, d) appropriate ‘functional’ spacing due to secondary structure after conformation change, and e) appropriate spacing and sufficient valency.

a) Hetero-ligand nanomaterials



b) Homo-ligand polymers



Entangled homo-ligand polymers

Figure 4. Co-delivery of primary signal (antigen) and secondary signal (molecular adjuvant, costimulatory signal, co-receptor ligand): a) co-delivery on different nanomaterial backbones, b) co-delivery of primary and secondary signals by chain entanglement of two distinct homo-ligand polymers.

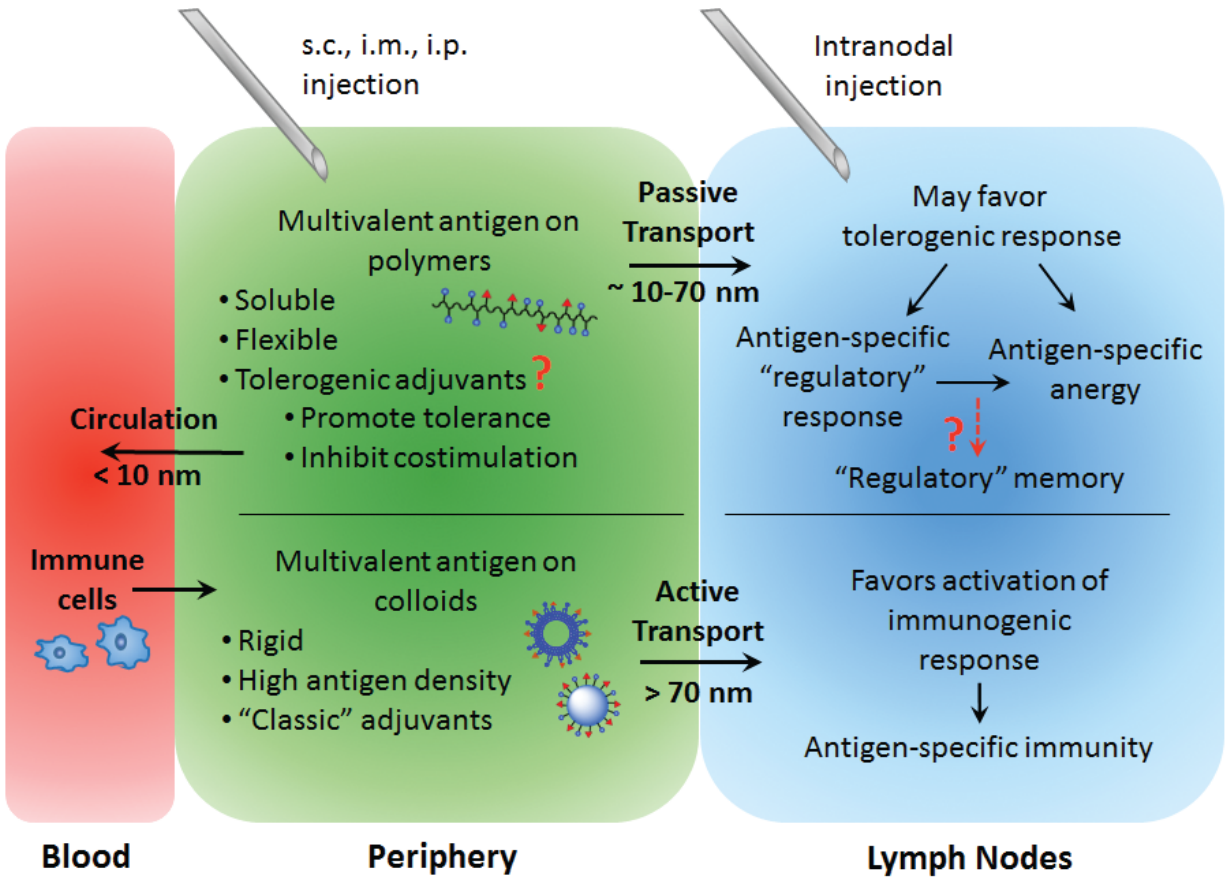


Figure 5. Potential transport mechanisms for multivalent nanomaterials: Soluble, flexible, linear polymers are prone to passively drain into systemic or lymphatic circulation, depending on size. Multivalent modification with antigen and tolerogenic adjuvant, in conjunction with quiet drainage to the lymph, may promote an antigen-specific tolerogenic response and lasting regulatory memory. Conversely, rigid colloidal particles are prone to form a depot at the injection site, attracting APCs for active transport into the lymph. Multivalent modification with a high density of antigen and classic adjuvant, in conjunction with active transport to the lymph, may promote peripheral activation of an immunogenic response and lasting antigen-specific immunity.

References

1. Zhang L, Gu FX, Chan JM, Wang AZ, Langer RS, Farokhzad OC 2008. Nanoparticles in medicine: therapeutic applications and developments. *Clinical pharmacology and therapeutics* 83(5):761-769.
2. Klippstein R, Pozo D 2010. Nanotechnology-based manipulation of dendritic cells for enhanced immunotherapy strategies. *Nanomedicine : nanotechnology, biology, and medicine* 6(4):523-529.
3. Brannon-Peppas L, Blanchette JO 2004. Nanoparticle and targeted systems for cancer therapy. *Advanced drug delivery reviews* 56(11):1649-1659.
4. Chittasupho C, Siahaan TJ, Vines CM, Berkland C 2011. Autoimmune therapies targeting costimulation and emerging trends in multivalent therapeutics. *Therapeutic delivery* 2(7):873-889.
5. Chen L, Flies DB 2013. Molecular mechanisms of T cell co-stimulation and co-inhibition. *Nature reviews Immunology* 13(4):227-242.
6. Frauwirth KA, Thompson CB 2002. Activation and inhibition of lymphocytes by costimulation. *The Journal of clinical investigation* 109(3):295-299.
7. Gupta RK, Siber GR 1995. Adjuvants for human vaccines--current status, problems and future prospects. *Vaccine* 13(14):1263-1276.
8. Coffman RL, Sher A, Seder RA 2010. Vaccine adjuvants: putting innate immunity to work. *Immunity* 33(4):492-503.
9. Fujita H, Meyer N, Akdis M, Akdis CA 2012. Mechanisms of immune tolerance to allergens. *Chemical immunology and allergy* 96:30-38.
10. Szczepanik M 2011. Mechanisms of immunological tolerance to the antigens of the central nervous system. Skin-induced tolerance as a new therapeutic concept. *Journal of physiology and pharmacology : an official journal of the Polish Physiological Society* 62(2):159-165.
11. Faria AM, Weiner HL 2006. Oral tolerance: therapeutic implications for autoimmune diseases. *Clinical & developmental immunology* 13(2-4):143-157.
12. Peek LJ, Middaugh CR, Berkland C 2008. Nanotechnology in vaccine delivery. *Advanced drug delivery reviews* 60(8):915-928.
13. Hogenesch H 2012. Mechanism of immunopotentiality and safety of aluminum adjuvants. *Frontiers in immunology* 3:406.
14. Pashine A, Valiante NM, Ulmer JB 2005. Targeting the innate immune response with improved vaccine adjuvants. *Nature medicine* 11(4 Suppl):S63-68.
15. Dintzis RZ 1992. Rational design of conjugate vaccines. *Pediatric research* 32(4):376-385.
16. Xiang SD, Scholzen A, Minigo G, David C, Apostolopoulos V, Mottram PL, Plebanski M 2006. Pathogen recognition and development of particulate vaccines: does size matter? *Methods* 40(1):1-9.
17. Leroux-Roels G 2010. Unmet needs in modern vaccinology: adjuvants to improve the immune response. *Vaccine* 28 Suppl 3:C25-36.
18. Boulikas T 1991. Relation between carcinogenesis, chromatin structure and poly(ADP-ribosylation) (review). *Anticancer research* 11(2):489-527.
19. Bachmann MF, Jennings GT 2010. Vaccine delivery: a matter of size, geometry, kinetics and molecular patterns. *Nature reviews Immunology* 10(11):787-796.

20. Cox JC, Coulter AR 1997. Adjuvants--a classification and review of their modes of action. *Vaccine* 15(3):248-256.
21. Garcon N, Hem, S., Friede, M. 2012. 5 - Evolution of adjuvants across the centuries. In Plotkin/Orenstein, editor *Vaccines*, 6th Edition ed.: Saunders.
22. Owen JA, Punt J, Stranford SA, Jones PP, Kuby J. 2013. *Kuby immunology*. 7th ed., New York: W.H. Freeman. p xxvii, 692, 109 p.
23. Moon JJ, Suh H, Polhemus ME, Ockenhouse CF, Yadava A, Irvine DJ 2012. Antigen-displaying lipid-enveloped PLGA nanoparticles as delivery agents for a *Plasmodium vivax* malaria vaccine. *PloS one* 7(2):e31472.
24. White RG, Coons AH, Connolly JM 1955. Studies on antibody production. III. The alum granuloma. *The Journal of experimental medicine* 102(1):73-82.
25. Hem SL, Hogenesch H 2007. Relationship between physical and chemical properties of aluminum-containing adjuvants and immunopotential. *Expert Rev Vaccines* 6(5):685-698.
26. O'Hagan DT, Ott GS, De Gregorio E, Seubert A 2012. The mechanism of action of MF59 - an innately attractive adjuvant formulation. *Vaccine* 30(29):4341-4348.
27. Roldao A, Mellado MC, Castilho LR, Carrondo MJ, Alves PM 2010. Virus-like particles in vaccine development. *Expert Rev Vaccines* 9(10):1149-1176.
28. Chackerian B, Lenz P, Lowy DR, Schiller JT 2002. Determinants of autoantibody induction by conjugated papillomavirus virus-like particles. *Journal of immunology* 169(11):6120-6126.
29. Ludwig C, Wagner R 2007. Virus-like particles-universal molecular toolboxes. *Current opinion in biotechnology* 18(6):537-545.
30. Gestwicki JE, Cairo CW, Strong LE, Oetjen KA, Kiessling LL 2002. Influencing receptor-ligand binding mechanisms with multivalent ligand architecture. *Journal of the American Chemical Society* 124(50):14922-14933.
31. Krishnamurthy VM, Estroff LA, Whitesides GM 2006. Multivalency in ligand design. *Fragment-based approaches in drug discovery* 34:11-53.
32. Kiessling LL, Strong LE, Gestwicki JE. 2000. Chapter 29. Principles for multivalent ligand design. *Annual Reports in Medicinal Chemistry*, ed.: Academic Press. p 321-330.
33. Bhanot G 2004. Results from modeling of B-Cell receptors binding to antigen. *Progress in biophysics and molecular biology* 85(2-3):343-352.
34. Puffer EB, Pontrello JK, Hollenbeck JJ, Kink JA, Kiessling LL 2007. Activating B cell signaling with defined multivalent ligands. *ACS chemical biology* 2(4):252-262.
35. Hat B, Kazmierczak B, Lipniacki T 2011. B cell activation triggered by the formation of the small receptor cluster: a computational study. *PLoS computational biology* 7(10):e1002197.
36. Crocker PR, Feizi T 1996. Carbohydrate recognition systems: functional triads in cell-cell interactions. *Current opinion in structural biology* 6(5):679-691.
37. Lee R, Lee Y. 1994. Enhanced biochemical affinities of multivalent neoglycoconjugates. ed.: Academic Press: San Diego, CA, USA. p 23-50.
38. Lin CC, Yeh YC, Yang CY, Chen GF, Chen YC, Wu YC, Chen CC 2003. Quantitative analysis of multivalent interactions of carbohydrate-encapsulated gold nanoparticles with concanavalin A. *Chemical communications* (23):2920-2921.
39. Chien YY, Jan MD, Adak AK, Tzeng HC, Lin YP, Chen YJ, Wang KT, Chen CT, Chen CC, Lin CC 2008. Globotriose-functionalized gold nanoparticles as multivalent probes

- for Shiga-like toxin. *Chembiochem : a European journal of chemical biology* 9(7):1100-1109.
40. Kiessling LL, Gestwicki JE, Strong LE 2000. Synthetic multivalent ligands in the exploration of cell-surface interactions. *Current opinion in chemical biology* 4(6):696-703.
 41. Cairo CW, Gestwicki JE, Kanai M, Kiessling LL 2002. Control of multivalent interactions by binding epitope density. *Journal of the American Chemical Society* 124(8):1615-1619.
 42. Minguet S, Dopfer EP, Schamel WW 2010. Low-valency, but not monovalent, antigens trigger the B-cell antigen receptor (BCR). *International immunology* 22(3):205-212.
 43. Griffith BR, Allen BL, Rapraeger AC, Kiessling LL 2004. A polymer scaffold for protein oligomerization. *Journal of the American Chemical Society* 126(6):1608-1609.
 44. Qhattal HS, Hye T, Alali A, Liu X 2014. Hyaluronan polymer length, grafting density, and surface poly(ethylene glycol) coating influence in vivo circulation and tumor targeting of hyaluronan-grafted liposomes. *ACS nano* 8(6):5423-5440.
 45. Qhattal HS, Liu X 2011. Characterization of CD44-mediated cancer cell uptake and intracellular distribution of hyaluronan-grafted liposomes. *Molecular pharmaceutics* 8(4):1233-1246.
 46. Gabizon A, Horowitz AT, Goren D, Tzemach D, Shmeeda H, Zalipsky S 2003. In vivo fate of folate-targeted polyethylene-glycol liposomes in tumor-bearing mice. *Clinical cancer research : an official journal of the American Association for Cancer Research* 9(17):6551-6559.
 47. Gu F, Zhang L, Teply BA, Mann N, Wang A, Radovic-Moreno AF, Langer R, Farokhzad OC 2008. Precise engineering of targeted nanoparticles by using self-assembled biointegrated block copolymers. *Proceedings of the National Academy of Sciences of the United States of America* 105(7):2586-2591.
 48. McNeeley KM, Annapragada A, Bellamkonda RV 2007. Decreased circulation time offsets increased efficacy of PEGylated nanocarriers targeting folate receptors of glioma. *Nanotechnology* 18(38):385101.
 49. Said Hassane F, Phalipon A, Tanguy M, Guerreiro C, Belot F, Frisch B, Mulard LA, Schuber F 2009. Rational design and immunogenicity of liposome-based diepitope constructs: application to synthetic oligosaccharides mimicking the *Shigella flexneri* 2a O-antigen. *Vaccine* 27(39):5419-5426.
 50. Champion JA, Katare YK, Mitragotri S 2007. Particle shape: a new design parameter for micro- and nanoscale drug delivery carriers. *Journal of controlled release : official journal of the Controlled Release Society* 121(1-2):3-9.
 51. Supersaxo A, Hein WR, Steffen H 1990. Effect of molecular weight on the lymphatic absorption of water-soluble compounds following subcutaneous administration. *Pharmaceutical research* 7(2):167-169.
 52. Kota J, Machavaram KK, McLennan DN, Edwards GA, Porter CJ, Charman SA 2007. Lymphatic absorption of subcutaneously administered proteins: influence of different injection sites on the absorption of darbepoetin alfa using a sheep model. *Drug metabolism and disposition: the biological fate of chemicals* 35(12):2211-2217.
 53. Oussoren C, Zuidema J, Crommelin DJ, Storm G 1997. Lymphatic uptake and biodistribution of liposomes after subcutaneous injection. II. Influence of liposomal size, lipid composition and lipid dose. *Biochimica et biophysica acta* 1328(2):261-272.

54. Noh YW, Kong SH, Choi DY, Park HS, Yang HK, Lee HJ, Kim HC, Kang KW, Sung MH, Lim YT 2012. Near-infrared emitting polymer nanogels for efficient sentinel lymph node mapping. *ACS nano* 6(9):7820-7831.
55. Niikura K, Matsunaga T, Suzuki T, Kobayashi S, Yamaguchi H, Orba Y, Kawaguchi A, Hasegawa H, Kajino K, Ninomiya T, Ijiro K, Sawa H 2013. Gold nanoparticles as a vaccine platform: influence of size and shape on immunological responses in vitro and in vivo. *ACS nano* 7(5):3926-3938.
56. Oyewumi MO, Kumar A, Cui Z 2010. Nano-microparticles as immune adjuvants: correlating particle sizes and the resultant immune responses. *Expert Rev Vaccines* 9(9):1095-1107.
57. Wooden SK, Kapur RP, Lee AS 1988. The organization of the rat GRP78 gene and A23187-induced expression of fusion gene products targeted intracellularly. *Exp Cell Res* 178(1):84-92.
58. Wang H, Wang J, Deng X, Sun H, Shi Z, Gu Z, Liu Y, Zhao Y 2004. Biodistribution of carbon single-wall carbon nanotubes in mice. *Journal of nanoscience and nanotechnology* 4(8):1019-1024.
59. Yoo JW, Doshi N, Mitragotri S 2011. Adaptive micro and nanoparticles: temporal control over carrier properties to facilitate drug delivery. *Advanced drug delivery reviews* 63(14-15):1247-1256.
60. Christian DA, Cai S, Garbuzenko OB, Harada T, Zajac AL, Minko T, Discher DE 2009. Flexible filaments for in vivo imaging and delivery: persistent circulation of filomicelles opens the dosage window for sustained tumor shrinkage. *Molecular pharmaceutics* 6(5):1343-1352.
61. Geng Y, Dalhaimer P, Cai S, Tsai R, Tewari M, Minko T, Discher DE 2007. Shape effects of filaments versus spherical particles in flow and drug delivery. *Nature nanotechnology* 2(4):249-255.
62. Decuzzi P, Godin B, Tanaka T, Lee SY, Chiappini C, Liu X, Ferrari M 2010. Size and shape effects in the biodistribution of intravascularly injected particles. *Journal of controlled release : official journal of the Controlled Release Society* 141(3):320-327.
63. Muro S, Garnacho C, Champion JA, Lefterovich J, Gajewski C, Schuchman EH, Mitragotri S, Muzykantov VR 2008. Control of endothelial targeting and intracellular delivery of therapeutic enzymes by modulating the size and shape of ICAM-1-targeted carriers. *Molecular therapy : the journal of the American Society of Gene Therapy* 16(8):1450-1458.
64. Li S, Nickels J, Palmer AF 2005. Liposome-encapsulated actin-hemoglobin (LEAcHb) artificial blood substitutes. *Biomaterials* 26(17):3759-3769.
65. Kolhar P, Anselmo AC, Gupta V, Pant K, Prabhakar Pandian B, Ruoslahti E, Mitragotri S 2013. Using shape effects to target antibody-coated nanoparticles to lung and brain endothelium. *Proceedings of the National Academy of Sciences of the United States of America* 110(26):10753-10758.
66. Barua S, Yoo JW, Kolhar P, Wakankar A, Gokam YR, Mitragotri S 2013. Particle shape enhances specificity of antibody-displaying nanoparticles. *Proceedings of the National Academy of Sciences of the United States of America* 110(9):3270-3275.
67. Champion JA, Mitragotri S 2009. Shape induced inhibition of phagocytosis of polymer particles. *Pharmaceutical research* 26(1):244-249.

68. Howard M, Zern BJ, Anselmo AC, Shuvaev W, Mitragotri S, Muzykantov V 2014. Vascular targeting of nanocarriers: perplexing aspects of the seemingly straightforward paradigm. *ACS nano* 8(5):4100-4132.
69. Champion JA, Mitragotri S 2006. Role of target geometry in phagocytosis. *Proceedings of the National Academy of Sciences of the United States of America* 103(13):4930-4934.
70. Sharma G, Valenta DT, Altman Y, Harvey S, Xie H, Mitragotri S, Smith JW 2010. Polymer particle shape independently influences binding and internalization by macrophages. *Journal of controlled release : official journal of the Controlled Release Society* 147(3):408-412.
71. Park K 2010. Effect of shape and size of polymer particles on cellular internalization. *Journal of controlled release : official journal of the Controlled Release Society* 147(3):313.
72. Heegaard PM, Boas U, Sorensen NS 2010. Dendrimers for vaccine and immunostimulatory uses. A review. *Bioconjugate chemistry* 21(3):405-418.
73. Boas U, Heegaard PM 2004. Dendrimers in drug research. *Chemical Society reviews* 33(1):43-63.
74. Hasegawa T, Kondoh S, Matsuura K, Kobayashi K 1999. Rigid Helical Poly(glycosyl phenyl isocyanide)s: Synthesis, Conformational Analysis, and Recognition by Lectins. *Macromolecules* 32(20):6595-6603.
75. Beningo KA, Wang YL 2002. Fc-receptor-mediated phagocytosis is regulated by mechanical properties of the target. *Journal of cell science* 115(Pt 4):849-856.
76. Venkataraman S, Hedrick JL, Ong ZY, Yang C, Ee PL, Hammond PT, Yang YY 2011. The effects of polymeric nanostructure shape on drug delivery. *Advanced drug delivery reviews* 63(14-15):1228-1246.
77. Kim Y, Dalhaimer P, Christian DA, Discher DE 2005. Polymeric worm micelles as nanocarriers for drug delivery. *Nanotechnology* 16(7):484-491.
78. Dintzis HM, Dintzis RZ, Vogelstein B 1976. Molecular determinants of immunogenicity: the immunon model of immune response. *Proceedings of the National Academy of Sciences of the United States of America* 73(10):3671-3675.
79. Dintzis HM, Dintzis RZ 1990. Antigens as immunoregulators. *Immunological reviews* 115:243-250; discussion 251.
80. Dintzis RZ, Middleton MH, Dintzis HM 1985. Inhibition of anti-DNP antibody formation by high doses of DNP-polyacrylamide molecules; effects of hapten density and hapten valence. *Journal of immunology* 135(1):423-427.
81. Siliciano RF, Colello RM, Keegan AD, Dintzis RZ, Dintzis HM, Shin HS 1985. Antigen valence determines the binding of nominal antigen to cytolytic T cell clones. *The Journal of experimental medicine* 162(2):768-773.
82. Symer DE, Dintzis RZ, Diamond DJ, Dintzis HM 1992. Inhibition or activation of human T cell receptor transfectants is controlled by defined, soluble antigen arrays. *The Journal of experimental medicine* 176(5):1421-1430.
83. Symer DE, Reim J, Dintzis RZ, Voss EW, Jr., Dintzis HM 1995. Durable elimination of high affinity, T cell-dependent antibodies by low molecular weight antigen arrays in vivo. *Journal of immunology* 155(12):5608-5616.

84. Reim JW, Symer DE, Watson DC, Dintzis RZ, Dintzis HM 1996. Low molecular weight antigen arrays delete high affinity memory B cells without affecting specific T-cell help. *Molecular immunology* 33(17-18):1377-1388.
85. Hafler DA, Weiner HL 1995. Immunologic mechanisms and therapy in multiple sclerosis. *Immunological reviews* 144:75-107.
86. Watson DC, Reim J, Dintzis HM 1996. Suppression of the antibody response to a polymorphic peptide from the platelet alloantigen integrin beta3 with low molecular weight antigen arrays. *Journal of immunology* 156(7):2443-2450.
87. Dintzis RZ, Middleton MH, Dintzis HM 1983. Studies on the immunogenicity and tolerogenicity of T-independent antigens. *Journal of immunology* 131(5):2196-2203.
88. Dintzis RZ, Vogelstein B, Dintzis HM 1982. Specific cellular stimulation in the primary immune response: experimental test of a quantized model. *Proceedings of the National Academy of Sciences of the United States of America* 79(3):884-888.
89. Gestwicki JE, Strong LE, Kiessling LL 2000. Tuning chemotactic responses with synthetic multivalent ligands. *Chemistry & biology* 7(8):583-591.
90. Snippe H, van Houte AJ, Lizzio EF, Willers JM, Merchant B 1982. Characterization of immunogenic properties of haptened liposomal model membranes in mice. VI. Response in B-cell-defective CBA/N mice. *Immunology* 45(3):545-551.
91. Van Houte AJ, Snippe H, Willers JM 1979. Characterization of immunogenic properties of haptened liposomal model membranes in mice. I. Thymus independence of the antigen. *Immunology* 37(2):505-514.
92. Snippe H, Van Houte AJ, Janssen A, Lizzio EF, Willers JM, Merchant B 1982. Characterization of immunogenic properties of haptened liposomal model membranes in mice. VII. Synergistic responses to haptened liposomes and haptened thymus-dependent antigens in CBA/N mice. *Immunology* 45(4):613-620.
93. Gestwicki JE, Strong LE, Cairo CW, Boehm FJ, Kiessling LL 2002. Cell aggregation by scaffolded receptor clusters. *Chemistry & biology* 9(2):163-169.
94. Andre S, Ortega PJ, Perez MA, Roy R, Gabius HJ 1999. Lactose-containing starburst dendrimers: influence of dendrimer generation and binding-site orientation of receptors (plant/animal lectins and immunoglobulins) on binding properties. *Glycobiology* 9(11):1253-1261.
95. Dintzis HM, Dintzis RZ 1992. Profound specific suppression by antigen of persistent IgM, IgG, and IgE antibody production. *Proceedings of the National Academy of Sciences of the United States of America* 89(3):1113-1117.
96. Dintzis RZ, Okajima M, Middleton MH, Greene G, Dintzis HM 1989. The immunogenicity of soluble haptened polymers is determined by molecular mass and hapten valence. *Journal of immunology* 143(4):1239-1244.
97. Diner UE, Kunitomo D, Diener E 1979. Carboxymethyl cellulose, a nonimmunogenic hapten carrier with tolerogenic properties. *Journal of immunology* 122(5):1886-1891.
98. Desaynard C 1977. Role of epitope density in the induction of immunity and tolerance with thymus-independent antigens. IV. Selective tolerance and IgE response by DNP-levan conjugates. *European journal of immunology* 7(9):646-649.
99. Desaynard C, Howard JG 1975. Role of epitope density in the induction of immunity and tolerance with thymus-independent antigens. II. Studies with 2,4-dinitrophenyl conjugates in vivo. *European journal of immunology* 5(8):541-545.

100. Desaynard C, Feldmann M 1975. Role of epitope density in the induction of immunity and tolerance with thymus-independent antigens. I. Studies with 2,4-dinitrophenyl conjugates in vitro. *European journal of immunology* 5(8):537-541.
101. Getts DR, Martin AJ, McCarthy DP, Terry RL, Hunter ZN, Yap WT, Getts MT, Pleiss M, Luo X, King NJ, Shea LD, Miller SD 2012. Microparticles bearing encephalitogenic peptides induce T-cell tolerance and ameliorate experimental autoimmune encephalomyelitis. *Nature biotechnology* 30(12):1217-1224.
102. Hunter Z, McCarthy DP, Yap WT, Harp CT, Getts DR, Shea LD, Miller SD 2014. A biodegradable nanoparticle platform for the induction of antigen-specific immune tolerance for treatment of autoimmune disease. *ACS nano* 8(3):2148-2160.
103. Wegmann KW, Wagner CR, Whitham RH, Hinrichs DJ 2008. Synthetic Peptide dendrimers block the development and expression of experimental allergic encephalomyelitis. *Journal of immunology* 181(5):3301-3309.
104. Choi S-K, Mammen M, Whitesides GM 1997. Generation and in Situ Evaluation of Libraries of Poly(acrylic acid) Presenting Sialosides as Side Chains as Polyvalent Inhibitors of Influenza-Mediated Hemagglutination. *Journal of the American Chemical Society* 119(18):4103-4111.
105. Brinas RP, Sundgren A, Sahoo P, Morey S, Rittenhouse-Olson K, Wilding GE, Deng W, Barchi JJ, Jr. 2012. Design and synthesis of multifunctional gold nanoparticles bearing tumor-associated glycopeptide antigens as potential cancer vaccines. *Bioconjugate chemistry* 23(8):1513-1523.
106. Courtney AH, Puffer EB, Pontrello JK, Yang ZQ, Kiessling LL 2009. Sialylated multivalent antigens engage CD22 in trans and inhibit B cell activation. *Proceedings of the National Academy of Sciences of the United States of America* 106(8):2500-2505.
107. Duong BH, Tian H, Ota T, Completo G, Han S, Vela JL, Ota M, Kubitz M, Bovin N, Paulson JC, Nemazee D 2010. Decoration of T-independent antigen with ligands for CD22 and Siglec-G can suppress immunity and induce B cell tolerance in vivo. *The Journal of experimental medicine* 207(1):173-187.
108. Sestak J, Mullins M, Northrup L, Thati S, Forrest ML, Siahaan TJ, Berkland C 2013. Single-step grafting of aminoxy-peptides to hyaluronan: a simple approach to multifunctional therapeutics for experimental autoimmune encephalomyelitis. *Journal of controlled release : official journal of the Controlled Release Society* 168(3):334-340.
109. Pfrengle F, Macauley MS, Kawasaki N, Paulson JC 2013. Copresentation of antigen and ligands of Siglec-G induces B cell tolerance independent of CD22. *Journal of immunology* 191(4):1724-1731.
110. Muller J, Nitschke L 2014. The role of CD22 and Siglec-G in B-cell tolerance and autoimmune disease. *Nature reviews Rheumatology* 10(7):422-428.
111. Thomann JS, Heurtault B, Weidner S, Braye M, Beyrath J, Fournel S, Schuber F, Frisch B 2011. Antitumor activity of liposomal ErbB2/HER2 epitope peptide-based vaccine constructs incorporating TLR agonists and mannose receptor targeting. *Biomaterials* 32(20):4574-4583.
112. Sestak JO, Sullivan BP, Thati S, Northrup L, Hartwell B, Antunez L, Forrest ML, Vines CM, Siahaan TJ, Berkland C 2014. Co-delivery of antigen and an immune cell adhesion inhibitor is necessary for efficacy of soluble antigen arrays in experimental autoimmune encephalomyelitis. *Molecular Therapy — Methods & Clinical Development* 1.

113. Marlin SD, Springer TA 1987. Purified intercellular adhesion molecule-1 (ICAM-1) is a ligand for lymphocyte function-associated antigen 1 (LFA-1). *Cell* 51(5):813-819.
114. Makgoba MW, Sanders ME, Ginther Luce GE, Dustin ML, Springer TA, Clark EA, Mannoni P, Shaw S 1988. ICAM-1 a ligand for LFA-1 dependent adhesion of B, T and myeloid cells. *Nature* 331(6151):86-88.
115. Dustin ML, Springer TA 1988. Lymphocyte function-associated antigen-1 (LFA-1) interaction with intercellular adhesion molecule-1 (ICAM-1) is one of at least three mechanisms for lymphocyte adhesion to cultured endothelial cells. *J Cell Biol* 107(1):321-331.
116. Dustin ML, Springer TA 1989. T-cell receptor cross-linking transiently stimulates adhesiveness through LFA-1. *Nature* 341(6243):619-624.
117. Van Seventer GA, Shimizu Y, Horgan KJ, Shaw S 1990. The LFA-1 ligand ICAM-1 provides an important costimulatory signal for T cell receptor-mediated activation of resting T cells. *Journal of immunology* 144(12):4579-4586.
118. Radhakrishnan S, Wiehagen KR, Pulko V, Van Keulen V, Faubion WA, Knutson KL, Pease LR 2007. Induction of a Th1 response from Th2-polarized T cells by activated dendritic cells: dependence on TCR:peptide-MHC interaction, ICAM-1, IL-12, and IFN-gamma. *Journal of immunology* 178(6):3583-3592.
119. Northrup L, Sestak JO, Sullivan BP, Thati S, Hartwell BL, Siahaan TJ, Vines CM, Berkland C 2014. Co-Delivery of Autoantigen and B7 Pathway Modulators Suppresses Experimental Autoimmune Encephalomyelitis. *The AAPS journal*.
120. Marradi M, Chiodo F, Garcia I, Penades S 2013. Glyconanoparticles as multifunctional and multimodal carbohydrate systems. *Chemical Society reviews* 42(11):4728-4745.
121. Yeste A, Nadeau M, Burns EJ, Weiner HL, Quintana FJ 2012. Nanoparticle-mediated co-delivery of myelin antigen and a tolerogenic small molecule suppresses experimental autoimmune encephalomyelitis. *Proceedings of the National Academy of Sciences of the United States of America* 109(28):11270-11275.
122. Macauley MS, Pfrengle F, Rademacher C, Nycholat CM, Gale AJ, von Drygalski A, Paulson JC 2013. Antigenic liposomes displaying CD22 ligands induce antigen-specific B cell apoptosis. *The Journal of clinical investigation* 123(7):3074-3083.
123. Jun JE, Goodnow CC 2003. Scaffolding of antigen receptors for immunogenic versus tolerogenic signaling. *Nat Immunol* 4(11):1057-1064.
124. Baxter AG, Hodgkin PD 2002. Activation rules: the two-signal theories of immune activation. *Nature reviews Immunology* 2(6):439-446.
125. Dresser DW, Mitchison NA 1968. The mechanism of immunological paralysis. *Adv Immunol* 8:129-181.
126. Goodnow CC 1996. Balancing immunity and tolerance: deleting and tuning lymphocyte repertoires. *Proceedings of the National Academy of Sciences of the United States of America* 93(6):2264-2271.
127. Grossman Z, Paul WE 1992. Adaptive cellular interactions in the immune system: the tunable activation threshold and the significance of subthreshold responses. *Proceedings of the National Academy of Sciences of the United States of America* 89(21):10365-10369.
128. Redmond WL, Marincek BC, Sherman LA 2005. Distinct requirements for deletion versus anergy during CD8 T cell peripheral tolerance in vivo. *Journal of immunology* 174(4):2046-2053.

129. Basten A, Silveira PA 2010. B-cell tolerance: mechanisms and implications. *Current opinion in immunology* 22(5):566-574.
130. Junt T, Scandella E, Ludewig B 2008. Form follows function: lymphoid tissue microarchitecture in antimicrobial immune defence. *Nature reviews Immunology* 8(10):764-775.
131. von Moos S, Kundig TM, Senti G 2011. Novel administration routes for allergen-specific immunotherapy: a review of intralymphatic and epicutaneous allergen-specific immunotherapy. *Immunology and allergy clinics of North America* 31(2):391-406, xi.
132. Smarr CB, Bryce PJ, Miller SD 2013. Antigen-specific tolerance in immunotherapy of Th2-associated allergic diseases. *Crit Rev Immunol* 33(5):389-414.
133. Kourtis IC, Hirosue S, de Titta A, Kontos S, Stegmann T, Hubbell JA, Swartz MA 2013. Peripherally administered nanoparticles target monocytic myeloid cells, secondary lymphoid organs and tumors in mice. *PloS one* 8(4).
134. Fong CL, Mok CL, Hui KM 2006. Intramuscular immunization with plasmid coexpressing tumour antigen and Flt-3L results in potent tumour regression. *Gene Ther* 13(3):245-256.
135. Senti G, Johansen P, Kundig TM 2009. Intralymphatic immunotherapy. *Current opinion in allergy and clinical immunology* 9(6):537-543.
136. Akdis CA, Akdis M 2011. Mechanisms of allergen-specific immunotherapy. *The Journal of allergy and clinical immunology* 127(1):18-27; quiz 28-19.
137. Bousquet J, Lockey R, Malling HJ 1998. Allergen immunotherapy: therapeutic vaccines for allergic diseases. A WHO position paper. *The Journal of allergy and clinical immunology* 102(4 Pt 1):558-562.

**Chapter II: Molecular Dynamics of Multivalent Soluble
Antigen Arrays Support Two-Signal Co-delivery Mechanism
in the Treatment of Experimental Autoimmune
Encephalomyelitis**

1. Introduction

Many autoimmune disorders are triggered by the immune system's misrecognition of self versus non-self epitopes, an event hypothesized to promote autoreactive T cell and/or B cell clonal expansion and attack against self-antigen(s). Many current therapies for patients with an autoimmune disease cause global immunosuppression, introducing risk of serious adverse side effects.¹⁻³ As a result, there is a strong interest in designing therapeutic agents to shift the autoreactive immune response towards tolerance of specific autoantigens.^{4,5} Multivalent antigen arrays, composed of antigen and an inhibitor co-grafted to a flexible polymer backbone (Table 1), are hypothesized to induce antigen-specific tolerance and thereby obviate the need for global immunosuppression.⁶⁻⁹ These arrays have emerged as a promising option with potential to induce an antigen-specific immune response to repress autoimmune disease.^{10,11}

Studies dating back to the 1970s have shown that polymeric multivalent antigen array physical characteristics such as antigen valency, density, and polymer molecular weight may be tailored to induce immune tolerance.^{6,7,12-15} The ability of these antigen arrays to modulate immune response may be explained in part by a cellular mechanism, whereby the appropriate physical presentation of multivalent antigen enables sufficient cell receptor clustering, engagement, and/or initiation of a tolerogenic cellular response.¹⁶⁻²⁰ Leveraging antigen-specificity and desired physical characteristics, multivalent antigen arrays could potentially guide the immune response to the conjugated antigen.

Previously, our group developed a multivalent soluble antigen array (SAGa) for the treatment of experimental autoimmune encephalomyelitis (EAE), a murine model of multiple sclerosis (MS).^{21,22} A SAGa molecule consists of a linear hyaluronic acid (HA) polymer backbone co-grafted with both myelin sheath antigenic peptide (proteolipid protein peptide,

PLP₁₃₉₋₁₅₁) and intercellular adhesion molecule-1 (ICAM-1) inhibitor peptide, LABL, derived from leukocyte function associated antigen-1 (LFA-1). SAgA co-presentation of two signals (PLP and LABL) seeks to exploit immunology dogma that says the presence of two signals, both primary antigen and secondary costimulatory or inhibitory signal, is especially effective and sometimes necessary for eliciting a robust immune response.^{10, 11, 23} The secondary signal may be costimulatory or inhibitory, acting as a context signal to direct the immune response towards the primary antigen.^{18, 24, 25} For example, the autoreactive myelin-specific T cell attack in MS is propagated by the immunological synapse between antigen presenting cells (APCs) and T cells, a signaling event which requires both a primary antigen-specific signal and a secondary signal.²⁶⁻³² In other cases, it's been shown that engaging the B cell receptor along with an inhibitory coreceptor inhibits B cell activation,³³ while co-delivery of a B cell epitope and T helper cell epitope induces antigenic protection.³⁴ SAgA molecules, by presenting autoantigen and secondary inhibitory signal on a polymer backbone, may target and interrupt antigen-specific signaling by APCs such as dendritic cells or B cells.³⁵ LABL may block immune cell adhesion, thereby inhibiting autoreactive T cell and/or B cell clonal expansion to redirect the immune response towards autoantigenic tolerance.^{36, 37} We propose that co-presentation of both primary and secondary signals in the same spatial and temporal context must occur for therapeutic efficacy (i.e. coincident two-signal co-delivery).

Various methods were employed to probe the mechanism of SAgA molecules and the properties that render them therapeutic. *In silico* molecular dynamics simulations were used to predict molecular conformation and conformational stability to further understand SAgA behavior on a molecular level under physiological conditions. Particle size was determined by dynamic light scattering to clarify particle transport behavior. EAE animal studies were

performed to assess the therapeutic efficacy of SAgA molecules compared to arrays of different design or composition. These studies were used to elucidate the role of two-signal co-delivery in determining therapeutic potential. By gaining a greater understanding of these molecules' properties and mode of action, we can refine the design criteria needed to better develop autoantigen-specific therapeutic agents to treat autoimmune disease.

2. Materials and Methods

2.1 Materials

Hyaluronic acid (HA) sodium salt (MW 16 kDa) was purchased from Lifecore Biomedical (Chaska, MN). Aminoxy-LABL (AoLABL, Aoa-itDGEATDSG-OH) and aminoxy-PLP (AoPLP, Aoa-HSLGKWLGHDPKF-OH) were purchased from PolyPeptide Laboratories (San Diego, CA). Incomplete Freund's adjuvant (IFA) and killed *Mycobacterium tuberculosis* strain H37RA were purchased from Difco (Sparks, MD). Pertussis toxin was purchased from List Biological Laboratories (Campbell, CA). All other chemicals and reagents were analytical grade and used as received.

2.2 Preparation and Characterization of Soluble Antigen Arrays

Synthesis of SAgAs was described previously.²¹ Aminoxy peptides AoLABL and/or AoPLP were reacted with 2 mg/ml HA by briefly dissolving in 20 mM acetate buffer (pH adjusted to 5.5±0.1) then stirring at 500 rpm for 24 hours at room temperature. The reaction solution was dialyzed (MWCO 6000-8000 Da, Spectrum Laboratories, Inc., Rancho Dominguez, CA) against 100X the reaction volume of deionized water and rinsed four times over 24 hours to remove unreacted free peptides and salts. Dialyzed samples were then frozen and lyophilized.

Peptide conjugation was determined through gradient reverse-phase analytical high-performance liquid chromatography (RP-HPLC) (Waters Corp., Milford, MA) on a C18 analytical column (Higgins Analytical, Proto200, 5 μm , 200 \AA , 250 x 4.6 mm^2 , Mountain View, CA), following cleavage of peptides in 0.1N HCl. Samples were compared to standard curves of AoPLP and AoLABL to determine peptide content. A gradient method with aqueous mobile phase A (94.9% d.d. H_2O , 5% acetonitrile, 0.1% trifluoroacetic acid (TFA)) and organic mobile phase B (99.9% acetonitrile, 0.1% TFA) was used to analyze samples. Samples were detected at 220 nm.

2.3 Particle Characterization by Dynamic Light Scattering

The size distribution of particles was evaluated using dynamic light scattering (Zeta-PALS, Brookhaven Instrument Corp., Holtsville, NY) measured at 90° and operated at 658 nm and 25°C . Hydrodynamic radius (R_h) was determined from the Stokes-Einstein equation:

$$R_h = \frac{k_b T}{6\pi\eta D_T} \quad (\text{Equation 1})$$

where k_b is the Boltzmann's constant, T is temperature (K), η is the solvent viscosity, and D_T is the translational diffusion coefficient. Particle size was reported as hydrodynamic diameter, D_h , where $D_h = 2 \times R_h$. Samples were measured ($n=5$) in phosphate-buffered saline (PBS, 0.137 M NaCl, pH 7.4) at ambient temperature after passing through a 0.45 μm PVDF filter. The particle size distribution was derived from the autocorrelation function using a non-negatively constrained least squares (NNLS) deconvolution algorithm.

Particle size of HA and SAgA_{PLP:LABL} (SAgA reacted with PLP and LABL) was first investigated as a function of sample molarity varying from 0.0134 to 0.428 mM in order to determine an appropriate concentration for further DLS characterization. All samples were then

characterized by DLS at a concentration of 0.0625 mM. In addition, HA particle size was observed in 0.1M ammonium acetate buffer (pH 5.0±0.1) as a function of salt concentration varying from 0.01 M to 1.0 M sodium chloride (NaCl) to observe aggregation behavior of molecules.

2.4 Clinical EAE Study in Mice

Animal studies were carried out with 4-6 week old SJL/J (H-2) female mice purchased from Harlan Laboratories (Indianapolis, IN). Mice were housed under specified, pathogen-free conditions at The University of Kansas and all experiments were approved by the University's Institutional Animal Care and Use Committee. Complete Freund's adjuvant (CFA) was made by combining IFA and killed *M. tuberculosis* strain H37RA at a final concentration of 4 mg/ml. Animals were induced with experimental autoimmune encephalomyelitis (EAE), the PLP-specific mouse model of relapsing-remitting MS, on day 0 of the study. Immunization was accomplished using a 0.2 ml emulsion containing 200 µg PLP₁₃₉₋₁₅₁ peptide, plus equal volumes of PBS and CFA. The emulsion was administered subcutaneously (s.c.) as a total of four 50 µl injections, located above each shoulder and each hind flank. Pertussis toxin (100 ng in 100 µl) was injected intraperitoneally on day 0 and day 2 post-immunization.

Treatments were administered on days 4, 7, and 10 as 100 µl subcutaneous injections at the nape of the neck (n=6 mice per treatment group). Samples and vehicle control (sterile PBS) were administered at a dose equivalent to 200 nmol PLP per 100 µl (2 mM PLP). This schedule and dose were found to be efficacious in a previous study.²² HA_{LABL} (SAgA containing LABL) was dosed at an equivalent LABL concentration (2 mM LABL) and HA was dosed at an equivalent SAgA concentration (0.214 mM). Disease progression was evaluated by a single observer using the following clinical score system: 0, no clinical disease symptoms; 1, weakness

or limpness of the tail; 2, weakness or partial paralysis of one or two hind limbs (paraparesis); 3, full paralysis of both hind limbs (paraplegia); 4, paraplegia plus weakness or paralysis of forelimbs; 5, moribund (at which point mice were euthanized). In addition to animal scoring, body weight measurements were performed daily for the 26-day duration of the EAE study.

2.5 Molecular Dynamics Simulations of Soluble Antigen Arrays

Molecular dynamics simulations were used to computationally simulate the physical forces acting on SAgAs and other molecules in order to evaluate their conformations over time scales of 20-40 ns. Several molecule configurations were simulated:

1. **HA:** One 16 kDa HA polymer backbone.
2. **HA_{LABL}:** One 16 kDa HA backbone with 20 side chains of LABL spaced equally along the backbone.
3. **HA_{PLP}:** One 16 kDa HA backbone with 20 side chains of PLP spaced equally along the backbone.
4. **SAgA_{PLP:LABL}:** One 16 kDa HA backbone with 10 side chains of PLP and 10 side chains of LABL, alternately spaced at equal distances along the backbone.
5. **Homopolymer mixture:** One full-length HA_{LABL} molecule as in (2) and one full-length HA_{PLP} molecule as in (3) placed side-by-side.
6. **SAgA component mixture:** One 16 kDa HA polymer backbone with 10 free PLP and 10 free LABL peptides.
7. **Peptide mixture:** Eight free PLP and eight free LABL peptides placed in a cube arrangement.

8. Heteropolymer mixture: Two full-length SAgA_{PLP:LABL} molecules as in (4) placed side-by-side.

The molecular dynamics simulations were performed using Desmond software.³⁸ The molecular systems were prepared for simulation and solvated using a single-point-charge (SPC) model. Further, Na⁺ and Cl⁻ ions were added to the system at a 0.15 M concentration in order to simulate physiological conditions. The force field used for simulations was OPLS2005 as available in Desmond.³⁹ The default system relaxation protocol was used to equilibrate the simulation systems prior to production simulation. An NPT (isothermal-isobaric) ensemble was then used in the production simulations, with constant temperature of 27°C (300K) and constant pressure of 1 atm (1.01325 bar). Production simulations were run for a total of 20-40 ns. The Nose-Hoover thermostat was used to control temperature,⁴⁰ and the Martyna-Tobias-Klein barostat was used to control pressure.⁴¹ Coulombic interactions were calculated using the Ewald smooth particle-mesh approach.⁴² The RESPA integrator was used with 2 fs time step intervals for bonded/non-bonded interactions at short ranges, and a 6 fs step was used for non-bonded interactions beyond the short range cutoff.⁴³ Additional potential energy calculation and analysis was performed using Molecular Operating Environment.⁴⁴

2.6 Statistical Analysis

GraphPad Prism (GraphPad Software Inc.) was used to perform statistical analysis including linear regression, area under the curve (AUC) analysis, and one-way or two-way analysis of variance (ANOVA) as appropriate. Two-way ANOVA was used to analyze clinical disease scores and weight loss compared to a PBS negative control; one-way ANOVA was used to analyze disease score AUC. Significance threshold was determined by $p < 0.05$ followed by

Bonferroni's multiple comparisons test. Additional statistics and data analysis for molecular dynamics energetics were performed using MATLAB.⁴⁵

3. Results

DLS, molecular dynamics, and animal studies were surveyed to probe the role of SAgA design elements in co-delivery of both autoantigen and secondary signals. These techniques were specifically selected to compliment methods used in our previous publications.^{21, 22, 46} Different approaches to co-delivery of PLP and LABL were probed (Table 1D-G). A SAgA_{PLP:LABL} molecule grafted with both PLP and LABL was included to evaluate the importance of two-signal presentation on a single HA backbone (Table 1D). A homopolymer mixture containing both HA_{PLP} and HA_{LABL} in a 1:1 molar ratio (Table 1E) was included to evaluate the importance of two-signal presentation on different HA backbones. A SAgA component mixture containing free PLP, LABL, and HA in a 10:10:1 molar ratio (Table 1F), which resembled the SAgA_{PLP:LABL} molecule in non-conjugated form, was included to evaluate the importance of linking all components. A peptide mixture containing PLP and LABL in a 1:1 molar ratio (Table 1G) was included to evaluate the importance of using HA as a carrier for co-delivery of the two peptides.

3.1 Synthesis and Characterization of Soluble Antigen Arrays

SAgAs were analyzed by RP-HPLC for approximate molecular weight and peptide conjugation as described previously.²¹ HPLC results indicated that SAgA_{PLP:LABL} contained approximately 9 PLP and 8 LABL peptides per HA backbone, while homopolymers HA_{PLP} and HA_{LABL} contained 10 or 12 peptides per HA backbone, respectively (Table 1, B-D).

3.2 Dynamic Light Scattering Demonstrates Aggregation and Formation of Nanoparticles

Dynamic light scattering was used to determine particle hydrodynamic radius (R_h , Equation 1). Particle size distributions were reported as the number-weighted hydrodynamic diameter (D_h) of each sample. HA is naturally polydisperse and consists of a range of molecular weights centered around 16 kDa. Therefore, it was expected that resulting particles (e.g. globular molecules or molecular complexes) of HA and HA-derived SAgAs would be somewhat polydisperse in size.

HA and SAgA_{PLP:LABL} particle sizes were first evaluated at various sample concentrations (0.0134 to 0.428 mM) in order to determine an appropriate concentration for further DLS characterization. The concentration range included 0.214 mM, equivalent to the *in vivo* dose used in animal studies (i.e., 2 mM of PLP, or approximately 10X the moles of SAgA_{PLP:LABL} with ~10 PLP per HA backbone). Linear regression indicated no statistical dependence of D_h on HA or SAgA_{PLP:LABL} concentration in this range (Figure 1A). Therefore, a molar concentration of 0.0625 mM, equivalent to 1 mg/ml HA, was used for remaining DLS studies (Table 1, Figure 1C). Upon comparison of all groups at this concentration, SAgA_{PLP:LABL} was observed to have the largest D_h at 8.85 ± 0.92 nm, followed by the homopolymer mixture (HA_{LABL}+HA_{PLP}). The peptide mixture (PLP+LABL) was observed to have the smallest D_h at 0.89 ± 0.15 nm, although this is approaching the lower limit of detection.

HA particle size at 0.0625 mM was further investigated as a function of salt concentration in 0.1M ammonium acetate buffer to observe aggregation behavior (Figure 1B). Particle size was predicted to decrease with increasing NaCl concentration due to the salt disrupting ionic or hydrogen bonding sites, thus preventing intermolecular interactions and reducing aggregation. By linear regression, D_h was found to significantly decrease with

increasing NaCl molarity ($p < 0.01$). The data suggested the particles observed by DLS in PBS (0.137 M NaCl) were aggregates of individual polymer molecules.

Measured particle D_h was compared to the empirical D_h (D_h^*) derived for HA, calculated from Equation 2 as previously reported (MW in kDa):^{47, 48}

$$D_h^* = 2(0.87 \cdot MW^{0.63}) \quad (\text{Equation 2})$$

D_h values measured by DLS were lower than those calculated by Equation 2. Empirical D_h^* of HA (16 kDa) was 9.98 nm, roughly twice as large as the measured value of 5.32 ± 1.30 nm. Similarly, D_h^* of SAgA_{PLP:LABL} (39 kDa) was 17.50 nm, compared to the measured value of 8.85 ± 0.93 nm. Equation 2 dictates that HA particle size should increase directly with polymer MW. While this trend held true for SAgA_{PLP:LABL} in relation to HA, it did not hold true for HA_{PLP} (32 kDa) and HA_{LABL} (28 kDa) which were calculated to have D_h^* of 15.45 and 14.20 nm, respectively. This discrepancy suggests the conjugated peptides may alter the conformation, and thus D_h , of the homopolymers and SAgA_{PLP:LABL}.

3.3 Clinical EAE Studies Indicate Therapeutic Efficacy

Animal studies were performed in SJL/J mice using experimental autoimmune encephalomyelitis (EAE) induced with PLP₁₃₉₋₁₅₁ to model the relapsing-remitting form of MS. Disease symptoms emerged on day 10-12 with peak of disease occurring on day 13-15 before progressing to remission around day 20-25. Statistical differences were determined by comparing treated groups with the negative PBS control (Table 2). Mice treated with SAgA_{PLP:LABL} had better clinical outcomes than mice treated with other groups based on evaluation of clinical score (Figure 2), clinical score area under the curve (AUC) relative to PBS controls (Figure 3), and % weight change (Supplementary Figure S1).

Clinical response to SAgA_{PLP:LABL} treatment was observed across four separate studies (Figure 2A-D). SAgA_{PLP:LABL} significantly alleviated EAE disease score compared to the PBS control in each Figure 2 study as follows: **A**) day 12-14 ($p<0.01$); **B**) day 11 ($p<0.001$), day 12-15 ($p<0.0001$), and day 17 ($p<0.05$); **C**) day 11-14 ($p<0.0001$) and day 15 ($p<0.01$); **D**) day 11 ($p<0.001$), day 12-15 ($p<0.0001$), and day 16 ($p<0.01$). The homopolymer mixture (HA_{PLP}+HA_{LABL}) also significantly alleviated disease score on day 11-12 ($p<0.001$), day 13 ($p<0.01$), and day 14-15 ($p<0.0001$) compared to the PBS control (Figure 2B). Additionally, treatments with SAgA_{PLP:LABL} and the homopolymer mixture significantly reduced weight loss on day 11-16 ($p<0.01$) and day 11-15 ($p<0.05$), respectively (Supplementary Figure S1). In contrast, the component mixture (HA+PLP+LABL) only alleviated disease score on day 11 ($p<0.001$), while the peptide mixture (PLP+LABL), HA_{PLP}, HA_{LABL}, and HA did not significantly alleviate disease score or reduce weight loss on any day of the study. (Figure 2, Table 2)

EAE disease score AUC was determined by taking the area under the curve from the clinical disease score profiles for each treatment group in Figure 2, relative to the PBS control (Figure 3, Table 2). AUC representation of clinical data has been reported as an informative secondary measure for overall extent of disease because it provides a cumulative measure that is not weighted or biased by the scaling or time course of disease.⁴⁹ SAgA_{PLP:LABL} treatment exhibited the lowest cumulative disease score relative to the PBS control ($p<0.0001$). The cumulative disease score of the homopolymer mixture treatment group was also significantly lower than the PBS control ($p<0.01$), suggesting these homopolymers may facilitate co-delivery of PLP and LABL. In contrast, administration of HA_{PLP}, HA_{LABL}, HA alone, the component mixture, or the peptide mixture did not significantly reduce extent of disease compared to PBS.

3.4 Molecular Dynamics Simulations of Soluble Antigen Arrays

The potential for co-delivery of SAgA components was assessed using computational modeling of different combinations of HA, PLP, LABL and homopolymers (HA_{PLP} and HA_{LABL}). Molecular dynamics simulations were performed on structures from each group (Table 1) over 20-40 ns. Analysis of molecular energies over these time periods indicated the molecules reached energetic stability after 20 ns. Final molecular conformations were shown as a side angle image in addition to a Van der Waals (VDW) surface. The latter viewing angle was from the right side at an approximate 45° angle above the long axis.

3.4.1 Final Conformations of Soluble Antigen Arrays

The final conformation of the HA backbone resembled a random coil (Table 1A, Figure S2), as expected from the literature on HA in solution.^{50, 51} The final conformations of single SAgA_{PLP:LABL} (Table 1D, Figure 4), HA_{LABL} (Table 1B, Figure S3), and HA_{PLP} (Table 1C, Figure S4) molecules demonstrated a tendency for PLP and/or LABL side chain interactions both with neighboring peptides and with the HA backbone.

Following a 20 ns simulation, the final SAgA_{PLP:LABL} molecule conformation exhibited an approximate chain diameter of ~30 Å and an end-to-end distance of ~300 Å (Figure 4). The HA backbone of SAgA_{PLP:LABL} turned and kinked in a helical fashion. Despite the helical nature of the individual SAgA_{PLP:LABL}, a simulation of two aligned SAgA_{PLP:LABL} molecules did not adopt a helical conformation (Figure 5). The neighboring SAgA_{PLP:LABL} molecules remained fairly linear, did not contract into a ball or coil tightly, but did demonstrate a tendency for side chain entanglement with the side chains and HA backbone of the neighboring SAgA_{PLP:LABL} molecule. Side chain entanglement occurred primarily through heterotypic peptide interactions.

Molecular dynamics simulations were then applied to a mixture of homopolymers and a mixture of PLP, LABL, and HA. A single HA_{PLP} aligned next to a single HA_{LABL} molecule (1:1 homopolymer mixture) exhibited significant intermolecular interactions between the peptide side chains and HA backbone, leading to chain entanglement (Table 1E, Figure 6). In contrast, the mixture of free, unlinked PLP, LABL, and HA (SAGa component mixture) exhibited minor interactions between the peptides and HA backbone, instead favoring the formation of primarily heterotypic peptide:peptide complexes (Table 1F, Figure 7). This result was corroborated by simulating a mixture of free PLP and LABL (peptide mixture), which exhibited weak intermolecular interactions and random aggregation (Table 1G, Figure 8).

3.4.2 Energetics of Soluble Antigen Array Simulations

The potential energy of each system was monitored over the duration of the simulations (Figure S5). Change in potential energy (PE) was presented as relative PE % relaxation from the initial simulation state, calculated from the final PE (PE_f) and initial PE (PE_i) as follows (Table 3):

$$PE \% \text{ Relaxation} = \frac{PE_f - PE_i}{PE_i} \quad \text{Equation 3}$$

Total PE % relaxation values were rather small (less than 1%) given the large energetic values of these systems. PE % relaxation was also calculated for the first half and last half of the simulations (Table 3). The latter stages of the simulations exhibited negligible change in PE over time, indicating energetic equilibrium and conformational stability were reached (Figure S5). Small spikes in energy are typically observed in large molecule simulations, for which fluctuations in side chain and backbone conformations cause rapid, momentary changes in

energy. The lack of significant changes in average energy over time, however, indicated no significant conformation changes occurred during these intervals.

PE % relaxation was compared among the simulations carried out over 40 ns, which included the homopolymer mixture (Figure S5E), SAgA component mixture (Figure S5F), and peptide mixture (Figure S5G). The homopolymer mixture exhibited the greatest PE % relaxation (0.1316%) compared to the component mixture (0.0931%) and the peptide mixture (0.0740%), signifying that greater conformational stability was reached at the end of the homopolymer mixture simulation (Table 3).

4. Discussion

Physicochemical properties of antigen arrays are known to skew the immune response towards immunogenicity or tolerance.¹⁰ Several investigators have proposed a correlation between immune response and antigen array properties such as polymer size, flexibility, antigen valency, and antigen spacing, suggesting these properties affect the ability of an array to cluster cell surface receptors and elicit a given immune response.^{8, 12, 14-16, 19, 52, 53} Moreover, multivalent antigen arrays provide an effective platform for the co-delivery of primary autoantigen and secondary signal in spatial and temporal proximity. Inclusion of a secondary costimulatory or inhibitory signal may shift the immune response to a given antigen towards protection or tolerance, respectively.^{11, 18, 33, 54-58} Such an array facilitates two-signal co-delivery by localizing exposure of the immune system to antigen and secondary signal within the same time and space. Delivery of both signals in this context may be important for eliciting the desired immune response due to (1) co-delivery to the tissue of interest and (2) engaging and clustering cell surface receptors to initiate a cellular response.¹⁰

Clinical EAE studies revealed that inclusion of both antigen and secondary signal were required for therapeutic efficacy, as the groups lacking two signals (HA, HA_{PLP}, and HA_{LABL}) did not alleviate disease. In addition, neither group containing a physical mixture of the two signals (component mixture and peptide mixture) alleviated disease, indicating that mere presence of both signals did not render efficacy. Rather, the groups containing both signals in linked arrays (SAgA_{PLP:LABL} and homopolymer mixture) significantly alleviated disease, indicating that *co-delivery* of both signals was necessary for efficacy. Others have also shown that conjugation between all components of an antigen-specific immunotherapy was necessary to achieve desired immune modulation.^{34, 58-62} Previously, we showed there was no difference in cytokine profiles generated from EAE mice splenocytes following *ex vivo* treatment with a mixture of HA, PLP, and LABL versus conjugated SAgA_{PLP:LABL}. The *ex vivo* cytokine screening environment effectively contains both signals in the same time and space (i.e., all components are together within the same well).²² These results suggest an *in vivo* delivery mechanism in which HA acts as a carrier for the co-delivery of autoantigen and secondary signal to the site of interest.

Transport to the site of interest, such as secondary lymphoid organs, is an important determinant for therapeutic efficacy. A major factor determining transport following subcutaneous injection is hydrodynamic diameter. Depending on the site of administration, particles <10 nm tend to drain into systemic circulation, particles between 10-70 nm tend to drain into the lymphatics, and particles >70 nm tend to form a depot at the injection site.^{10, 47, 63-69} DLS size distributions of SAgA_{PLP:LABL} and the homopolymer mixture overlapped with the 10 nm threshold, suggesting these could drain with interstitial fluid through the peripheral lymphatics to allow for encounters with resident APCs. While the average particle sizes of SAgA_{PLP:LABL}

(8.85 ± 0.92 nm) and homopolymer mixture (6.69 ± 1.19 nm) at simulated physiological conditions were the largest among all groups, they did not differ significantly from the particle sizes of HA, HA_{PLP}, HA_{LABL}, or the SAgA component mixture. In contrast, the particle size of the peptide mixture (0.89 ± 0.15 nm) was significantly smaller. The particle size distribution was sufficiently below the 10 nm threshold such that peptide drainage into systemic circulation was highly probable, increasing clearance and reducing efficacy.⁶⁶

Building upon this hypothesized mechanism of transport, molecular dynamics simulations allowed us to predict likely molecular conformations to better understand why certain groups (i.e. homopolymer mixture) might facilitate two-signal co-delivery to improve treatment efficacy, while others (i.e. component mixture, peptide mixture) do not. The significant intermolecular interactions and peptide/polymer chain entanglement exhibited by neighboring molecules in the homopolymer mixture suggest effective co-delivery of both signals as if presented along a single backbone. Conversely, the weak, random interactions exhibited by molecules in the peptide mixture and SAgA component mixture (i.e. HA, PLP, and LABL) may not provide a sufficiently stable vehicle for spatial and temporal co-delivery of both signals.

Furthermore, comparison of PE % relaxation between the homopolymer mixture, component mixture, and free peptide mixture over a 40 ns simulation revealed the greatest % relaxation for the homopolymer mixture. The greater reduction in PE exhibited by the homopolymer mixture signified that greater conformational stability was achieved through intermolecular interactions between the homopolymers, compared to intermolecular interactions between the components (HA, PLP, LABL) or free peptides (PLP, LABL). Thus, intermolecular complexes formed in the homopolymer mixture may be more likely to persist after administration *in vivo*, potentially facilitating co-delivery. If the weaker complexes formed by

the component mixture do not persist under physiological conditions, it increases the probability that the peptides will dissociate and drain into systemic circulation, diminishing the likelihood of co-delivery.

5. Conclusions

Two-signal co-delivery is an important factor for directing immune response. Our results from previous publications suggest it is critical for alleviating disease in EAE.^{21,22} Multivalent soluble antigen arrays offer promising options for antigen-specific immunotherapy and provide a platform for two-signal co-delivery. $\text{SAgA}_{\text{PLP:LABL}}$ and a mixture of $\text{HA}_{\text{PLP}} + \text{HA}_{\text{LABL}}$ were found to be therapeutically effective in EAE through co-delivery of primary autoantigen, PLP, and a secondary inhibitory signal, LABL. DLS and molecular dynamics simulations shed light on the mechanisms by which co-delivery was achieved. It is believed that therapeutically effective antigen arrays possessed physical characteristics that facilitated co-transport of the two signals. Intermolecular interactions and chain entanglement suggested facilitation of two-signal co-delivery via entangled homopolymers each displaying one signal. These findings refine our understanding of the mechanisms by which soluble antigen arrays enact their therapeutic effect, and guide the development of future multivalent antigen-specific immunotherapies.

Table 1. Visual diagrams and characteristics of each sample used for dynamic light scattering (DLS) characterization and animal studies.

Sample	Molar Ratio per HA Polymer ^{a,b} (PLP:LABL:HA)	Approx. MW (kDa) ^c	D _h in PBS (nm) ^d
A) HA	0:0:1	16	5.32 ± 1.30
B) HA _{LABL}	0:12:1	28	5.94 ± 0.84
C) HA _{PLP}	10:0:1	32	3.52 ± 0.44
D) SAgA _{PLP:LABL}	9:8:1	39	8.85 ± 0.92
E) Homopolymer mixture: HA _{PLP} +HA _{LABL}	10:12:2	n/a	6.69 ± 1.19
F) SAgA component mixture: HA+PLP+LABL	10:10:1	n/a	4.48 ± 0.89
G) Peptide mixture: PLP+LABL	1:1:0	n/a	0.89 ± 0.15

^aPeptide molar conjugation was determined by reverse-phase HPLC and results are an average of triplicate injections from a single batch preparation.

^bHA, hyaluronic acid; PLP, proteolipid protein peptide; LABL, inhibitor peptide derived from leukocyte function associated antigen-1

^cCalculated from RP-HPLC data. MW, molecular weight.

^dDetermined by DLS at a concentration of 0.0625 mM in PBS (n=5). D_h, hydrodynamic diameter; PBS, phosphate-buffered saline.

Table 2. Statistical summary of EAE disease response following *in vivo* treatments.

Treatment Group	Clinical Score Days of Significance ^a	% Weight Change Days of Significance ^a	Disease Score AUC Relative to PBS ^b
<i>Two-Component Co-delivery Systems</i>			
SAg_{PLP:LABL}	Day 11 (<i>p</i> <0.001)	Day 11-14 (<i>p</i> <0.0001)	0.38 ± 0.22 (<i>p</i> <0.0001) ^d
	Day 12-15 (<i>p</i> <0.0001)	Day 15 (<i>p</i> <0.001)	
	Day 16 (<i>p</i> <0.01) ^c	Day 16 (<i>p</i> <0.01) ^c	
HA_{PLP}+HA_{LABL}	Day 11-12 (<i>p</i> <0.001)	Day 11, 13 (<i>p</i> <0.01) Day 12, 14-15 (<i>p</i> <0.05)	0.44 ± 0.41 (<i>p</i> <0.01)
	Day 13 (<i>p</i> <0.01)		
	Day 14-15 (<i>p</i> <0.0001)		
<i>Two-Component Mixtures</i>			
HA+PLP+LABL	Day 11 (<i>p</i> <0.001)	<i>ns</i>	0.72 ± 0.35
PLP+LABL	<i>ns</i>	<i>ns</i>	1.05 ± 0.26
<i>Single-Component Controls</i>			
HA_{PLP}	<i>ns</i>	<i>ns</i>	0.68 ± 0.43
HA_{LABL}	<i>ns</i>	<i>ns</i>	1.11 ± 0.63
HA	<i>ns</i>	<i>ns</i>	0.95 ± 0.39
PBS	<i>ns</i>	<i>ns</i>	1.00 ± 0.46 ^d

^aStatistical significance determined relative to PBS using two-way ANOVA followed by Bonferroni's post-hoc test with *p*<0.05 (n=6 per treatment group)

^bData expressed as mean ± SD (n=6 unless otherwise noted). AUC relative to PBS, where PBS = 1. AUC, area under the curve; PBS, phosphate-buffered saline.

^cData from study in Figure 2D.

^dAverage of four pooled studies from Figure 2 (n=24)

^eHA, hyaluronic acid; PLP, proteolipid protein peptide; LABL, inhibitor peptide derived from leukocyte function associated antigen-1; *ns*, no statistical significance.

Table 3. Relative potential energy (PE) % relaxation over the duration of the simulations indicates the change in PE from initial to final conformations.

Sample	Simulation Duration (ns)	PE % Relaxation ^a		
		Total	First Half	Last Half
Homopolymer Mixture (HA _{PLP} +HA _{LABL})	40	0.1316	0.1117	0.0198
Component Mixture (HA+PLP+LABL)	40	0.0931	0.0781	0.0150
Free Peptide Mixture (PLP+LABL)	40	0.0740	0.0638	0.0101
SAgA _{PLP:LABL} x2	10	0.0607	0.0541	0.0066
HA	10	0.0467	0.0393	0.0074
HA _{PLP}	10	0.0408	0.0234	0.0174
SAgA _{PLP:LABL}	20	0.0314	0.0311	0.0003
HA _{LABL}	20	0.0302	0.0253	0.0049

^a% Relaxation values were calculated from Equation 3. PE absolute values were determined from Desmond molecular dynamics simulations. PE, potential energy.

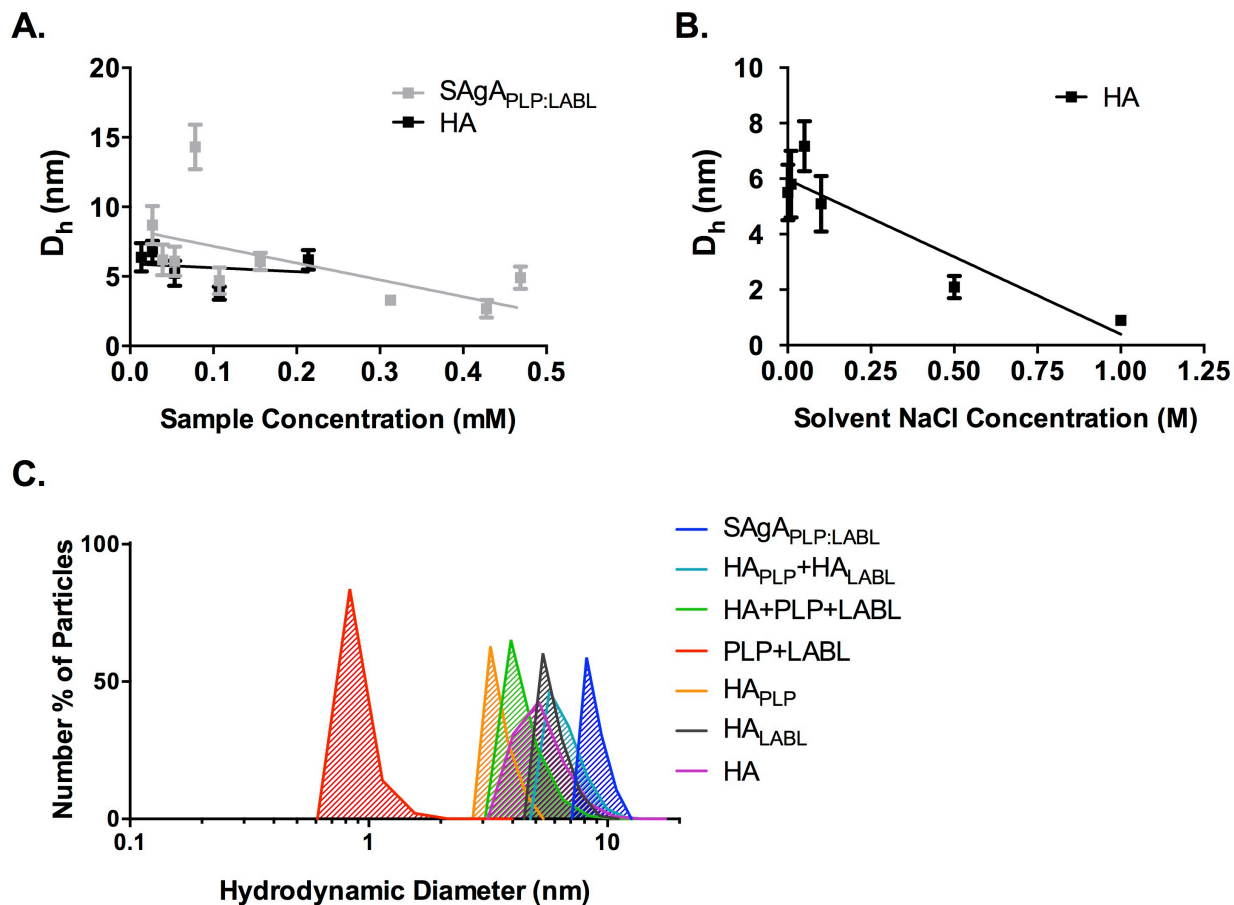


Figure 1. Nanoparticle characterization: Number-weighted hydrodynamic diameter (D_h) determined by dynamic light scattering (DLS). A) Particle size dependence of HA and $SAgA_{PLP:LABL}$ on solute molarity. Linear regression indicated no statistical dependence of HA or $SAgA_{PLP:LABL}$ particle size on solute concentration in this range. B) Particle size distribution of all groups at 0.0625 mM in PBS. C) Particle size dependence of HA on solvent NaCl molarity. Linear regression determined HA particle size was statistically dependent ($p < 0.01$) on NaCl concentration in this range. Data presented as mean \pm SD ($n=5$) with $p < 0.05$.

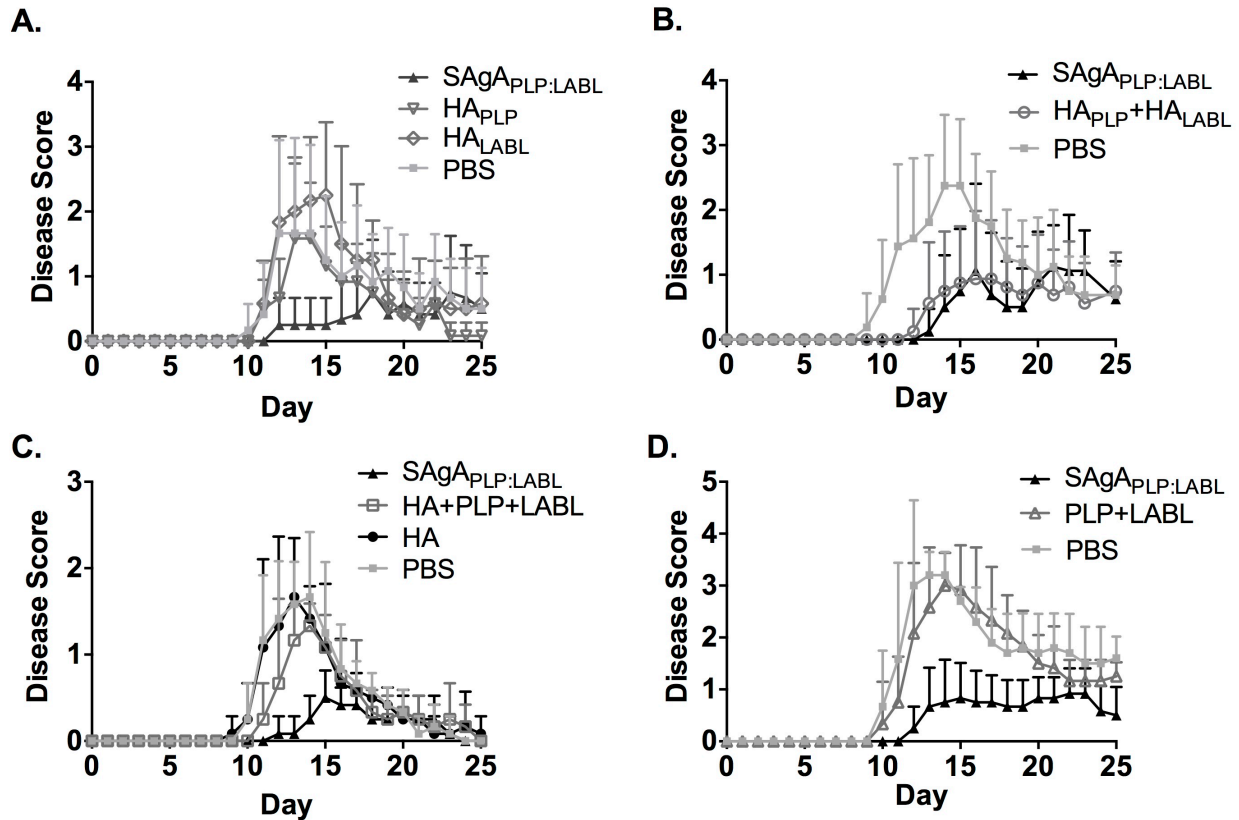


Figure 2. Clinical EAE disease scores in mice comparing treatment groups to a PBS negative control across four separate studies: **A)** SAgA_{PLP:LABL}, HA_{LABL}, and HA_{PLP}; **B)** SAgA_{PLP:LABL} and homopolymer mixture (HA_{PLP}+HA_{LABL}); **C)** SAgA_{PLP:LABL}, component mixture (HA+PLP+LABL), and HA alone; and **D)** SAgA_{PLP:LABL} and peptide mixture (PLP+LABL). SAgA_{PLP:LABL} significantly alleviated EAE disease score compared to the PBS control in each study as follows: **A)** day 12-14 ($p < 0.01$); **B)** day 11 ($p < 0.001$), day 12-15 ($p < 0.0001$), and day 17 ($p < 0.05$); **C)** day 11-14 ($p < 0.0001$) and day 15 ($p < 0.01$); **D)** day 11 ($p < 0.001$), day 12-15 ($p < 0.0001$), and day 16 ($p < 0.01$). The homopolymer mixture (HA_{PLP}+HA_{LABL}) significantly alleviated disease score on day 11-12 ($p < 0.001$), day 13 ($p < 0.01$), and day 14-15 ($p < 0.0001$) compared to the PBS control (**B**). The component mixture (HA+PLP+LABL) significantly alleviated disease score on day 11 ($p < 0.001$) (**C**). Data presented from four separate studies as mean+SD using a two-way ANOVA followed by Bonferroni's multiple comparisons test with $p < 0.05$ ($n=6$).

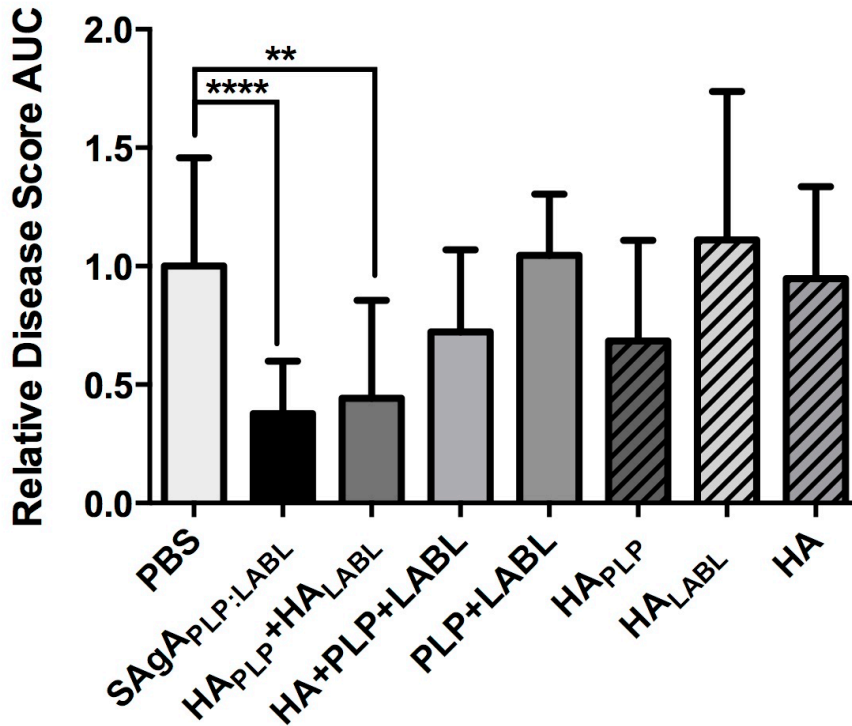


Figure 3. Relative EAE disease score area under the curve: Area under the curve (AUC) of clinical EAE disease scores in mice relative to the PBS control, indicating therapeutic efficacy. Relative disease score AUC shows SAgA_{PLP:LABL} (**** $p < 0.0001$) and homopolymer mixture (** $p < 0.01$) significantly alleviated disease compared to PBS. Data presented as mean+SD. Statistical significance determined using one-way ANOVA in comparison to PBS followed by Bonferroni's multiple comparison test with $p < 0.05$ and $n = 6$ (for PBS and SAgA_{PLP:LABL}, $n = 24$).

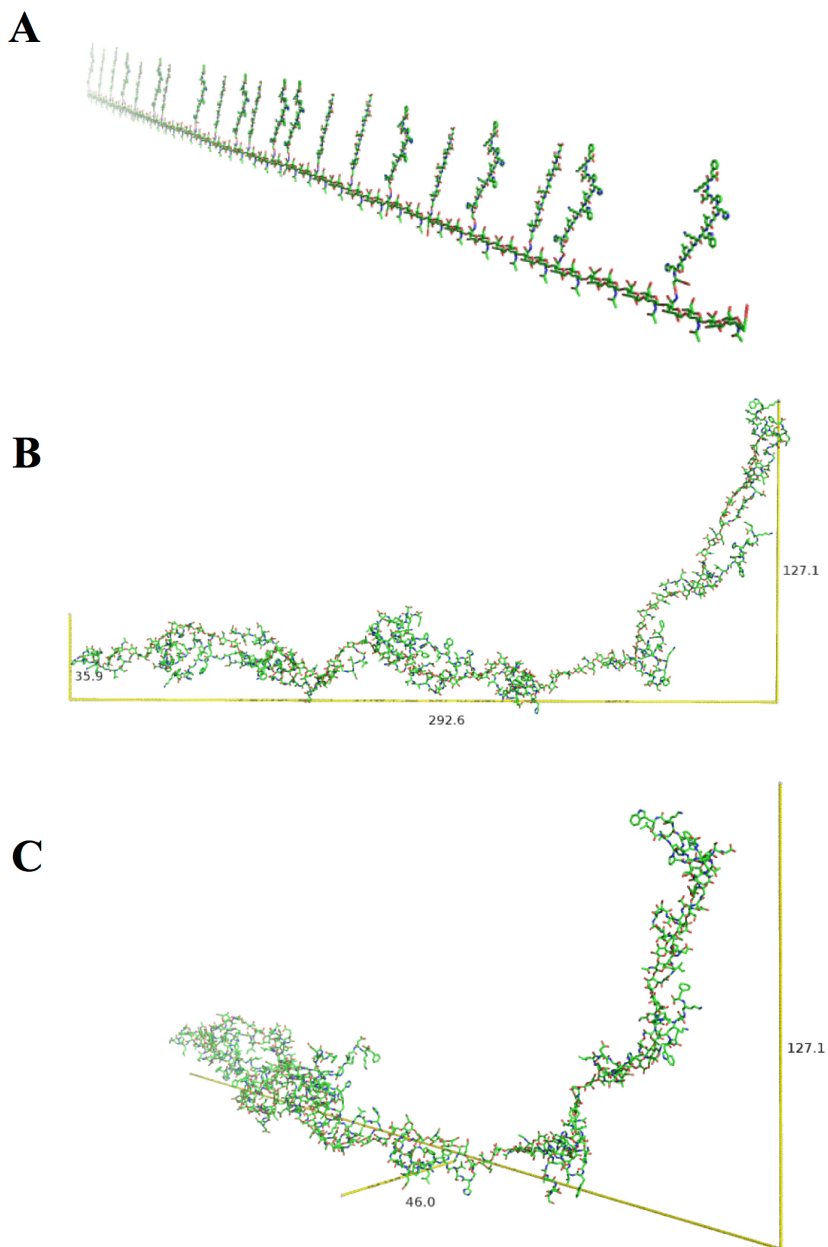


Figure 4. SAg_{PLP:LABL} molecular dynamics: Single SAg_{PLP:LABL} molecule in A) initial conformation prior to molecular dynamics simulation, B) final conformation after a 40 ns molecular dynamics simulation in side view, and C) final conformation in angled view of VDW surface. Helical behavior was exhibited by the molecule. Dimensions in Å.

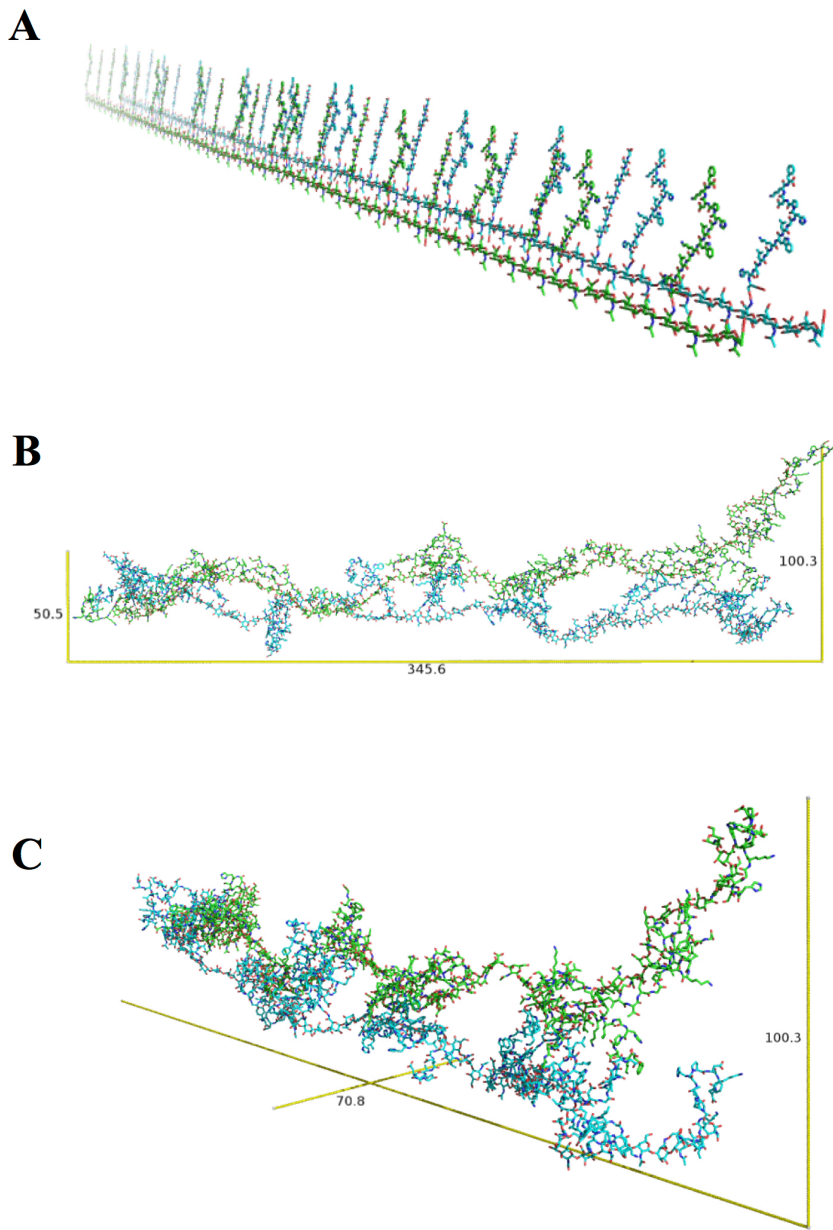


Figure 5. Neighboring SAgA_{PLP:LABL} molecular dynamics: Two SAgA_{PLP:LABL} molecules (green and cyan) shown in A) initial conformation prior to molecular dynamics simulation, B) final conformation after a 20 ns molecular dynamics simulation in side view, and C) final conformation in angled view of VDW surface. Intermolecular side chain interactions were exhibited between the neighboring molecules. Dimensions in Å.

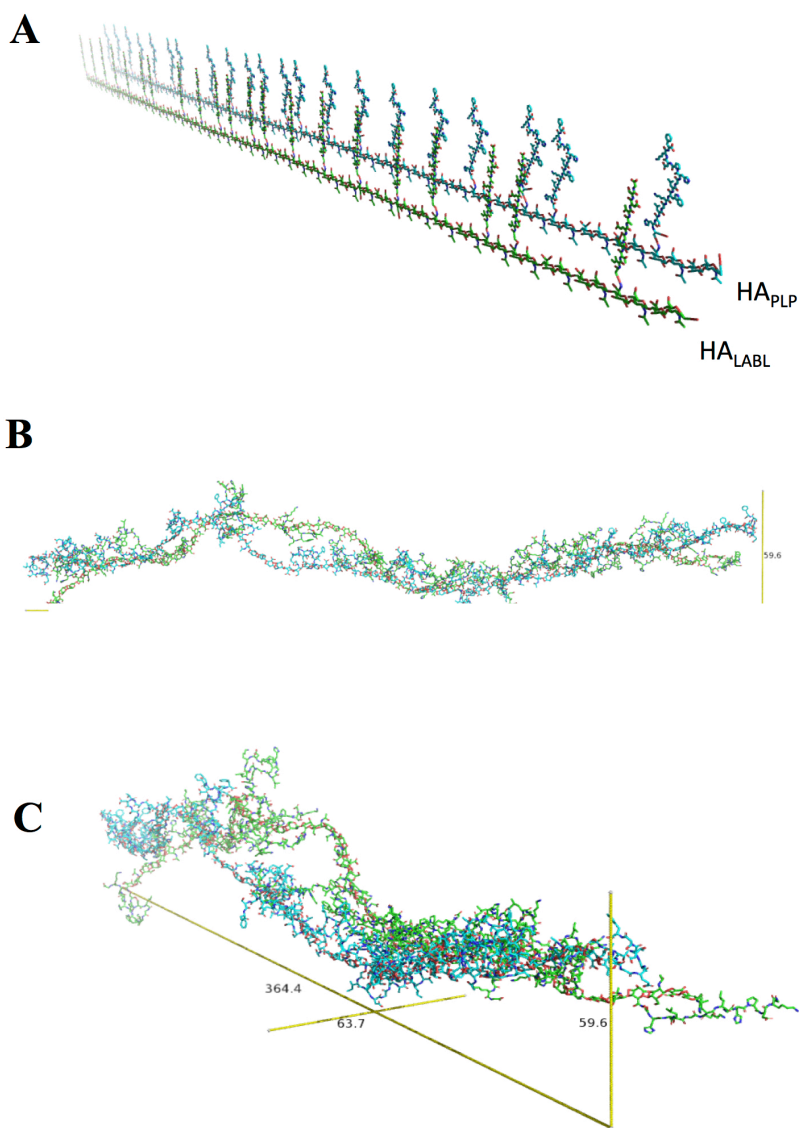


Figure 6. Homopolymer mixture (HA_{PLP}+HA_{LABL}) molecular dynamics: One HA_{PLP} (cyan) plus one HA_{LABL} (green) molecule shown in A) initial conformation prior to molecular dynamics simulation spaced approximately 20 Å apart, B) final conformation after a 40 ns molecular dynamics simulation in side view, and C) final conformation in angled view of VDW surface. Significant intermolecular interactions between peptide side chains and HA backbone were exhibited between the neighboring molecules, leading to chain entanglement. Dimensions in Å.

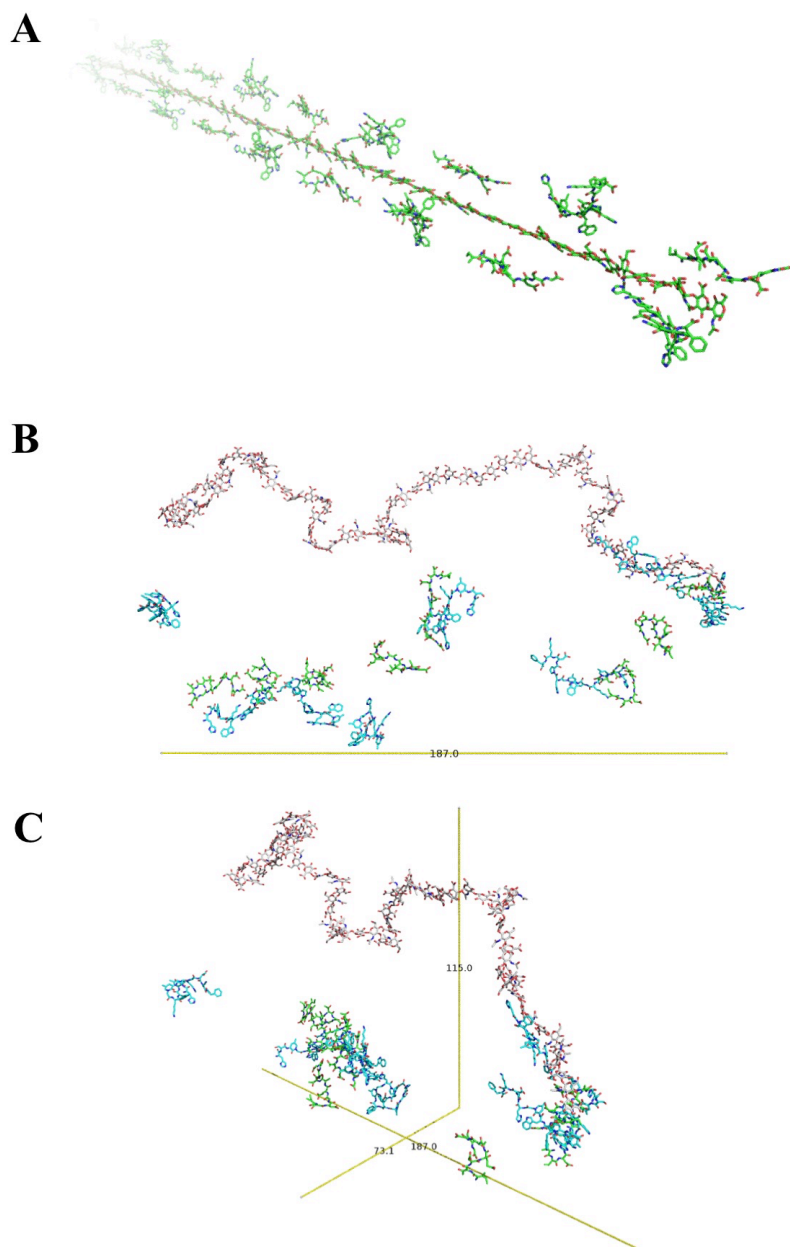


Figure 7. Component mixture (HA+PLP+LABL) molecular dynamics: Free, unlinked PLP (cyan), LABL (green), and HA (10:10:1) shown in A) initial conformation prior to molecular dynamics simulation, B) final conformation after a 40 ns molecular dynamics simulation in side view, and C) final conformation in angled view of VDW surface. Minor interactions between the peptides and HA backbone were exhibited, instead favoring the formation of primarily heterotypic peptide:peptide complexes. Dimensions in Å.

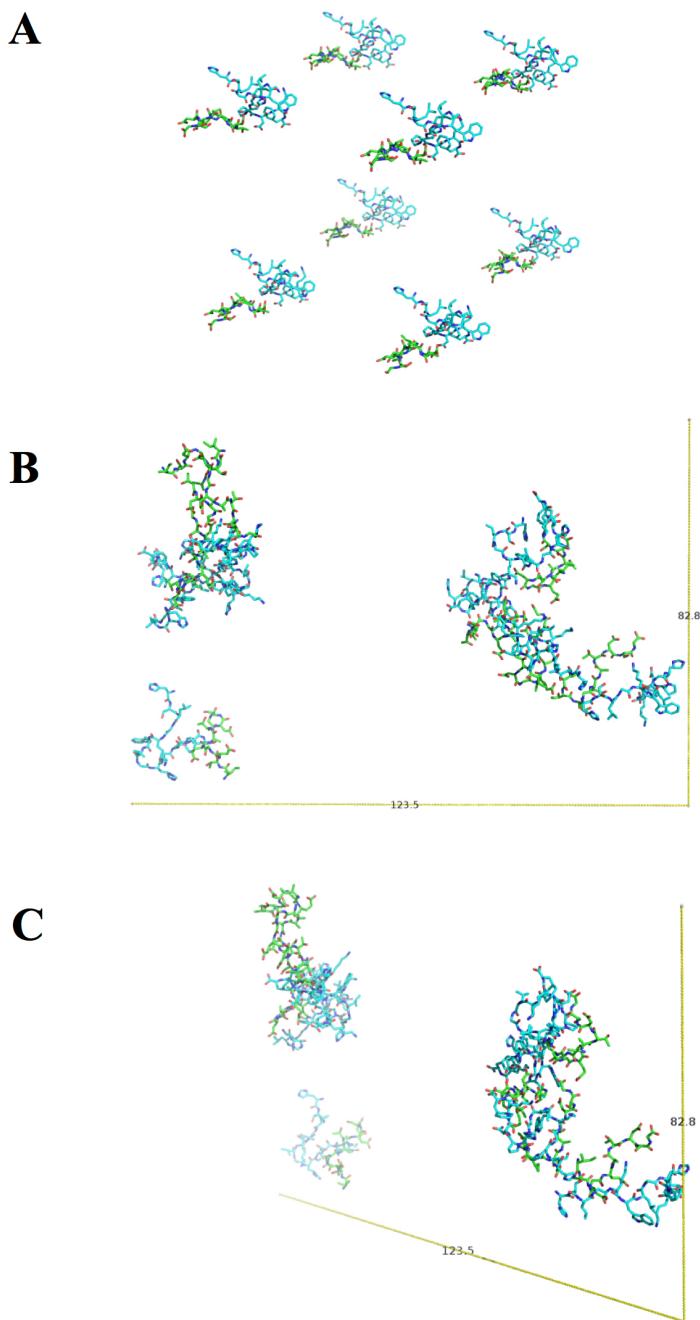
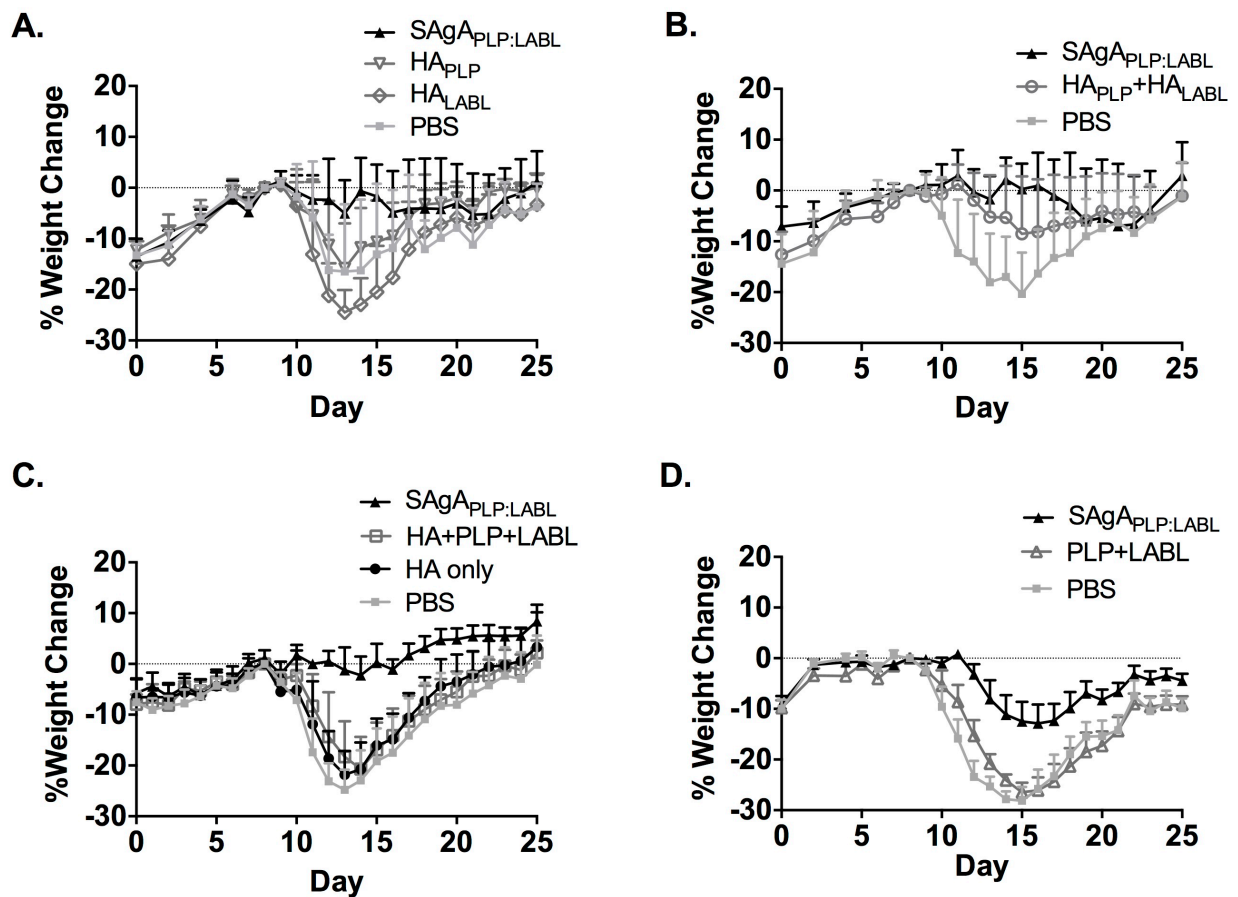
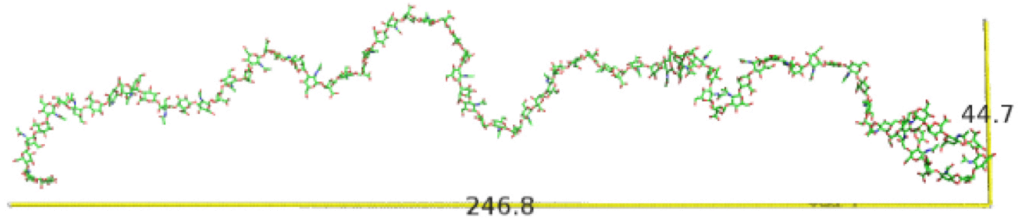
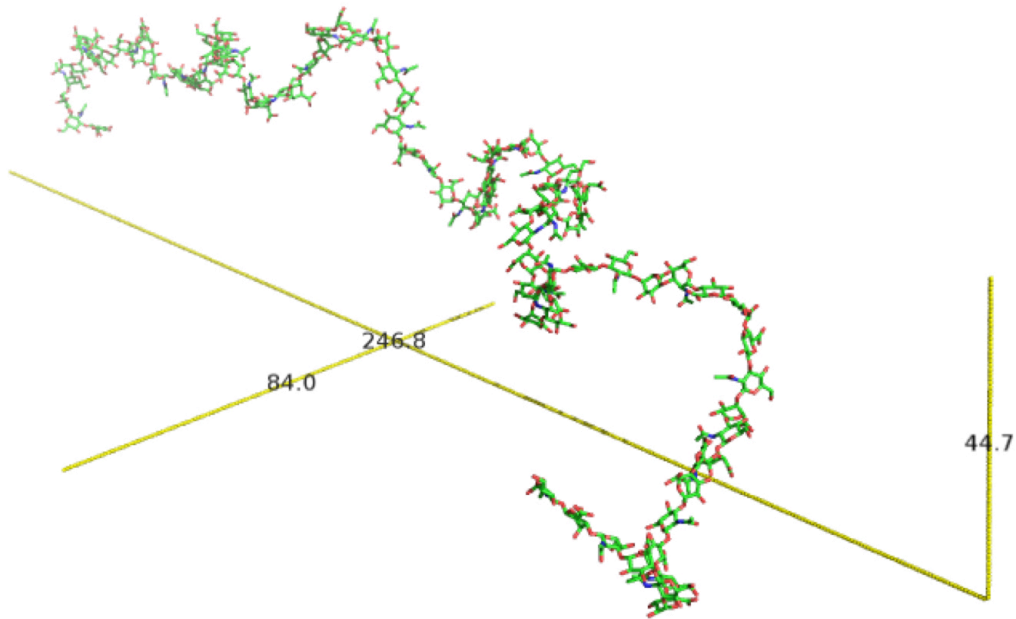


Figure 8. Peptide mixture (PLP+LABL) molecular dynamics: Free, unlinked LABL (green) and PLP (cyan) peptides (1:1) shown in A) initial conformation in a cube arrangement with ~ 70 Å in each dimension prior to molecular dynamics simulation, B) final conformation after a 40 ns molecular dynamics simulation in side view, and C) final conformation in front view. Weak intermolecular interactions and random aggregation were exhibited between peptides. Dimensions in Å.

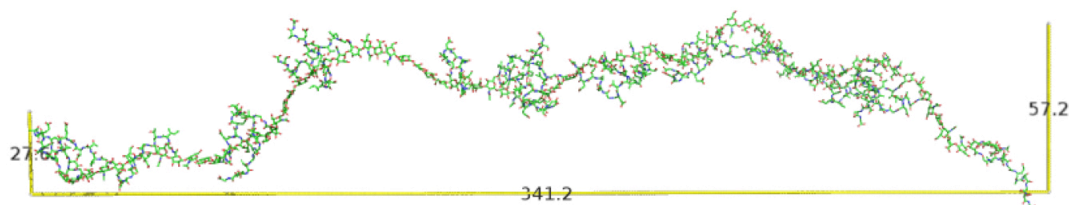
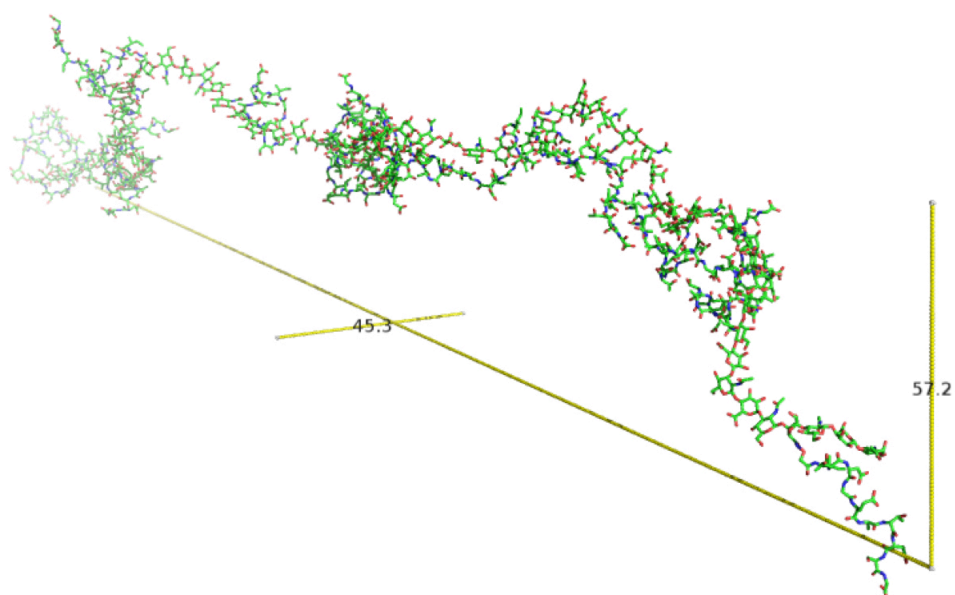
Supplemental Information



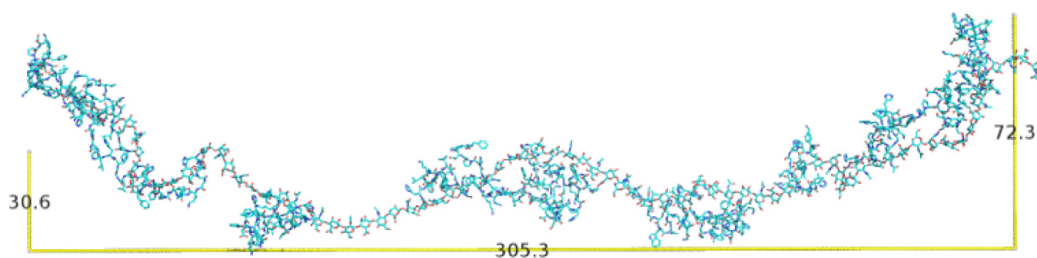
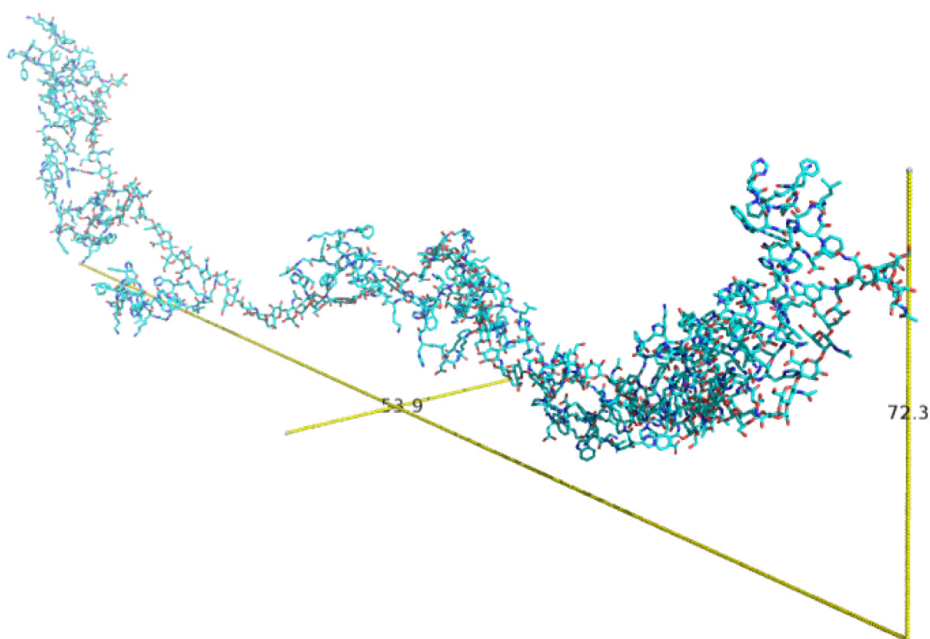
Supplemental Figure 1. Percent weight change in EAE clinical studies, comparing PBS negative control to A) SAgA_{PLP:LABL} and individual homopolymers HA_{PLP} and HA_{LABL}, B) SAgA_{PLP:LABL} and homopolymer mixture (HA_{PLP} + HA_{LABL}) C) SAgA_{PLP:LABL}, component mixture (HA + PLP + LABL), and HA alone, and D) SAgA_{PLP:LABL} and peptide mixture (PLP + LABL). SAgA_{PLP:LABL} significantly reduced weight loss compared to the PBS control in each study as follows: **A)** day 12 ($p < 0.05$) and day 14 ($p < 0.01$); **B)** day 11 and 13 ($p < 0.001$), day 12 ($p < 0.01$), day 14-16 ($p < 0.0001$), and day 17 ($p < 0.05$); **C)** day 10 ($p < 0.05$) and day 11-20 ($p < 0.0001$); **D)** day 11-14 ($p < 0.0001$), day 15 ($p < 0.001$), and day 16 ($p < 0.01$). The homopolymer mixture (HA_{PLP}+HA_{LABL}) also significantly reduced weight loss on day 11 and 13 ($p < 0.01$) and day 12, 14-15 ($p < 0.05$) (**B**). Data presented from four separate studies as mean+SD using a two-way ANOVA followed by Bonferroni's multiple comparisons test with $p < 0.05$ ($n=6$).

A**B**

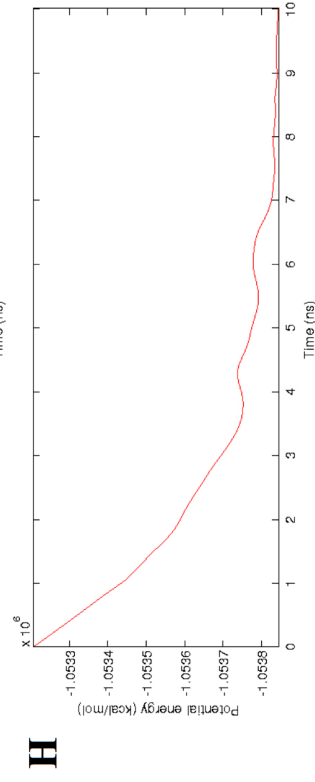
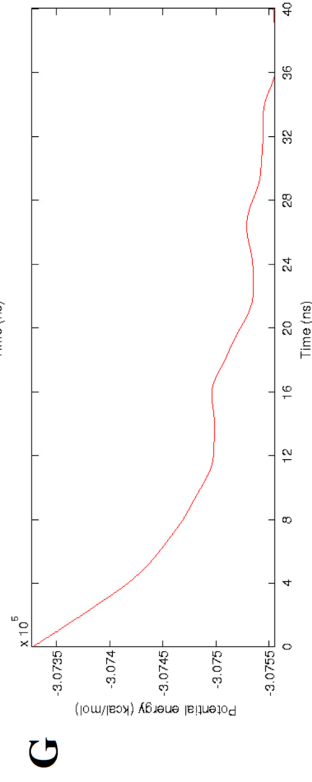
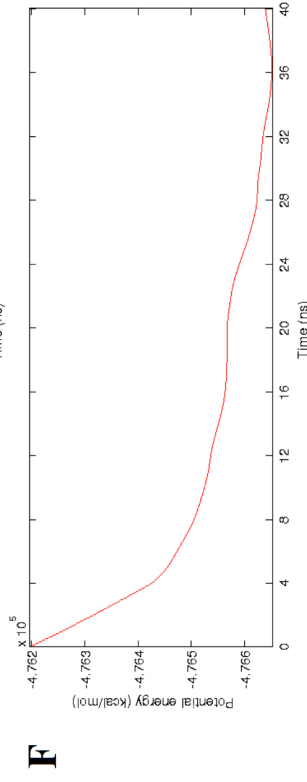
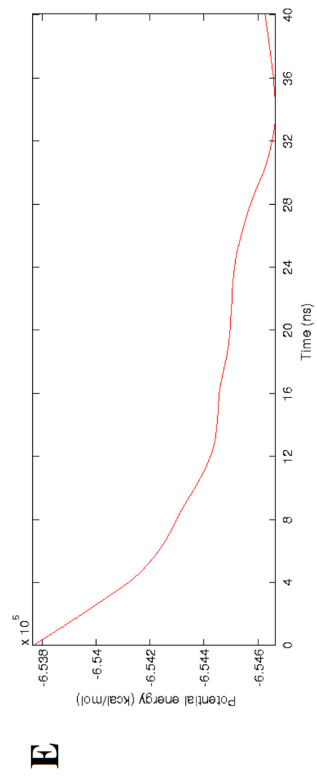
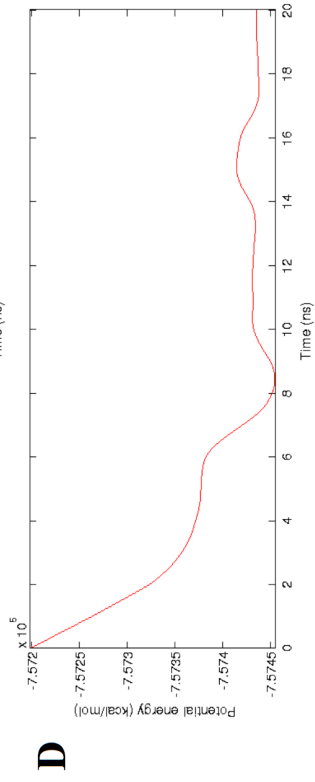
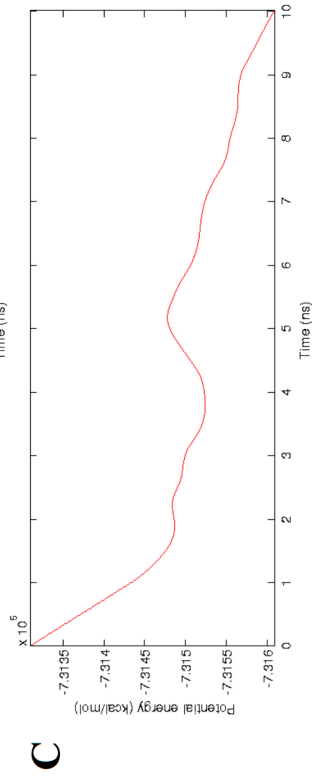
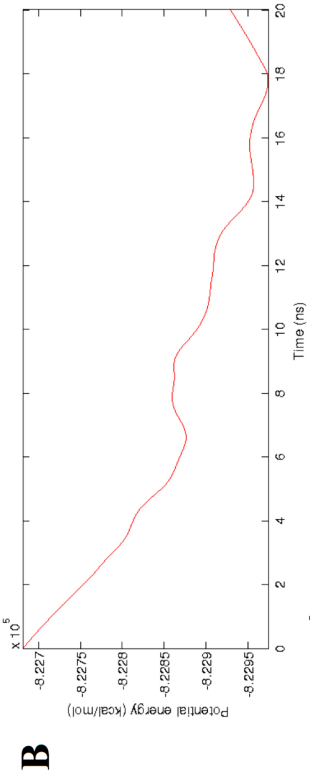
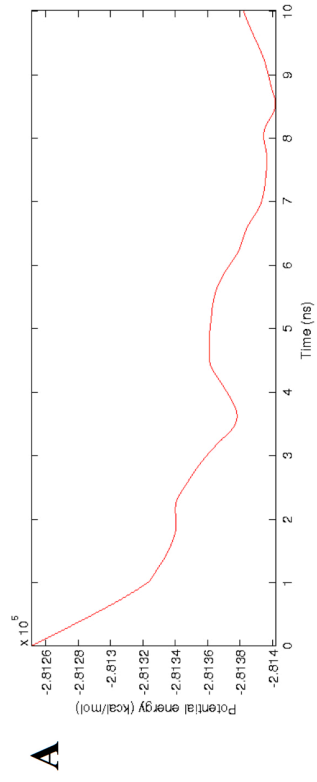
Supplemental Figure 2. Final conformation of 16 kDa HA following a 20 ns molecular dynamics simulation, showing A) side view and B) angled view of VDW surface. The final conformation resembled a random coil. Dimensions in Å.

A**B**

Supplemental Figure 3. Final conformation of HA_LABL following a 20 ns molecular dynamics simulation, showing A) side view and B) angled view of VDW surface. A tendency for LABL side chain interactions with neighboring peptides and the HA backbone was exhibited. Dimensions in Å.

A**B**

Supplemental Figure 4. Final conformation of HA_{PLP} following a 20 ns molecular dynamics simulation, showing A) side view and B) angled view of VDW surface. A tendency for PLP side chain interactions with neighboring peptides and the HA backbone was exhibited. Dimensions in Å.



Supplemental Figure 5. Molecular dynamics potential energy (kcal/mol) versus time (ns) over the duration of the simulation: A) HA, B) HA_{LABL}, C) HA_{PLP}, D) SAgA_{PLP:LABL}, E) homopolymer mixture (HA_{PLP} + HA_{LABL}), F) component mixture (HA + PLP + LABL), G) peptide mixture (PLP + LABL), H) SAgA_{PLP:LABL} x2. Negligible changes in PE over the latter stages of the simulations indicated energetic equilibrium and conformational stability were reached.

References

1. Langer-Gould, A.; Atlas, S. W.; Green, A. J.; Bollen, A. W.; Pelletier, D., Progressive Multifocal Leukoencephalopathy in a Patient Treated with Natalizumab. *The New England Journal of Medicine* **2005**, *353* (4), 375-381.
2. Cross, A. H.; Naismith, R. T., Established and novel disease-modifying treatments in multiple sclerosis. *Journal of internal medicine* **2014**, *275* (4), 350.
3. Jones, J. L.; Coles, A. J., New treatment strategies in multiple sclerosis. *Experimental Neurology* **2010**, *225* (1), 34-39.
4. Miller, S. D.; Turley, D. M.; Podojil, J. R., Antigen-specific tolerance strategies for the prevention and treatment of autoimmune disease. *Nature Reviews Immunology* **2007**, *7* (9), 665.
5. Feldmann, M.; Steinman, L., Design of effective immunotherapy for human autoimmunity. *Nature* **2005**, *435* (7042), 612.
6. Dintzis, R.; Middleton, M.; Dintzis, H., Inhibition of anti-DNP antibody formation by high doses of DNP-polyacrylamide molecules; effects of hapten density and hapten valence. *The Journal of Immunology* **1985**, *135* (1), 423-427.
7. Symer, D. E.; Reim, J.; Dintzis, R. Z.; Voss, E.; Dintzis, H. M., Durable elimination of high affinity, T cell-dependent antibodies by low molecular weight antigen arrays in vivo. *The Journal of Immunology* **1995**, *155* (12), 5608-5616.
8. Reim, J. W.; Symer, D. E.; Watson, D. C.; Dintzis, R. Z.; Dintzis, H. M., Low molecular weight antigen arrays delete high affinity memory B cells without affecting specific T-cell help. *Molecular immunology* **1996**, *33* (17-18), 1377.
9. Dintzis, H. M.; Dintzis, R. Z., Profound specific suppression by antigen of persistent IgM, IgG, and IgE antibody production. *Proceedings of the National Academy of Sciences* **1992**, *89* (3), 1113-1117.
10. Hartwell, B. L.; Antunez, L.; Sullivan, B. P.; Thati, S.; Sestak, J. O.; Berkland, C., Multivalent Nanomaterials: Learning from Vaccines and Progressing to Antigen-Specific Immunotherapies. *Journal of pharmaceutical sciences* **2014**.
11. Chittasupho, C.; Siahaan, T. J.; Vines, C. M.; Berkland, C., Autoimmune therapies targeting costimulation and emerging trends in multivalent therapeutics. *Therapeutic delivery* **2011**, *2* (7), 873-889.
12. Dintzis, R.; Middleton, M.; Dintzis, H., Studies on the immunogenicity and tolerogenicity of T-independent antigens. *The Journal of Immunology* **1983**, *131* (5), 2196-2203.
13. Symer, D. E.; Dintzis, R. Z.; Diamond, D. J.; Dintzis, H. M., Inhibition or activation of human T cell receptor transfectants is controlled by defined, soluble antigen arrays. *The Journal of experimental medicine* **1992**, *176* (5), 1421-1430.
14. Dintzis, R. Z.; Okajima, M.; Middleton, M.; Greene, G.; Dintzis, H., The immunogenicity of soluble haptenedated polymers is determined by molecular mass and hapten valence. *The Journal of Immunology* **1989**, *143* (4), 1239-1244.
15. Desaymard, C.; Howard, J., Role of epitope density in the induction of immunity and tolerance with thymus-independent antigens. II. Studies with 2, 4-dinitrophenyl conjugates in vivo. *European journal of immunology* **1975**, *5* (8), 541-545.

16. Dintzis, H.; Dintzis, R.; Vogelstein, B., Molecular determinants of immunogenicity: the immunon model of immune response. *Proceedings of the National Academy of Sciences* **1976**, *73* (10), 3671-3675.
17. Gestwicki, J. E.; Strong, L. E.; Kiessling, L. L., Tuning chemotactic responses with synthetic multivalent ligands. *Chemistry & biology* **2000**, *7* (8), 583-591.
18. Jun, J. E.; Goodnow, C. C., Scaffolding of antigen receptors for immunogenic versus tolerogenic signaling. *Nature immunology* **2003**, *4* (11), 1057-1064.
19. Puffer, E. B.; Pontrello, J. K.; Hollenbeck, J. J.; Kink, J. A.; Kiessling, L. L., Activating B cell signaling with defined multivalent ligands. *ACS chemical biology* **2007**, *2* (4), 252-262.
20. Kiessling, L. L.; Gestwicki, J. E.; Strong, L. E., Synthetic multivalent ligands in the exploration of cell-surface interactions. *Current opinion in chemical biology* **2000**, *4* (6), 696-703.
21. Sestak, J.; Mullins, M.; Northrup, L.; Thati, S.; Forrest, M. L.; Siahaan, T. J.; Berkland, C., Single-step grafting of aminooxy-peptides to hyaluronan: a simple approach to multifunctional therapeutics for experimental autoimmune encephalomyelitis. *Journal of Controlled Release* **2013**, *168* (3), 334-340.
22. Sestak, J. O.; Sullivan, B. P.; Thati, S.; Northrup, L.; Hartwell, B.; Antunez, L.; Forrest, M. L.; Vines, C. M.; Siahaan, T. J.; Berkland, C., Co-delivery of antigen and an immune cell adhesion inhibitor is necessary for efficacy of soluble antigen arrays in experimental autoimmune encephalomyelitis. *Molecular Therapy—Methods & Clinical Development* **2014**, *1*.
23. Irvine, D. J.; Swartz, M. A.; Szeto, G. L., Engineering synthetic vaccines using cues from natural immunity. *Nature materials* **2013**, *12* (11), 978-990.
24. Chen, L.; Flies, D. B., Molecular mechanisms of T cell co-stimulation and co-inhibition. *Nature Reviews Immunology* **2013**, *13* (4), 227-242.
25. Frauwirth, K. A.; Thompson, C. B., Activation and inhibition of lymphocytes by costimulation. *The Journal of clinical investigation* **2002**, *109* (109 (3)), 295-299.
26. Herz, J.; Zipp, F.; Siffrin, V., Neurodegeneration in autoimmune CNS inflammation. *Experimental neurology* **2010**, *225* (1), 9-17.
27. Kutzelnigg, A.; Lassmann, H., Pathology of multiple sclerosis and related inflammatory demyelinating diseases. *Handb Clin Neurol* **2014**, *122*, 15-58.
28. Lassmann, H., Mechanisms of inflammation induced tissue injury in multiple sclerosis. *Journal of the neurological sciences* **2008**, *274* (1), 45-47.
29. Grakoui, A.; Bromley, S. K.; Sumen, C.; Davis, M. M.; Shaw, A. S.; Allen, P. M.; Dustin, M. L., The immunological synapse: a molecular machine controlling T cell activation. *Science* **1999**, *285* (5425), 221-227.
30. Iezzi, G.; Karjalainen, K.; Lanzavecchia, A., The duration of antigenic stimulation determines the fate of naive and effector T cells. *Immunity* **1998**, *8* (1), 89-95.
31. Baxter, A. G.; Hodgkin, P. D., Activation rules: the two-signal theories of immune activation. *Nature Reviews Immunology* **2002**, *2* (6), 439-446.
32. Bromley, S. K.; Iaboni, A.; Davis, S. J.; Whitty, A.; Green, J. M.; Shaw, A. S.; Weiss, A.; Dustin, M. L., The immunological synapse and CD28-CD80 interactions. *Nature immunology* **2001**, *2* (12), 1159-1166.

33. Courtney, A. H.; Puffer, E. B.; Pontrello, J. K.; Yang, Z.-Q.; Kiessling, L. L., Sialylated multivalent antigens engage CD22 in trans and inhibit B cell activation. *Proceedings of the National Academy of Sciences* **2009**, *106* (8), 2500-2505.
34. Hassane, F. S.; Phalipon, A.; Tanguy, M.; Guerreiro, C.; Bélot, F.; Frisch, B.; Mulard, L. A.; Schuber, F., Rational design and immunogenicity of liposome-based diepitope constructs: application to synthetic oligosaccharides mimicking the *Shigella flexneri* 2a O-antigen. *Vaccine* **2009**, *27* (39), 5419-5426.
35. Chittasupho, C.; Sestak, J.; Shannon, L.; Siahaan, T. J.; Vines, C. M.; Berkland, C., Hyaluronic acid graft polymers displaying peptide antigen modulate dendritic cell response in vitro. *Molecular pharmaceutics* **2013**, *11* (1), 367-373.
36. Mossman, K. D.; Campi, G.; Groves, J. T.; Dustin, M. L., Altered TCR signaling from geometrically repatterned immunological synapses. *Science* **2005**, *310* (5751), 1191-1193.
37. Ridwan, R.; Kiptoo, P.; Kobayashi, N.; Weir, S.; Hughes, M.; Williams, T.; Soegianto, R.; Siahaan, T. J., Antigen-specific suppression of experimental autoimmune encephalomyelitis by a novel bifunctional peptide inhibitor: structure optimization and pharmacokinetics. *Journal of Pharmacology and Experimental Therapeutics* **2010**, *332* (3), 1136-1145.
38. Bowers, K. J.; Chow, E.; Xu, H.; Dror, R. O.; Eastwood, M. P.; Gregersen, J. L.; Klepeis, I. K.; Moraes, M. A.; Sacerdoti, F. D.; Salmon, J. K.; Shan, Y.; Shaw, D. E., Scalable Algorithms for Molecular Dynamics Simulations on Commodity Clusters. *Proceedings of the ACM/IEEE Conference on Supercomputing (SC06)* **2006**.
39. Kaminski, G. A.; Friesner, R. A., Evaluation and reparameterization of the OPLS-AA force field for proteins via comparison with accurate quantum chemical calculations on peptides. *J Phys Chem B* **2001**, *105* (28), 6474-6487.
40. Hoover, W. G., Canonical dynamics: equilibrium phase-space distributions. *Phys Rev A* **1985**, *31*, 1695-1697.
41. Martyna, G. J.; Tobias, D. J.; Klein, M. L., Constant pressure molecular dynamics algorithms. *J Chem Phys* **1994**, *101*, 4177-4189.
42. Essmann, U.; Perera, L.; Berkowitz, M. L.; Darden, T.; Lee, H.; Pedersen, L. G., A smooth particle mesh Ewald method. *J Chem Phys* **1995**, *103*, 8577-8593.
43. Humphreys, D. D.; Friesner, R. A.; Berne, B. J., A multiple-time-step molecular dynamics algorithm for macromolecules. *J Phys Chem* **1994**, *98*, 6885-6892.
44. Inc., C. C. G., Molecular Operating Environment (MOE), 2013.08. **2013**.
45. Inc., T. M., MATLAB version 2013a. **2013**.
46. Sestak, J. O.; Fakhari, A.; Badawi, A. H.; Siahaan, T. J.; Berkland, C., Structure, size, and solubility of antigen arrays determines efficacy in experimental autoimmune encephalomyelitis. *The AAPS journal* **2014**, *16* (6), 1185-1193.
47. Bagby, T. R.; Cai, S.; Duan, S.; Thati, S.; Aires, D. J.; Forrest, L., Impact of molecular weight on lymphatic drainage of a biopolymer-based imaging agent. *Pharmaceutics* **2012**, *4* (2), 276-295.
48. Takahashi, R.; Kubota, K.; Kawada, M.; Okamoto, A., Effect of Molecular Weight Distribution on the Solution Properties of Sodium Hyaluronate in 0.2M NaCl Solution. *Biopolymers* **1999**, *50*, 87-98.

49. Fleming, K. K.; Bovaird, J. A.; Mosier, M. C.; Emerson, M. R.; LeVine, S. M.; Marquis, J. G., Statistical analysis of data from studies on experimental autoimmune encephalomyelitis. *Journal of neuroimmunology* **2005**, *170* (1), 71-84.
50. La Gatta, A.; De Rosa, M.; Marzaioli, I.; Busico, T.; Schiraldi, C., A complete hyaluronan hydrodynamic characterization using a size exclusion chromatography–triple detector array system during in vitro enzymatic degradation. *Analytical biochemistry* **2010**, *404* (1), 21-29.
51. Kaminski, T.; Siebrasse, J.-P.; Gieselmann, V.; Kubitscheck, U.; Kappler, J., Imaging and tracking of single hyaluronan molecules diffusing in solution. *Glycoconjugate journal* **2008**, *25* (6), 555-560.
52. Dintzis, H. M.; Dintzis, R. Z., Antigens as immunoregulators. *Immunological reviews* **1990**, *115* (1), 243-250.
53. Desaynard, C.; Ivanyi, L., Comparison of in vitro immunogenicity, tolerogenicity and mitogenicity of dinitrophenyl-levan conjugates with varying epitope density. *Immunology* **1976**, *30* (5), 647.
54. Cherukuri, A.; Cheng, P. C.; Sohn, H. W.; Pierce, S. K., The CD19/CD21 complex functions to prolong B cell antigen receptor signaling from lipid rafts. *Immunity* **2001**, *14* (2), 169-179.
55. Duong, B. H.; Tian, H.; Ota, T.; Completo, G.; Han, S.; Vela, J. L.; Ota, M.; Kubitz, M.; Bovin, N.; Paulson, J. C., Decoration of T-independent antigen with ligands for CD22 and Siglec-G can suppress immunity and induce B cell tolerance in vivo. *The Journal of experimental medicine* **2010**, *207* (1), 173-187.
56. Pfrengle, F.; Macauley, M. S.; Kawasaki, N.; Paulson, J. C., Copresentation of antigen and ligands of Siglec-G induces B cell tolerance independent of CD22. *The Journal of Immunology* **2013**, *191* (4), 1724-1731.
57. Northrup, L.; Sestak, J. O.; Sullivan, B. P.; Thati, S.; Hartwell, B. L.; Siahaan, T. J.; Vines, C. M.; Berkland, C., Co-delivery of autoantigen and b7 pathway modulators suppresses experimental autoimmune encephalomyelitis. *The AAPS journal* **2014**, *16* (6), 1204-1213.
58. Yeste, A.; Nadeau, M.; Burns, E. J.; Weiner, H. L.; Quintana, F. J., Nanoparticle-mediated co-delivery of myelin antigen and a tolerogenic small molecule suppresses experimental autoimmune encephalomyelitis. *Proceedings of the National Academy of Sciences* **2012**, *109* (28), 11270-11275.
59. Badawi, A. H.; Kiptoo, P.; Wang, W.-T.; Choi, I.-Y.; Lee, P.; Vines, C. M.; Siahaan, T. J., Suppression of EAE and prevention of blood–brain barrier breakdown after vaccination with novel bifunctional peptide inhibitor. *Neuropharmacology* **2012**, *62* (4), 1874-1881.
60. Manikwar, P.; Büyüktimkin, B.; Kiptoo, P.; Badawi, A. H.; Galeva, N. A.; Williams, T. D.; Siahaan, T. J., I-domain-antigen conjugate (IDAC) for delivering antigenic peptides to APC: synthesis, characterization, and in vivo EAE suppression. *Bioconjugate chemistry* **2012**, *23* (3), 509-517.
61. Brinas, R. P.; Sundgren, A.; Sahoo, P.; Morey, S.; Rittenhouse-Olson, K.; Wilding, G. E.; Deng, W.; Barchi Jr, J. J., Design and synthesis of multifunctional gold nanoparticles bearing tumor-associated glycopeptide antigens as potential cancer vaccines. *Bioconjugate chemistry* **2012**, *23* (8), 1513-1523.

62. Macauley, M. S.; Pfrengle, F.; Rademacher, C.; Nycholat, C. M.; Gale, A. J.; von Drygalski, A.; Paulson, J. C., Antigenic liposomes displaying CD22 ligands induce antigen-specific B cell apoptosis. *The Journal of clinical investigation* **2013**, *123* (7), 3074.
63. Supersaxo, A.; Hein, W. R.; Steffen, H., Effect of molecular weight on the lymphatic absorption of water-soluble compounds following subcutaneous administration. *Pharmaceutical research* **1990**, *7* (2), 167-169.
64. Oussoren, C.; Storm, G., Liposomes to target the lymphatics by subcutaneous administration. *Advanced drug delivery reviews* **2001**, *50* (1), 143-156.
65. Oussoren, C.; Zuidema, J.; Crommelin, D.; Storm, G., Lymphatic uptake and biodistribution of liposomes after subcutaneous injection.: II. Influence of liposomal size, lipid composition and lipid dose. *Biochimica et Biophysica Acta (BBA)-Biomembranes* **1997**, *1328* (2), 261-272.
66. Wang, H.; Wang, J.; Deng, X.; Sun, H.; Shi, Z.; Gu, Z.; Liu, Y.; Zhaoc, Y., Biodistribution of carbon single-wall carbon nanotubes in mice. *Journal of nanoscience and nanotechnology* **2004**, *4* (8), 1019-1024.
67. Thati, S.; Kuehl, C.; Hartwell, B.; Sestak, J.; Siahaan, T.; Forrest, M. L.; Berkland, C., Routes of Administration and Dose Optimization of Soluble Antigen Arrays in Mice with Experimental Autoimmune Encephalomyelitis. *Journal of pharmaceutical sciences* **2014**.
68. Hawley, A.; Davis, S.; Illum, L., Targeting of colloids to lymph nodes: influence of lymphatic physiology and colloidal characteristics. *Advanced drug delivery reviews* **1995**, *17* (1), 129-148.
69. Strand, S.; Bergqvist, L., Radiolabeled colloids and macromolecules in the lymphatic system. *Critical reviews in therapeutic drug carrier systems* **1988**, *6* (3), 211-238.

Supplemental References for Molecular Dynamics Methods

The molecular dynamics simulations were performed using Desmond software.

- S1. Bowers, K. J.; Chow, E.; Xu, H.; Dror, R. O.; Eastwood, M. P.; Gregersen, J. L.; Klepeis, I. K.; Moraes, M. A.; Sacerdoti, F. D.; Salmon, J. K.; Shan, Y.; Shaw, D. E., Scalable Algorithms for Molecular Dynamics Simulations on Commodity Clusters. *Proceedings of the ACM/IEEE Conference on Supercomputing (SC06)* **2006**.

The force field used for simulations was OPLS2005 as available in Desmond.

- S2. Kaminski, G. A.; Friesner, R. A., Evaluation and reparameterization of the OPLS-AA force field for proteins via comparison with accurate quantum chemical calculations on peptides. *J Phys Chem B* **2001**, *105* (28), 6474-6487.

The Nose-Hoover thermostat was used to control temperature.

- S3. Hoover, W. G., Canonical dynamics: equilibrium phase-space distributions. *Phys Rev A* **1985**, *31*, 1695-1697.

The Martyna-Tobias-Klein barostat was used to control pressure.

S4. Martyna, G. J.; Tobias, D. J.; Klein, M. L., Constant pressure molecular dynamics algorithms. *J Chem Phys* **1994**, *101*, 4177-4189.

Coulombic interactions were calculated using the Ewald smooth particle-mesh approach.

S5. Essmann, U.; Perera, L.; Berkowitz, M. L.; Darden, T.; Lee, H.; Pedersen, L. G., A smooth particle mesh Ewald method. *J Chem Phys* **1995**, *103*, 8577-8593.

The RESPA integrator was used with 2 fs time step intervals for bonded/non-bonded interactions at short ranges, and a 6 fs step was used for non-bonded interactions beyond the short range cutoff.

S6. Humphreys, D. D.; Friesner, R. A.; Berne, B. J., A multiple-time-step molecular dynamics algorithm for macromolecules. *J Phys Chem* **1994**, *98*, 6885-6892.

Additional potential energy calculation and analysis was performed using Molecular Operating Environment.

S7. Inc., C. C. G., Molecular Operating Environment (MOE), 2013.08. **2013**.

Chapter III: Antigen-Specific Binding of Multivalent Soluble Antigen Arrays Induces Receptor Clustering and Impedes B Cell Receptor Mediated Signaling

1. Introduction

Autoimmunity stems from the immune system's misrecognition of self versus non-self epitopes, leading to an autoreactive T and/or B cell response against autoantigens.^{1,2} Due to their multifaceted role in autoimmunity, B cells are a likely target for autoimmune therapies. Various treatment approaches (i.e. glucocorticoids, IFN β , mitoxantrone, rituximab) affect B cells, but do so in a non-specific manner resulting in general B cell depletion or down-regulation.^{3,4} In fact, many current therapies for autoimmune diseases act broadly against the immune response, lacking the capability to target specific immune cells and pathways responsible for disease propagation.⁵ These options often yield limited therapeutic efficacy, global immunosuppression, and adverse side effects for patients.⁶⁻⁸ A pressing need persists for antigen-specific immunotherapies (ASITs) that shift the autoreactive immune response towards selective autoantigenic tolerance while avoiding deleterious global immunosuppression.⁹⁻¹¹

T cells and B cells, which are responsible for antigen specificity, memory, diversity, and self-recognition in acquired immunity, are often dysfunctional in autoimmunity. The autoimmune breakdown in MS is believed to be triggered by both autoreactive T cell and B cell clonal expansion and attack against myelin sheath autoantigens, leading to chronic inflammation, demyelination, and subsequent axonal and neuronal degeneration.^{6, 7, 12-14} T cell-mediated attack against autoantigens following T cell clonal expansion is propagated by the immunological synapse between antigen presenting cells (APC) and T cells.¹⁵⁻¹⁷ This signaling event requires both a primary antigen-specific signal and a secondary context signal, which may be costimulatory or inhibitory to direct the immune response towards the antigen.¹⁸⁻²⁴ B cells may play a role in the priming and activation of naïve T cells by acting as antigen presenting cells, and may also contribute to autoimmunity by several humoral immune response pathways.²⁵⁻²⁷

Elevated levels of clonally expanded B cells, myelin-specific plasma cells, and memory B cells in cerebrospinal fluid (CSF) and of myelin-specific autoantibodies in CSF, serum, and MS lesions have implicated B cells in the pathogenesis and immune regulation of multiple sclerosis.^{11, 26, 28-35} Like other autoimmune diseases, MS is plagued by a lack of safe and effective treatments that offer antigen specificity without broad immune suppression.

To address this need, we have developed soluble antigen arrays (SAGAs), which are polymeric multivalent ASIT molecules designed to induce selective antigenic tolerance in MS.³⁶ SAgA_{PLP:LABL} molecules consist of a hyaluronic acid (HA) linear polymer backbone co-presenting both myelin autoantigen peptide (proteolipid protein peptide, PLP₁₃₉₋₁₅₁) and intracellular adhesion molecule-1 (ICAM-1) inhibitor peptide derived from leukocyte function associated antigen-1 (LFA-1), LABL. Preclinical studies in experimental autoimmune encephalomyelitis (EAE), a murine model of MS, showed that treatment with SAgA_{PLP:LABL} was effective at alleviating disease. In contrast, treatment with a mixture of the components (HA, PLP, LABL), HA alone, HA grafted with PLP only (HA_{PLP}), or HA grafted with LABL only (HA_{LABL}) did not alleviate disease, indicating that co-presentation of both signals on HA was necessary for therapeutic efficacy.³⁷ SAgA_{PLP:LABL} molecules are hypothesized to target, engage, and interrupt antigen-specific signaling by presenting both primary autoantigen and secondary inhibitory signals, thereby inhibiting autoreactive T cell and/or B cell clonal expansion while promoting selective autoantigenic tolerance.^{38, 39} A main mechanism for SAgA_{PLP:LABL} therapeutic efficacy, therefore, may be the enhanced ability of the molecule to bind APCs involved in the immunological synapse or other PLP-specific signaling pathways. We hypothesize that incorporation of both signals in a multivalent array causes (1) an increase in

overall binding with APCs, (2) specific binding due to targeting by the antigenic peptide, and (3) modulation of the cell signaling response.

The binding properties of SAgA_{PLP:LABL} (two-signal multivalent array) were compared to ‘homopolymers’ containing one signal (HA_{PLP} or HA_{LABL}), and to the polymer backbone alone (HA). Due to their antigen specificity and implication in immune regulation, B cells were chosen as a model cell system in which to observe SAgA binding. The B cell receptor (BCR) imbues B cells with a superior ability to specifically bind and concentrate antigen over other types of cells, making them highly efficient APCs.^{3, 40, 41} Flow cytometry was performed with immortalized human Raji B cells and fluorescently labeled SAgA molecules (fSAgAs) to quantify binding extent and specificity. Fluorescence microscopy supplemented these studies with visualization of real-time fSAgA binding and progressive receptor clustering in live cells. Calcium flux flow cytometry assays were used to probe the signaling response. These studies revealed molecular mechanisms that may contribute to SAgA_{PLP:LABL} therapeutic efficacy, and more broadly, strengthen our understanding of antigen-specific multivalent immunotherapies designed for the effective treatment of autoimmune disease.

2. Materials and Methods

2.1 Materials

Hyaluronic acid (HA) sodium salt (MW 16 kDa) was purchased from Lifecore Biomedical (Chaska, MN). Aminoxy-LABL (AoLABL, Aoa-itDGEATDSG-OH), aminoxy-PLP (AoPLP, Aoa-HSLGKWLGHDPKF-OH), LABL (NH₂-itDGEATDSG-OH), and PLP (NH₂-HSLGKWLGHDPKF-OH) peptides were purchased from PolyPeptide Laboratories (San

Diego, CA). Fluorescein isothiocyanate (FITC) and Fluo-4 AM calcium indicator were purchased from Thermo Fisher Scientific (Waltham, MA). Immortalized human Raji B cells were purchased from American Type Culture Collection (ATCC, Manassas, VA). Recombinant human tumor necrosis factor- α (TNF- α) was purchased from PeproTech (Rocky Hill, NJ). R-phycoerythrin (PE)-conjugated anti-human CD54, FITC-conjugated anti-human CD44, purified anti-human IgM, and respective isotype control antibodies were purchased from BioLegend (San Diego, CA). Affinity purified F(ab')₂ fragment goat anti-human IgM was purchased from Jackson ImmunoResearch Laboratories (West Grove, PA). All other chemicals and reagents were analytical grade and used as received.

2.2 Peptide Synthesis

OVA peptide (NH₂-ISQAVHAAHAEINEAGR-OH) was synthesized as previously described,⁴² using 9-fluorenylmethylmethoxycarbonyl-protected amino acid chemistry on polyethylene glycol-polystyrene resins. Peptides were deprotected, cleaved from resin, and isolated using precipitation in ether, then purified by preparatory high performance liquid chromatography (HPLC) followed by lyophilization. Peptide identity was confirmed by electrospray ionization mass spectroscopy. Purity was evaluated by analytical HPLC.

2.3 SAgA and FITC-Labeled SAgA Synthesis

To synthesize SAgAs, HA was grafted with aminooxy peptides AoPLP and/or AoLABL as previously described to make HA_{PLP} (HA and AoPLP), HA_{LABL} (HA and AoLABL), and SAgA_{PLP:LABL} (HA, AoPLP, and AoLABL).³⁶ HA was dissolved (2 mg/ml) in a 20mM acetate buffer at pH 5.5, then combined with respective peptide(s) to achieve a target conjugation efficiency per peptide of 25% (or approximately 10 of each peptide per fHA backbone). Solution pH was readjusted to pH 5.5 and stirred at 400 rpm for 24 hours. Samples were dialyzed in d.d.

H₂O (100X volume) to remove free peptides using 6000-8000 MWCO regenerated cellulose dialysis tubing over 24 hours with a total of 4 washes, then frozen and lyophilized.

To synthesize FITC-labeled SAgAs (fSAgAs), HA (16 kDa) was first reacted with FITC to make labeled HA-FITC (fHA).⁴³ HA was gently dissolved in d.d. H₂O (5 mg/ml), then combined with an equal volume of DMSO containing sodium bicarbonate (2.5 mg/ml), dibutyltin dilaurate (3.96 mM), and FITC (6 mg/ml). The reaction mixture was heated in an oil bath at 50°C for 30 minutes while stirring at 70 rpm, then quenched by drop-wise addition to cold ethanol (17.5X volume). Dialysis took place in d.d. H₂O (100X volume) to remove free FITC using 3500 MWCO regenerated cellulose dialysis tubing (Spectrum Laboratories, Rancho Dominguez, CA), rinsing every 6-12 hours for a total of six washes. The fHA solution was then frozen and lyophilized. Peptide conjugation with fHA was performed as detailed above to make fHA_{PLP}, fHA_{LABL}, and fSAgA_{PLP:LABL}. All fHA synthesis and subsequent handling was performed under protection from light.

2.4 SAgA and FITC-Labeled SAgA Characterization

Peptide conjugation of each sample was determined through gradient reverse-phase analytical high-performance liquid chromatography (RP-HPLC) (Waters Corp., Milford, MA) on a C18 analytical column (Higgins Analytical, Proto200, 5 µm, 200 Å, 250 x 4.6 mm², Mountain View, CA) following cleavage of peptides in 0.1N HCl. Samples were compared to standard curves of AoPLP and AoLABL to determine peptide content. A gradient method using aqueous mobile phase A (94.9% d.d. H₂O, 5% acetonitrile, 0.1% trifluoroacetic acid (TFA)) and organic mobile phase B (99.9% acetonitrile, 0.1% TFA) was used to analyze samples. Samples were detected at 220 nm.

FITC fluorescence intensity varied slightly between fSAgA groups, presenting the need to normalize flow cytometry binding results according to respective fluorescence intensities of the fSAgA molecules. Relative FITC fluorescence of labeled samples was determined spectrofluorometrically on a fluorescent plate reader (SpectraMax M5e, Molecular Devices, Sunnyvale, CA). A fluorescence calibration curve was generated for each sample ranging from 0 to 0.5 mg/ml, and the relative fluorescence intensity (f) was determined in the linear region of the calibration curve at 0.4 μ M relative to fHA ($f_{\text{HA}}=1$). The relative fluorescence intensity of each test article was used to normalize flow cytometry FITC fluorescence.

2.5 Cell Culture and Activation

Raji B cells (human B lymphocytes, ATCC) were cultured in RPMI-1640 supplemented with L-Glutamine, 10% fetal bovine serum (FBS), and 1% penicillin/streptomycin (P/S) at 37°C and 5% CO₂. Cell assays were consistently performed after cells reached confluency (~2 weeks) and following no more than 8-10 passages, per ATCC guidelines. Cells were activated with 1000 U/ml TNF- α and primed with 27.1 μ M PLP₁₃₉₋₁₅₁ peptide for 24 hours prior to experiments. Cell activation by TNF- α and PLP was examined by flow cytometry for expression of intracellular adhesion molecule-1 (ICAM-1, CD54) and CD44. ICAM-1 expression was evaluated using mouse anti-human PE-conjugated CD54 and mouse IgG1 κ isotype control antibodies. CD44 expression was evaluated using mouse anti-human FITC-conjugated CD44 and mouse IgG1 κ isotype control antibodies.

2.6 Flow Cytometry Binding Studies

Association and competitive dissociation binding studies were performed by flow cytometry (MoFlo XDP Cell Sorter, Beckman Coulter Inc., Brea, CA). Cell nuclei were stained with Hoechst, while Q-Nuclear Red or propidium iodide (PI) was used as a dead cell indicator.

Cell samples were warmed to 37°C prior to flow cytometry analysis. Data acquisition was triggered off the Hoechst signal. Fluorescence was excited using 488, 405, and 640 nm lasers and was collected using 529/28, 457/40, and 670/30 bandpass emission filters.

2.6.1 Maximum Steady State Binding

To observe maximum steady state binding, cells were mixed with fSAgA to achieve a final concentration of 1×10^6 cells/ml immediately before injecting on the flow cytometer. Sample concentration was determined from preliminary saturation studies with fHA. Samples were added at an equimolar PLP dose (353.18 μ M PLP for fHA_{PLP} and fSAgA_{PLP:LABL}, or 353.18 μ M LABL for fHA_{LABL}) and fHA was dosed at 39.19 μ M (the HA molar equivalent to a 353.18 μ M PLP dose of fSAgA_{PLP:LABL}) to mimic animal studies. The sample was allowed to run until maximum steady state binding was reached, at which point ~ 10 X molar excess unlabeled reagent (HA, PLP, or LABL) was added to competitively dissociate the bound, labeled SAgA. Samples were allowed to run until the dissociation steady state (representing nonspecific binding) was reached. fHA, fHA_{LABL}, and fHA_{PLP} were dissociated by competition with HA, LABL, and PLP, respectively, to determine specificity of binding.

2.6.2 Competitive Dissociation

fSAgA_{PLP:LABL} was dissociated by competition with its various unlabeled components (HA, PLP, and LABL), including a nonspecific control peptide (OVA), to determine the specific binding contribution of each individual component. Dissociation by addition of an equal volume of media was included as a control to account for dissociation due to dilution and resulting shift in equilibrium. Cells (1×10^6 cells/ml) were mixed with fSAgA_{PLP:LABL} (444 μ M PLP, near-saturation concentration) and allowed to reach maximum steady state binding, at which point ~ 20 X molar excess (400 μ l) unlabeled HA, PLP, LABL, OVA, or media was added.

fSAgA_{PLP:LABEL} concentration was determined from preliminary saturation studies with fSAgA_{PLP:LABEL}. Samples were run until dissociation steady state was reached.

2.6.3 IgM Blocking

Raji B cells (10^6 cells) were incubated with or without mouse anti-human IgM (0.5 μ g per 100 μ l) (BioLegend) for one hour on ice following FcR blocking. Maximum steady state binding was performed by flow cytometry as detailed above, to evaluate fSAgA_{PLP:LABEL} binding following BCR blocking with anti-IgM. fSAgA_{PLP:LABEL} was dosed at 353.18 μ M PLP with a final cell concentration of 1×10^6 cells/ml.

Flow cytometry binding data was first gated to remove dead cells and debris using Kaluza Flow Analysis software (Beckman Coulter, Inc., Brea, CA) (Supplemental Figure 1). Additional data processing was performed using KNIME software (Konstanz Information Miner, KNIME, Zurich, Switzerland). Nonlinear regression and additional statistical analysis was performed using GraphPad Prism (GraphPad Software, Inc., La Jolla, CA).

2.7 Fluorescence Microscopy Using a Microfluidics Platform

Live cell imaging of fSAgA binding was observed under fluorescence microscopy (Olympus IX81 Inverted Epifluorescence Microscope) using the same concentrations from flow cytometry association binding experiments. CellASIC ONIX M04S Microfluidics Switching Plates and Microfluidics Platform (EMD Millipore, Billerica, MA) were utilized for controlled perfusion of fluorescent samples and media with cells during real-time imaging. Raji B cells were stained with Hoechst and loaded into the imaging chamber. fSAgA was perfused into the chamber for 10 minutes (1 psi for 5 minutes, 0.25 psi for 5 minutes) to allow binding with cells, followed by gentle media perfusion (0.25 psi for 5 minutes) to rinse unbound fSAgA, followed

by immediate image capture ($t=0$). Images were captured across time intervals of [0-5), [5-10), and >10 minutes. Images were analyzed using Slidebook 5.5 (Intelligent Imaging Innovations, Inc., Denver, CO). For each sample and time interval, several fields were randomly selected and 40–200 FITC positive cells total were counted and scored for diffuse versus punctate staining. Of the punctate positive cells, ‘fully punctate’ cells were also distinguished. Punctate staining was defined by multiple areas of discrete high intensity fluorescence totaling <50% of the cell surface; fully punctate staining was defined by one predominant area of discrete high intensity fluorescence totaling <50% of the cell surface. The results are a composite analysis of two independent experiments.

2.8 Calcium Flux Signaling Flow Cytometry Assay

Raji B cells were loaded with 5 μM Fluo-4 AM for 30 minutes at room temperature in PBS, then kept on ice in HBSS (Hanks Balanced Salt Solution) containing 1.3 mM Ca^{2+} and 0.9 mM Mg^{2+} before analysis. Cells were run through a BD FACSFusion cytometer and fluorescence was monitored in the 530/30 channel. After baseline quantification for ~ 1 minute, crosslinking goat anti-human IgM (Jackson ImmunoResearch) was added at 20 $\mu\text{g}/\text{ml}$ to stimulate the cells. Changes in Fluo-4 fluorescence were measured for ~ 1 minute to establish an anti-IgM stimulated baseline, followed by SAgA addition (dosed at 353.18 μM PLP, the same concentration used in binding studies) to determine the effect on IgM-stimulated signaling. Data was acquired for an additional 3 minutes until steady state was established. To measure inhibition of anti-IgM stimulation, SAgA_{PLP:LABEL} was added to cells prior to anti-IgM stimulation. Data was analyzed using FlowJo, FCS Express, and GraphPad Prism. Baselines were subtracted from mean fluorescence intensity levels for each experimental condition.

2.9 Resazurin Cell Metabolism Assay

Cells were plated in a 96-well plate to achieve a final concentration of 1×10^6 cells/ml in a final volume of 150 μ l/well. Test compounds (SAgA_{PLP:LABL}, HA_{PLP}, HA_{LABL}, and HA) were added at a dose of 353.18 μ M PLP and incubated for 24 hours at 37°C. Resazurin (0.01% v/v in RPMI) was then added to each well (20 μ l per 100 μ l cells) and incubated for an additional 6 hours. Resazurin fluorescence (560/590 nm) was measured on a SpectraMax Fluorescent Plate Reader.

2.10 Statistical Analysis

GraphPad Prism was used to perform statistical analysis including sigmoidal nonlinear regression, ordinary one-way or two-way analysis of variance (ANOVA), and unpaired t-test (n=3). ANOVA was followed by Tukey's post-hoc test. The threshold for statistical significance was set to $p < 0.05$.

3. Results

3.1 SAgA and FITC-Labeled SAgA Characterization

SAgAs and fSAgAs were synthesized and analyzed by RP-HPLC to determine molecular weight and peptide conjugation as described previously.³⁶ HPLC results indicated fHA_{PLP} homopolymer contained ~9 PLP, fHA_{LABL} homopolymer contained ~10 LABL, and fSAgA_{PLP:LABL} contained ~10 PLP and ~13 LABL peptides per HA backbone, respectively (Table 1). HA_{PLP} homopolymer contained ~6 PLP, HA_{LABL} homopolymer contained ~6 LABL, and SAgA_{PLP:LABL} contained ~8 PLP and ~7 LABL peptides per HA backbone, respectively.

3.2 Cell Activation

Raji B cells were evaluated by flow cytometry for CD54 and CD44 expression levels following 24-hour activation and priming with TNF- α and PLP. Intercellular adhesion molecule-1 (ICAM-1, CD54) is expressed on activated immune cells and plays a role in cellular adhesion and inflammation; it binds LFA-1 and its cell surface expression is upregulated by cell activation.^{18, 44, 45} CD44, an adhesion molecule expressed on leukocytes, is also upregulated in B and T cells upon activation and progression to the memory cell stage.⁴⁶⁻⁴⁸

Comparison of each antibody with isotype and unstained controls showed that neither antibody exhibited nonspecific staining (Supplemental Figure 2). Naïve and activated cells stained with FITC anti-CD44 exhibited minimal CD44 expression (Figure 1A). Less than 5% of the cells were CD44-positive after 24 hours of activation, and expression did not differ significantly between unstained, naïve, and activated cells. In contrast, naïve and activated cells stained with PE anti-CD54 exhibited significant CD54 expression compared to the unstained control (Figure 1B). Nearly 100% of cells were CD54-positive, but expression did not differ significantly between naïve and activated cells. Additionally, a resazurin assay indicated no differences in cell metabolic activity between naïve versus primed/activated cells (Supplemental Figure 4). These results suggest that treatment with media versus TNF- α and PLP over a 24 hour period did not lead to significantly altered levels of cell activation.

3.3 Flow Cytometry Binding Studies: Association and Competitive Dissociation

Flow cytometry association and competitive dissociation studies evaluated maximum steady state binding and specific binding, respectively. Figure 2 shows binding curves and associated binding values with homopolymers to illustrate how these studies were carried out and interpreted. Initial evaluation of fHA, fHA_{PLP}, and fHA_{LABL} binding in naïve B cells showed

that fHA_{PLP} exhibited the highest amount of binding at equilibrium, while both fHA_{PLP} and fHA_{LABL} exhibited significantly higher binding than fHA (Figure 2AB). Specific binding of fHA, fHA_{PLP}, and fHA_{LABL} was determined through competitive dissociation by addition of excess unlabeled HA, PLP, and LABL, respectively. Specific binding was evaluated as the difference between maximum steady state (SS_{max}) and dissociation steady state (SS_{ns}), which represented nonspecific binding (Figure 2B):

$$\text{Specific Binding} = SS_{max} - SS_{ns} \quad (\text{Equation 1})$$

Both fHA_{PLP} and fHA_{LABL} exhibited significantly higher specific binding than fHA. Percent (%) dissociation was evaluated as the amount of dissociation relative to maximum steady state binding, calculated as follows (Figure 2C):

$$\% \text{ Dissociation} = \frac{SS_{max} - SS_{ns}}{SS_{max}} \quad (\text{Equation 2})$$

This value provides the relative amount of maximum binding that is attributed to specific binding. Approximately 60% of the binding sites occupied by fHA_{PLP} and fHA_{LABL} at equilibrium were dissociated after addition of unlabeled PLP or LABL, respectively, while approximately 40% of the binding sites occupied by fHA at equilibrium were dissociated after addition of unlabeled HA. Significantly higher specific binding took place with fHA_{PLP} and fHA_{LABL} compared to fHA. Thus, HA displaying multiple copies of PLP or LABL peptide exhibited both increased binding and increased specificity of binding with B cells compared to the polymer alone.

Binding of fHA, fHA_{PLP}, fHA_{LABL}, and fSagA_{PLP:LABL} was also evaluated separately in naïve and activated cells (Figure 3). Kinetic binding curves show fSagA_{PLP:LABL} exhibited the

fastest and highest amount of binding in Raji B cells (Figure 3A). In naïve and activated cells, fSAgA_{PLP:LABL} exhibited a significantly higher SS_{max} compared to fHA_{PLP}, fHA_{LABL}, and fHA (Figure 3B). Minimal differences in SS_{max} were expected in activated cells compared to naïve cells since there was a negligible change in CD54 and CD44 expression levels. However, the difference in SS_{max} of fSAgA_{PLP:LABL} compared to fHA_{PLP} and fHA_{LABL} was more statistically significant in activated cells ($p < 0.001$) than in naïve cells ($p < 0.05$). Displaying both peptides, PLP and LABL, on the fSAgA_{PLP:LABL} heteropolymer array significantly enhanced binding compared to displaying multiple copies of one of these peptides on HA.

Specific binding was evaluated for fHA, fHA_{PLP}, and fHA_{LABL} in naïve and activated cells, revealing similar trends (Figure 3C). In naïve cells, fHA_{PLP} and fHA_{LABL} exhibited significantly higher specific binding than fHA. In activated cells, fHA_{PLP} exhibited significantly higher specific binding than fHA; no significance was detected when fHA_{LABL} was compared to fHA. As negligible differences were observed in activation levels, maximum binding, and specific binding between activated versus naïve cells, the remaining results herein include only naïve cells.

Competitive dissociation of fSAgA_{PLP:LABL} by excess addition of unlabeled components (HA, PLP, or LABL) was evaluated to determine the component of fSAgA_{PLP:LABL} primarily responsible for binding (Figure 4). Percent dissociation (Equation 2) was evaluated for HA, PLP, LABL, OVA nonspecific peptide control, and media (Figure 4B). Dissociation caused by OVA, a nonspecific peptide included as a control for selectivity, was comparable to that caused by media, a control included to show dissociation by dilution and the resulting shift in equilibrium. In contrast, dissociation by LABL was significantly greater than that by media ($p < 0.01$) and

OVA ($p < 0.05$), while dissociation by PLP was significantly greater than that by media and OVA ($p < 0.001$) and HA ($p < 0.01$). These results indicate specificity with the LABL and PLP peptides.

To determine % specific binding, % dissociation by the media control was subtracted from % dissociation by PLP, LABL, and HA to account for dissociation due to dilution (Figure 4C):

$$\% \text{ Specific Binding}_{HA,PLP,or\ LABL} = \% \text{ Dissociation}_{HA,PLP,or\ LABL} - \% \text{ Dissociation}_{media}$$

(Equation 3)

PLP exhibited the highest % specific binding followed by LABL, and both were significantly higher than HA. Relative to the maximum equilibrium binding of fSAgA_{PLP:LABL}, PLP was responsible for ~20% binding, LABL for ~13%, and HA for ~2%. Addition of PLP or LABL to naïve cells with bound fSAgA_{PLP:LABL} caused significantly higher % dissociation than addition of HA. Thus, binding specificity of fSAgA_{PLP:LABL} was attributed to both peptides, PLP and LABL, and was largely driven by PLP.

3.4 Fluorescence Microscopy Using a Microfluidics Platform

Fluorescence microscopy of binding with Raji B cells was performed using a microfluidics platform (CellASIC Onix) in order to control perfusion of fluorescent samples and media rinse into the cell environment and capture images of binding in real time. Images show cell membrane localization of fHA (Figure 5A), fHA_{LABL} (Figure 5B), fHA_{PLP} (Figure 5C), and fSAgA_{PLP:LABL} (Figure 5D) from 0 to >10 minutes. Regions of heightened, punctate fluorescence intensity were observed on the surface of the cells, suggesting that binding and subsequent receptor clustering were taking place. Fluorescence on the surface of the cell was characterized as diffuse, punctate, or fully punctate (Figure 6A). Punctate staining was defined by multiple

areas of discrete high intensity fluorescence totaling <50% of the cell surface; fully punctate staining was defined by one predominant area of discrete high intensity fluorescence totaling <50% of the cell surface. Progression from diffuse FITC fluorescence (0-5 min) towards fully punctate fluorescence on the cell surface (>10 min) was indicative of progressive receptor clustering following binding, which was observed most significantly in fSAgA_{PLP:LABEL} (Figure 5D) but also to a lesser extent in fHA_{LABEL} (Figure 5B) and fHA_{PLP} (Figure 5C).

Percent (%) punctate positive cells was determined quantitatively across FITC positive cells for each treatment group and time interval (Figure 6B). Of the punctate positive cells, fully punctate cells were also distinguished (Figure 6C). Similar trends were observed in % punctate positive cells across samples and time intervals (Figure 6B), but differences were observed in % fully punctate cells (Figure 6C). Although fHA exhibited slightly higher % punctate positive cells compared to other samples, % fully punctate cells remained low and unchanged with time, whereas fSAgA_{PLP:LABEL} exhibited a steep increase in % fully punctate cells and the highest relative amount of fully punctate cells >10 minutes (Figure 6C). Comparing % fully punctate vs. % punctate cells, fSAgA_{PLP:LABEL} exhibited the greatest slope followed by fHA_{LABEL}, while fHA exhibited a near-zero slope (Figure 6D). Thus, of the punctate positive cells, fSAgA_{PLP:LABEL} induced the most rapid progression and highest amount of fully punctate fluorescence.

3.5 Calcium Flux Signaling Flow Cytometry Assay

Flow cytometry calcium flux was used to assay cellular response to SAgA_{PLP:LABEL} binding in anti-IgM-stimulated cells. Response was evaluated in Fluo-4 loaded Raji B cells after stimulation (Figure 7AB) and prior to stimulation (Figure 7CD) with crosslinking anti-IgM. Signaling kinetics show an abrupt reduction in signaling from addition of SAgA_{PLP:LABEL}, HA_{PLP}, and HA_{LABEL}, but negligible change from baseline after addition of vehicle (HBSS) or HA (Figure

7A). The relative signal reduction from stimulated baseline was determined using mean values at steady state. HA_{PLP}, HA_{LABL}, and SAgA_{PLP:LABL} exhibited significantly greater reduction in signaling than HA (Figure 7B) ($p < 0.0001$), while HA_{PLP} ($p < 0.05$) and SAgA_{PLP:LABL} ($p < 0.001$) exhibited significantly greater reduction in signaling than HA_{LABL}. Signal reduction was not observed in non-stimulated cells (Supplemental Figure 3). Furthermore, SAgA_{PLP:LABL} was effective at inhibiting anti-IgM stimulation ($p < 0.05$) compared to the vehicle (Figure 7CD). It is important to note the reduction in calcium signaling was not accompanied by a reduction in cell metabolic activity, as indicated by a resazurin cell metabolic assay (Supplemental Figure 4).

3.6 IgM Blocking

fSAgA_{PLP:LABL} binding following blocking of the BCR by anti-IgM was evaluated by flow cytometry to provide further context to the calcium flux studies (Figure 7EF). Blocking with anti-IgM reduced fSAgA_{PLP:LABL} maximum steady state binding by over 50%, from 1.38×10^9 a.u (arbitrary fluorescence units) to 7.10×10^8 a.u. fSAgA_{PLP:LABL} binding was significantly inhibited following IgM blocking ($p < 0.0001$), suggesting that BCR is a target for fSAgA_{PLP:LABL} binding. This result corroborates the calcium flux data, indicating that SAgA_{PLP:LABL} binding dampens BCR-mediated signaling.

4. Discussion

Multivalent polymeric antigen arrays (i.e. many copies of an antigen epitope) have emerged as a promising option for ASITs with potential to modulate the immune response to specific, disease-causing autoantigens.^{49, 50} Compared to monovalent antigen, multivalent antigens have been found to exhibit superior binding avidity, higher ‘effective concentration’, and an enhanced ability to activate or regulate cells.^{11, 51-54} This concept has long been utilized in vaccine design to elicit strong antigen-specific immune responses. More recent studies have

suggested that tailoring multivalent array properties such as polymer or particle size, flexibility, antigen valency, and antigen spacing may direct the immune response towards tolerance versus immunogenicity.^{32, 33, 55-60} Furthermore, these arrays provide an efficient platform for co-delivery of two signals (primary antigen and secondary signal), which many believe to be essential for induction of an antigen-specific immune response. For example, incorporation of a costimulatory or inhibitory secondary signal may skew the immune response towards immunogenicity or tolerance of antigen, respectively.^{24, 50, 61-66}

Extrapolating from this rationale, SAg_{PLP:LABL} molecules are designed to engage cell surface receptors to modulate antigen-specific signaling by incorporating multiple copies of autoantigen (PLP) and inhibitory signal (LABL). PLP autoantigen may target antigen-specific receptors such as the BCR or perhaps MHCII on autoreactive APCs that are involved in antigen-specific signaling pathways.⁶⁷⁻⁶⁹ The secondary LABL peptide is derived from LFA-1, an adhesion molecule present on T cells that engages ICAM-1 on APCs to provide a secondary context signal.^{18, 44} LFA-1/ICAM-1 interaction promotes cell adhesion during signaling, so in addition to directing the immune response to PLP antigen, LABL may enhance B cell binding.^{22-24, 70-72} The HA polymer backbone is believed to act as a carrier to facilitate spatial and temporal co-delivery of PLP and LABL. The MW of HA was selected to direct transport as a function of its MW, as molecules greater than 16 kDa are likely to preferentially drain into the lymphatics following subcutaneous injection.⁷³⁻⁷⁷ HA may also affect the ability of multivalent PLP and/or LABL to engage and cluster receptors.^{31, 32, 49}

Our results showed significant ICAM-1 expression and minimal CD44 expression in both naïve and activated cells. Negligible differences in expression of either cell surface marker between the naïve and activated cells implied that treatment with TNF- α and PLP over 24 hours

did not cause a significant increase in activation levels. High expression of ICAM-1 in naïve cells suggests the cells persist in an inherently activated state, perhaps because Raji B cells are positive for Epstein-Barr virus (EBV).⁷⁸ EBV activates B cells and persists as a latent infection, causing differentiation into memory B cells. Increasing evidence also implicates EBV in the pathogenesis of MS, which may contribute to MS as a result of cross-reactivity between EBV and myelin antigens.⁷⁹⁻⁸⁴ Molecular mimicry between these antigens was reported to cause cross-recognition between EBV- and myelin-specific B and T cells.^{82, 85-92} These reports may provide an explanation for the insignificant differences in binding between naïve and activated Raji B cells. Naïve Raji B cells may exhibit significant specific binding with the PLP antigen due to cross-reactivity between EBV and myelin antigens.

Flow cytometry studies showed inclusion of peptides, PLP or LABL, on the HA backbone increased binding of the polymer array with B cells (Figure 2). Incorporation of both PLP and LABL signals on the HA backbone, however, procured a cooperative effect and significantly increased B cell binding beyond that observed with the homopolymers (Figure 3). These results correlate with previous observations of *in vivo* EAE therapeutic efficacy, in which SAg_{PLP:LABL} alleviated disease while HA_{PLP}, HA_{LABL}, and HA did not.³⁷ Therefore, enhanced binding with B cell APCs may be a main mechanism for the previously observed SAg_{PLP:LABL} therapeutic effect.^{36, 37, 65, 93, 94}

Enhanced binding is desired for producing a strong immune response, but specific binding is thought to be critical for producing an antigen-specific response. Incorporation of peptides onto the HA backbone significantly increased specific binding of homopolymers (Figure 3), as evidenced by competitive dissociation by flow cytometry. Evaluation of specific binding with SAg_{PLP:LABL} revealed that both PLP and LABL contributed significantly to

specific binding compared to HA, but specific binding was primarily driven by PLP (Figure 4). Binding specificity dominated by PLP supports our hypothesis that $\text{SAgA}_{\text{PLP:LABEL}}$ targets cells in an antigen-specific manner.

Fluorescence microscopy images confirmed binding of the polymer arrays on the cell membrane and visible areas of heightened punctate fluorescence intensity provided evidence for receptor clustering. Receptor clustering in B cells (i.e. of BCR and ICAM-1) has been recognized as a marker for cell receptor engagement, signaling, and subsequent cellular activation.^{31, 52, 70, 95-97} In fact, a proposed mechanism for the induction of a strong immune response by multivalent antigen is the ability of this antigen presentation format to sufficiently engage and cluster receptors, thereby initiating a cellular response.^{24, 32, 54, 98} A minimum valency of 20 appropriately spaced antigens was proposed by Dintzis and others in 1976 to sufficiently engage and cluster a unit of receptors, forming an “immunon” capable of initiating response.³²

The fluorescence microscopy images resemble those of others showing specific, localized receptor clustering in B cells (Figure 5).^{31, 70, 99} Furthermore, the microfluidics platform allowed unique observation of sensitive changes in cell surface binding and receptor clustering behavior with time. Cell surface fluorescence was characterized as diffuse, punctate, or fully punctate, where degree of punctate fluorescence was indicative of the extent of receptor clustering (Figure 6A). Interestingly, $\text{fSAgA}_{\text{PLP:LABEL}}$ exhibited the highest relative amount of fully punctate cells with time – that is, of the increasing number of punctate positive cells, most were fully punctate (i.e., exhibited one discrete area of fluorescence) (Figure 6C). In contrast, fHA exhibited an unchanged amount of fully punctate positive cells with time. These results suggest that $\text{fSAgA}_{\text{PLP:LABEL}}$ induced more developed, mature receptor clustering as compared to the

homopolymers, while clustering induced by fHA did not fully develop with time. Furthermore, the steep slope of % fully punctate vs. % punctate cells for fHA_{LABL} was most similar to the trend observed for fSAgA_{PLP:LABL}, suggesting that LABL, rather than PLP, may drive fully developed receptor clustering (Figure 6D). An integral role of LABL in receptor clustering is consistent with evidence that LFA-1/ICAM-1 interactions promote cell adhesion and signaling.⁷⁰ Similarly, our results corroborate observations of increased localized density of ICAM-1 on the surface of B cells during signaling and activation.⁹⁷ These imaging observations therefore provide complementary insight into the SAgA_{PLP:LABL} cellular mechanism: while PLP drives crucial antigen-specific binding, LABL may drive receptor clustering to facilitate a stronger cellular response.





Valency-induced receptor clustering and localization in B cells has been correlated with increased calcium signaling, which is a key marker for cellular response following antigen-specific binding.^{31, 100, 101} However, receptor engagement and clustering can also induce a robust tolerogenic or inhibitory response.⁴⁹ For example, it has been shown that engagement and clustering of BCR with an inhibitory co-receptor can cause inhibition of B cell activation.⁶¹ Indeed, our calcium flux results showed that SAgA_{PLP:LABL} induced an abrupt *reduction* in IgM-stimulated signaling in Raji B cells, while pretreatment with SAgA_{PLP:LABL} was capable of significantly inhibiting IgM stimulation. Furthermore, fSAgA_{PLP:LABL} binding was significantly inhibited following IgM blocking, suggesting that BCR is a target for the fSAgA_{PLP:LABL} molecule and corroborating the competitive dissociation data showing specific PLP binding. Taken together, these results indicate that SAgA_{PLP:LABL} binding dampens BCR-mediated signaling.

In comparison to SAg_{PLP:LABL}, HA_{PLP} and HA_{LABL} had less effect on calcium signaling, and HA did not cause a significant change. While the time scales are different between the calcium flux experiment (0-5 minutes) and the fluorescence microscopy binding experiment (0-5, 5-10, >10 minutes), it is notable that HA, which did not exhibit an increase in ‘fully punctate’ binding, also did not induce a change in calcium flux. Thus, our results suggest that progression to ‘fully punctate’ binding correlated with a greater reduction in calcium flux.

5. Conclusions

Results reported here offer a therapeutic mechanism to support previously reported *in vivo* observations, which indicated that co-presentation of both signals on HA was necessary for therapeutic efficacy. SAg_{PLP:LABL} co-presentation of PLP autoantigen and LABL cell adhesion inhibitor resulted in greatly enhanced B cell binding *in vitro* compared to HA arrays presenting only one signal. Furthermore, SAg_{PLP:LABL} exhibited specific binding that was increased by the presence of both peptides and largely driven by the antigenic PLP peptide, supporting our hypothesis that SAg_{PLP:LABL} acts in an antigen-specific manner. While the primary antigen PLP drives specific binding, the secondary signal LABL appears to play an important role in progressing to fully developed receptor clustering. SAg_{PLP:LABL} progressed to fully punctate receptor clustering to a greater extent than HA, HA_{PLP}, or HA_{LABL}, which correlated with greater reduction in BCR-mediated calcium signaling. In addition to elucidating SAg_{PLP:LABL} cellular mechanisms, the methods developed in these studies lay the foundation to further investigate design criteria for specific-targeting immunotherapies and progress towards safer and more effective treatments for autoimmune disease.

Table 1. Peptide molar conjugation was determined by reverse-phase HPLC and results are an average of triplicate injections from a single batch preparation.

Sample	Approx. MW (kDa) ^a	Molar Ratio per Polymer ^b		% Molar Conjugation	
		PLP:HA	LABL:HA	PLP	LABL
fHA 	16.6	0	0	0	0
fHA _{PLP} 	30.4	9	0	21	0
fHA _{LABL} 	26.0	0	10	0	24
fSagA _{PLP:LABL} 	46.3	10	13	24	31

^a Calculated from RP-HPLC data. MW, molecular weight.

^b HA, hyaluronic acid; PLP, proteolipid protein peptide; LABL, inhibitor peptide derived from leukocyte function associated antigen-1

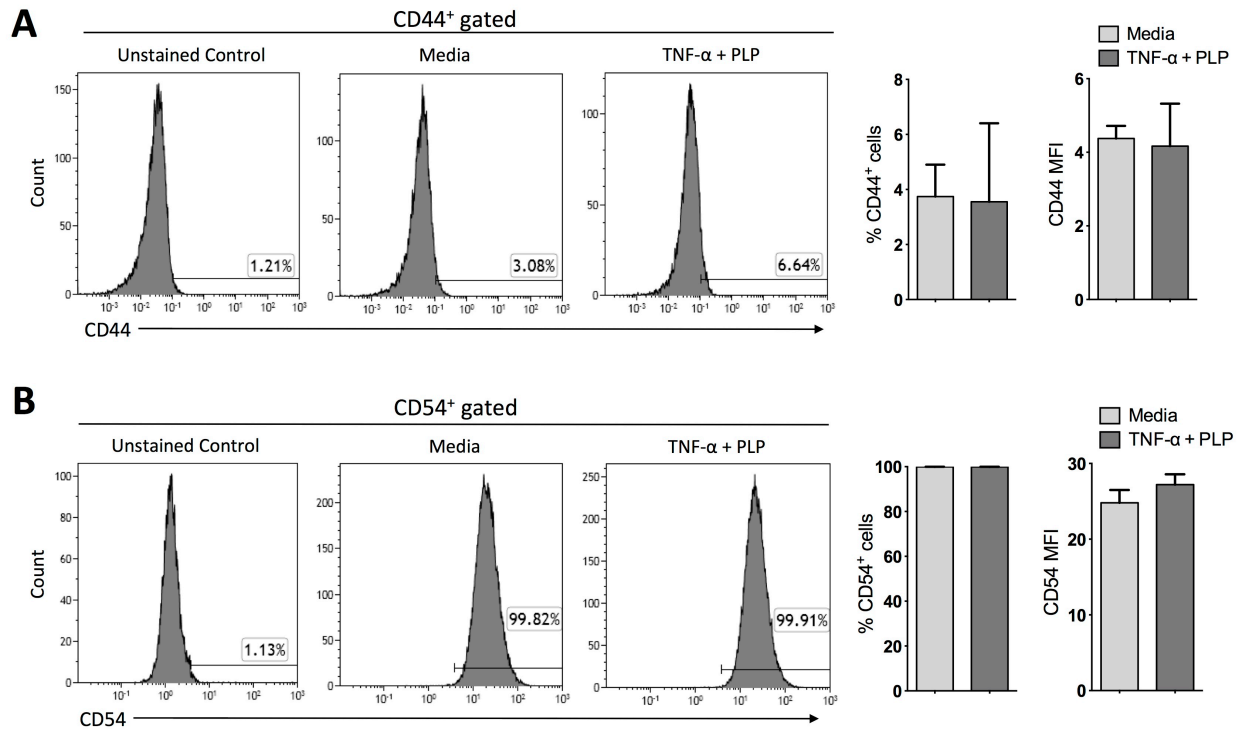


Figure 1. Activation marker expression in Raji B cells observed by flow cytometry: **A)** CD44 and **B)** CD54 (ICAM-1) expression is shown through representative histograms, % positive cells, and mean fluorescence intensity (MFI) of FITC anti-CD44 or PE anti-CD54 stained samples, respectively. Naïve cells were untreated (incubated in media) while primed/activated cells were stimulated with TNF- α and primed with PLP for 24 hours. Cells exhibited minimal expression of CD44 but significant expression of CD54. Primed/activated cells and naïve cells showed similar expression of CD44 and CD54. (n=3)

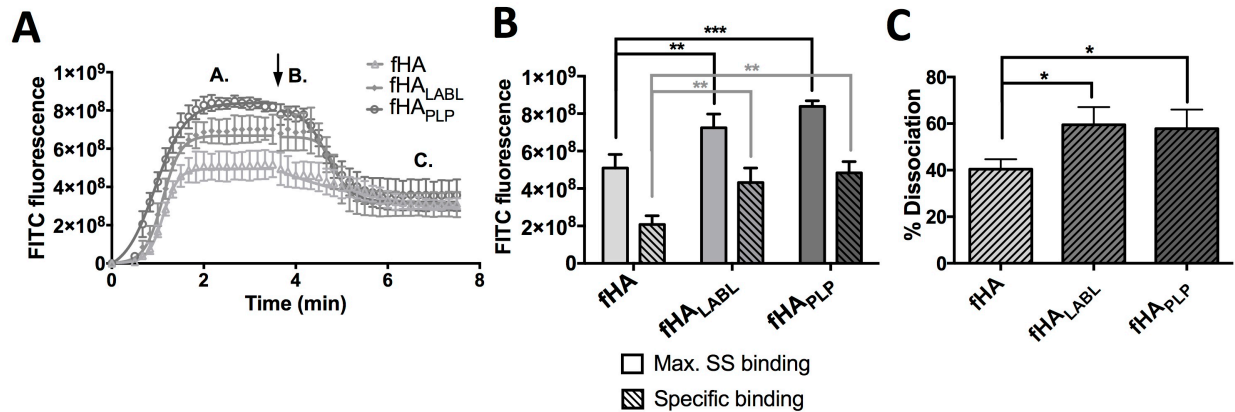


Figure 2. Association, dissociation, and specific binding of homopolymers in naïve Raji B cells determined by flow cytometry. **A)** Kinetic binding curves show association of fHA, fHA_{LABL}, and fHA_{PLP} carried out until maximum steady state (SS_{max}) was reached, followed by competitive dissociation (arrow) through addition of excess unlabeled HA, LABL, or PLP, respectively. The final steady state following dissociation represents nonspecific binding (SS_{ns}). **B)** SS_{max} binding and specific binding (calculated from the difference between SS_{max} and SS_{ns}, Equation 1) for each sample from **A**. **C)** Percent (%) dissociation was determined from specific binding relative to SS_{max} binding (Equation 2). Statistical significance determined by ANOVA followed by Tukey’s post-hoc test with $p < 0.05$ ($n=3$). Robust curve fitting in **A** was performed using sigmoidal nonlinear regression. (* $p < 0.05$, ** $p < 0.01$, *** $p < 0.001$, **** $p < 0.0001$)

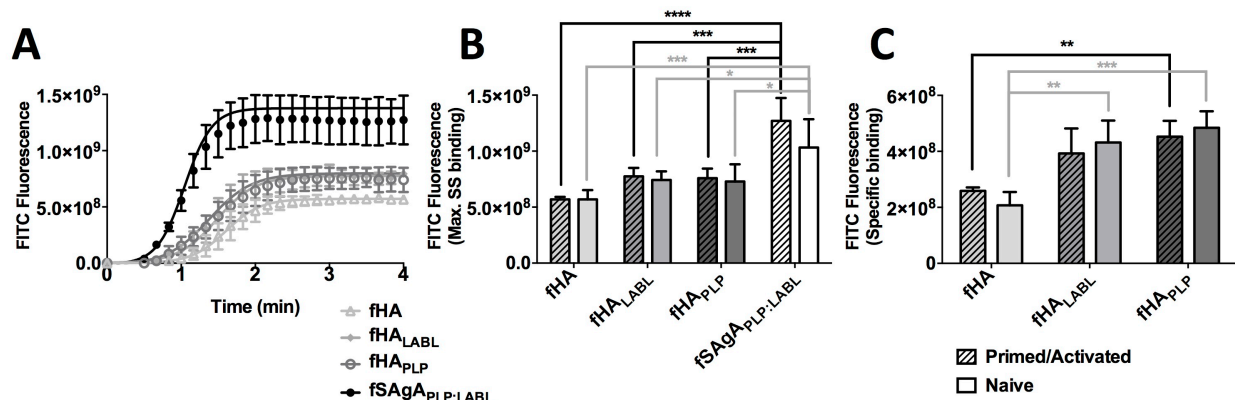


Figure 3. Binding of fSAgA_{PLP:LABL} in naïve and primed/activated Raji B cells determined by flow cytometry: **A)** Kinetic binding curves show association of fHA, fHA_{LABL}, fHA_{PLP}, and fSAgA_{PLP:LABL} in primed/activated Raji B cells. **B)** Maximum steady state (SS_{max}) binding of fHA, fHA_{LABL}, fHA_{PLP}, and fSAgA_{PLP:LABL} determined from association. **C)** Specific binding of fHA, fHA_{LABL}, and fHA_{PLP} determined from competitive dissociation with excess unlabeled HA, LABL, or PLP, respectively. Primed/activated cells were stimulated with TNF- α and primed with PLP for 24 hours. Statistical significance determined by ANOVA followed by Tukey's post-hoc test with $p < 0.05$ ($n = 3$). Robust curve fitting in **A** was performed using sigmoidal nonlinear regression. (* $p < 0.05$, ** $p < 0.01$, *** $p < 0.001$, **** $p < 0.0001$)

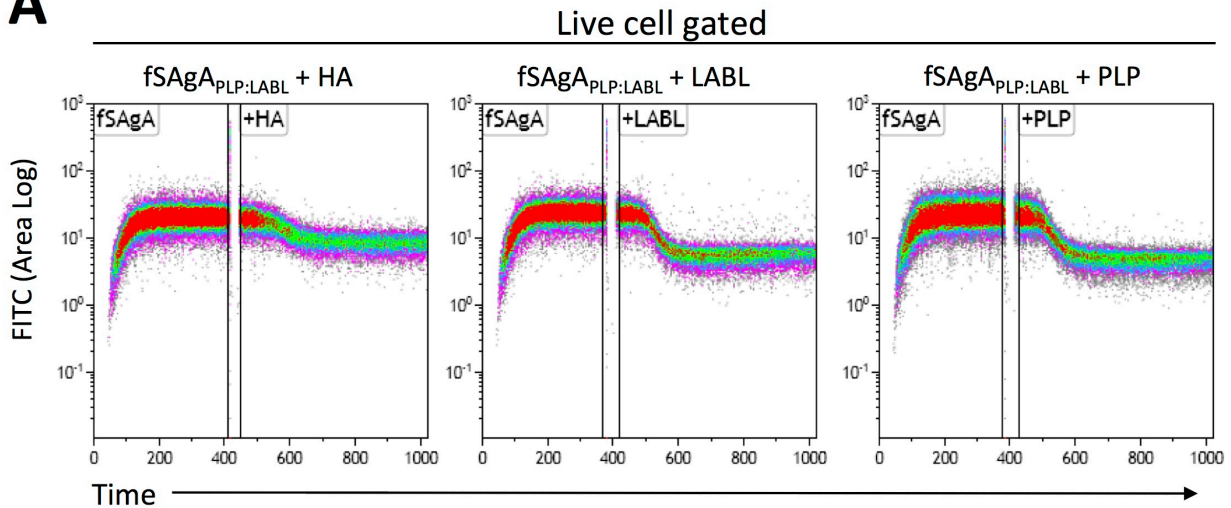
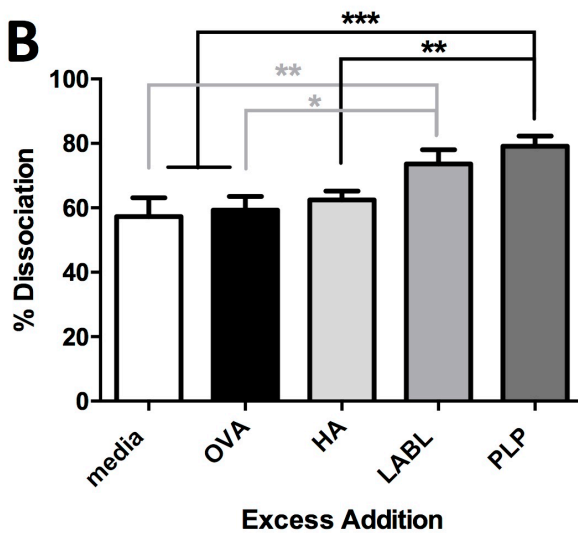
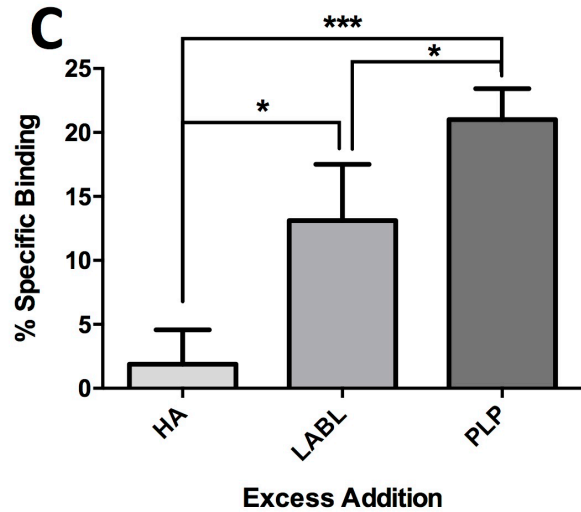
A**B****C**

Figure 4. Specific binding of fSagA_{PLP:LABL} in naïve Raji B cells determined by flow cytometry competitive dissociation: **A)** Representative kinetic scatter plots of FITC fluorescence varying with time, showing three separate runs of fSagA_{PLP:LABL} association followed by competitive dissociation with HA, LABL, or PLP. **B)** Percent (%) dissociation from competition with media control, OVA nonspecific peptide control, HA, LABL, or PLP, determined from specific binding relative to maximum steady state (SS_{max}) binding. **C)** Percent (%) specific binding determined from dissociation with HA, LABL, and PLP (subtracting dissociation from media control, Equation 3). Statistical significance determined by ANOVA followed by Tukey's post-hoc test with $p < 0.05$ ($n=3$). (* $p < 0.05$, ** $p < 0.01$, *** $p < 0.001$, **** $p < 0.0001$)

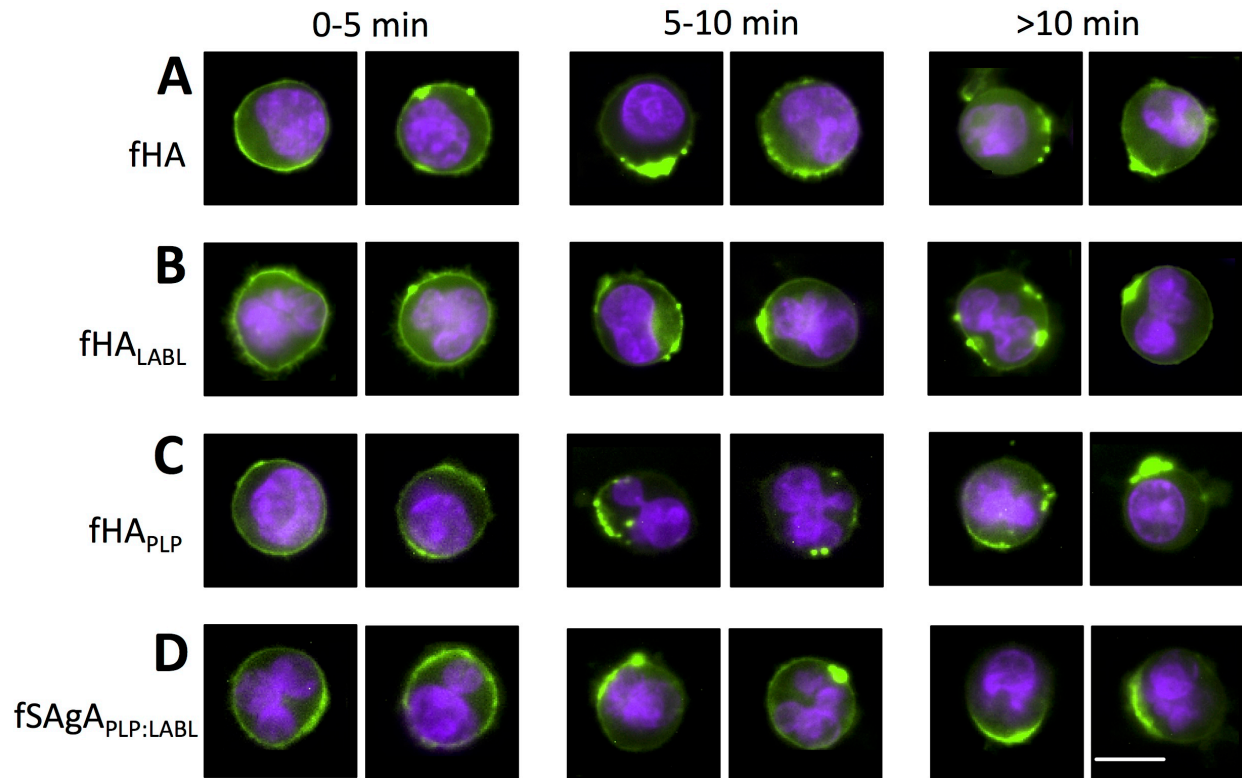


Figure 5. Fluorescence microscopy showing real-time fSagA binding with live Raji B cells following perfusion of **A)** fHA, **B)** fHA_{LABL}, **C)** fHA_{PLP}, and **D)** fSagA_{PLP:LABL}. Following perfusion of treatment groups into the cell mixing chamber for 5 minutes and gentle media perfusion for an additional 5 minutes to rinse, images were captured from (t=0) across time intervals of [0-5), [5-10), and >10 minutes. Images show cells stained with Hoechst (violet) and FITC-labeled samples (green). Progression from diffuse FITC fluorescence (0-5 min) towards punctate FITC fluorescence on the cell surface (>10 min) suggests progressive receptor clustering resulting from fSagA binding. Captured using the M04S plate and CellASIC Onyx Microfluidics platform on an Olympus IX81 inverted Epifluorescence microscope. Magnification: 60X Air. Exposure: Hoechst (exc. 384 nm) 125 ms, FITC (exc. 484 nm) 3000 ms. Scale bar equals 10 μ m.

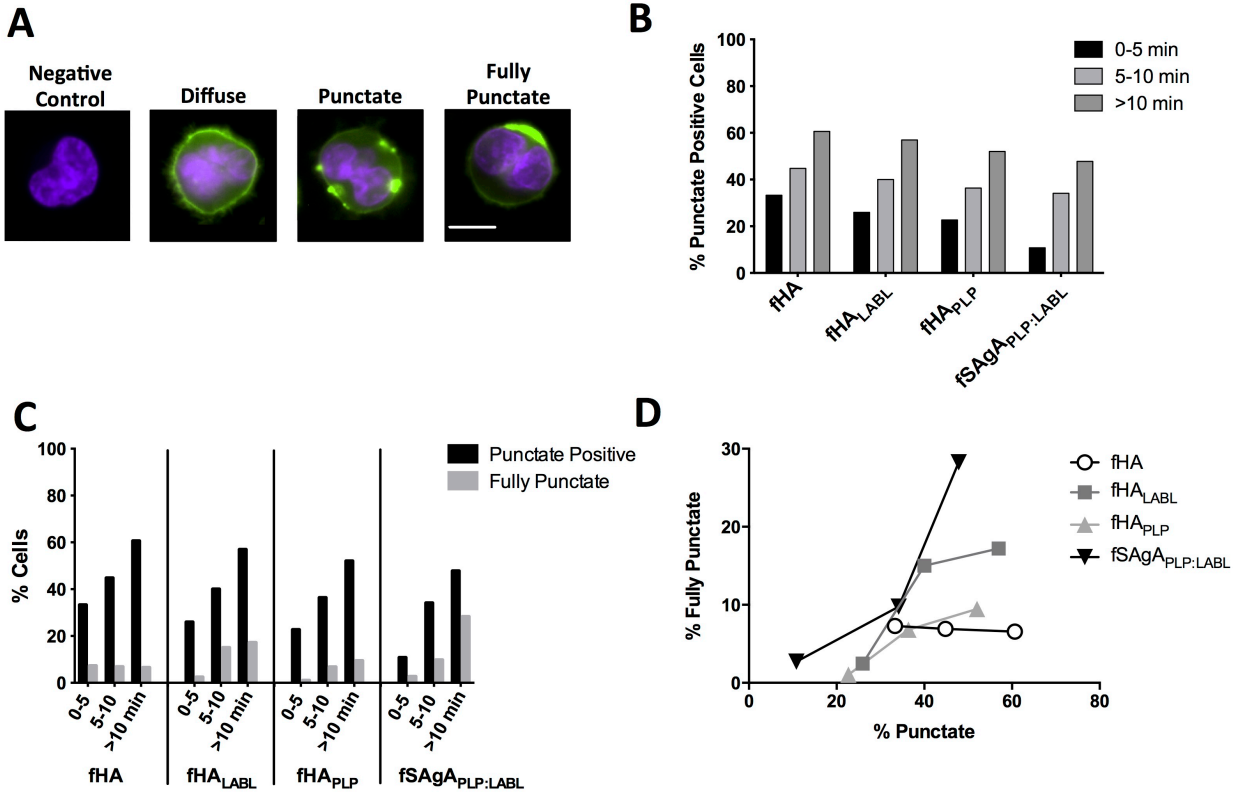


Figure 6. Analysis of progressive receptor clustering in Raji B cells following fSAgA binding was determined by fluorescence microscopy. **A)** Characteristic examples of diffuse, punctate, or fully punctate cell surface binding in Raji B cells are shown. Punctate staining was defined by multiple areas of discrete high intensity fluorescence totaling <50% of the cell surface; fully punctate staining was defined by one predominant area of discrete high intensity fluorescence totaling <50% of the cell surface. Images show cells stained with Hoechst (violet) and FITC-labeled samples (green). Scale bar equals 10 μm . **B)** Percent (%) punctate positive cells was determined across FITC positive cells for each treatment group per time interval. For each sample and time interval, several fields were randomly selected and 40–200 FITC positive cells total were counted and scored for diffuse versus punctate staining. **C)** Of the punctate positive cells, fully punctate cells were also distinguished. **D)** Percent (%) fully punctate versus % punctate cells shows the greatest slope for fSAgA_{PLP:LABL} and a near-zero slope for fHA. Composite analysis from two independent experiments.

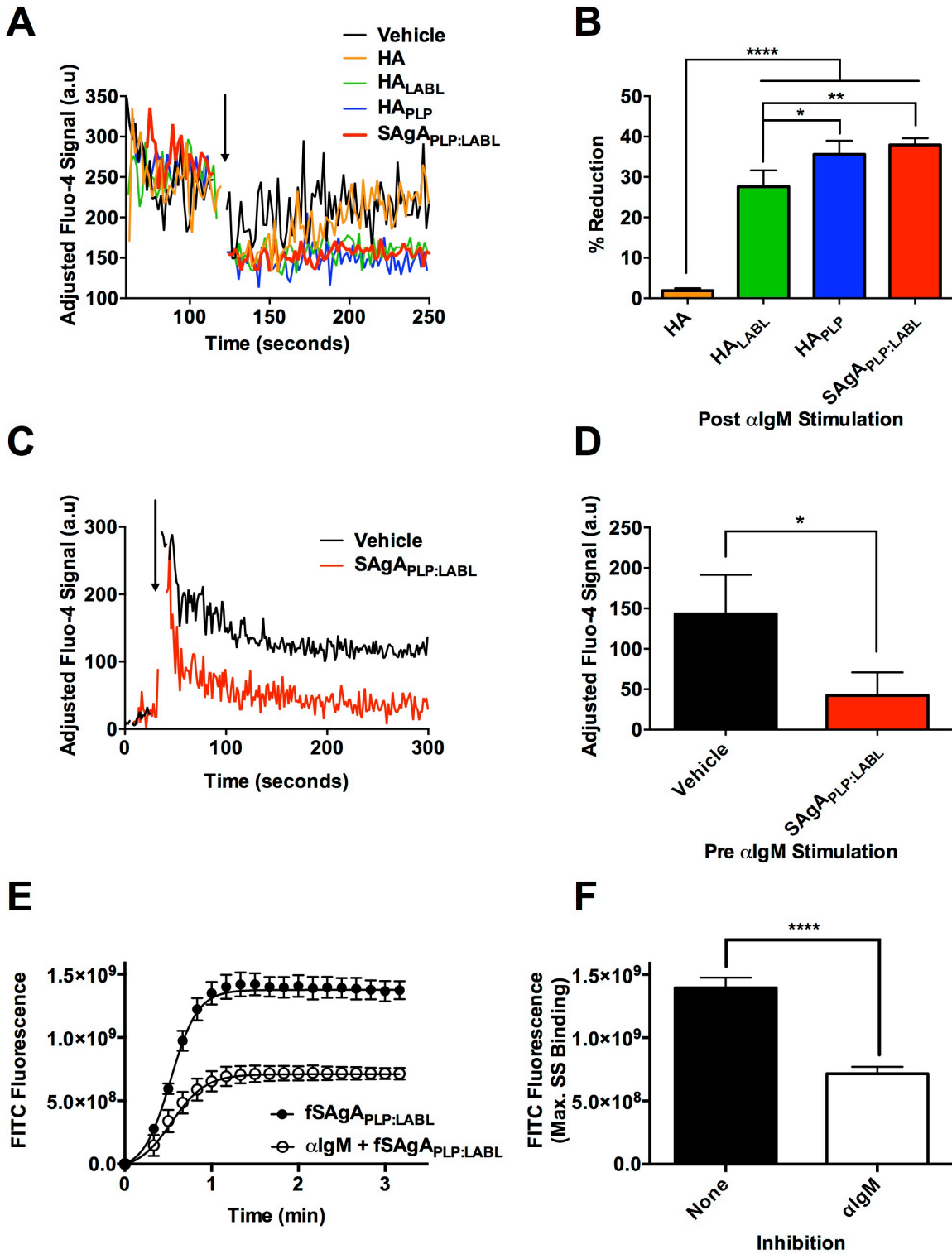
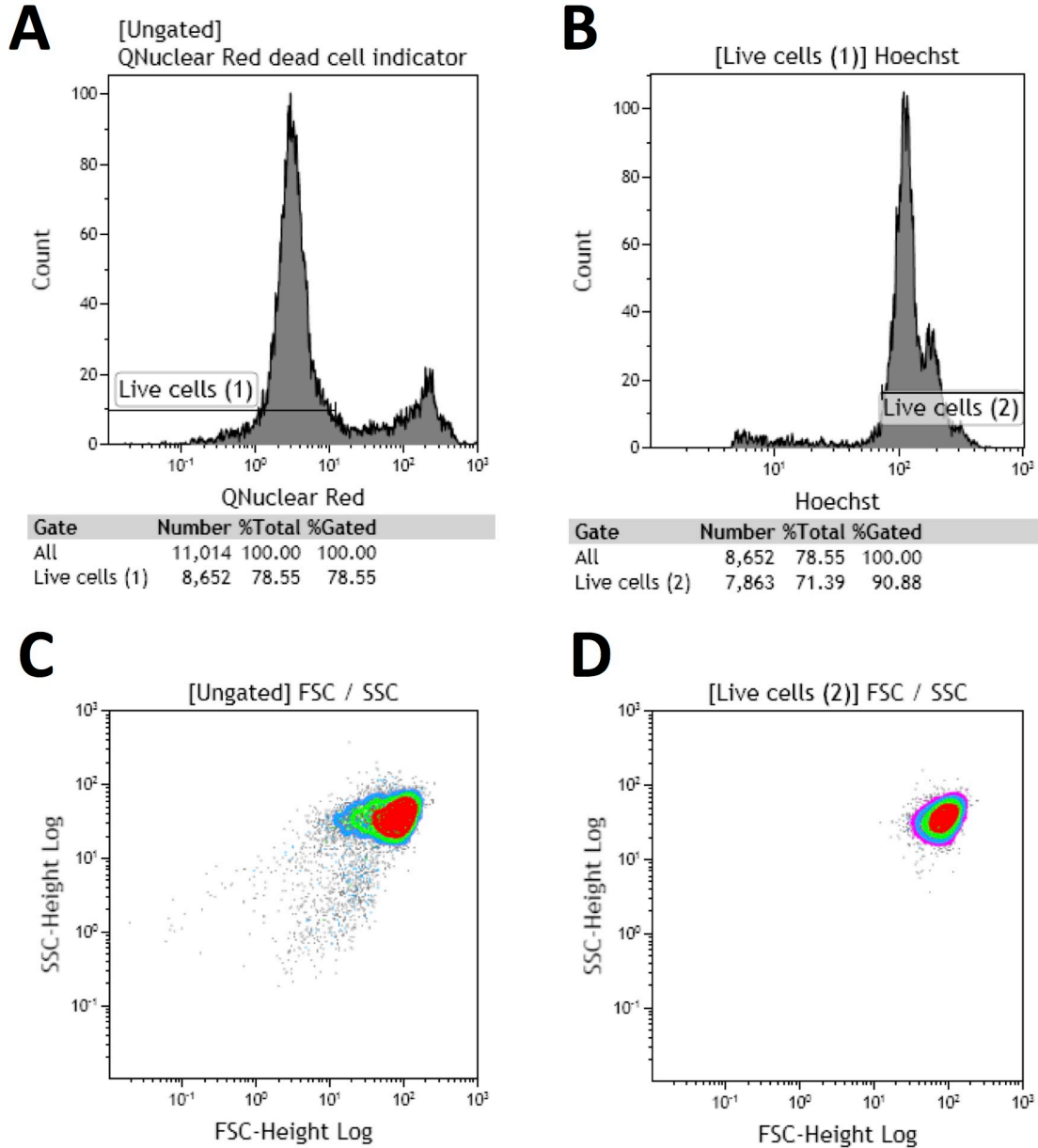


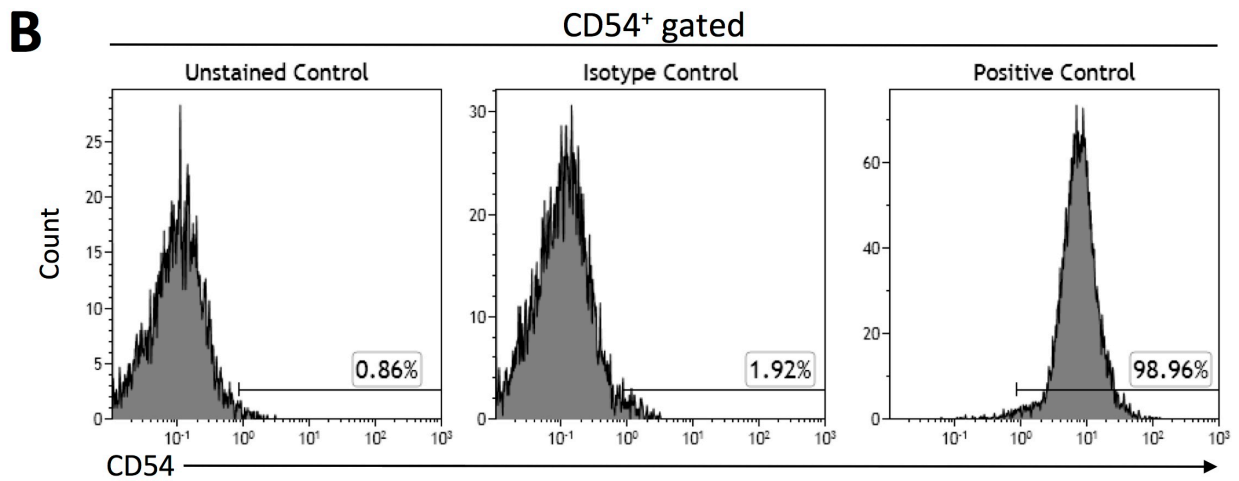
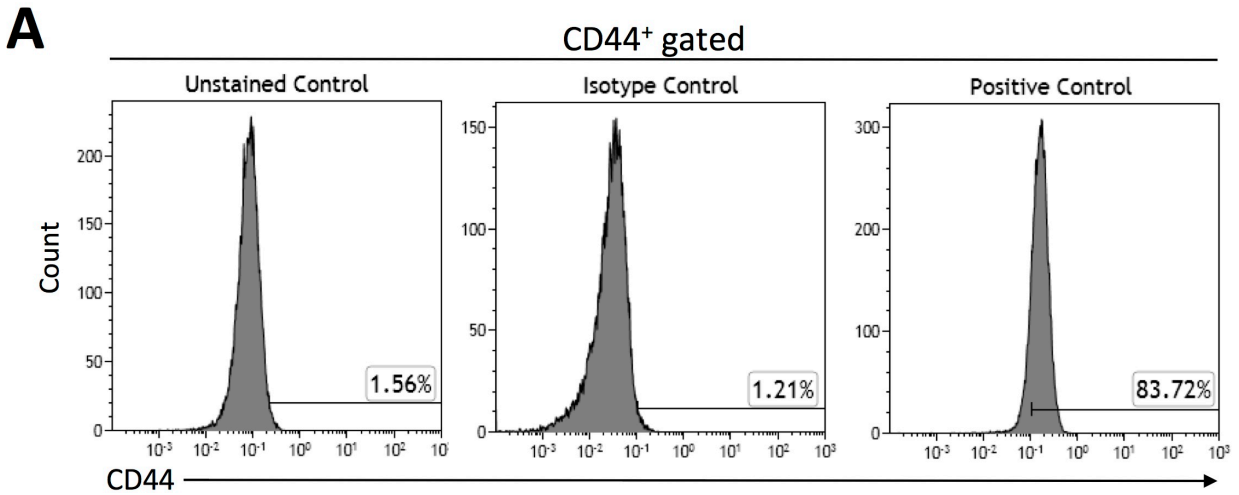
Figure 7. IgM-stimulated (BCR-mediated) signaling response was evaluated in Raji B cells through flow cytometry calcium flux. **A) Reduction:** Fluo-4 loaded cells were stimulated with

anti-IgM (α IgM) at 50 s, then treated with an addition of vehicle (HBSS), HA, HA_{PLP}, HA_{LABL}, or SAgA_{PLP:LABL} at ~120 s (black arrow) to evaluate signaling reduction. Kinetics show median Fluo-4 fluorescence values. **B)** Percent reduction from stimulated baseline caused by addition of samples in figure A, determined from mean steady state values. **C) Inhibition:** Fluo-4 loaded cells were first pre-treated with an addition of vehicle (HBSS) or SAgA_{PLP:LABL}, then stimulated with α IgM (black arrow) to evaluate signaling inhibition. **D)** Relative α IgM stimulation in signaling following pre-treatment with vehicle or SAgA_{PLP:LABL}. Baseline-adjusted values determined from mean steady state values. **E) Targeting:** fSAgA_{PLP:LABL} binding was evaluated by flow cytometry following blocking of BCR by α IgM. **F)** Maximum steady state (SS_{max}) binding of fSAgA_{PLP:LABL} compared in Raji B cells following blocking by α IgM. Statistical significance determined by ANOVA followed by Tukey's post hoc test (**B**) or unpaired t-test (**D**, **F**) with $p < 0.05$ ($n=3$). Robust curve fitting (**E**) was performed using sigmoidal nonlinear regression. (* $p < 0.05$, ** $p < 0.01$, *** $p < 0.001$, **** $p < 0.0001$)

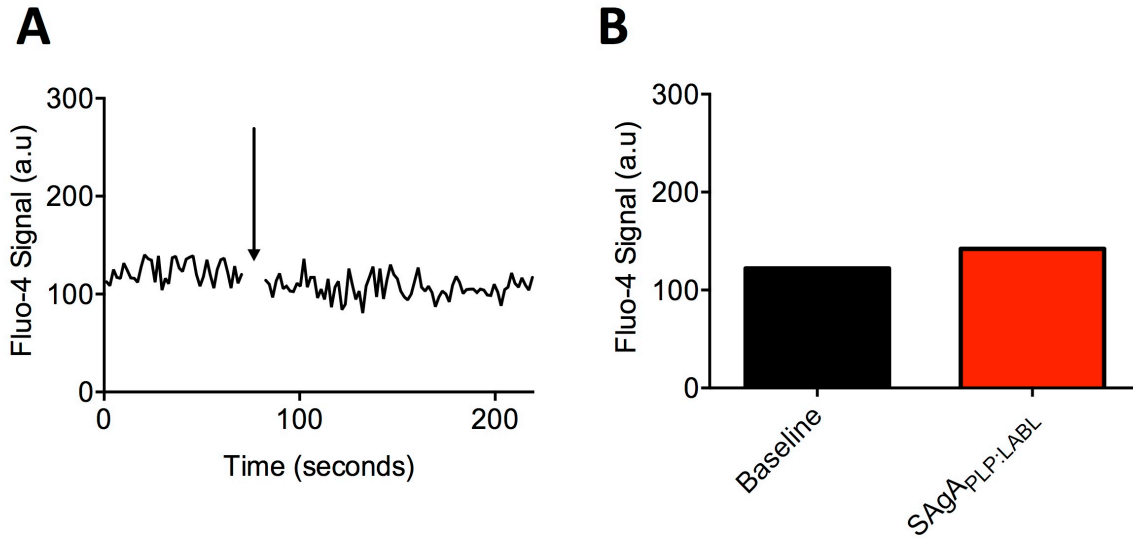
Supplemental Information



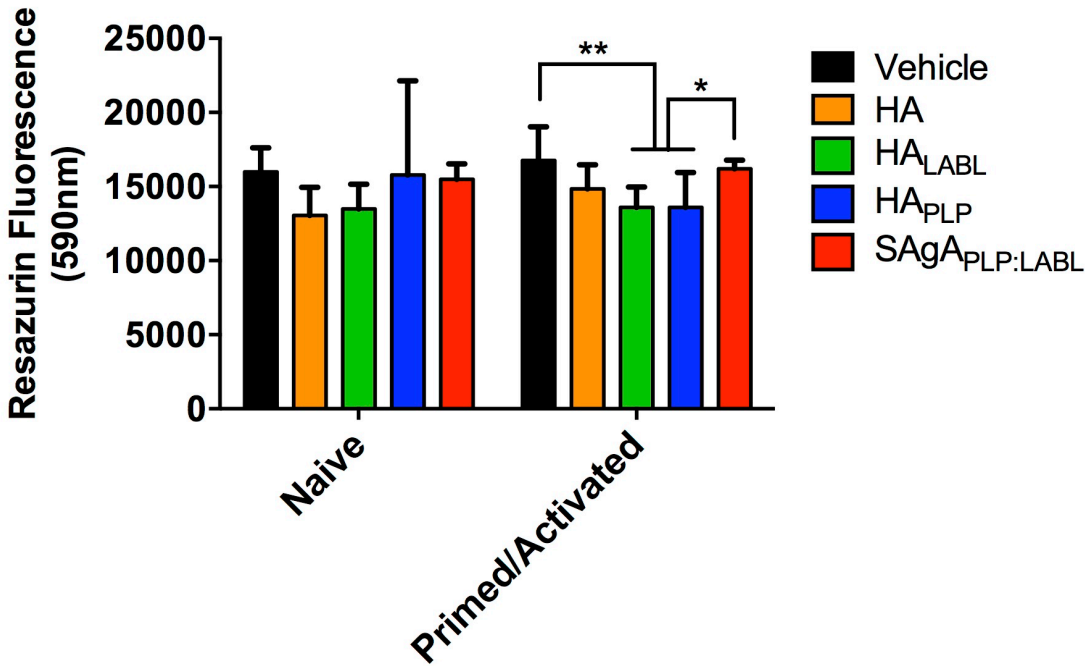
Supplemental Figure 1. Flow cytometry histograms showing the gating protocol used to remove **A)** dead cells and **B)** debris from analysis. Scatter plots show **C)** ungated and **D)** live cell populations. QNuclear Red (or propidium iodide, PI) was used as a dead cell indicator and Hoechst was used as a nuclei stain. Plots generated in Kaluza Flow Analysis software.



Supplemental Figure 2. Flow cytometry histograms showing unstained controls, isotype controls, and positive stains for **A)** FITC-CD44 antibody labeling and **B)** PE-CD54 antibody labeling in Raji B cells.



Supplemental Figure 3. Flow cytometry calcium flux in Fluo-4 loaded Raji B cells shows **A)** no signaling change in non-stimulated cells upon addition of SAgA_{PLP:LABEL} (black arrow). Kinetics show median Fluo-4 fluorescence values. **B)** Fluo-4 signal from figure **A** determined from mean steady state values.



Supplemental Figure 4. Resazurin cell metabolic assay in naïve and primed/activated Raji B cells shows metabolic activity in response to 24 hour treatment with vehicle (media), HA, HA_{LABL}, HA_{PLP}, or SAgA_{PLP:LABL}. Statistical significance determined by two-way ANOVA followed by Tukey’s post hoc test with $p < 0.05$ ($n=3$). (* $p < 0.05$, ** $p < 0.01$, *** $p < 0.001$, **** $p < 0.0001$)

References

1. Gonsette, R., Self-tolerance in multiple sclerosis. *Acta Neurologica Belgica* **2012**, *112* (2), 133-140.
2. Carson, M. J.; Doose, J. M.; Melchior, B.; Schmid, C. D.; Ploix, C. C., CNS immune privilege: hiding in plain sight. *Immunological reviews* **2006**, *213* (1), 48-65.
3. Boster, A.; Ankeny, D. P.; Racke, M. K., The potential role of B cell-targeted therapies in multiple sclerosis. *Drugs* **2010**, *70* (18), 2343-2356.
4. Oh, S.; Cudrici, C.; Ito, T.; Rus, H., B-cells and humoral immunity in multiple sclerosis. Implications for therapy. *Immunologic research* **2008**, *40* (3), 224-234.
5. Bates, D., Treatment effects of immunomodulatory therapies at different stages of multiple sclerosis in short-term trials. *Neurology* **2011**, *76* (1 Supplement 1), S14-S25.
6. Jones, J. L.; Coles, A. J., New treatment strategies in multiple sclerosis. *Experimental Neurology* **2010**, *225* (1), 34-39.
7. Vosoughi, R.; Freedman, M. S., Therapy of MS. *Clinical neurology and neurosurgery* **2010**, *112* (5), 365-385.
8. Langer-Gould, A.; Steinman, L., Progressive multifocal leukoencephalopathy and multiple sclerosis: lessons from natalizumab. *Current neurology and neuroscience reports* **2006**, *6* (3), 253-258.
9. Feldmann, M.; Steinman, L., Design of effective immunotherapy for human autoimmunity. *Nature* **2005**, *435* (7042), 612.
10. Miller, S. D.; Turley, D. M.; Podojil, J. R., Antigen-specific tolerance strategies for the prevention and treatment of autoimmune disease. *Nature Reviews Immunology* **2007**, *7* (9), 665.
11. Jones, D. S., Multivalent compounds for antigen-specific B cell tolerance and treatment of autoimmune diseases. *Current medicinal chemistry* **2005**, *12* (16), 1887-1904.
12. Mills, K.; Fletcher, J., T cells in multiple sclerosis and experimental autoimmune encephalomyelitis. **2010**.
13. Barnett, M. H.; Sutton, I., The pathology of multiple sclerosis: a paradigm shift. *Current opinion in neurology* **2006**, *19* (3), 242-247.
14. Amor, S.; Puentes, F.; Baker, D.; Van Der Valk, P., Inflammation in neurodegenerative diseases. *Immunology* **2010**, *129* (2), 154-169.
15. Herz, J.; Zipp, F.; Siffrin, V., Neurodegeneration in autoimmune CNS inflammation. *Experimental neurology* **2010**, *225* (1), 9-17.
16. Kutzelnigg, A.; Lassmann, H., Pathology of multiple sclerosis and related inflammatory demyelinating diseases. *Handb Clin Neurol* **2014**, *122*, 15-58.
17. Lassmann, H., Mechanisms of inflammation induced tissue injury in multiple sclerosis. *Journal of the neurological sciences* **2008**, *274* (1), 45-47.
18. Grakoui, A.; Bromley, S. K.; Sumen, C.; Davis, M. M.; Shaw, A. S.; Allen, P. M.; Dustin, M. L., The immunological synapse: a molecular machine controlling T cell activation. *Science* **1999**, *285* (5425), 221-227.
19. Iezzi, G.; Karjalainen, K.; Lanzavecchia, A., The duration of antigenic stimulation determines the fate of naive and effector T cells. *Immunity* **1998**, *8* (1), 89-95.
20. Baxter, A. G.; Hodgkin, P. D., Activation rules: the two-signal theories of immune activation. *Nature Reviews Immunology* **2002**, *2* (6), 439-446.

21. Bromley, S. K.; Iaboni, A.; Davis, S. J.; Whitty, A.; Green, J. M.; Shaw, A. S.; Weiss, A.; Dustin, M. L., The immunological synapse and CD28-CD80 interactions. *Nature immunology* **2001**, *2* (12), 1159-1166.
22. Chen, L.; Flies, D. B., Molecular mechanisms of T cell co-stimulation and co-inhibition. *Nature Reviews Immunology* **2013**, *13* (4), 227-242.
23. Frauwirth, K. A.; Thompson, C. B., Activation and inhibition of lymphocytes by costimulation. *The Journal of clinical investigation* **2002**, *109* (109 (3)), 295-299.
24. Jun, J. E.; Goodnow, C. C., Scaffolding of antigen receptors for immunogenic versus tolerogenic signaling. *Nature immunology* **2003**, *4* (11), 1057-1064.
25. Moser, M.; Leo, O., Key concepts in immunology. *Vaccine* **2010**, *28*, C2-C13.
26. Archelos, J. J.; Storch, M. K.; Hartung, H. P., The role of B cells and autoantibodies in multiple sclerosis. *Annals of neurology* **2000**, *47* (6), 694-706.
27. Lassmann, H.; Brunner, C.; Bradl, M.; Linington, C., Experimental allergic encephalomyelitis: the balance between encephalitogenic T lymphocytes and demyelinating antibodies determines size and structure of demyelinated lesions. *Acta neuropathologica* **1988**, *75* (6), 566-576.
28. Racke, M. K., The role of B cells in multiple sclerosis: rationale for B-cell-targeted therapies. *Current opinion in neurology* **2008**, *21*, S9-S18.
29. Zouali, M., Tweaking the B lymphocyte compartment in autoimmune diseases. *Nature immunology* **2014**, *15* (3), 209-212.
30. Wang, R.-X.; Yu, C.-R.; Dambuza, I. M.; Mahdi, R. M.; Dolinska, M. B.; Sergeev, Y. V.; Wingfield, P. T.; Kim, S.-H.; Egwuagu, C. E., Interleukin-35 induces regulatory B cells that suppress autoimmune disease. *Nature medicine* **2014**, *20* (6), 633-641.
31. Puffer, E. B.; Pontrello, J. K.; Hollenbeck, J. J.; Kink, J. A.; Kiessling, L. L., Activating B cell signaling with defined multivalent ligands. *ACS chemical biology* **2007**, *2* (4), 252-262.
32. Dintzis, H.; Dintzis, R.; Vogelstein, B., Molecular determinants of immunogenicity: the immunon model of immune response. *Proceedings of the National Academy of Sciences* **1976**, *73* (10), 3671-3675.
33. Reim, J. W.; Symer, D. E.; Watson, D. C.; Dintzis, R. Z.; Dintzis, H. M., Low molecular weight antigen arrays delete high affinity memory B cells without affecting specific T-cell help. *Molecular immunology* **1996**, *33* (17-18), 1377.
34. Berer, K.; Wekerle, H.; Krishnamoorthy, G., B cells in spontaneous autoimmune diseases of the central nervous system. *Molecular immunology* **2011**, *48* (11), 1332-1337.
35. McHeyzer-Williams, M. G.; Ahmed, R., B cell memory and the long-lived plasma cell. *Current opinion in immunology* **1999**, *11* (2), 172-179.
36. Sestak, J.; Mullins, M.; Northrup, L.; Thati, S.; Forrest, M. L.; Siahaan, T. J.; Berkland, C., Single-step grafting of aminoxy-peptides to hyaluronan: a simple approach to multifunctional therapeutics for experimental autoimmune encephalomyelitis. *Journal of Controlled Release* **2013**, *168* (3), 334-340.
37. Sestak, J. O.; Sullivan, B. P.; Thati, S.; Northrup, L.; Hartwell, B.; Antunez, L.; Forrest, M. L.; Vines, C. M.; Siahaan, T. J.; Berkland, C., Co-delivery of antigen and an immune cell adhesion inhibitor is necessary for efficacy of soluble antigen arrays in experimental autoimmune encephalomyelitis. *Molecular Therapy—Methods & Clinical Development* **2014**, *1*.

38. Mossman, K. D.; Campi, G.; Groves, J. T.; Dustin, M. L., Altered TCR signaling from geometrically repatterned immunological synapses. *Science* **2005**, *310* (5751), 1191-1193.
39. Ridwan, R.; Kiptoo, P.; Kobayashi, N.; Weir, S.; Hughes, M.; Williams, T.; Soegianto, R.; Siahaan, T. J., Antigen-specific suppression of experimental autoimmune encephalomyelitis by a novel bifunctional peptide inhibitor: structure optimization and pharmacokinetics. *Journal of Pharmacology and Experimental Therapeutics* **2010**, *332* (3), 1136-1145.
40. Rock, K. L.; Benacerraf, B.; Abbas, A. K., Antigen presentation by hapten-specific B lymphocytes. I. Role of surface immunoglobulin receptors. *The Journal of experimental medicine* **1984**, *160* (4), 1102-1113.
41. Constant, S. L., B lymphocytes as antigen-presenting cells for CD4⁺ T cell priming in vivo. *The Journal of Immunology* **1999**, *162* (10), 5695-5703.
42. Chittasupho, C.; Sestak, J.; Shannon, L.; Siahaan, T. J.; Vines, C. M.; Berkland, C., Hyaluronic acid graft polymers displaying peptide antigen modulate dendritic cell response in vitro. *Molecular pharmaceuticals* **2013**, *11* (1), 367-373.
43. Kaminski, T.; Siebrasse, J.-P.; Gieselmann, V.; Kubitscheck, U.; Kappler, J., Imaging and tracking of single hyaluronan molecules diffusing in solution. *Glycoconjugate journal* **2008**, *25* (6), 555-560.
44. Delon, J.; Germain, R. N., Information transfer at the immunological synapse. *Current Biology* **2000**, *10* (24), R923-R933.
45. Wither, J. E.; Roy, V.; Brennan, L. A., Activated B cells express increased levels of costimulatory molecules in young autoimmune NZB and (NZB× NZW) F1 mice. *Clinical immunology* **2000**, *94* (1), 51-63.
46. Johnson, P.; Ruffell, B., CD44 and its role in inflammation and inflammatory diseases. *Inflammation & Allergy-Drug Targets (Formerly Current Drug Targets-Inflammation & Allergy)* **2009**, *8* (3), 208-220.
47. Gee, K.; Kryworuchko, M.; Kumar, A., Recent advances in the regulation of CD44 expression and its role in inflammation and autoimmune diseases. *ARCHIVUM IMMUNOLOGIAE ET THERAPIAE EXPERIMENTALIS-ENGLISH EDITION-* **2004**, *52* (1), 13-26.
48. Zhao, C.; Davies, J. D., A peripheral CD4⁺ T cell precursor for naive, memory, and regulatory T cells. *The Journal of experimental medicine* **2010**, *207* (13), 2883-2894.
49. Hartwell, B. L.; Antunez, L.; Sullivan, B. P.; Thati, S.; Sestak, J. O.; Berkland, C., Multivalent Nanomaterials: Learning from Vaccines and Progressing to Antigen-Specific Immunotherapies. *Journal of pharmaceutical sciences* **2014**.
50. Chittasupho, C.; Siahaan, T. J.; Vines, C. M.; Berkland, C., Autoimmune therapies targeting costimulation and emerging trends in multivalent therapeutics. *Therapeutic delivery* **2011**, *2* (7), 873-889.
51. Symer, D. E.; Dintzis, R. Z.; Diamond, D. J.; Dintzis, H. M., Inhibition or activation of human T cell receptor transfectants is controlled by defined, soluble antigen arrays. *The Journal of experimental medicine* **1992**, *176* (5), 1421-1430.
52. Gestwicki, J. E.; Cairo, C. W.; Strong, L. E.; Oetjen, K. A.; Kiessling, L. L., Influencing receptor-ligand binding mechanisms with multivalent ligand architecture. *Journal of the American Chemical Society* **2002**, *124* (50), 14922-14933.

53. Krishnamurthy, V. M.; Estroff, L. A.; Whitesides, G. M., Multivalency in ligand design. *Fragment-based approaches in drug discovery* **2006**, *34*, 11-53.
54. Kiessling, L. L.; Gestwicki, J. E.; Strong, L. E., Synthetic multivalent ligands in the exploration of cell-surface interactions. *Current opinion in chemical biology* **2000**, *4* (6), 696-703.
55. Dintzis, R. Z.; Okajima, M.; Middleton, M.; Greene, G.; Dintzis, H., The immunogenicity of soluble haptenated polymers is determined by molecular mass and hapten valence. *The Journal of Immunology* **1989**, *143* (4), 1239-1244.
56. Dintzis, H. M.; Dintzis, R. Z., Antigens as immunoregulators. *Immunological reviews* **1990**, *115* (1), 243-250.
57. Dintzis, R.; Middleton, M.; Dintzis, H., Studies on the immunogenicity and tolerogenicity of T-independent antigens. *The Journal of Immunology* **1983**, *131* (5), 2196-2203.
58. Desaymard, C.; Ivanyi, L., Comparison of in vitro immunogenicity, tolerogenicity and mitogenicity of dinitrophenyl-levan conjugates with varying epitope density. *Immunology* **1976**, *30* (5), 647.
59. Desaymard, C.; Howard, J., Role of epitope density in the induction of immunity and tolerance with thymus-independent antigens. II. Studies with 2, 4-dinitrophenyl conjugates in vivo. *European journal of immunology* **1975**, *5* (8), 541-545.
60. Symer, D. E.; Reim, J.; Dintzis, R. Z.; Voss, E.; Dintzis, H. M., Durable elimination of high affinity, T cell-dependent antibodies by low molecular weight antigen arrays in vivo. *The Journal of Immunology* **1995**, *155* (12), 5608-5616.
61. Courtney, A. H.; Puffer, E. B.; Pontrello, J. K.; Yang, Z.-Q.; Kiessling, L. L., Sialylated multivalent antigens engage CD22 in trans and inhibit B cell activation. *Proceedings of the National Academy of Sciences* **2009**, *106* (8), 2500-2505.
62. Cherukuri, A.; Cheng, P. C.; Sohn, H. W.; Pierce, S. K., The CD19/CD21 complex functions to prolong B cell antigen receptor signaling from lipid rafts. *Immunity* **2001**, *14* (2), 169-179.
63. Duong, B. H.; Tian, H.; Ota, T.; Completo, G.; Han, S.; Vela, J. L.; Ota, M.; Kubitz, M.; Bovin, N.; Paulson, J. C., Decoration of T-independent antigen with ligands for CD22 and Siglec-G can suppress immunity and induce B cell tolerance in vivo. *The Journal of experimental medicine* **2010**, *207* (1), 173-187.
64. Pfengle, F.; Macauley, M. S.; Kawasaki, N.; Paulson, J. C., Copresentation of antigen and ligands of Siglec-G induces B cell tolerance independent of CD22. *The Journal of Immunology* **2013**, *191* (4), 1724-1731.
65. Northrup, L.; Sestak, J. O.; Sullivan, B. P.; Thati, S.; Hartwell, B. L.; Siahaan, T. J.; Vines, C. M.; Berkland, C., Co-delivery of autoantigen and b7 pathway modulators suppresses experimental autoimmune encephalomyelitis. *The AAPS journal* **2014**, *16* (6), 1204-1213.
66. Yeste, A.; Nadeau, M.; Burns, E. J.; Weiner, H. L.; Quintana, F. J., Nanoparticle-mediated co-delivery of myelin antigen and a tolerogenic small molecule suppresses experimental autoimmune encephalomyelitis. *Proceedings of the National Academy of Sciences* **2012**, *109* (28), 11270-11275.
67. Tsourkas, P. K.; Baumgarth, N.; Simon, S. I.; Raychaudhuri, S., Mechanisms of B-cell synapse formation predicted by Monte Carlo simulation. *Biophysical journal* **2007**, *92* (12), 4196-4208.

68. Badawi, A.; Kiptoo, P.; Siahaan, T., Immune Tolerance Induction against Experimental Autoimmune Encephalomyelitis (EAE) Using A New PLP-B7AP Conjugate that Simultaneously Targets B7/CD28 Costimulatory Signal and TCR/MHC-II Signal. *J Mult Scler* **2014**, *1* (131), 2376-0389.1000131.
69. Manikwar, P.; Kiptoo, P.; Badawi, A. H.; Büyüktimkin, B.; Siahaan, T. J., Antigen-specific blocking of CD4-Specific immunological synapse formation using BPI and current therapies for autoimmune diseases. *Medicinal research reviews* **2012**, *32* (4), 727-764.
70. Carrasco, Y. R.; Fleire, S. J.; Cameron, T.; Dustin, M. L.; Batista, F. D., LFA-1/ICAM-1 interaction lowers the threshold of B cell activation by facilitating B cell adhesion and synapse formation. *Immunity* **2004**, *20* (5), 589-599.
71. Anderson, M. E.; Siahaan, T. J., Targeting ICAM-1/LFA-1 interaction for controlling autoimmune diseases: designing peptide and small molecule inhibitors. *Peptides* **2003**, *24* (3), 487-501.
72. Tibbetts, S. A.; Jois, D. S.; Siahaan, T. J.; Benedict, S. H.; Chan, M. A., Linear and cyclic LFA-1 and ICAM-1 peptides inhibit T cell adhesion and function. *Peptides* **2000**, *21* (8), 1161-1167.
73. Supersaxo, A.; Hein, W. R.; Steffen, H., Effect of molecular weight on the lymphatic absorption of water-soluble compounds following subcutaneous administration. *Pharmaceutical research* **1990**, *7* (2), 167-169.
74. Bagby, T. R.; Cai, S.; Duan, S.; Thati, S.; Aires, D. J.; Forrest, L., Impact of molecular weight on lymphatic drainage of a biopolymer-based imaging agent. *Pharmaceutics* **2012**, *4* (2), 276-295.
75. Oussoren, C.; Storm, G., Liposomes to target the lymphatics by subcutaneous administration. *Advanced drug delivery reviews* **2001**, *50* (1), 143-156.
76. Rao, D. A.; Forrest, M. L.; Alani, A. W.; Kwon, G. S.; Robinson, J. R., Biodegradable PLGA based nanoparticles for sustained regional lymphatic drug delivery. *Journal of pharmaceutical sciences* **2010**, *99* (4), 2018-2031.
77. Oussoren, C.; Zuidema, J.; Crommelin, D.; Storm, G., Lymphatic uptake and biodistribution of liposomes after subcutaneous injection.: II. Influence of liposomal size, lipid composition and lipid dose. *Biochimica et Biophysica Acta (BBA)-Biomembranes* **1997**, *1328* (2), 261-272.
78. Karpova, M.; Schoumans, J.; Ernberg, I.; Henter, J.; Nordenskjöld, M.; Fadeel, B., Raji revisited: cytogenetics of the original Burkitt's lymphoma cell line. *Leukemia* **2005**, *19* (1), 159-161.
79. Pender, M. P.; Burrows, S. R., Epstein–Barr virus and multiple sclerosis: potential opportunities for immunotherapy. *Clinical & Translational Immunology* **2014**, *3* (10), e27.
80. Pender, M. P., The essential role of Epstein-Barr virus in the pathogenesis of multiple sclerosis. *The Neuroscientist* **2010**, 1073858410381531.
81. Pender, M. P.; Csurhes, P. A.; Smith, C.; Beagley, L.; Hooper, K. D.; Raj, M.; Coulthard, A.; Burrows, S. R.; Khanna, R., Epstein–Barr virus-specific adoptive immunotherapy for progressive multiple sclerosis. *Multiple Sclerosis Journal* **2014**, 1352458514521888.
82. Ascherio, A.; Munger, K. L., Epstein–Barr virus infection and multiple sclerosis: a review. *Journal of Neuroimmune Pharmacology* **2010**, *5* (3), 271-277.

83. Bagert, B. A., Epstein-Barr virus in multiple sclerosis. *Current neurology and neuroscience reports* **2009**, *9* (5), 405-410.
84. Serafini, B.; Rosicarelli, B.; Franciotta, D.; Magliozzi, R.; Reynolds, R.; Cinque, P.; Andreoni, L.; Trivedi, P.; Salvetti, M.; Faggioni, A., Dysregulated Epstein-Barr virus infection in the multiple sclerosis brain. *The Journal of experimental medicine* **2007**, *204* (12), 2899-2912.
85. Rand, K. H.; Houck, H.; Denslow, N. D.; Heilman, K. M., Epstein-Barr virus nuclear antigen-1 (EBNA-1) associated oligoclonal bands in patients with multiple sclerosis. *Journal of the neurological sciences* **2000**, *173* (1), 32-39.
86. Vaughan, J.; Riise, T.; Rhodes, G.; Nguyen, M.-D.; Barrett-Connor, E.; Nyland, H., An Epstein Barr virus-related cross reactive autoimmune response in multiple sclerosis in Norway. *Journal of neuroimmunology* **1996**, *69* (1), 95-102.
87. Pender, M. P., Infection of autoreactive B lymphocytes with EBV, causing chronic autoimmune diseases. *Trends in immunology* **2003**, *24* (11), 584-588.
88. Höllsberg, P.; Hansen, H.; Haahr, S., Altered CD8+ T cell responses to selected Epstein-Barr virus immunodominant epitopes in patients with multiple sclerosis. *Clinical & Experimental Immunology* **2003**, *132* (1), 137-143.
89. Holmøy, T.; Kvale, E. Ø.; Vartdal, F., Cerebrospinal fluid CD4+ T cells from a multiple sclerosis patient cross-recognize Epstein-Barr virus and myelin basic protein. *Journal of neurovirology* **2004**, *10* (5), 278-283.
90. Lünemann, J. D.; Edwards, N.; Muraro, P. A.; Hayashi, S.; Cohen, J. I.; Münz, C.; Martin, R., Increased frequency and broadened specificity of latent EBV nuclear antigen-1-specific T cells in multiple sclerosis. *Brain* **2006**, *129* (6), 1493-1506.
91. Lang, H. L.; Jacobsen, H.; Ikemizu, S.; Andersson, C.; Harlos, K.; Madsen, L.; Hjorth, P.; Sondergaard, L.; Svejgaard, A.; Wucherpfennig, K., A functional and structural basis for TCR cross-reactivity in multiple sclerosis. *Nature immunology* **2002**, *3* (10), 940-943.
92. Lünemann, J. D.; Jelčić, I.; Roberts, S.; Lutterotti, A.; Tackenberg, B.; Martin, R.; Münz, C., EBNA1-specific T cells from patients with multiple sclerosis cross react with myelin antigens and co-produce IFN- γ and IL-2. *The Journal of experimental medicine* **2008**, *205* (8), 1763-1773.
93. Sestak, J. O.; Fakhari, A.; Badawi, A. H.; Siahaan, T. J.; Berkland, C., Structure, size, and solubility of antigen arrays determines efficacy in experimental autoimmune encephalomyelitis. *The AAPS journal* **2014**, *16* (6), 1185-1193.
94. Thati, S.; Kuehl, C.; Hartwell, B.; Sestak, J.; Siahaan, T.; Forrest, M. L.; Berkland, C., Routes of Administration and Dose Optimization of Soluble Antigen Arrays in Mice with Experimental Autoimmune Encephalomyelitis. *Journal of pharmaceutical sciences* **2014**.
95. Cairo, C. W.; Gestwicki, J. E.; Kanai, M.; Kiessling, L. L., Control of multivalent interactions by binding epitope density. *Journal of the American Chemical Society* **2002**, *124* (8), 1615-1619.
96. Germain, R. N., Modern concepts in immune recognition and lymphocyte activation: relevance for the development of useful vaccines. *International journal of technology assessment in health care* **1994**, *10* (01), 81-92.
97. Wülfing, C.; Sjaastad, M. D.; Davis, M. M., Visualizing the dynamics of T cell activation: intracellular adhesion molecule 1 migrates rapidly to the T cell/B cell interface and acts to sustain calcium levels. *Proceedings of the National Academy of Sciences* **1998**, *95* (11), 6302-6307.

98. Gestwicki, J. E.; Strong, L. E.; Kiessling, L. L., Tuning chemotactic responses with synthetic multivalent ligands. *Chemistry & biology* **2000**, *7* (8), 583-591.
99. Murray, J. S.; Oney, S.; Page, J. E.; Kratochvil-Stava, A.; Hu, Y.; Makagiarsar, I. T.; Brown, J. C.; Kobayashi, N.; Siahaan, T. J., Suppression of type 1 diabetes in NOD mice by bifunctional peptide inhibitor: modulation of the immunological synapse formation. *Chemical biology & drug design* **2007**, *70* (3), 227-236.
100. Dal Porto, J. M.; Gauld, S. B.; Merrell, K. T.; Mills, D.; Pugh-Bernard, A. E.; Cambier, J., B cell antigen receptor signaling 101. *Molecular immunology* **2004**, *41* (6), 599-613.
101. Gold, M. R., To make antibodies or not: signaling by the B-cell antigen receptor. *Trends in pharmacological sciences* **2002**, *23* (7), 316-324.

**Chapter IV: Multivalent Antigen Arrays Exhibit High
Avidity Binding and Modulation of B Cell Receptor-
Mediated Signaling to Drive Efficacy Against Experimental
Autoimmune Encephalomyelitis**

1. Introduction

Autoimmune diseases such as multiple sclerosis (MS) are typified by a breakdown of healthy immune regulation and subsequent misrecognition of self for non-self.^{1,2} The autoimmune breakdown in MS is largely propagated by autoreactive T and/or B cell clonal expansion and attack against myelin sheath autoantigens, leading to demyelination and neurodegeneration.³⁻⁶ Activation of naïve T cells against autoantigen requires two signals from an antigen presenting cell (APC): (1) primary antigenic signal delivered through the major histocompatibility complex (MHC) on the APC to the T cell receptor (TCR) on the T cell, and (2) secondary costimulatory signal (i.e., CD80/CD86) delivered to the conjugate receptor (i.e., CD28) on the T cell.⁷⁻¹⁵ B cells, as professional APCs that possess antigen specificity and immunological memory, play a particularly pivotal role in immune regulation.¹⁶⁻¹⁸ Indeed, loss of B cell tolerance has been implicated in numerous autoimmune diseases.¹⁹⁻²¹ B cell autoimmune therapies have been successful in the clinic (i.e., rituximab), but general B cell depletion or inactivation may induce global immunosuppression, may trigger adverse side effects, and may suffer from limited efficacy.²²⁻²⁴ Development of antigen-specific immunotherapy (ASIT) that targets and silences autoreactive B cells in a selective manner would address an important need for safer and more effective treatment.²⁵⁻²⁷

Modulation of B cells in a direct, antigen-specific manner requires targeting of the B cell receptor (BCR).¹⁸ Antigen binding to the BCR can trigger receptor clustering and antigen-specific B cell activation.²⁸⁻³² However, continuous antigen binding and occupation of the BCR in the absence of secondary costimulatory signals results in B cell anergy, or a state of antigen unresponsiveness, that is marked by reduced calcium signaling and down-regulation of costimulatory markers such as CD80/CD86.^{27, 33-35} Similarly, costimulatory signal presentation

by APCs is essential for autoreactive T cell activation; reception of the primary antigenic signal in the absence of secondary costimulatory signal leads to T cell anergy.^{15, 25, 26, 36} Induction of B cell anergy can therefore have a two-fold therapeutic effect by inducing (1) an effector B cell population that is not responsive to autoantigen and (2) B cells with reduced APC capacity. Thus, a promising avenue for modulating the immune response in an antigen specific manner is to induce these B cell phenotypes through BCR engagement.

Multivalent linear polymers are especially adept at engaging cell surface receptors such as the BCR.^{30, 37-43} We previously reported on multivalent soluble antigen arrays (SAgA_{PLP:LABL}) consisting of a linear hyaluronic acid (HA) polymer co-grafted with myelin autoantigen peptide (proteolipid protein peptide, PLP₁₃₉₋₁₅₁) and intracellular adhesion molecule-1 (ICAM-1) inhibitor peptide derived from leukocyte function associated antigen-1 (LFA-1), known as LABL.⁴⁴⁻⁵⁰ SAgA_{PLP:LABL} exhibited antigen-specific binding with B cells, targeted the BCR, and dampened BCR-mediated signaling.⁴⁴ Treatment with SAgA_{PLP:LABL} *in vivo* significantly alleviated experimental autoimmune encephalomyelitis (EAE), a murine model of relapsing-remitting multiple sclerosis.⁴⁶⁻⁵⁰ Here, we have developed a new version of the SAgA molecule, termed ‘click SAgA’ (cSAgA_{PLP:LABL}), using click conjugation rather than hydrolyzable grafting of multivalent PLP and LABL peptides to HA using a hydrolyzable oxime bond. We explore whether this non-hydrolyzable conjugation chemistry will improve B cell engagement and modulation of BCR-mediated signaling, and if *in vivo* efficacy is correspondingly improved.

B cell binding, signaling, and therapeutic efficacy in EAE were compared between SAgA_{PLP:LABL} (oxime conjugation chemistry) and cSAgA_{PLP:LABL} (‘click’ conjugation chemistry) through a combination of *in vitro* and *in vivo* studies. Binding avidity was evaluated in immortalized human Raji B cells as a model APC system using flow cytometry binding assays

developed previously.⁴⁴ Modulation of BCR-mediated signaling was assessed using flow cytometry calcium flux assays. Engagement and organization of BCR on the cell surface was observed through real-time fluorescence microscopy. Lastly, *in vivo* efficacy was compared across various doses in the EAE model.

2. Materials and Methods

2.1 Materials

Hyaluronic acid (HA) sodium salt (MW 16 kDa) was purchased from Lifecore Biomedical (Chaska, MN). Aminoxy-LABL (AoLABL, Aoa-itDGEATDSG-OH), aminoxy-PLP (AoPLP, Aoa-HSLGKWLGHDPKF-OH), and PLP (NH₂-HSLGKWLGHDPKF-OH) peptides were purchased from PolyPeptide Laboratories (San Diego, CA). 11-azido-3,6,9-trioxaundecan-1-amine (NH₂-PEG₃-N₃), N-hydroxysuccinimide, N-(3-dimethylaminopropyl)-N'-ethylcarbodiimide hydrochloride (EDC), 2-(N-morpholino)ethane-sulfonic acid sodium salt (MES), tris(3-hydroxypropyltriazolylmethyl)amine, and sodium ascorbate (NaAsc) were purchased from Sigma-Aldrich (St. Louis, MO) and used as received without further purification. Copper(II) sulfate pentahydrate (CuSO₄ • 5H₂O) was purchased from Acros Organics (Geel, Belgium). Alkyne-functionalized peptides bearing an N-terminal 4-pentynoic acid (homopropargyl, hp) modification were originally synthesized in our laboratory via solid phase peptide synthesis, but larger quantities of both hpPLP₁₃₉₋₁₅₁ and hpLABL peptides were obtained from Biomatik USA, LLC (Wilmington, DE). Incomplete Freund's adjuvant (IFA) and killed *Mycobacterium tuberculosis* strain H37RA were purchased from Difco (Sparks, MD). Pertussis toxin was purchased from List Biological Laboratories (Campbell, CA). Fluorescein isothiocyanate (FITC) and Fluo-4 AM calcium indicator were purchased from Thermo Fisher

Scientific (Waltham, MA). Immortalized human Raji B cells were purchased from American Type Culture Collection (ATCC, Manassas, VA). AffiniPure F(ab')₂ fragment goat anti-human IgM and AlexaFluor 647 AffiniPure F(ab')₂ fragment goat anti-human IgM were purchased from Jackson ImmunoResearch Laboratories (West Grove, PA). All other chemicals and reagents were analytical grade and used as received.

2.2 SAgA Synthesis and FITC Labeling

To synthesize SAgAs, HA was grafted with aminooxy peptides AoPLP and/or AoLABL as previously described to make HA_{PLP} (HA and AoPLP), HA_{LABL} (HA and AoLABL), and SAgA_{PLP:LABL} (HA, AoPLP, and AoLABL).⁴⁷ HA was dissolved (2 mg/ml) in a 20mM acetate buffer at pH 5.5, then combined with respective peptide(s) to achieve a target conjugation efficiency per peptide of 25% (or approximately 10 of each peptide per fHA backbone). Solution pH was readjusted to pH 5.5 and stirred at 400 rpm for 24 hours. Samples were dialyzed in d.d. H₂O (100X volume) to remove free peptides using 6000-8000 MWCO regenerated cellulose dialysis tubing over 24 hours with a total of 4 washes, then frozen and lyophilized.

To synthesize FITC-labeled SAgAs (fSAgAs), HA (16 kDa) was first reacted with FITC to make labeled HA-FITC (fHA).⁵¹ HA was gently dissolved in d.d. H₂O (5 mg/ml), then combined with an equal volume of DMSO containing sodium bicarbonate (2.5 mg/ml), dibutyltin dilaurate (3.96 mM), and FITC (6 mg/ml). The reaction mixture was heated in an oil bath at 50°C for 30 minutes while stirring at 70 rpm, then quenched by drop-wise addition to cold ethanol (17.5X volume). Dialysis took place in d.d. H₂O (100X volume) to remove free FITC using 3500 MWCO regenerated cellulose dialysis tubing (Spectrum Laboratories, Rancho Dominguez, CA), rinsing every 6-12 hours for a total of six washes. The fHA solution was then frozen and lyophilized. Peptide conjugation with fHA was performed as detailed above to make

fHA_{PLP}, fHA_{LABL}, and fSAgA_{PLP:LABL}. All fHA synthesis and subsequent handling was performed under protection from light.

2.3 SAgA and FITC-SAgA Analytical Characterization

Peptide conjugation of each sample was determined through gradient reverse-phase analytical high-performance liquid chromatography (RP-HPLC) (Waters Corp., Milford, MA) on a C18 analytical column (Higgins Analytical, Proto200, 5 μm , 200 \AA , 250 x 4.6 mm², Mountain View, CA) following cleavage of peptides in 0.1N HCl. Samples were compared to standard curves of AoPLP and AoLABL to determine peptide content. A gradient method using aqueous mobile phase A (94.9% d.d. H₂O, 5% acetonitrile, 0.1% trifluoroacetic acid (TFA)) and organic mobile phase B (99.9% acetonitrile, 0.1% TFA) was used to analyze samples. Samples were detected at 220 nm.

Relative FITC fluorescence of labeled samples was determined spectrofluorometrically on a fluorescent plate reader (SpectraMax M5e, Molecular Devices, Sunnyvale, CA). A fluorescence calibration curve was generated for each sample ranging from 0 to 0.5 mg/ml, and the relative fluorescence intensity (f) was determined in the linear region of the calibration curve at 0.4 μM relative to fHA ($f_{\text{HA}}=1$). The relative fluorescence intensity of each test article was used to normalize flow cytometry FITC fluorescence.

2.4 Click-conjugated ‘cSAgA’ Synthesis and PennGreen Labeling

2.4.1 Synthesis of HA-N₃

Synthesis of HA-N₃ was adapted from Hu *et al* and Di Meo *et al.*^{52, 53} Sodium hyaluronate (93.9 μmol , assumed 16 kDa average MW) was added to a 250 mL round bottom flask with stir bar, followed by 100 mL of 50 mM MES buffer (pH = 4.0). The mixture was

stirred until in solution (~15 min) before EDC (23.1 mmol) was added neat, then N-hydroxysuccinimide (18.8 mmol) added neat. The mixture was stirred for 5 min before H₂N-PEG₃-N₃ (4.51 mmol) in 20 mL MES buffer was added. The solution was then stirred for 24 hr at room temperature before being dialyzed in 6-8 kDa cutoff dialysis tubing against 4.5 L of 1.0 M NaCl solution for 24 hr, then 4.5 L of deionized water (4 x 12 hr). The volume in the bag was then transferred to vials, slow-frozen, and lyophilized to yield a white powder. Yield: 1.605 g (95.0%). (Refer to Scheme 1)

2.4.2 Synthesis of cSAgA

HA-N₃ (2 μmol, assumed 20 kDa average MW) was added as a 50 μM solution in deionized H₂O to a 250 mL round bottom flask with stir bar. Each component peptide (40 μmol) was then added as a ~3 μM solution in deionized H₂O, followed by a premixed solution of THPTA (70 μmol) and CuSO₄ • 5H₂O (14 μmol) in deionized water. The solution was allowed to stir for 1-2 min before a 100 μL aliquot was removed for HPLC analysis. NaAsc (300 μmol) was then added to the reaction mixture as a 100 μM solution in deionized water. The reaction was allowed to proceed for 24 hrs at 55°C. Additional 100 μL aliquots were removed throughout the course of the reaction and analyzed by RP-HPLC to determine the extent of conjugation. Once target conjugation values were achieved, the reaction solution was transferred to 6-8 kDa dialysis tubing and dialyzed against 4.5 L of 1.0 M NaCl (3 x 8 hr), then 4.5 L of deionized H₂O (5 x 8 hr). The volume in the bag was then transferred to vials, slow-frozen, and lyophilized to yield a white powder. (Refer to Scheme 2)

2.4.3 Click-conjugated cSAgA Analytical Characterization

FTIR spectra were collected on a Bruker Tensor 27 FTIR spectrometer equipped with an Attenuated Total Reflectance (ATR) cell, analyzing purified samples at ambient temperature in

the solid state, and collecting a total of 32 scans per sample. NMR spectra were collected on a Bruker Avance AVIII 500 MHz spectrometer equipped with a dual carbon/proton cryoprobe, and all samples were dissolved in 650 μ L of D₂O for analysis. RP-HPLC and SEC analysis were conducted using a Waters Alliance HPLC system equipped with either a diode array detector or dual wavelength UV/Vis detector. For the quantitative determination of peptide conjugation by RP-HPLC, the following equation was used:

$$N_{con} = \left[\left(\frac{n_{pep}}{n_{HA}} \right) \left(\frac{V_{pre} - V_{sam}}{V_{pre}} \right) \right] \left(1 - \frac{PA_t}{PA_{start}} \right) \quad \text{Equation 1}$$

where N_{con} = number of conjugated peptides per backbone, n_{pep} = moles of peptide used in reaction, n_{HA} = moles of HA-N₃ used in reaction, V_{pre} = total reaction volume before NaAsc is added, V_{sam} = volume of “pre-NaAsc” sample removed from reaction mixture, PA_t = measured peak area of peptide at time t , PA_{start} = measured peak area of free peptide before NaAsc is added to the reaction. General chromatographic conditions employed a Waters XBridge C₄, 3.5 μ m, 300 Å stationary phase under ion pairing (0.05% TFA in H₂O and MeCN) mobile phase conditions, utilizing a linear elution gradient (5-60%) with detection at 214 nm.

2.5 Cell Culture

Raji B cells (human B lymphocytes, ATCC) were cultured in RPMI-1640 supplemented with L-Glutamine, 10% fetal bovine serum (FBS), and 1% penicillin/streptomycin (P/S) at 37°C and 5% CO₂. Cell assays were consistently performed after cells reached confluency (~2 weeks) and following no more than 8-10 passages, per ATCC guidelines.

2.6 Flow Cytometry Binding Assay

Association binding studies were performed by flow cytometry (MoFlo XDP Cell Sorter, Beckman Coulter Inc., Brea, CA), as previously reported.⁴⁴ Cell nuclei were stained with

Hoechst and propidium iodide (PI) was used as a dead cell indicator; data acquisition was triggered off the Hoechst signal. Cell samples were warmed to 37°C for 2 minutes prior to the flow cytometry run. Fluorescence was excited using 488, 405, and 640 nm lasers and was collected using 529/28, 457/40, and 670/30 bandpass emission filters.

To observe maximum steady state binding, cells were mixed with the treatment to achieve a final concentration of 1×10^6 cells/ml immediately before injecting on the flow cytometer. Sample concentration was determined from preliminary saturation studies.⁴⁴ Samples were added at an equimolar PLP dose (353.18 μ M PLP for fHA_{PLP} and fSAgA_{PLP:LABEL}, or 353.18 μ M LABEL for fHA_{LABEL}) and fHA was dosed at 39.19 μ M (the HA molar equivalent to a 353.18 μ M PLP dose of fSAgA_{PLP:LABEL}) to mimic animal studies. The sample was allowed to run until maximum steady state was established.

Flow cytometry binding data was first gated to remove doublets, dead cells, and debris using Kaluza Flow Analysis software (Beckman Coulter, Inc., Brea, CA) (Supplemental Figure 1). Additional data processing was performed using KNIME software (Konstanz Information Miner, KNIME, Zurich, Switzerland). Nonlinear regression and additional statistical analysis was performed using GraphPad Prism (GraphPad Software, Inc., La Jolla, CA).

2.7 Calcium Flux Signaling Assay

Raji B cells were loaded with 5 μ M Fluo-4 AM for 30 minutes at room temperature in PBS, then kept on ice in HBSS (Hanks Balanced Salt Solution) containing 1.3 mM Ca²⁺ and 0.9 mM Mg²⁺ before analysis. Cells were run through a BD FACSFusion cytometer and fluorescence was monitored in the 530/30 channel. After baseline quantification for ~30 seconds, crosslinking goat anti-human IgM (Jackson ImmunoResearch) was added at 20 μ g/ml to

stimulate the cells. Changes in Fluo-4 fluorescence were measured for 1 minute to establish an anti-IgM stimulated baseline, followed by addition of SAgA treatment (dosed at 353.18 μ M PLP, same concentration used in binding studies) to determine the effect on IgM-stimulated signaling. Data was acquired for an additional 3 minutes until steady state was established. To measure inhibition of anti-IgM stimulation, cSAgA_{PLP:LABEL} was added to cells prior to anti-IgM stimulation. KNIME was used to process and plot the kinetic data, while Kaluza and GraphPad Prism were used for the remaining analysis.

2.8 Fluorescence Microscopy

Live cell imaging of fcSAgA binding and surface IgM clustering was observed under fluorescence microscopy (Olympus IX81 Inverted Epifluorescence Microscope) using the same concentrations from flow cytometry association binding experiments. CellASIC ONIX M04S Microfluidics Switching Plates and Microfluidics Platform (EMD Millipore, Billerica, MA) were utilized for controlled perfusion of fluorescent samples and media with cells during real-time imaging. Raji B cells were stained with Hoechst and mixed with AlexaFluor 647 goat anti-human IgM (Jackson ImmunoResearch) at 20 μ g/ml to stimulate the cells and label surface IgM, then loaded into the imaging chamber. fcSAgA was perfused into the chamber for 10 minutes (1 psi for 5 minutes, 0.25 psi for 5 minutes) to allow binding with cells, followed by gentle media perfusion (0.25 psi for 5 minutes) to rinse unbound fcSAgA, followed by immediate image capture. Images were analyzed using Slidebook 5.5 (Intelligent Imaging Innovations, Inc., Denver, CO).

2.9 Clinical EAE Study in Mice

Animal studies were carried out with 4-6 week old SJL/J (H-2) female mice purchased from Envigo Laboratories (Indianapolis, IN). Mice were housed under specified, pathogen-free

conditions at The University of Kansas and all experiments were approved by the University's Institutional Animal Care and Use Committee. Complete Freund's adjuvant (CFA) was made by combining IFA and killed *M. tuberculosis* strain H37RA at a final concentration of 4 mg/ml. Animals were induced with experimental autoimmune encephalomyelitis (EAE), the PLP-specific mouse model of relapsing-remitting MS, on day 0 of the study. Immunization was accomplished using a 0.2 ml emulsion containing 200 µg PLP₁₃₉₋₁₅₁ peptide, plus equal volumes of PBS and CFA. The emulsion was administered subcutaneously (s.c.) as a total of four 50 µl injections, located above each shoulder and each hind flank. Pertussis toxin (100 ng in 100 µl) was injected intraperitoneally on day 0 and day 2 post-immunization.

Treatments were administered on days 4, 7, and 10 as 100 µl subcutaneous injections at the nape of the neck (n=3-6 mice per treatment group), with the exception of one group in the dosing study that received treatments on days 4 and 7 only. Samples were administered at a dose equivalent to 50, 133, or 200 nmol PLP per 100 µl (0.5, 1.33, or 2 mM PLP, respectively). This three-day dosing schedule and dose of 200 nmol PLP were found to be efficacious in a previous SAg_{PLP:LABL} study.⁴⁹ Disease progression was evaluated by a single observer using the following clinical score system: 0, no clinical disease symptoms; 1, weakness or limpness of the tail; 2, weakness or partial paralysis of one or two hind limbs (paraparesis); 3, full paralysis of both hind limbs (paraplegia); 4, paraplegia plus weakness or paralysis of forelimbs; 5, moribund (at which point mice were euthanized). In addition to animal scoring, body weight measurements were performed daily for the 26-day duration of the EAE study.

2.10 Statistical Analysis

GraphPad Prism was used to perform statistical analysis including sigmoidal nonlinear regression, ordinary one-way or two-way analysis of variance (ANOVA), and unpaired t-test.

ANOVA was followed by Tukey's or Sidak's post-hoc test, where appropriate. The threshold for statistical significance was set to $p < 0.05$.

3. Results and Discussion

3.1 cSAgA Structural Design

Previous soluble antigen arrays studied in our research group employed a hydrolyzable linker chemistry to conjugate both PLP and LABL peptides to HA, and have been shown to significantly suppress disease severity in EAE.⁴⁴⁻⁵⁰ To evaluate the possibility that release of PLP or LABL encountered *in vivo* or *in vitro* may influence the observed efficacy of SAgA treatments, we synthesized click-SAgA (cSAgA) variants that exploit non-cleavable linker chemistry. The cSAgA multivalent arrays utilize the Copper-catalyzed Azide-Alkyne Cycloaddition (CuAAC) reaction as a stable attachment chemistry, which carries significant literature precedence with respect to application^{54, 55} and optimization^{56, 57}. In addition to bond stability, the versatility of the CuAAC reaction was a major consideration in the implementation of an alternative conjugation chemistry, as the wide range of available reaction conditions can enable improved control over valency.

3.2 cSAgA Analytical Characterization

Characterization was completed using a variety of qualitative and quantitative analytical techniques. Initial azide-functionalization was confirmed by FTIR spectroscopy, showing the presence of a characteristic azide stretching band after synthesis of HA-N₃, which disappeared following utilization of the azide moiety during conjugation (Figure 1). Quantitative analysis of peptide conjugation efficiency was conducted via RP-HPLC by measuring the decrease in peak

area of the free alkyne-containing peptide(s) after the reaction (Table 1). The CuAAC conjugation chemistry requires an active Cu^{1+} catalyst for the reaction to proceed, which is generated *in situ* through addition of the reducing agent NaAsc to an inactive Cu^{2+} in solution. Prior to this final NaAsc addition step, an aliquot of the reaction mixture is removed for HPLC analysis to establish a baseline response correlating to the stoichiometric peptide equivalents used in the reaction (Figure 2). Subsequent to the addition of NaAsc, any decrease in peak area of free alkyne-containing peptide can be attributed to conjugation. Standard curves for both peptides were linear to 110% of the nominal concentrations used in the reaction mixture (0.81 mM for hpPLP₁₃₉₋₁₅₁ and 0.71 mM for hpLABL), exhibiting R^2 values >0.99 upon linear regression analysis. Additional control experiments showed both peptides displayed $<5\%$ degradation at 37°C in H_2O over 20 hr in the absence of all other reaction components, indicating a minimal impact of peptide degradation on the accuracy of the analytical methodology. Quantitative peptide conjugation of representative test articles is provided in Table 1, showing that target conjugation efficiencies of approximately 25% per peptide were achieved in cHA_{PLP} (10 PLP), cHA_{LABL} (12 LABL), and $\text{cSAgA}_{\text{PLP:LABL}}$ (11 PLP, 9 LABL).

NMR spectroscopy was used qualitatively to confirm the existence of resonances present in both peptide samples, which carried over to the final dialyzed product. Quantitation by ^1H NMR proved challenging due to signal broadening of the increasingly heterogeneous polymeric systems, and the high molecular weight of the multivalent arrays leads to decreasing sensitivity with increasing conjugation, eventually limited by sample solubility. Figure 3 shows a representative analysis via Distortionless Enhancement by Polarization Transfer (^{13}C DEPT-135) NMR spectroscopy where CH and CH_3 resonances are out of phase with CH_2 resonances, yielding signals in the final $\text{cSAgA}_{\text{PLP:LABL}}$ compound which are both present and in the correct

phase with the free component peptides. $^1\text{H}/^{13}\text{C}$ Heteronuclear Single Quantum Coherence (HSQC) NMR experiments also showed the disappearance of the terminal alkyne resonance from the linker on each peptide, with the concomitant appearance of a broadened aromatic resonance not present in any individual component.

3.3 SAgA Analytical Characterization

SAgAs and fSAgAs were analyzed by RP-HPLC to determine molecular weight and peptide conjugation, as described previously.⁴⁷ Quantitative peptide conjugation of representative test articles is provided in Table 1, showing that target conjugation efficiencies of approximately 25% per peptide were achieved in HA_{PLP} (9 PLP), HA_{LABL} (10 LABL), and $\text{SAgA}_{\text{PLP:LABL}}$ (10 PLP, 13 LABL).

3.4 Flow Cytometry Binding Assay

A flow cytometry binding assay was used to compare the relative binding avidities of hydrolyzable fSAgA and click-conjugated fcSAgA with Raji B cells. Binding kinetics were observed during association between the fluorescently labeled polymer arrays and Raji B cells until maximum steady state (max. SS) was reached, illustrated in Figure 4A. It was previously observed that $\text{fSAgA}_{\text{PLP:LABL}}$, co-grafted with both PLP and LABL, exhibited greater binding with Raji B cells than the polymer alone (fHA) or the homopolymers grafted with only one signal (fHA_{PLP} or fHA_{LABL}).⁴⁴ A similar trend was observed with click-conjugated arrays: $\text{fcSAgA}_{\text{PLP:LABL}}$ exhibited the highest amount of binding, followed by fHA_{PLP} , while fHA exhibited the lowest amount of binding (Figure 4A). Comparison of the max. SS indicates that $\text{fcSAgA}_{\text{PLP:LABL}}$ binding was significantly greater than that of fcHA_{PLP} , $\text{fcHA}_{\text{LABL}}$, and fcHA, while fcHA_{PLP} binding was significantly greater than that of $\text{fcHA}_{\text{LABL}}$ and fcHA (Figure 4B). Thus, multivalent PLP and LABL appear to have a cooperative effect on avidity. We previously

reported that SAg_{PLP:LABL} exhibited PLP-specific binding and BCR targeting, implying that PLP may enhance B cell avidity by providing specific affinity for the BCR.⁴⁴ Meanwhile, LABL, derived from LFA-1 and specific for ICAM-1, may enhance B cell avidity by promoting cell adhesion through the LFA-1/ICAM-1 interaction.^{7, 11-13, 58-61}

Comparison of click-conjugated versus hydrolyzable compound binding revealed that both fcSAg_{PLP:LABL} and fcHA_{PLP} exhibited significantly enhanced binding compared to their hydrolyzable counterparts, fSAg_{PLP:LABL} and fHA_{PLP}, respectively (Figure 4C). Differences in kinetics and max. SS binding between fcSAg_{PLP:LABL}, fSAg_{PLP:LABL}, and fHA illustrate how avidity is altered when multivalent peptide is conjugated to HA in a hydrolyzable versus non-hydrolyzable manner (Figure 5AB). While both methods of multivalent modification resulted in significantly increased binding compared to the polymer alone, click-conjugated fcSAg_{PLP:LABL} exhibited significantly greater max. SS binding ($p < 0.001$) than hydrolyzable SAg_{PLP:LABL}. Thus, multivalent co-presentation of PLP and LABL through non-hydrolyzable modification increased the avidity of the polymer array over hydrolyzable modification. This result is supportive of literature stating that multivalent antigens exhibit superior binding avidity, higher ‘effective concentration’, and an enhanced ability to engage cell receptors compared to monovalent (or in this case, hydrolyzable) antigen.^{27, 38, 39, 41, 62}

3.5 Calcium Flux Signaling Flow Cytometry Assay

Flow cytometry calcium flux assays were used to compare the ability of SAgA and cSAgA molecules to modulate BCR-mediated signaling in Raji B cells. Signaling modulation was evaluated in Fluo-4 loaded Raji B cells prior to stimulation (Figure 5CD) and after stimulation (Figure 5EF) with crosslinking α IgM. The relative signal increase from resting

baseline (Figure 5D) or reduction from stimulated baseline (Figure 5F) was determined using mean Fluo-4 fluorescence values at steady state.

We reported previously that SAgA_{PLP:LABEL} was capable of both inhibiting and reducing IgM-stimulated signaling.⁴⁴ Here, pre-treatment with SAgA_{PLP:LABEL} prior to addition of α IgM significantly inhibited IgM-stimulated calcium signaling compared to the vehicle ($p < 0.05$) (Figure 5CD). However, pre-treatment with cSAgA_{PLP:LABEL} significantly inhibited IgM-stimulated calcium signaling to a greater extent ($p < 0.01$), largely preventing even the initial spike in calcium flux observed with SAgA_{PLP:LABEL} after α IgM addition. Similarly, addition of cSAgA_{PLP:LABEL} after α IgM stimulation caused a greater reduction in calcium signaling than SAgA_{PLP:LABEL} ($p < 0.01$) (Figure 5EF). cSAgA_{PLP:LABEL} reduced signaling by ~60% while SAgA_{PLP:LABEL} reduced signaling by ~40% relative to the vehicle control. These results indicated that click-conjugated cSAgA_{PLP:LABEL} is significantly more effective at dampening BCR-mediated signaling – both through inhibition and reduction – compared to its hydrolyzable counterpart.

Previously, we reported a significant reduction in signaling from addition of SAgA_{PLP:LABEL}, HA_{PLP}, and HA_{LABEL}, but negligible change in signaling from addition of vehicle (HBSS) or HA.⁴⁴ The click conjugates exhibited a similar trend: cSAgA_{PLP:LABEL} caused the greatest reduction in signaling while cHA caused the smallest reduction ($p < 0.05$) (Figure 6A). However, while cSAgA_{PLP:LABEL} caused a greater reduction than hydrolyzable SAgA_{PLP:LABEL}, there was not a significant difference between cHA_{PLP} vs. HA_{PLP} and cHA_{LABEL} vs. HA_{LABEL} (Figure 6B). It is also interesting to note that cHA (HA-N₃) caused a greater reduction than unmodified HA, which may be due to the presence of azide groups on the HA backbone leading to a greater degree of nonspecific binding.

3.6 Fluorescence Microscopy

Fluorescence microscopy was performed with a microfluidics platform that enabled real time observation of binding and BCR clustering on the cell surface. Previously, we observed that fSAgA_{PLP:LABL} binding induced mature receptor clustering in Raji B cells while the polymer alone did not, and concluded that LABL may contribute to the SAgA_{PLP:LABL} molecule's ability to cluster receptors.⁴⁴ Here, we observed receptor clustering following binding and also labeled IgM to monitor BCR organization on the cell surface. BCR clustering was observed in cells treated with fcHA_{LABL} (Figure 7C), fcHA_{PLP} (Figure 7D), and fcSAgA_{PLP:LABL} (Figure 7E) but not in those treated with unmodified fcHA polymer (Figure 7B). These trends echo our previous observations that multivalent polymer modified with PLP and LABL, but not unmodified HA, induced mature receptor clustering. BCR clustering in cells treated with fcSAgA_{PLP:LABL} and fcHA_{PLP} may be attributed in part to the antigen-specific binding affinity of PLP. BCR clustering in cells treated with fcHA_{LABL} may be promoted by the affinity of LABL for ICAM-1, since ICAM-1 clusters together with the BCR during signaling.^{7, 11-13, 58-61}

These observations also corroborate the calcium flux results which show that cHA_{PLP}, cHA_{LABL}, and in particular cSAgA_{PLP:LABL} reduced BCR-mediated signaling to a greater extent than cHA. Combined with previous evidence supporting BCR as a target for SAgA_{PLP:LABL} binding,⁴⁴ these results suggest that cSAgA_{PLP:LABL} engagement and subsequent clustering of the BCR may dampen signaling. Our observations are consistent with reports that continuous BCR engagement and clustering are a mechanism for inducing B cell anergy that is accompanied by reduced calcium flux signaling.^{34, 35}

3.7 Clinical EAE Studies

Therapeutic efficacy of SAgA_{PLP:LABEL} and cSAgA_{PLP:LABEL} was evaluated in mice with EAE induced with PLP₁₃₉₋₁₅₁ to model the relapsing-remitting form of MS. Disease symptoms emerged on day 10-12 with peak of disease occurring on day 13-15 before progressing to remission around day 20-25. Efficacy was measured by clinical score, weight change, and clinical score area under the curve (AUC) relative to the PBS control. AUC representation of clinical data has been reported as an informative secondary measure for overall extent of disease because it provides a cumulative measure not weighted by the scaling or time course of disease.⁶³ Statistical differences were determined by comparing treated groups with the negative PBS control.

A three-day dosing schedule with a dose equivalent to 200 nmol PLP administered on days 4, 7, and 10 was found to be efficacious in previous SAgA_{PLP:LABEL} studies.⁴⁵⁻⁵⁰ This dose and schedule was mirrored in a preliminary *in vivo* study with cSAgA_{PLP:LABEL}. It is important to note that shortly after the third administration on day 10, five out of six mice that received cSAgA_{PLP:LABEL} died from apparent anaphylaxis. Therefore, a combination of lower doses was investigated in a small-scale dosing study (Figure 8). To determine whether the total cumulative dose or the number of injections caused the negative response, a group was included with the same dose per injection (200 nmol PLP) but only administered on two days (days 4, 7). In another group, an equivalent cumulative dose was administered over three days (133 nmol PLP on days 4, 7, 10). A final group was included with a low dose of 50 nmol PLP, administered on all three days. All dosing groups significantly alleviated disease compared to the PBS control according to clinical disease score (Figure 8A) and clinical score AUC (Figure 8C). A cSAgA_{PLP:LABEL} dose of 50 nmol PLP caused a significant reduction in clinical score on the

greatest number of days (days 12-18) and exhibited the greatest reduction in clinical score AUC compared to PBS ($p < 0.001$). Therefore, a cSAgA_{PLP:LABEL} dose of 50 nmol PLP was selected for studies going forward.

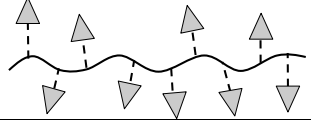
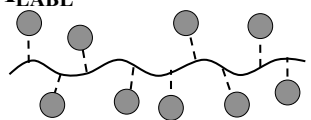
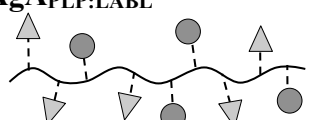
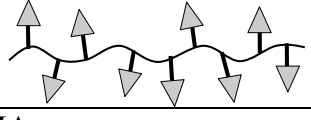
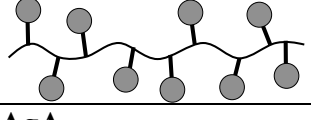
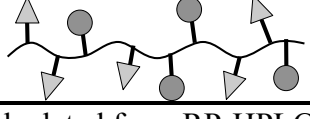
Next, *in vivo* efficacy of click-conjugated cSAgA_{PLP:LABEL} was compared to hydrolyzable SA_{gA}_{PLP:LABEL} (Figure 9). At the original therapeutic dose equivalent to 200 nmol PLP, SA_{gA}_{PLP:LABEL} significantly reduced clinical score on days 11-20 (Figure 9A) and significantly reduced total disease score AUC compared to PBS ($p < 0.0001$) (Figure 9E). At only a quarter of the dose, cSAgA_{PLP:LABEL} (50 nmol PLP) significantly reduced total clinical score AUC to an equivalent extent as SA_{gA}_{PLP:LABEL} at 200 nmol PLP (Figure 9E). Furthermore, cSAgA_{PLP:LABEL} (50 nmol PLP) significantly reduced clinical score on days 10-17 to a greater extent than SA_{gA}_{PLP:LABEL} at the 200 nmol dose (Figure 9B). In contrast, the 50 nmol dose of SA_{gA}_{PLP:LABEL} significantly reduced clinical score only on days 11 and 14 (Figure 9B), and reduced clinical score AUC to a significantly lesser extent ($p < 0.001$) than cSAgA_{PLP:LABEL} (50 nmol PLP) (Figure 9E). While SA_{gA}_{PLP:LABEL} (200 nmol PLP) significantly alleviated weight loss on days 11-22 (Figure 9C), cSAgA_{PLP:LABEL} (50 nmol PLP) significantly alleviated weight loss over a larger portion of the study, on days 11-25 (Figure 9D). In contrast, SA_{gA}_{PLP:LABEL} (50 nmol PLP) did not alleviate weight loss on any day of the study (Figure 9D).

cSAgA_{PLP:LABEL} achieved equivalent *in vivo* efficacy as SA_{gA}_{PLP:LABEL} at one quarter of the antigen dose. Thus, compared to hydrolyzable multivalent modification, non-hydrolyzable click conjugation rendered greater therapeutic efficacy.

4. Conclusions

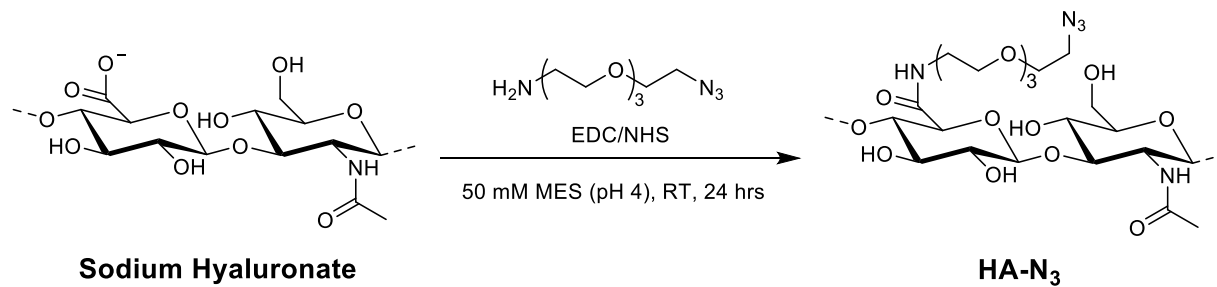
Here we present the development of click-conjugated multivalent soluble antigen arrays and their evaluation *in vitro* and *in vivo* as therapeutic agents in a murine model of MS. Hydrolyzable SAg_{PLP:LABL}, which we have studied extensively,⁴⁴⁻⁵⁰ employs a degradable linker to co-deliver antigen (PLP) and cell adhesion inhibitor (LABL) peptides, and has been shown to significantly suppress EAE. cSAg_{PLP:LABL} is a modified version of the SAg_{PLP:LABL} molecule with multiple PLP and LABL peptides conjugated to HA using non-hydrolyzable linker chemistry (Copper-catalyzed Azide-Alkyne Cycloaddition (CuAAC)). Building upon previous work, these studies sought to establish therapeutic efficacy of cSAg_{PLP:LABL} *in vivo* while identifying a potential therapeutic mechanism by evaluating binding avidity and signaling modulation *in vitro*. Click-conjugated cSAg_{PLP:LABL} exhibited greatly enhanced binding in B cells compared to hydrolyzable SAg_{PLP:LABL}, indicating that non-hydrolyzable multivalent ligand increases the avidity of the molecule. Furthermore, cSAg_{PLP:LABL} exhibited greater capacity for reducing and inhibiting BCR-mediated signaling as compared to SAg_{PLP:LABL}. Imaging revealed that cSAg_{PLP:LABL} binding caused BCR clustering, another marker indicative of BCR engagement and signaling modulation. Lastly, cSAg_{PLP:LABL} exhibited enhanced *in vivo* efficacy against EAE, achieving equivalent efficacy as SAg_{PLP:LABL} at one quarter of the dose. Taken together, these results indicate that non-hydrolyzable conjugation increases the avidity of cSAg_{PLP:LABL}, and this enhanced binding drives *in vivo* efficacy through modulated BCR-mediated signaling.

Table 1. Peptide molar conjugation of hydrolyzable and click conjugates was determined by reverse-phase HPLC. Results are an average of triplicate injections from a single batch preparation. In the molecule schematics, dotted lines represent hydrolyzable oxime linker chemistry while solid lines represent non-hydrolyzable ‘click’ linker chemistry.

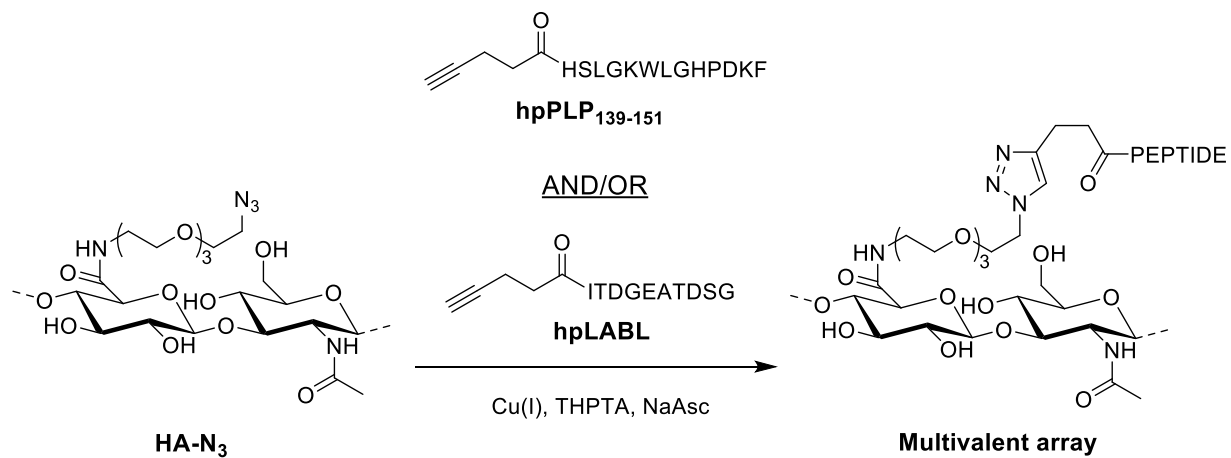
Sample	Approx. MW (kDa) ^a	Molar Ratio per Polymer ^b		% Molar Conjugation	
		PLP:HA	LABL:HA	PLP	LABL
HA_{PLP} 	30.4	9	0	21	0
HA_{LABL} 	26.0	0	10	0	24
SAgA_{PLP:LABL} 	46.3	10	13	24	31
cHA_{PLP} 	41.2	10	0	24	0
cHA_{LABL} 	37.2	0	12	0	28
cSAgA_{PLP:LABL} 	52.1	11	9	26	21

^a Calculated from RP-HPLC data. MW, molecular weight.

^b HA, hyaluronic acid; PLP, proteolipid protein peptide; LABL, inhibitor peptide derived from leukocyte function associated antigen-1



Scheme 1: Synthesis of azide-functionalized hyaluronic acid.



Scheme 2: Synthesis of cSagA multivalent arrays.

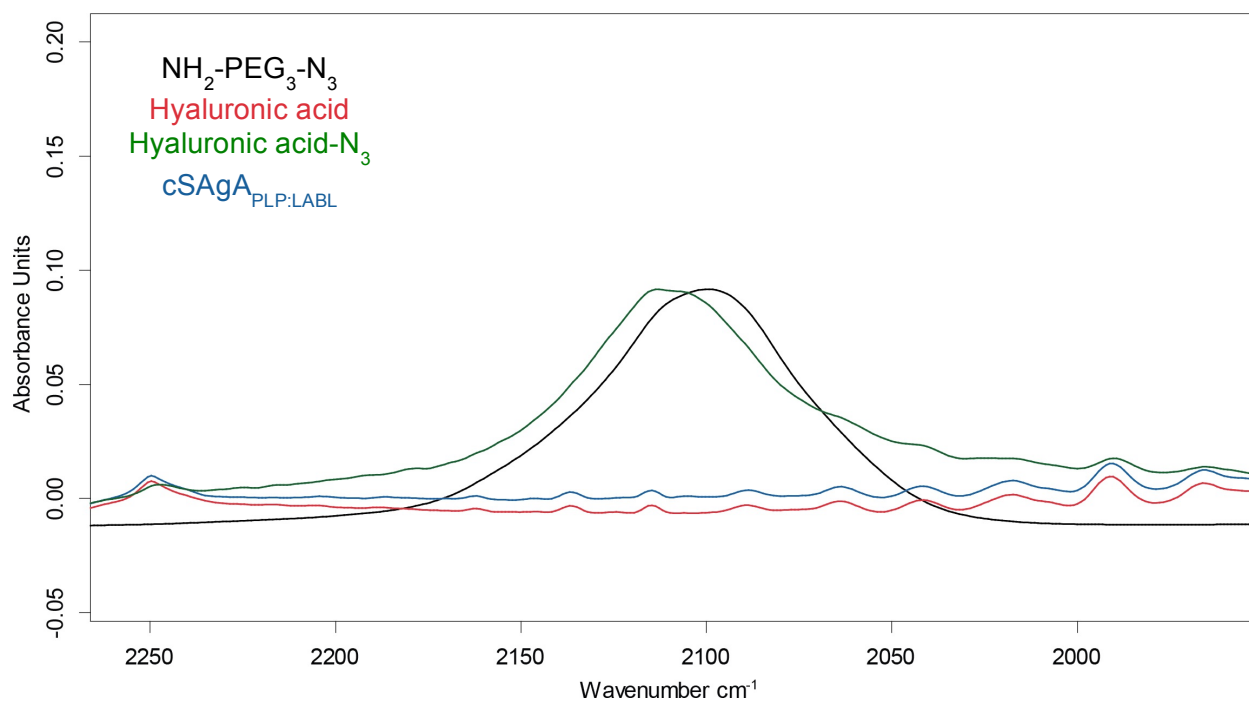


Figure 1: FTIR spectra collected after various synthetic steps.

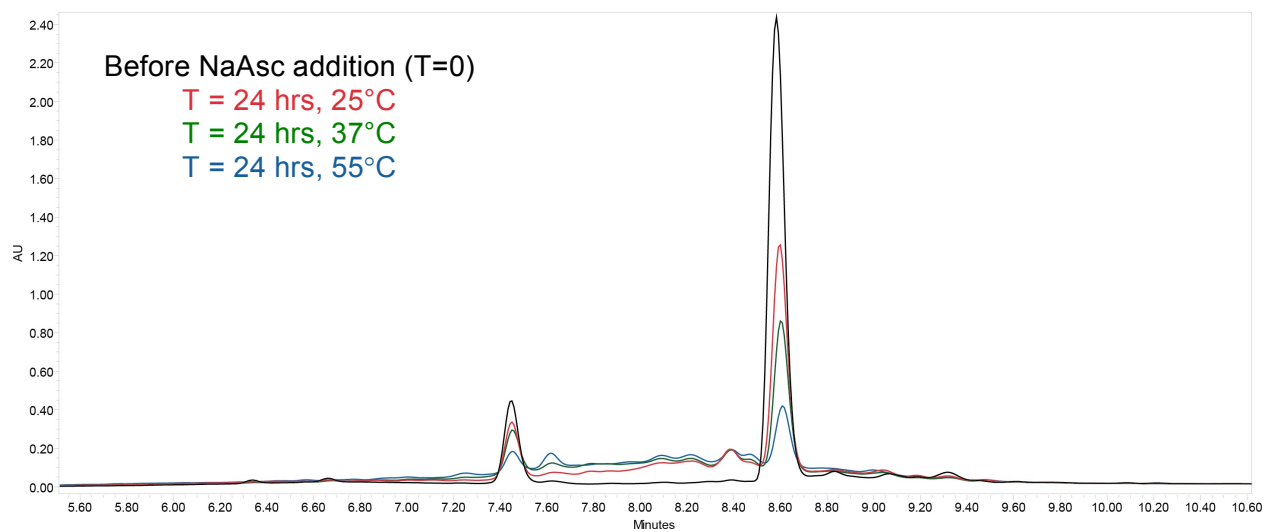


Figure 2: Representative HPLC chromatograms used to quantify the number of conjugated peptides as a function of reaction temperature. Chromatographic conditions – column: Waters XBridge C₄, 300 Å, 3.5 µm, 4.6x150 mm; Mobile Phase A: 0.05% TFA in H₂O; Mobile Phase B: 0.05% TFA in MeCN; 5-60% B gradient elution over 14 min; Detection: UV at 214 nm.

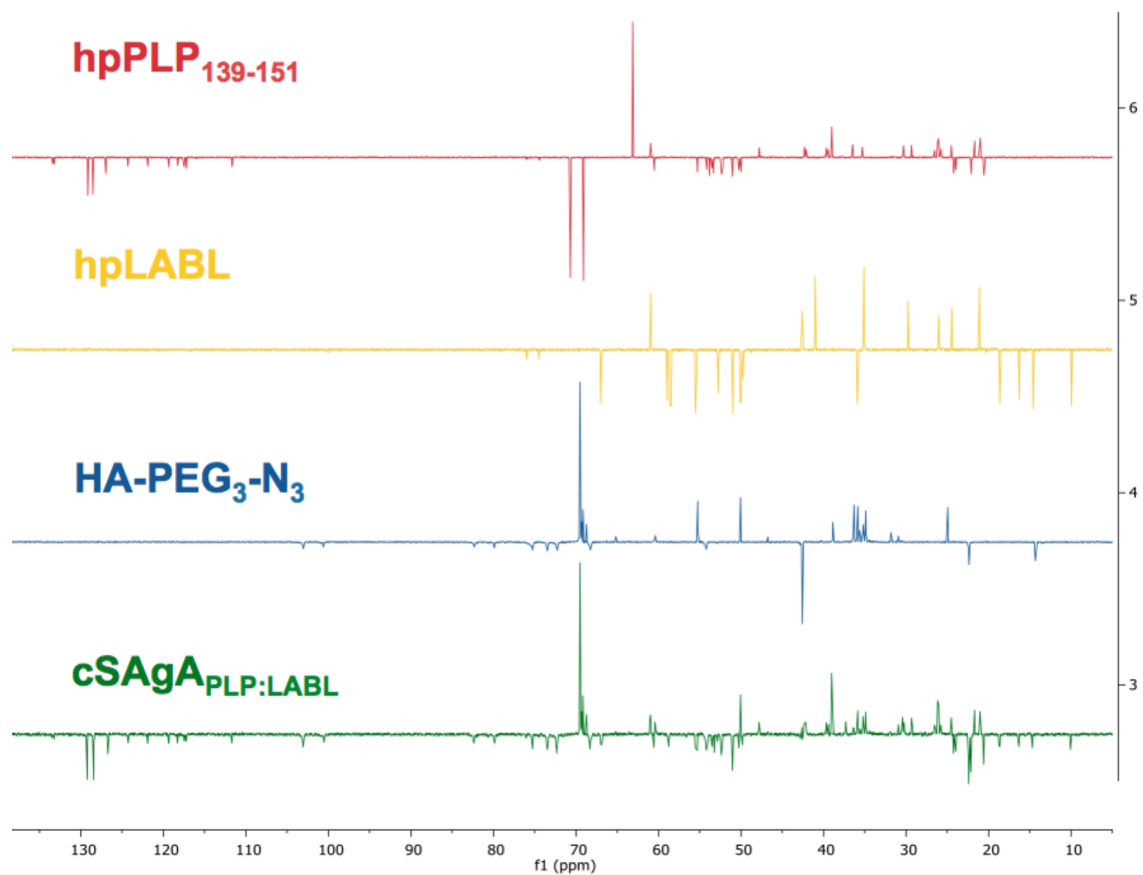


Figure 3: Qualitative confirmation of conjugation by ^{13}C DEPT-135 NMR spectroscopy, where CH_2 signals are oriented up.

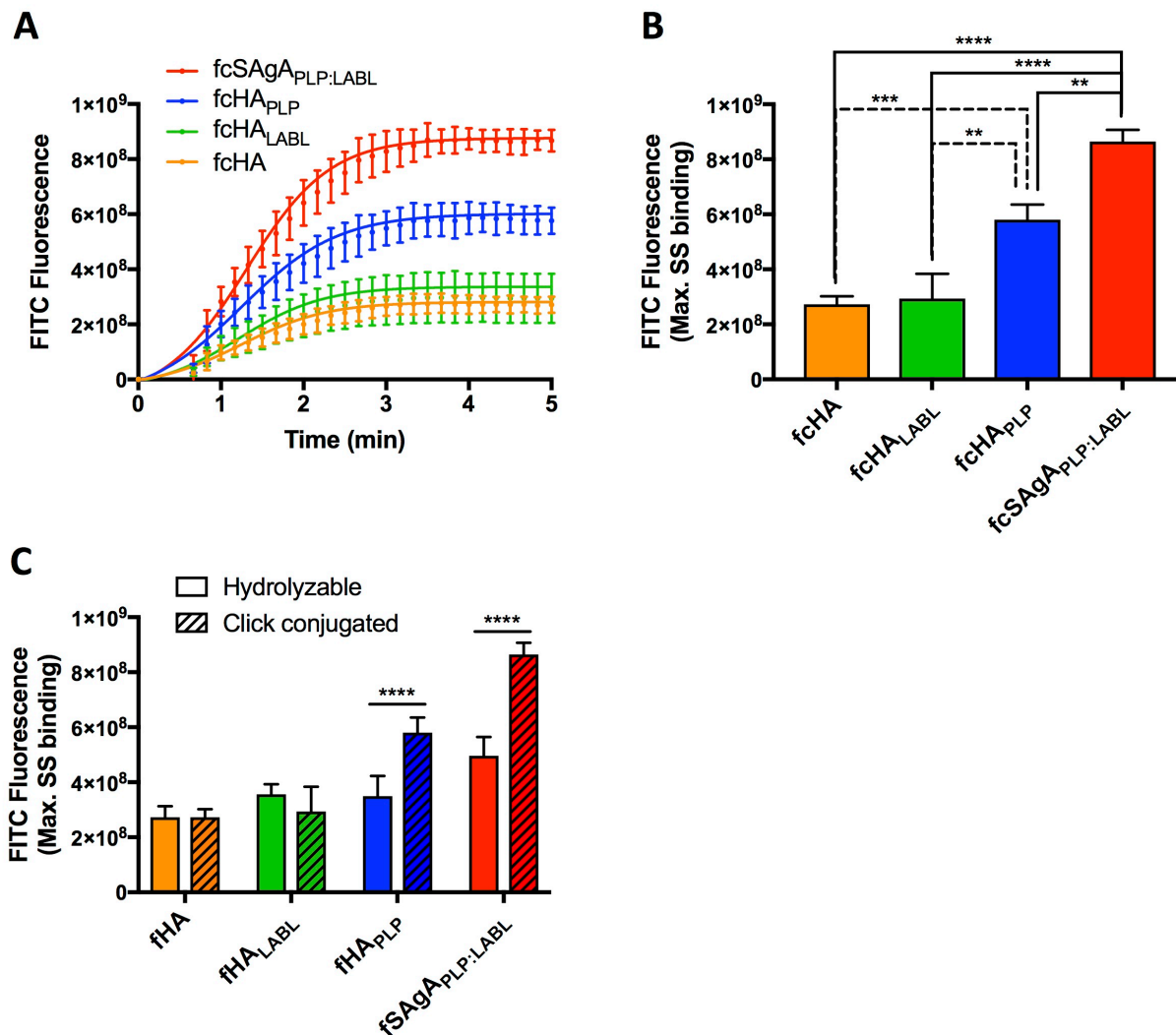


Figure 4. Binding of $fcHA$, $fcHA_{LABL}$, $fcHA_{PLP}$, and $fcSagA_{PLP:LABL}$ with Raji B cells determined by flow cytometry: **(A)** Binding kinetics showing association through steady state. **(B)** Relative binding at maximum steady state (max. SS). **(C)** Comparison of max. SS binding with hydrolyzable versus click-conjugated arrays. Statistical significance determined by ANOVA followed by Tukey's (B) or Sidak's (C) post hoc test with $p < 0.05$ and $n = 3$ ($*p < 0.05$, $**p < 0.01$, $***p < 0.001$, $****p < 0.0001$). Robust curve fitting in (A) was performed using sigmoidal nonlinear regression.

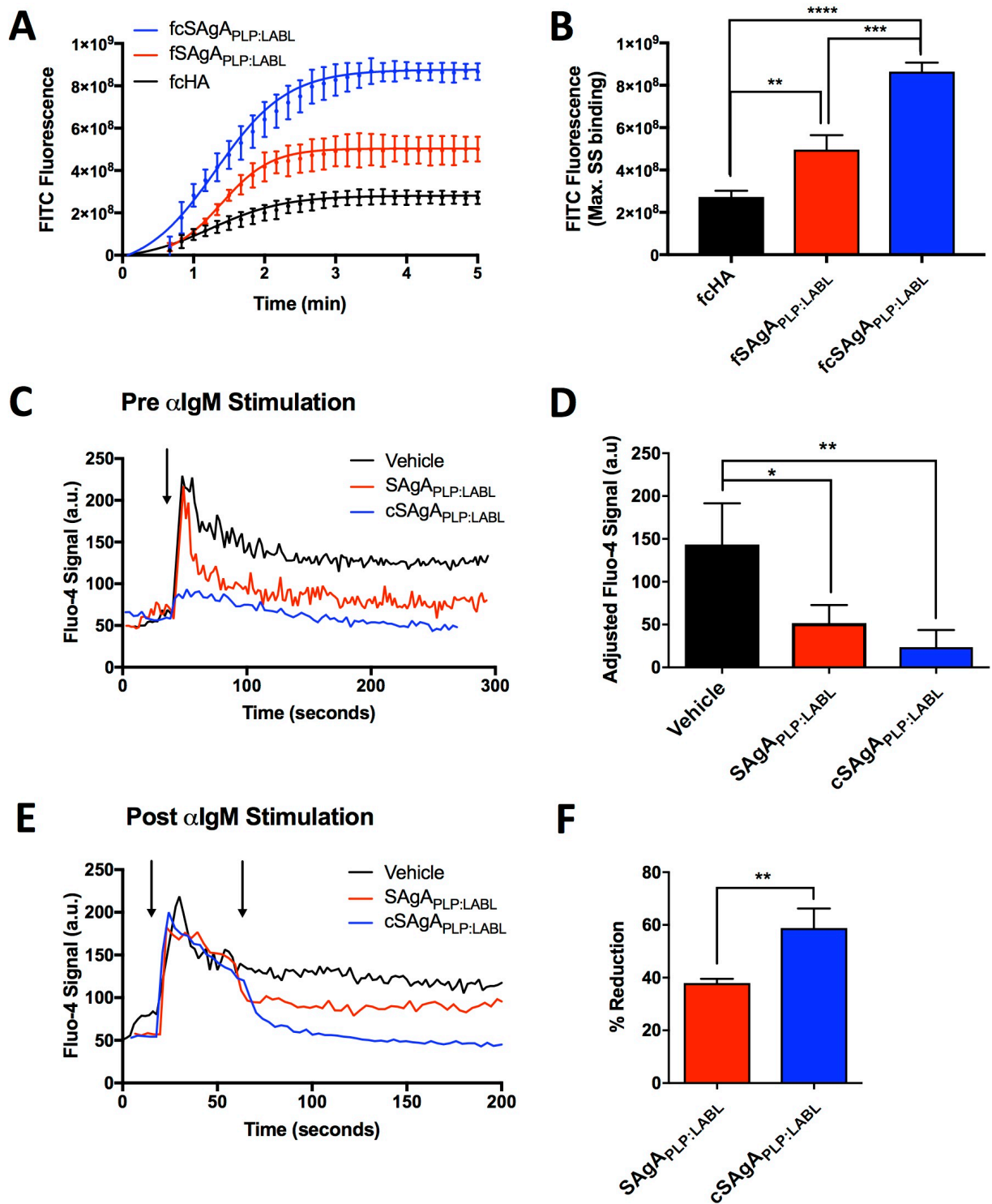


Figure 5. Comparing SAgA_{PLP:LABL} and cSAgA_{PLP:LABL} binding and IgM-stimulated (BCR-mediated) calcium flux signaling in Raji B cells through flow cytometry assays: **(A)** Binding kinetics and **(B)** maximum steady state (max. SS) binding with fSAgA_{PLP:LABL}, fcSAgA_{PLP:LABL},

and fcHA. **(C)** Calcium flux inhibition: Fluo-4 loaded cells were first pretreated with vehicle (HBSS), SAg_{PLP:LABEL}, or cSAg_{PLP:LABEL}, then stimulated with anti-IgM (α IgM, black arrow) to evaluate signaling inhibition. **(D)** Relative IgM signaling stimulation following pretreatment; baseline-adjusted values determined from mean steady state values. **(E)** Calcium flux reduction: Fluo-4 loaded cells were first stimulated with α IgM at ~30 s (black arrow), then treated with vehicle (HBSS), SAg_{PLP:LABEL}, or cSAg_{PLP:LABEL} after ~60 s (black arrow) to evaluate signaling reduction. **(F)** Percent reduction from IgM-stimulated baseline following sample addition, determined from mean steady state values. Statistical significance was determined by ANOVA followed by Tukey's post hoc test with $p < 0.05$ and $n = 3$ (* $p < 0.05$, ** $p < 0.01$, *** $p < 0.001$, **** $p < 0.0001$). Calcium flux kinetics in (C) and (D) show median Fluo-4 fluorescence values. Robust curve fitting in (A) was performed using sigmoidal nonlinear regression. Calcium flux data was pooled from three independent experiments.

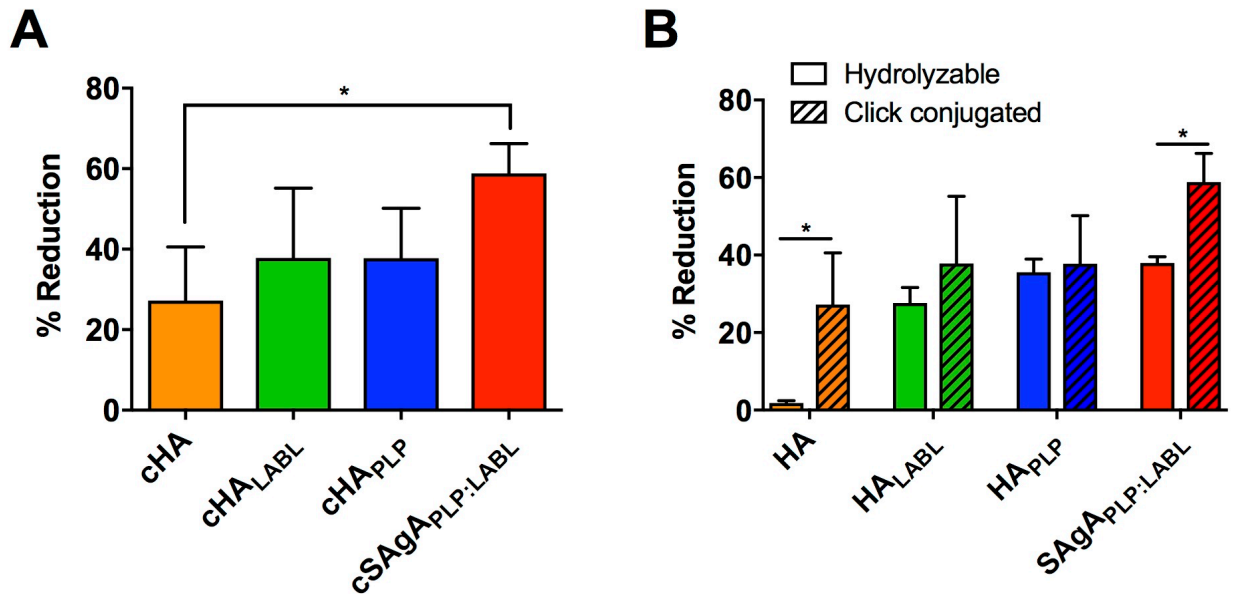


Figure 6. Reduction in IgM-stimulated (BCR-mediated) calcium flux signaling in Fluo-4 loaded Raji B cells determined by flow cytometry: **(A)** Percent reduction from α IgM-stimulated baseline following addition of cHA, cHA_{LABL}, cHA_{PLP}, or cSAgA_{PLP:LABL}, determined from mean steady state values. **(B)** Comparison of reduction in α IgM-stimulated signaling from hydrolyzable versus click-conjugated arrays. Data was pooled from three independent experiments. Statistical significance was determined by ANOVA followed by Tukey's post hoc test (A) or unpaired t-test (B) with $p < 0.05$ and $n = 3$ (* $p < 0.05$, ** $p < 0.01$, *** $p < 0.001$, **** $p < 0.0001$).

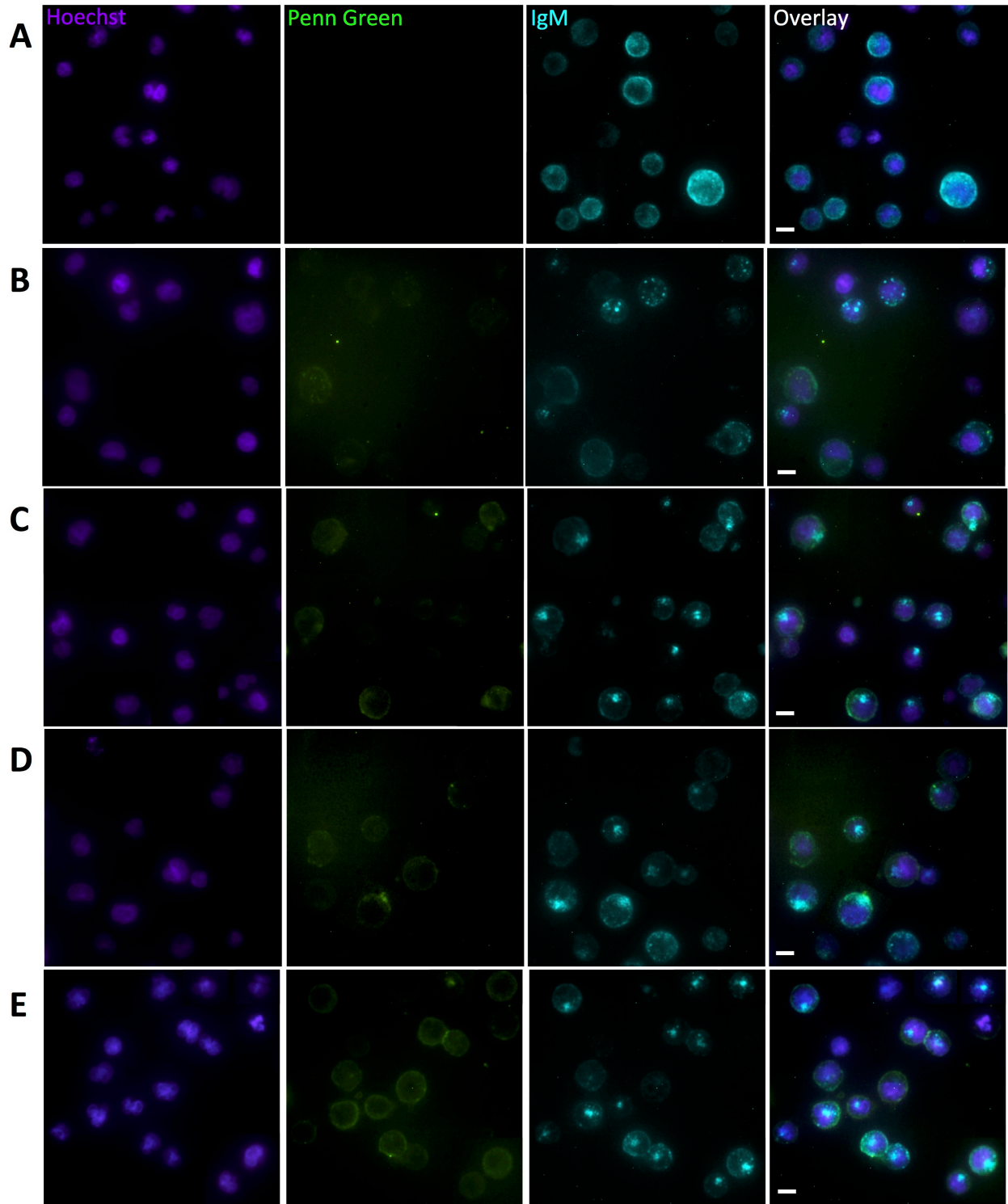


Figure 7. Fluorescence microscopy showing binding and BCR clustering in Raji B cells following perfusion of **(A)** vehicle, **(B)** fcHA, **(C)** fcHA_{LABEL}, **(D)** fcHA_{PLP}, and **(E)** fcSAgA_{PLP:LABEL}. Cell nuclei were stained with Hoechst (violet – Panel 1) and surface IgM was

stained with AlexaFluor 647-conjugated α IgM (blue – Panel 3). Penn Green-labeled polymer arrays are shown binding to the cell surface (green – Panel 2). In contrast to the diffuse IgM fluorescence in (A), highly localized punctate IgM fluorescence in (C), (D), and (E) indicates BCR clustering in cells treated with $fcHA_{\text{LABEL}}$, $fcHA_{\text{PLP}}$, and $fcSAgA_{\text{PLP:LABEL}}$. Captured using the M04S plate and CellASIC Onyx Microfluidics platform on an Olympus IX81 inverted Epifluorescence microscope. Magnification: 60X air. Scale bar equals 10 μm .

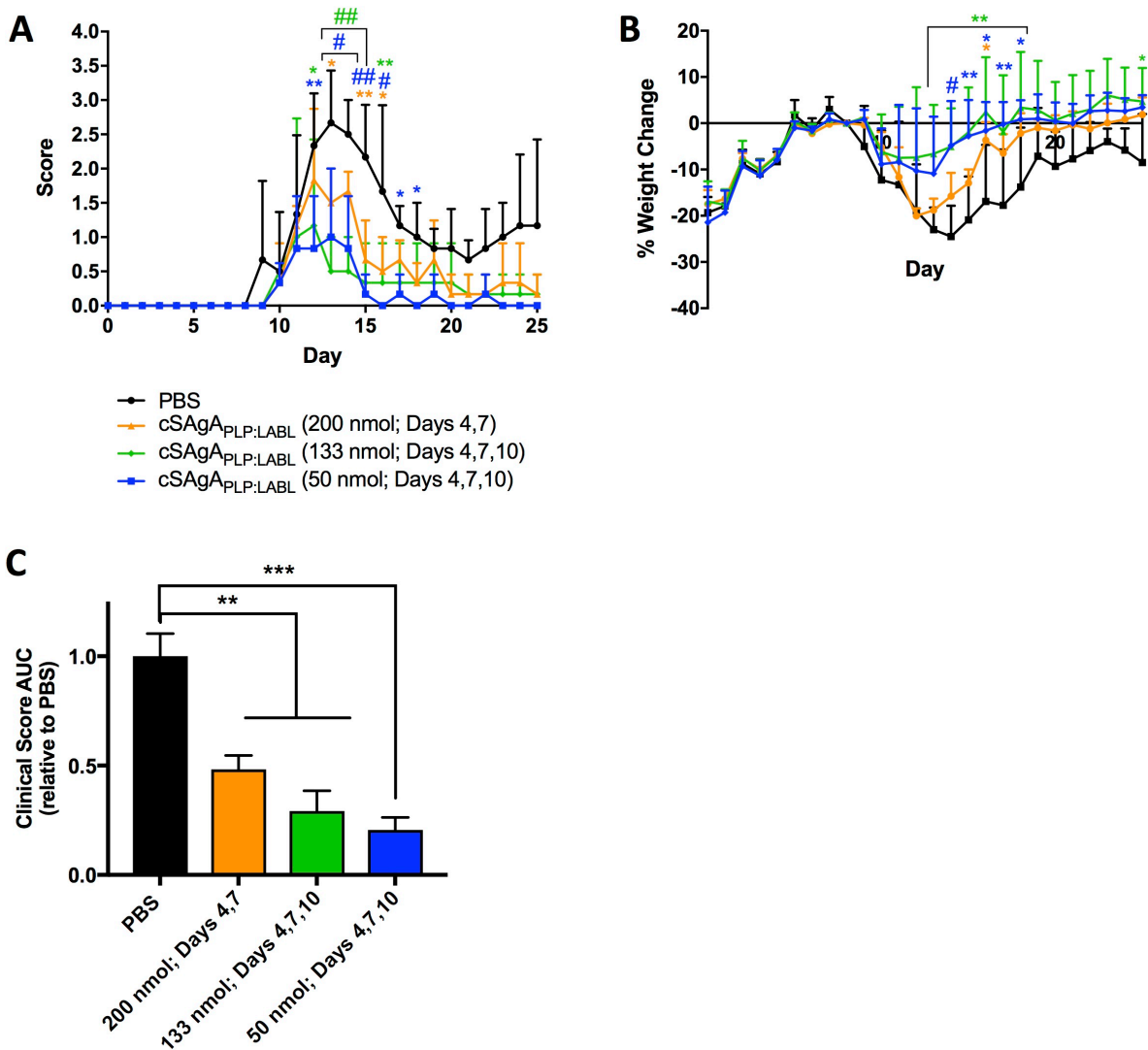


Figure 8. Clinical EAE dosing study with cSAgA_{PLP:LABEL}: cSAgA_{PLP:LABEL} was administered on days 4 and 7 at a dose equivalent to 200 nmol PLP and on days 4, 7, and 10 at a dose equivalent to 50 or 133 nmol PLP. Therapeutic efficacy evaluated by comparing (A) clinical disease score, (B) percent weight change, and (C) clinical score area under the curve (AUC). Statistical significance (compared to the negative PBS control) was determined by ANOVA followed by Tukey's post hoc test with $p < 0.05$ and $n = 3$ (* $p < 0.05$, ** $p < 0.01$, #/ $***p < 0.001$, ##/ $****p < 0.0001$).

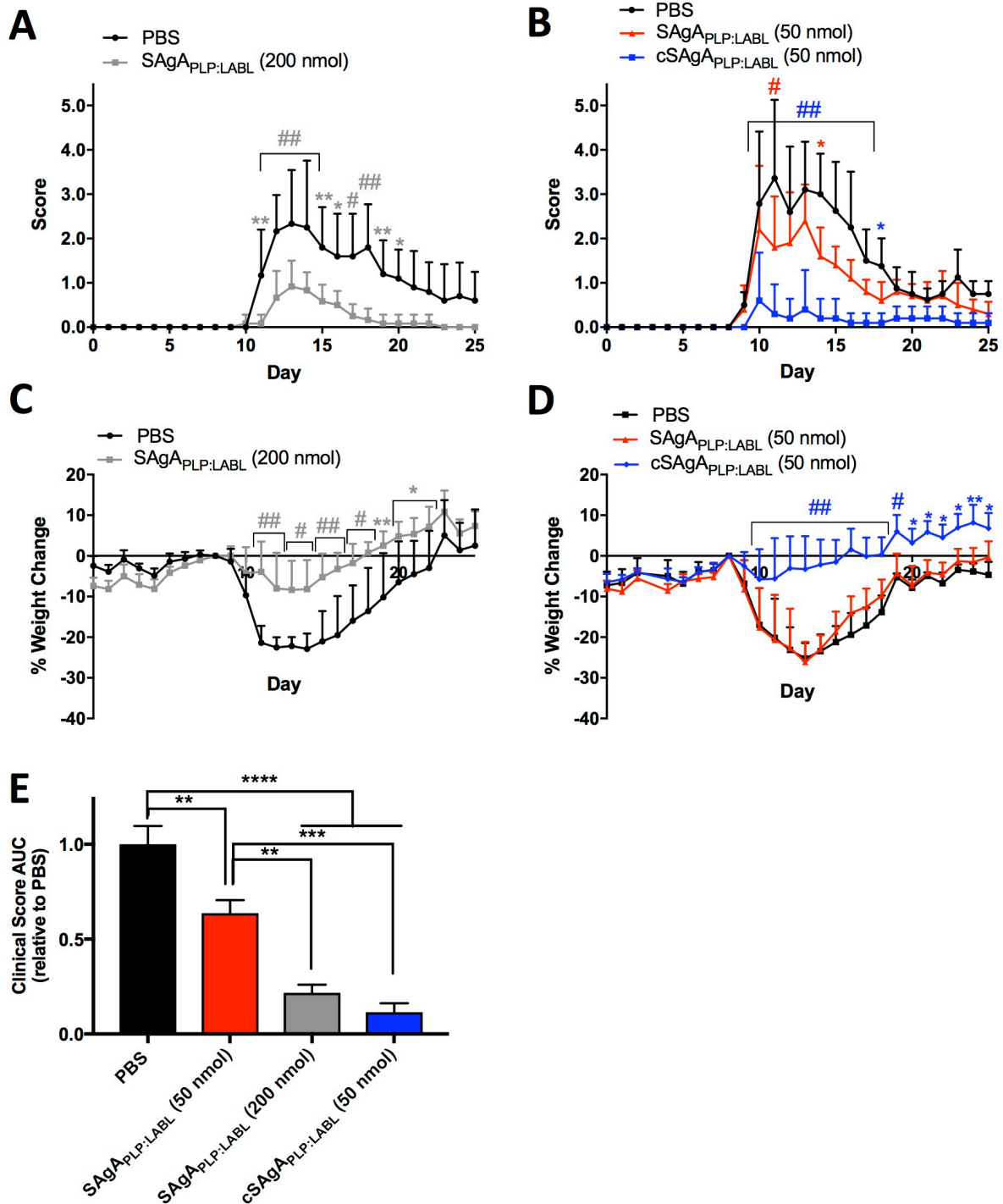
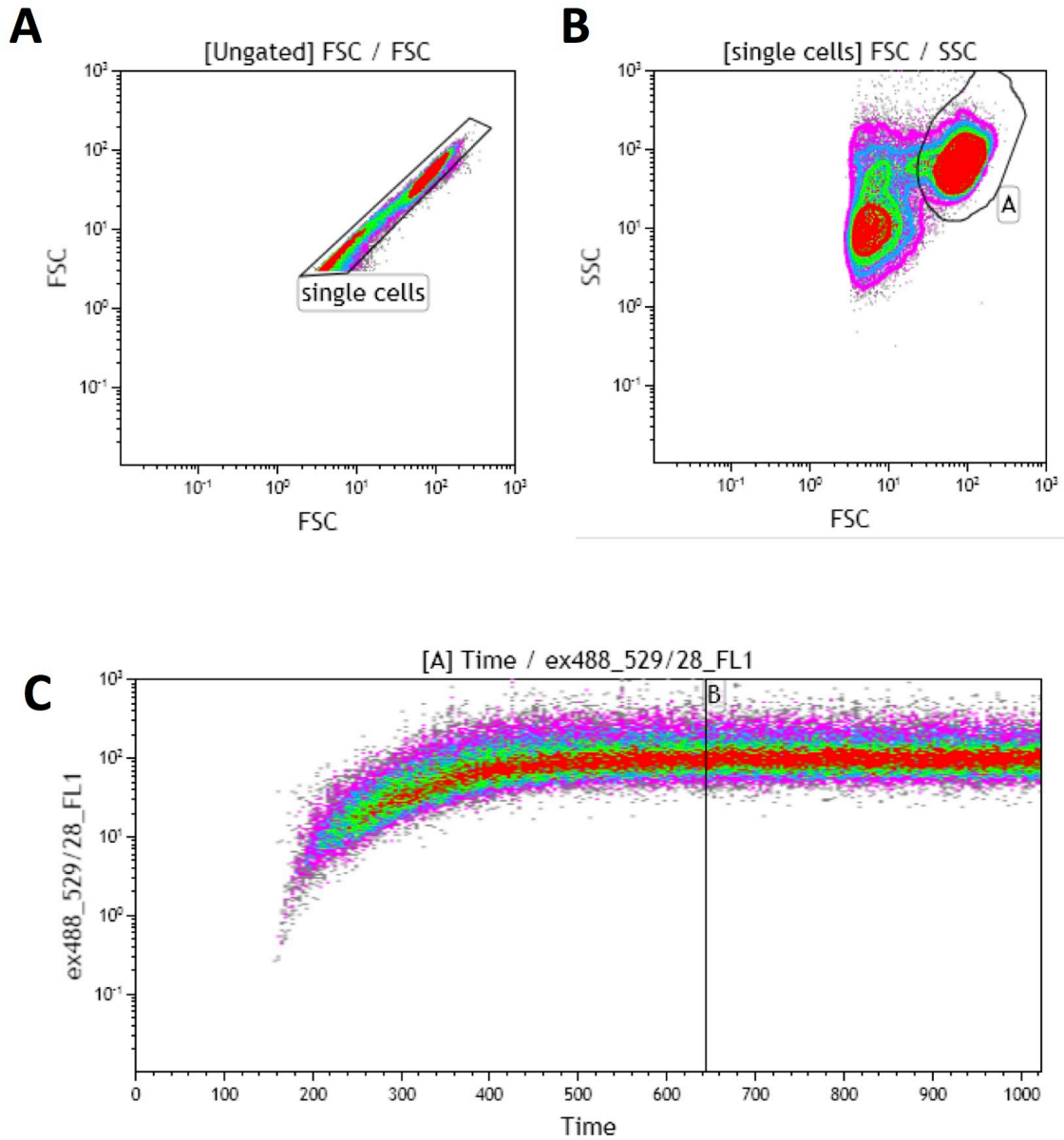


Figure 9. Comparing SAgA_{PLP:LABL} and cSAgA_{PLP:LABL} therapeutic efficacy in EAE: (A) SAgA_{PLP:LABL} (200 nmol PLP dose) clinical scores (n=6), (B) cSAgA_{PLP:LABL} versus SAgA_{PLP:LABL} (50 nmol PLP dose) clinical scores (n=5), (C) SAgA_{PLP:LABL} (200 nmol PLP dose) weight change, (D) cSAgA_{PLP:LABL} versus SAgA_{PLP:LABL} (50 nmol PLP dose) weight change, and

(E) clinical score area under the curve (AUC) relative to PBS. Statistical significance was determined by ANOVA followed by Dunnet's (A-D) or Tukey's (E) post hoc test with $p < 0.05$ (* $p < 0.05$, ** $p < 0.01$, #/** $p < 0.001$, ##/**** $p < 0.0001$).

Supplemental Information



Supplemental Figure 1. Raji B cell calcium binding gating scheme: **A)** Identify single cells and gate out doublets; **B)** Identify live cells and gate out dead cells and debris; **C)** Plot FITC vs. time and identify steady state region (shown as gate B).

References

1. Gonsette, R., Self-tolerance in multiple sclerosis. *Acta Neurologica Belgica* **2012**, *112* (2), 133-140.
2. Carson, M. J.; Doose, J. M.; Melchior, B.; Schmid, C. D.; Ploix, C. C., CNS immune privilege: hiding in plain sight. *Immunological reviews* **2006**, *213* (1), 48-65.
3. Mills, K.; Fletcher, J., T cells in multiple sclerosis and experimental autoimmune encephalomyelitis. **2010**.
4. Amor, S.; Puentes, F.; Baker, D.; Van Der Valk, P., Inflammation in neurodegenerative diseases. *Immunology* **2010**, *129* (2), 154-169.
5. Herz, J.; Zipp, F.; Siffrin, V., Neurodegeneration in autoimmune CNS inflammation. *Experimental neurology* **2010**, *225* (1), 9-17.
6. Lassmann, H., Mechanisms of inflammation induced tissue injury in multiple sclerosis. *Journal of the neurological sciences* **2008**, *274* (1), 45-47.
7. Grakoui, A.; Bromley, S. K.; Sumen, C.; Davis, M. M.; Shaw, A. S.; Allen, P. M.; Dustin, M. L., The immunological synapse: a molecular machine controlling T cell activation. *Science* **1999**, *285* (5425), 221-227.
8. Iezzi, G.; Karjalainen, K.; Lanzavecchia, A., The duration of antigenic stimulation determines the fate of naive and effector T cells. *Immunity* **1998**, *8* (1), 89-95.
9. Baxter, A. G.; Hodgkin, P. D., Activation rules: the two-signal theories of immune activation. *Nature Reviews Immunology* **2002**, *2* (6), 439-446.
10. Bromley, S. K.; Iaboni, A.; Davis, S. J.; Whitty, A.; Green, J. M.; Shaw, A. S.; Weiss, A.; Dustin, M. L., The immunological synapse and CD28-CD80 interactions. *Nature immunology* **2001**, *2* (12), 1159-1166.
11. Chen, L.; Flies, D. B., Molecular mechanisms of T cell co-stimulation and co-inhibition. *Nature Reviews Immunology* **2013**, *13* (4), 227-242.
12. Frauwirth, K. A.; Thompson, C. B., Activation and inhibition of lymphocytes by costimulation. *The Journal of clinical investigation* **2002**, *109* (109 (3)), 295-299.
13. Jun, J. E.; Goodnow, C. C., Scaffolding of antigen receptors for immunogenic versus tolerogenic signaling. *Nature immunology* **2003**, *4* (11), 1057-1064.
14. Zhang, Q.; Vignali, D. A., Co-stimulatory and co-inhibitory pathways in autoimmunity. *Immunity* **2016**, *44* (5), 1034-1051.
15. Mueller, D. L.; Jenkins, M. K.; Schwartz, R. H., Clonal expansion versus functional clonal inactivation: a costimulatory signalling pathway determines the outcome of T cell antigen receptor occupancy. *Annual review of immunology* **1989**, *7* (1), 445-480.
16. Rock, K. L.; Benacerraf, B.; Abbas, A. K., Antigen presentation by hapten-specific B lymphocytes. I. Role of surface immunoglobulin receptors. *The Journal of experimental medicine* **1984**, *160* (4), 1102-1113.
17. Constant, S. L., B lymphocytes as antigen-presenting cells for CD4+ T cell priming in vivo. *The Journal of Immunology* **1999**, *162* (10), 5695-5703.
18. Kontos, S.; Grimm, A. J.; Hubbell, J. A., Engineering antigen-specific immunological tolerance. *Current opinion in immunology* **2015**, *35*, 80-88.
19. Kinzel, S.; Weber, M. S., B Cell-Directed Therapeutics in Multiple Sclerosis: Rationale and Clinical Evidence. *CNS drugs* **2016**, 1-12.

20. Jackson, S. W.; Kolhatkar, N. S.; Rawlings, D. J., B cells take the front seat: dysregulated B cell signals orchestrate loss of tolerance and autoantibody production. *Current opinion in immunology* **2015**, *33*, 70-77.
21. Khan, W. N.; Wright, J. A.; Kleiman, E.; Boucher, J. C.; Castro, I.; Clark, E. S., B-lymphocyte tolerance and effector function in immunity and autoimmunity. *Immunologic research* **2013**, *57* (1-3), 335-353.
22. Boster, A.; Ankeny, D. P.; Racke, M. K., The potential role of B cell-targeted therapies in multiple sclerosis. *Drugs* **2010**, *70* (18), 2343-2356.
23. Oh, S.; Cudrici, C.; Ito, T.; Rus, H., B-cells and humoral immunity in multiple sclerosis. Implications for therapy. *Immunologic research* **2008**, *40* (3), 224-234.
24. Bates, D., Treatment effects of immunomodulatory therapies at different stages of multiple sclerosis in short-term trials. *Neurology* **2011**, *76* (1 Supplement 1), S14-S25.
25. Feldmann, M.; Steinman, L., Design of effective immunotherapy for human autoimmunity. *Nature* **2005**, *435* (7042), 612.
26. Miller, S. D.; Turley, D. M.; Podojil, J. R., Antigen-specific tolerance strategies for the prevention and treatment of autoimmune disease. *Nature Reviews Immunology* **2007**, *7* (9), 665.
27. Jones, D. S., Multivalent compounds for antigen-specific B cell tolerance and treatment of autoimmune diseases. *Current medicinal chemistry* **2005**, *12* (16), 1887-1904.
28. Ketchum, C.; Miller, H.; Song, W.; Upadhyaya, A., Ligand mobility regulates B cell receptor clustering and signaling activation. *Biophysical journal* **2014**, *106* (1), 26-36.
29. Batista, F. D.; Iber, D.; Neuberger, M. S., B cells acquire antigen from target cells after synapse formation. *Nature* **2001**, *411* (6836), 489-494.
30. Puffer, E. B.; Pontrello, J. K.; Hollenbeck, J. J.; Kink, J. A.; Kiessling, L. L., Activating B cell signaling with defined multivalent ligands. *ACS chemical biology* **2007**, *2* (4), 252-262.
31. Tolar, P.; Sohn, H. W.; Pierce, S. K., The initiation of antigen-induced B cell antigen receptor signaling viewed in living cells by fluorescence resonance energy transfer. *Nature immunology* **2005**, *6* (11), 1168-1176.
32. Harwood, N. E.; Batista, F. D., Early events in B cell activation. *Annual review of immunology* **2009**, *28*, 185-210.
33. Getahun, A.; O'Neill, S. K.; Cambier, J. C., Establishing anergy as a bona fide in vivo mechanism of B cell tolerance. *The Journal of Immunology* **2009**, *183* (9), 5439-5441.
34. Gauld, S. B.; Benschop, R. J.; Merrell, K. T.; Cambier, J. C., Maintenance of B cell anergy requires constant antigen receptor occupancy and signaling. *Nature immunology* **2005**, *6* (11), 1160-1167.
35. Cambier, J. C.; Gauld, S. B.; Merrell, K. T.; Vilen, B. J., B-cell anergy: from transgenic models to naturally occurring anergic B cells? *Nature Reviews Immunology* **2007**, *7* (8), 633-643.
36. Mueller, D. L., Mechanisms maintaining peripheral tolerance. *Nature immunology* **2010**, *11* (1), 21-27.
37. Cairo, C. W.; Gestwicki, J. E.; Kanai, M.; Kiessling, L. L., Control of multivalent interactions by binding epitope density. *Journal of the American Chemical Society* **2002**, *124* (8), 1615-1619.

38. Gestwicki, J. E.; Cairo, C. W.; Strong, L. E.; Oetjen, K. A.; Kiessling, L. L., Influencing receptor-ligand binding mechanisms with multivalent ligand architecture. *Journal of the American Chemical Society* **2002**, *124* (50), 14922-14933.
39. Kiessling, L. L.; Gestwicki, J. E.; Strong, L. E., Synthetic multivalent ligands in the exploration of cell-surface interactions. *Current opinion in chemical biology* **2000**, *4* (6), 696-703.
40. Hartwell, B. L.; Antunez, L.; Sullivan, B. P.; Thati, S.; Sestak, J. O.; Berkland, C., Multivalent Nanomaterials: Learning from Vaccines and Progressing to Antigen-Specific Immunotherapies. *Journal of pharmaceutical sciences* **2014**.
41. Krishnamurthy, V. M.; Estroff, L. A.; Whitesides, G. M., Multivalency in ligand design. *Fragment-based approaches in drug discovery* **2006**, *34*, 11-53.
42. Dintzis, H.; Dintzis, R.; Vogelstein, B., Molecular determinants of immunogenicity: the immunon model of immune response. *Proceedings of the National Academy of Sciences* **1976**, *73* (10), 3671-3675.
43. Kiessling, L. L.; Gestwicki, J. E.; Strong, L. E., Synthetic multivalent ligands as probes of signal transduction. *Angewandte Chemie International Edition* **2006**, *45* (15), 2348-2368.
44. Hartwell, B. L.; Martinez-Becerra, F. J.; Chen, J.; Shinogle, H.; Sarnowski, M.; Moore, D. S.; Berkland, C., Antigen-Specific Binding of Multivalent Soluble Antigen Arrays Induces Receptor Clustering and Impedes B Cell Receptor Mediated Signaling. *Biomacromolecules* **2016**, *17* (3), 710-722.
45. Hartwell, B. L.; Smalter Hall, A.; Swafford, D.; Sullivan, B. P.; Garza, A.; Sestak, J. O.; Northrup, L.; Berkland, C., Molecular Dynamics of Multivalent Soluble Antigen Arrays Support a Two-Signal Co-delivery Mechanism in the Treatment of Experimental Autoimmune Encephalomyelitis. *Molecular pharmaceuticals* **2016**, *13* (2), 330-343.
46. Northrup, L.; Sestak, J. O.; Sullivan, B. P.; Thati, S.; Hartwell, B. L.; Siahaan, T. J.; Vines, C. M.; Berkland, C., Co-delivery of autoantigen and b7 pathway modulators suppresses experimental autoimmune encephalomyelitis. *The AAPS journal* **2014**, *16* (6), 1204-1213.
47. Sestak, J.; Mullins, M.; Northrup, L.; Thati, S.; Forrest, M. L.; Siahaan, T. J.; Berkland, C., Single-step grafting of aminooxy-peptides to hyaluronan: a simple approach to multifunctional therapeutics for experimental autoimmune encephalomyelitis. *Journal of Controlled Release* **2013**, *168* (3), 334-340.
48. Sestak, J. O.; Fakhari, A.; Badawi, A. H.; Siahaan, T. J.; Berkland, C., Structure, size, and solubility of antigen arrays determines efficacy in experimental autoimmune encephalomyelitis. *The AAPS journal* **2014**, *16* (6), 1185-1193.
49. Sestak, J. O.; Sullivan, B. P.; Thati, S.; Northrup, L.; Hartwell, B.; Antunez, L.; Forrest, M. L.; Vines, C. M.; Siahaan, T. J.; Berkland, C., Co-delivery of antigen and an immune cell adhesion inhibitor is necessary for efficacy of soluble antigen arrays in experimental autoimmune encephalomyelitis. *Molecular Therapy—Methods & Clinical Development* **2014**, *1*.
50. Thati, S.; Kuehl, C.; Hartwell, B.; Sestak, J.; Siahaan, T.; Forrest, M. L.; Berkland, C., Routes of Administration and Dose Optimization of Soluble Antigen Arrays in Mice with Experimental Autoimmune Encephalomyelitis. *Journal of pharmaceutical sciences* **2014**.

51. Kaminski, T.; Siebrasse, J.-P.; Gieselmann, V.; Kubitscheck, U.; Kappler, J., Imaging and tracking of single hyaluronan molecules diffusing in solution. *Glycoconjugate journal* **2008**, *25* (6), 555-560.
52. Hu, X.; Li, D.; Zhou, F.; Gao, C., Biological hydrogel synthesized from hyaluronic acid, gelatin and chondroitin sulfate by click chemistry. *Acta biomaterialia* **2011**, *7* (4), 1618-1626.
53. Di Meo, C.; Panza, L.; Campo, F.; Capitani, D.; Mannina, L.; Banzato, A.; Rondina, M.; Rosato, A.; Crescenzi, V., Novel Types of Carborane-Carrier Hyaluronan Derivatives via "Click Chemistry". *Macromolecular bioscience* **2008**, *8* (7), 670-681.
54. Tang, W.; Becker, M. L., "Click" reactions: a versatile toolbox for the synthesis of peptide-conjugates. *Chemical Society Reviews* **2014**, *43* (20), 7013-7039.
55. Sokolova, N. V.; Nenajdenko, V. G., Recent advances in the Cu (i)-catalyzed azide-alkyne cycloaddition: focus on functionally substituted azides and alkynes. *RSC Advances* **2013**, *3* (37), 16212-16242.
56. Presolski, S. I.; Hong, V. P.; Finn, M., Copper-Catalyzed Azide-Alkyne Click Chemistry for Bioconjugation. *Current protocols in chemical biology* **2011**, 153-162.
57. Presolski, S. I.; Hong, V.; Cho, S.-H.; Finn, M., Tailored ligand acceleration of the Cu-catalyzed azide-alkyne cycloaddition reaction: practical and mechanistic implications. *Journal of the American Chemical Society* **2010**, *132* (41), 14570-14576.
58. Carrasco, Y. R.; Fleire, S. J.; Cameron, T.; Dustin, M. L.; Batista, F. D., LFA-1/ICAM-1 interaction lowers the threshold of B cell activation by facilitating B cell adhesion and synapse formation. *Immunity* **2004**, *20* (5), 589-599.
59. Anderson, M. E.; Siahaan, T. J., Targeting ICAM-1/LFA-1 interaction for controlling autoimmune diseases: designing peptide and small molecule inhibitors. *Peptides* **2003**, *24* (3), 487-501.
60. Tibbetts, S. A.; Jois, D. S.; Siahaan, T. J.; Benedict, S. H.; Chan, M. A., Linear and cyclic LFA-1 and ICAM-1 peptides inhibit T cell adhesion and function. *Peptides* **2000**, *21* (8), 1161-1167.
61. Delon, J.; Germain, R. N., Information transfer at the immunological synapse. *Current Biology* **2000**, *10* (24), R923-R933.
62. Symer, D. E.; Dintzis, R. Z.; Diamond, D. J.; Dintzis, H. M., Inhibition or activation of human T cell receptor transfectants is controlled by defined, soluble antigen arrays. *The Journal of experimental medicine* **1992**, *176* (5), 1421-1430.
63. Fleming, K. K.; Bovaird, J. A.; Mosier, M. C.; Emerson, M. R.; LeVine, S. M.; Marquis, J. G., Statistical analysis of data from studies on experimental autoimmune encephalomyelitis. *Journal of neuroimmunology* **2005**, *170* (1), 71-84.

Chapter V: Conclusions and Future Work

1. Conclusions

Multivalent soluble antigen arrays have emerged as a promising option for antigen-specific immunotherapy (ASIT) with potential to modulate the immune response to specific, disease-causing autoantigens. Creation of antigen-specific tolerogenic therapies in humans would be groundbreaking, reducing or eliminating the risk of global immunosuppression in the treatment of autoimmune disease. As reviewed in Chapter 1, multivalent antigen presentation has long been utilized in vaccine design to elicit an antigen-specific immunogenic response, but has since evolved for applications where immune tolerance is desired, such as reversing autoimmunity. Nanomaterials can be engineered to have specific physicochemical properties (i.e., size, charge, and shape) to influence biodistribution and immune response, while multivalent ligand display (i.e., number, density, ratio, and incorporation of secondary inhibitory signals) can be tailored to direct the cellular response towards tolerance versus immunogenicity.

Multivalent soluble antigen arrays (S $A_gA_{PLP:LABL}$) were designed using this rationale, consisting of a flexible hyaluronic acid (HA) linear polymer backbone co-grafted with multiple copies of autoantigen peptide (PLP) and cell adhesion inhibitor peptide (LABL), to induce tolerance to a specific multiple sclerosis autoantigen. Previous studies showed that S $A_gA_{PLP:LABL}$ significantly alleviated disease in EAE, a murine model of MS.¹⁻³ Our original hypothesis was that the two signals, PLP and LABL, enabled S $A_gA_{PLP:LABL}$ to target antigen presenting cells (APCs) and interrupt signaling during the immunological synapse, which requires both a primary antigenic signal and secondary costimulatory signal to activate T cells against autoantigen. Chapters 2, 3, and 4 sought to evaluate this hypothesis and elucidate therapeutic cellular mechanisms while identifying molecular properties that contribute to therapeutic efficacy against EAE.

In Chapter 2, we explored the role of two-signal co-delivery in determining $\text{SAgA}_{\text{PLP:LABL}}$ therapeutic potential by evaluating EAE clinical results, *in silico* molecular dynamics simulations, and nanomaterial properties for various covalent and physical combinations of HA, PLP, and LABL. Only $\text{SAgA}_{\text{PLP:LABL}}$ and a mixture of $\text{HA}_{\text{PLP}}+\text{HA}_{\text{LABL}}$ were therapeutic against EAE, while a mixture of the components (HA+ PLP+LABL), HA alone, HA grafted with PLP only (HA_{PLP}), and HA grafted with LABL only (HA_{LABL}) were not, indicating that co-presentation of both signals on HA was necessary for therapeutic efficacy. Molecular dynamics simulations revealed that stable intermolecular interactions and chain entanglement between HA_{PLP} and HA_{LABL} in the homopolymer mixture likely facilitated co-transport of the two signals. The results suggested that co-delivery of both primary autoantigen and secondary inhibitory signal in the same spatial and temporal context was necessary for therapeutic efficacy, and that $\text{SAgA}_{\text{PLP:LABL}}$ provided an effective platform for two-signal co-delivery.

In Chapter 3, we investigated the $\text{SAgA}_{\text{PLP:LABL}}$ cellular mechanism in a model B cell system by evaluating binding, specificity, and signaling modulation *in vitro*. These studies were based on the hypothesis that $\text{SAgA}_{\text{PLP:LABL}}$ targets B cells (as APCs) and inhibits antigen-specific signaling to mediate the autoimmune response. Indeed, $\text{SAgA}_{\text{PLP:LABL}}$ exhibited enhanced B cell binding compared to HA, HA_{PLP} , and HA_{LABL} . Specific binding was driven by the PLP peptide and it was determined through IgM blocking studies that BCR was a target of $\text{SAgA}_{\text{PLP:LABL}}$ binding, supporting our hypothesis that $\text{SAgA}_{\text{PLP:LABL}}$ targets B cells in an antigen-specific manner. $\text{SAgA}_{\text{PLP:LABL}}$ induced mature receptor clustering to a greater extent than HA, HA_{PLP} , or HA_{LABL} , which correlated with greater reduction in BCR-mediated calcium signaling. Taken together, these results indicated that mechanisms of enhanced antigen-specific binding, mature

receptor clustering, and dampened BCR-mediated signaling in B cells may contribute to SAg_{PLP:LABL} therapeutic efficacy.

In Chapter 4, we developed new click-conjugated multivalent soluble antigen arrays and evaluated them *in vitro* and *in vivo* as therapeutic agents in EAE. Hydrolyzable SAg_{PLP:LABL}, studied up to this point, employed a degradable linker to co-deliver antigen (PLP) and cell adhesion inhibitor (LABL) peptides. This approach was consistent with our earlier two-signal hypothesis of SAgA molecules, which would necessitate antigen uptake, processing, and presentation. Conversely, ‘click SAg_{PLP:LABL}’, or cSAg_{PLP:LABL}, is a modified version of the SAg_{PLP:LABL} molecule with multiple PLP and LABL peptides conjugated to HA using non-hydrolyzable linker chemistry (Copper-catalyzed Azide-Alkyne Cycloaddition (CuAAC)). Building upon work from Chapter 3, these studies sought to establish therapeutic efficacy of cSAg_{PLP:LABL} *in vivo* while identifying a potential therapeutic mechanism by evaluating binding avidity and signaling modulation *in vitro*. Click-conjugated cSAg_{PLP:LABL} exhibited greatly enhanced binding in B cells compared to hydrolyzable SAg_{PLP:LABL}, indicating that non-hydrolyzable multivalent ligand increased the avidity of the molecule. Furthermore, cSAg_{PLP:LABL} exhibited greater capacity for reducing and inhibiting BCR-mediated signaling as compared to SAg_{PLP:LABL}. Imaging revealed that cSAg_{PLP:LABL} binding caused BCR clustering, another marker indicative of BCR engagement and signaling modulation. Lastly, cSAg_{PLP:LABL} exhibited significantly enhanced *in vivo* efficacy against EAE, achieving equivalent efficacy as SAg_{PLP:LABL} at only a quarter of the dose. Taken together, these results indicated that non-hydrolyzable conjugation increased the avidity of cSAg_{PLP:LABL} and that enhanced binding drives *in vivo* efficacy through modulated BCR-mediated signaling.

To conclude, this dissertation covered the development of multivalent soluble antigen arrays as a promising option for ASIT while elucidating molecular and cellular mechanisms that contribute to therapeutic efficacy against EAE. The molecular properties of (1) multivalent presentation of antigen, (2) co-presentation of autoantigen and adhesion inhibitor, and (3) non-hydrolyzable conjugation were combined in cSAgA_{PLP:LABL} to achieve significant therapeutic efficacy in EAE. Results from Chapters 3 and 4 disputed our early two-signal hypothesis that SAgAs target the immunological synapse, and instead pointed to a mechanism in which SAgAs target BCR signaling while remaining on the cell surface. These results indicated that efficacy was driven by enhanced, antigen-specific binding with B cells and subsequent dampening of BCR-mediated signaling. Enhanced binding avidity may be attributed to combined affinities of both PLP-driven specific binding and LABL-promoted adhesion. Antigen-specific targeting of the BCR was supported by binding and imaging studies that showed BCR binding and clustering, and by calcium flux studies that showed modulation of BCR-mediated signaling. These observations are consistent with B cell anergy, a state of antigen unresponsiveness that is induced through continuous BCR binding, occupation, and clustering in the absence of secondary costimulatory signal and marked by reduced calcium flux signaling.⁴⁻⁷ Thus, our conclusions point to B cell anergy as the cSAgA_{PLP:LABL} therapeutic mechanism and present a promising strategy for inducing antigen-specific tolerance in autoimmunity.

2. Future Work

Thus far, we have drilled into the cSAgA_{PLP:LABL} cellular mechanism in the context of an immortalized B cell line and our results have pointed to the induction of B cell anergy. However, the cellular mechanism should be evaluated in a disease-specific primary cell system to fully

understand how SAgAs are interacting in an antigen-educated mixed cell population. Ongoing work in our laboratory has been seeking to determine whether multivalent soluble antigen arrays target B cells in an EAE mouse splenocyte mixed immune cell population and whether this results in an anergic phenotype.

cSAgA binding and targeting was evaluated *ex vivo* in mixed splenocytes isolated from healthy and EAE mice using flow cytometry binding assays developed in Chapter 3. Splenocytes were antibody-labeled for B cells (CD19⁺), T cells (CD3⁺), and dendritic cells (CD11c⁺). Binding trends again reflected those observed in Chapters 3 and 4, where fcSAgA_{PLP:LABEL} exhibited the highest amount of binding followed by fcHA_{PLP} (Figure 1). fcSAgA_{PLP:LABEL} preferentially targeted B cells, in particular a subclass of B cells called autoimmune-associated B cells (ABCs) (CD19⁺CD11c⁺) that are potent antigen presenting cells found in the spleen during autoimmune disease (Figure 1B, Figure 2).⁸⁻¹⁰ Furthermore, binding was significantly higher in EAE B cells than healthy B cells, indicating disease-specific targeting, which was not the case in T cells (Figure 3). These results support our hypothesis that soluble antigen arrays target B cells and APCs over other cell types, and do so in a disease-specific manner.

In addition to reduced calcium flux signaling, another result of B cell anergy is down-regulation of costimulatory markers such as CD80 and CD86.⁴⁻⁷ Costimulatory signal presentation by APCs is essential for autoreactive T cell activation; reception of a primary antigenic signal in the absence of a secondary costimulatory signal leads to T cell anergy.¹¹⁻¹⁴ Induction of B cell anergy can therefore have a two-fold therapeutic effect by inducing (1) an effector B cell population that is not responsive to autoantigen and (2) B cells with reduced APC capacity.

Thus, we investigated CD80/CD86 expression in splenocytes under two conditions: (1) harvested from EAE mice at peak of disease and treated *in vitro* during simultaneous PLP challenge to evaluate the effect on costimulatory signaling, and (2) harvested from mice treated *in vivo* and re-challenged with PLP *ex vivo* to evaluate lasting tolerance. First, *in vitro* treatment with cSAgA_{PLP:LABEL}, cHA_{PLP}, and cHA_{PLP}+cHA_{LABEL} caused significant down-regulation of CD86 in EAE splenocytes harvested from mice at peak of disease, causing B cells and autoimmune-associated B cells (ABCs) to signal more like healthy cells rather than activated APCs (Figure 4BC). Furthermore, *in vivo* treatment with cSAgA_{PLP:LABEL}, cHA_{PLP}, and cHA_{PLP}+cHA_{LABEL} significantly alleviated disease in EAE (Figure 4A). Upon *ex vivo* rechallenge with PLP, B cells and ABCs from these mice did not respond with a significant increase in CD80/CD86 expression like the PBS control, again behaving more like healthy cells (Figure 4DE). Combined, these results indicate that treatment with cSAgA_{PLP:LABEL}, cHA_{PLP}, and cHA_{PLP}+cHA_{LABEL} induced PLP-specific anergy in B cells, resulting in reduced APC capacity and lasting tolerance to autoantigen.

These exciting preliminary results have encouraged us to continue exploring cSAgA as a therapeutic platform, B cells as a therapeutic target, and induction of B cell anergy as a therapeutic cellular mechanism. In particular, autoimmune-associated B cells have emerged as a therapeutic target of interest; specific targeting and effects on this population should be investigated in future work. Additional studies should be performed to validate B cell anergy as the cellular mechanism in EAE splenocytes. Calcium flux signaling assays will be performed in antibody-labeled splenocytes to determine whether BCR-mediated signaling is reduced in primary B cells, as in Raji B cells. Reduction of BCR-mediated signaling in EAE B cells (while unchanged in healthy B cells) would indicate that cSAgA_{PLP:LABEL} is acting in an antigen-specific

manner. Another result of B cell anergy is apoptosis and reduced B cell lifespan.^{4-6, 12} Thus, induction of anergy may be explored by evaluating apoptosis and cell death through flow cytometry assays (i.e., using Annexin-V/PI staining) in antibody-labeled splenocytes. Again, increased apoptosis in EAE B cells over healthy B cells would suggest an antigen-specific mechanism.

Downstream T cell response should be investigated to reveal whether T cell activation is in fact inhibited as a result of the observed B cell anergic behavior. IL-2, TNF- α , and IFN- γ are key cytokines associated with an inflammatory T cell response, while IL-10 is associated with anergy and a regulatory lymphocyte response. These cytokines will be measured in EAE splenocytes following *in vivo* treatment and *in vitro* PLP rechallenge using enzyme-linked immunosorbent analysis (ELISA) to identify a reduction in T cell activation and shift towards a regulatory response. T cell activation, which triggers T cell clonal expansion, may also be evaluated using a carboxyfluorescein succinimidyl ester (CFSE) flow cytometry assay to measure T cell proliferation in EAE splenocytes following *in vitro* treatment with cSAg_{PLP:LABEL}.

Our *in vivo* results point to another avenue to explore. cHA_{PLP} (with a conjugation of ~15 PLP per backbone) exhibited significant therapeutic efficacy *in vivo*, to a similar extent as cSAg_{PLP:LABEL} (with a conjugation of ~10 PLP and ~10 LABEL per backbone) (Figure 4A). cHA_{PLP} *in vivo* efficacy was matched by significant reduction in CD80/CD86 expression in EAE splenocytes (Figure 4B-E). These results suggest that non-hydrolyzable conjugation of antigen at a slightly higher valency may enhance avidity to a similar extent as two signals in cSAg_{PLP:LABEL}. It will be interesting in future studies to investigate varying antigen valency in

cHA_{PLP} and the effect on B cell binding, BCR-mediated signaling, and therapeutic efficacy *in vivo*.

Finally, multivalent soluble antigen arrays provide a versatile and translatable platform with tremendous potential for application to other autoimmune diseases. This is particularly the case now that we have identified cornerstone therapeutic molecular properties and a probable therapeutic cellular mechanism. Additionally, the versatility of the click conjugation reaction in the new cSAgA platform enables improved control over valency and ligand selection. cSAgA can be applied to other autoimmune diseases that are propagated by a B cell response by changing the autoantigen to one that is disease-specific. For example, cSAgA can be applied to type 1 diabetes by conjugating hormonally inactive insulin to the HA backbone in various contexts. Ongoing work in this area will continue to strengthen our understanding of antigen-specific multivalent immunotherapies and refine the design criteria needed to develop better ASIT to treat autoimmune disease.

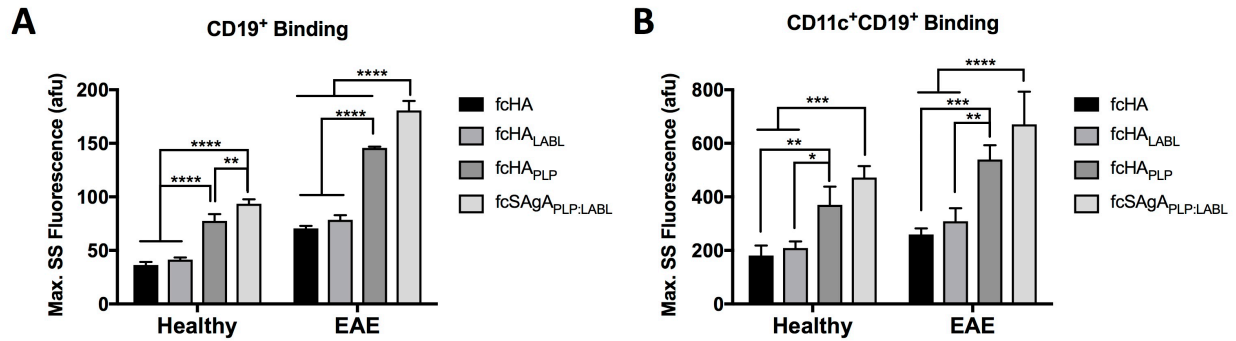


Figure 1. Maximum steady state (max. SS) binding in antibody-labeled splenocytes isolated from EAE and healthy mice determined by flow cytometry, comparing binding of fluorescently-labeled click conjugates with **(A)** CD19⁺ B cells and **(B)** CD19⁺CD11c⁺ autoimmune-associated B cells (ABCs). Splenocytes were isolated from mice at peak of disease and cultured for 72 hr prior to the experiment. Statistical significance (between fcHA, fcHA_{LABL}, fcHA_{PLP}, and fcSAgA_{PLP:LABL}) was determined by ANOVA followed by Tukey's post hoc test with $p < 0.05$ and $n = 3$ (* $p < 0.05$, ** $p < 0.01$, *** $p < 0.001$, **** $p < 0.0001$).

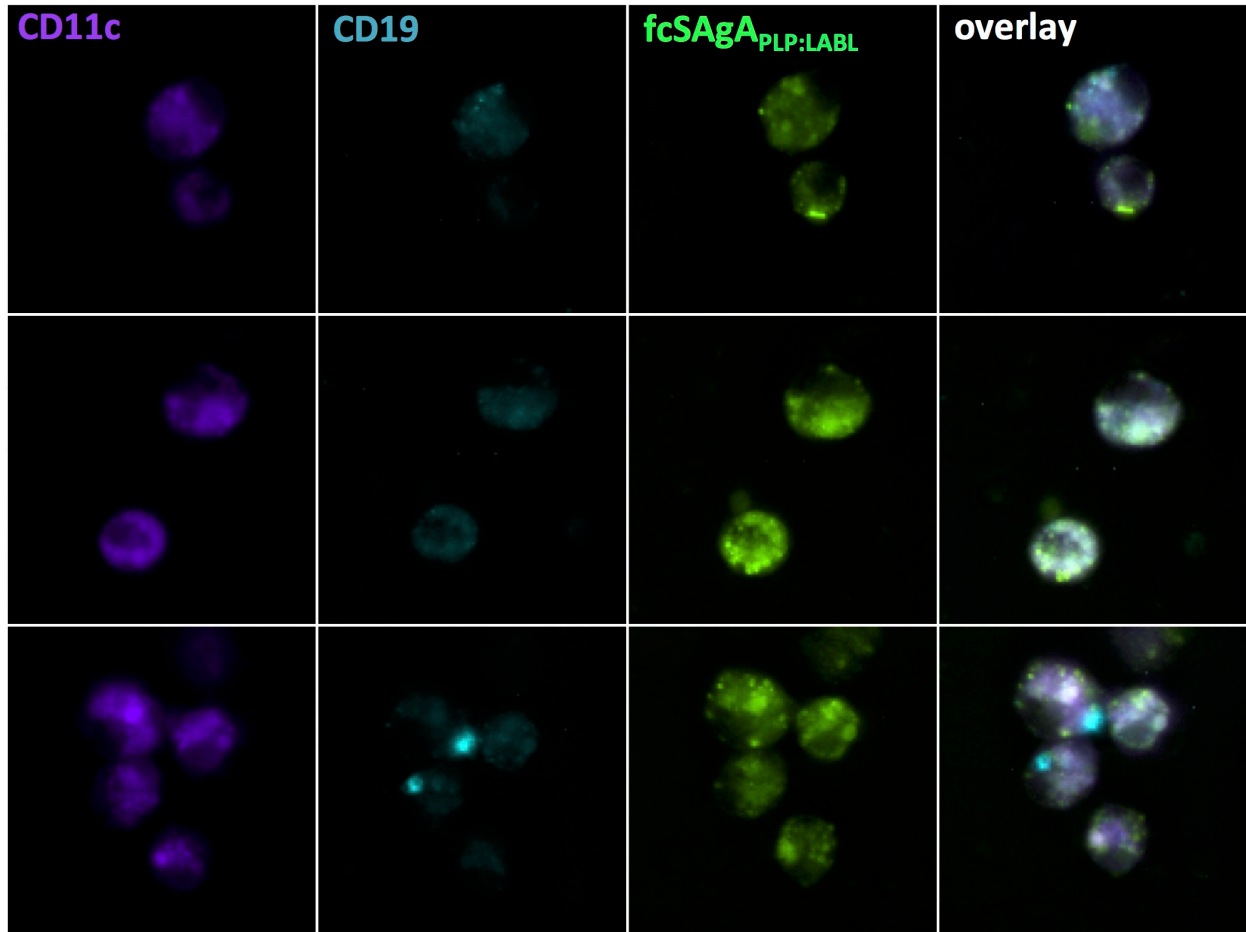


Figure 2. Fluorescence microscopy showing binding of Penn Green-labeled $\text{fcSAgA}_{\text{PLP:LABEL}}$ (Panel 3) with $\text{CD19}^+\text{CD11c}^+$ autoimmune-associated B cells (ABCs) isolated from the spleen of an EAE mouse. Splenocytes were antibody-labeled with Pacific Blue-conjugated CD11c (Panel 1) and AlexaFluor 647-conjugated CD19 (Panel 2) to identify ABCs. Captured using the M04S plate and CellASIC Onyx Microfluidics platform on an Olympus IX81 inverted Epifluorescence microscope. Magnification: 60X air.

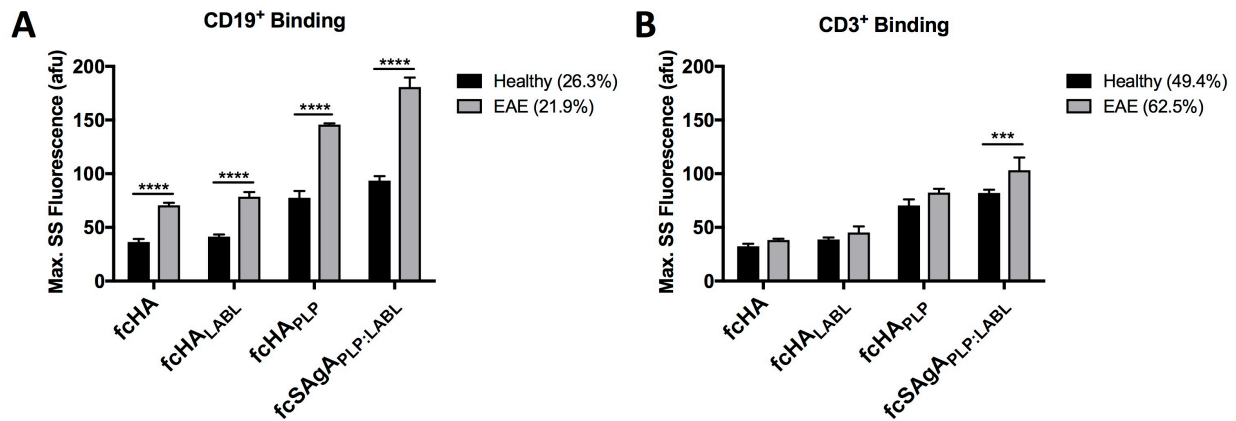


Figure 3. Maximum steady state (max. SS) binding in antibody-labeled splenocytes isolated from EAE and healthy mice determined by flow cytometry, comparing binding of fluorescently-labeled click conjugates with **(A)** CD19⁺ B cells and **(B)** CD3⁺ T cells. Splenocytes were isolated from mice at peak of disease and cultured for 72 hr prior to the experiment. Statistical significance (between healthy and EAE) was determined by ANOVA followed by Tukey’s post hoc test with $p < 0.05$ and $n = 3$ (* $p < 0.05$, ** $p < 0.01$, *** $p < 0.001$, **** $p < 0.0001$).

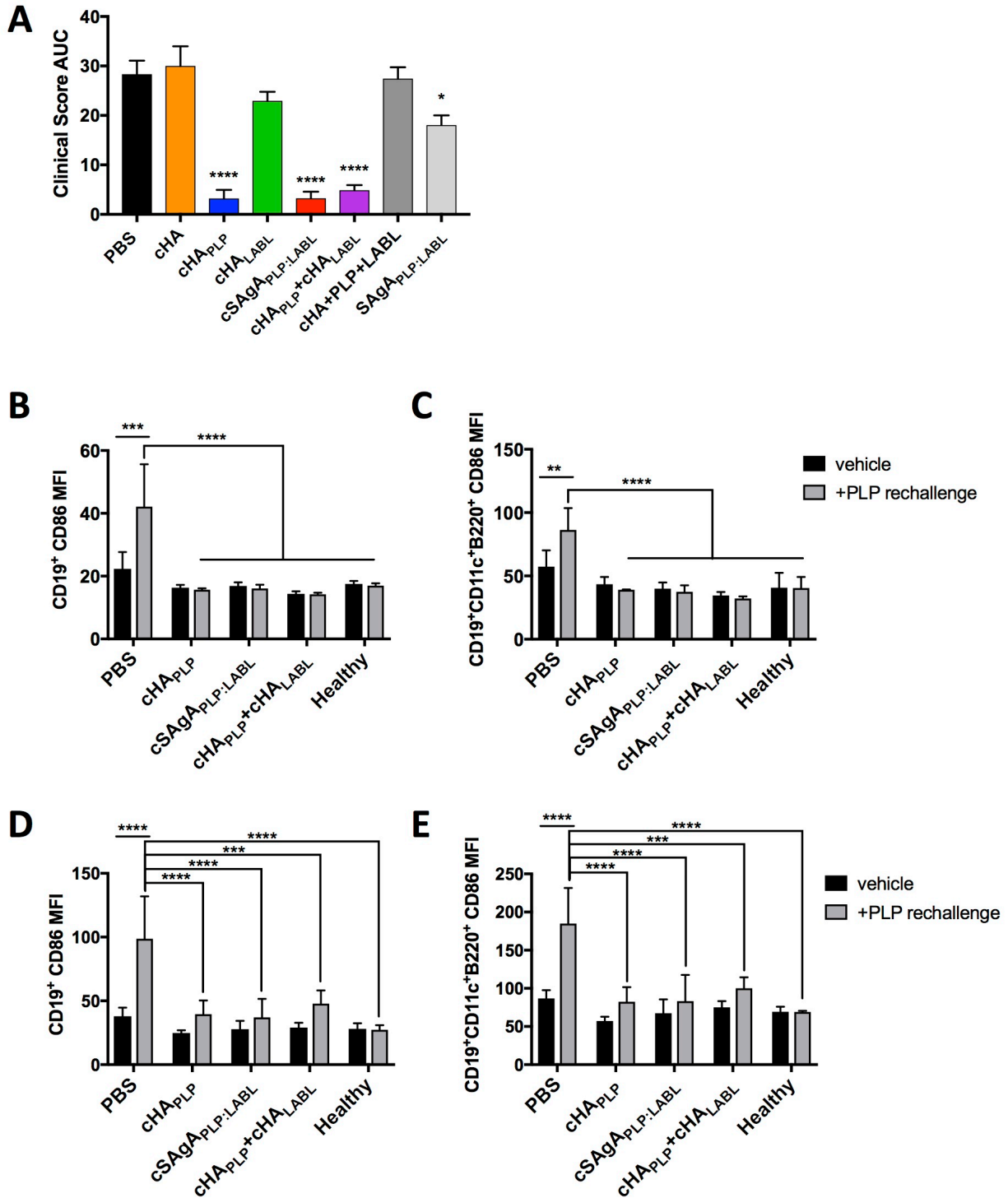


Figure 4. Costimulatory marker expression was evaluated in antibody-labeled EAE splenocytes following *in vitro* or *in vivo* treatment with click conjugates. **(A)** EAE clinical disease score area under the curve (AUC) indicated significant therapeutic efficacy from *in vivo* treatment with

cHA_{PLP}, cSAgA_{PLP:LABEL}, and cHA_{PLP}+cHA_{LABL} (50 nmol PLP dose). **(B/C)** Splenocytes isolated from EAE mice at peak of disease were treated with the groups from (A) for 72 hr *in vitro* in the presence or absence of PLP. CD86 expression (anti-CD86 mean fluorescence intensity, MFI) was evaluated by flow cytometry in **(B)** CD19⁺ B cells and **(C)** CD19⁺CD11c⁺B220⁺ autoimmune-associated B cells (ABCs) to evaluate APC costimulatory signaling. **(D/E)** Splenocytes isolated from mice on day 25 following *in vivo* treatment in (A) were rechallenged with/without PLP for 72 hr. CD86 expression was evaluated by flow cytometry in **(B)** CD19⁺ B cells and **(C)** CD19⁺CD11c⁺B220⁺ ABCs to evaluate lasting tolerance to autoantigen. Statistical significance (compared to the negative PBS control) was determined by ANOVA followed by Tukey's post hoc test with $p < 0.05$ and $n = 3$ (* $p < 0.05$, ** $p < 0.01$, *** $p < 0.001$, **** $p < 0.0001$).

References

1. Sestak, J.; Mullins, M.; Northrup, L.; Thati, S.; Forrest, M. L.; Siahaan, T. J.; Berkland, C., Single-step grafting of aminoxy-peptides to hyaluronan: a simple approach to multifunctional therapeutics for experimental autoimmune encephalomyelitis. *Journal of Controlled Release* **2013**, *168* (3), 334-340.
2. Sestak, J. O.; Fakhari, A.; Badawi, A. H.; Siahaan, T. J.; Berkland, C., Structure, size, and solubility of antigen arrays determines efficacy in experimental autoimmune encephalomyelitis. *The AAPS journal* **2014**, *16* (6), 1185-1193.
3. Sestak, J. O.; Sullivan, B. P.; Thati, S.; Northrup, L.; Hartwell, B.; Antunez, L.; Forrest, M. L.; Vines, C. M.; Siahaan, T. J.; Berkland, C., Co-delivery of antigen and an immune cell adhesion inhibitor is necessary for efficacy of soluble antigen arrays in experimental autoimmune encephalomyelitis. *Molecular Therapy—Methods & Clinical Development* **2014**, *1*.
4. Getahun, A.; O'Neill, S. K.; Cambier, J. C., Establishing anergy as a bona fide in vivo mechanism of B cell tolerance. *The Journal of Immunology* **2009**, *183* (9), 5439-5441.
5. Gauld, S. B.; Benschop, R. J.; Merrell, K. T.; Cambier, J. C., Maintenance of B cell anergy requires constant antigen receptor occupancy and signaling. *Nature immunology* **2005**, *6* (11), 1160-1167.
6. Cambier, J. C.; Gauld, S. B.; Merrell, K. T.; Vilen, B. J., B-cell anergy: from transgenic models to naturally occurring anergic B cells? *Nature Reviews Immunology* **2007**, *7* (8), 633-643.
7. Jones, D. S., Multivalent compounds for antigen-specific B cell tolerance and treatment of autoimmune diseases. *Current medicinal chemistry* **2005**, *12* (16), 1887-1904.
8. Rubtsov, A. V.; Rubtsova, K.; Kappler, J. W.; Jacobelli, J.; Friedman, R. S.; Marrack, P., CD11c-expressing B cells are located at the T cell/B cell border in spleen and are potent APCs. *The Journal of Immunology* **2015**, *195* (1), 71-79.
9. Rubtsov, A. V.; Rubtsova, K.; Fischer, A.; Meehan, R. T.; Gillis, J. Z.; Kappler, J. W.; Marrack, P., Toll-like receptor 7 (TLR7)-driven accumulation of a novel CD11c+ B-cell population is important for the development of autoimmunity. *Blood* **2011**, *118* (5), 1305-1315.
10. Rubtsov, A. V.; Rubtsova, K.; Kappler, J. W.; Marrack, P., TLR7 drives accumulation of ABCs and autoantibody production in autoimmune-prone mice. *Immunologic research* **2013**, *55* (1-3), 210-216.
11. Mueller, D. L.; Jenkins, M. K.; Schwartz, R. H., Clonal expansion versus functional clonal inactivation: a costimulatory signalling pathway determines the outcome of T cell antigen receptor occupancy. *Annual review of immunology* **1989**, *7* (1), 445-480.
12. Feldmann, M.; Steinman, L., Design of effective immunotherapy for human autoimmunity. *Nature* **2005**, *435* (7042), 612.
13. Miller, S. D.; Turley, D. M.; Podojil, J. R., Antigen-specific tolerance strategies for the prevention and treatment of autoimmune disease. *Nature Reviews Immunology* **2007**, *7* (9), 665.
14. Mueller, D. L., Mechanisms maintaining peripheral tolerance. *Nature immunology* **2010**, *11* (1), 21-27.